UAB
Universitat Autònoma de Barcelona

G protein-coupled receptors: providing mechanistic explanations to ligand-receptor and receptor-receptor interactions through in silico studies

A doctoral thesis

Directors: Jesús Giraldo and James Dalton

Doctoral student: Adrián Ricarte

Laboratory of Molecular Neuropharmacology and Bioinformatics, Unitat de Bioestadística and Institut de Neurociències, Universitat Autònoma de Barcelona, 08193 Bellaterra, Spain

Unitat de Neurociència Traslacional, Parc Taulí Hospital Universitari, Institut d'Investigació i Innovació Parc Taulí (I3PT), Institut de Neurociències, Universitat Autònoma de Barcelona, Spain

Instituto de Salud Carlos III, Centro de Investigación Biomédica en Red de Salud Mental, CIBERSAM, Spain

Abstract

G protein-coupled receptors (GPCRs) constitute the largest family of membrane proteins in the human genome. These membrane proteins are made up of seven transmembrane helices connected by intracellular and extracellular loops. The GPCR superfamily can be classified into five families or classes, with many implications in the regulation of the central nervous system (CNS). Therefore, they represent main drug-targets to therapeutically regulate neurologic disorders such as Alzheimer's disease, frontotemporal dementia, Parkinson's disease, Huntington's disease, schizophrenia, pain and addiction. These seven-helix transmembrane receptors have gained increasing interest to mechanistically elucidate the molecular determinants of receptor activation and the effect that the membrane environment has on their functionality.

By making use of molecular computational techniques, this study examines the effect that either ligand binding or receptor oligomerization has on the conformational landscape of GPCRs. Molecular dynamics simulations enable the time-dependent study of GPCRs at an atomic level. Trajectories at a microsecond time-scale may allow the mechanistic description of dynamic atomic interactions that occur in the receptor structure and determine its activation state and functionality. Results obtained from these computational techniques were aimed to provide theoretical structural explanations to experimental functional evidence.

A number of GPCRs are included in this study. Briefly, the viability of formation, molecular stability and receptor-receptor cross-modulation are analyzed for: angiotensin 1 receptor (AT1R) and adenosine 2A receptor (A2AR) heterotetramers, serotonin 2A receptor (5-HT$_{2A}$R) and metabotropic glutamate receptor 2 (mGlu2R) hetero-oligomers, and dopamine D2 receptor (D2R) protomers within homodimeric complexes. In addition to these studies on GPCR oligomerization, a detailed analysis of monomeric GPCR activation is made by comparing two structurally and functionally different agonists, morphine and fentanyl, on the activation of the μ-opioid receptor.

The results presented in this thesis show the influence of time-dependent ligand-protein and protein-protein interactions on the modulation of the conformational landscape and functionality of class A and class C GPCRs from an atomic perspective. The computational work has been done either in collaboration with experimental groups or independently. The results show the contribution of molecular modelling, molecular dynamics simulations and other computational techniques to the

mechanistic understanding of GPCR function. These computational approaches complement experimental ones on structure-based GPCR drug design and mechanistic-based molecular therapies.

List of Contents

List of Illustrations

Abbreviations of keywords

GPCR	G protein-coupled receptor
TM	Transmembrane helix
TMD	Transmembrane domain
ECL	Extracellular loop
ICL	Intracellular loop
MD	Molecular dynamics
AT1R	Angiotensin receptor type 1
A2AR	Adenosine A2A receptor
D2R	Dopamine D2 receptor
mGlu2R	Metabotropic glutamate receptor 2
$5\text{-}HT_{2A}R$	Serotonin 2A receptor
mMOR / hMOR	Murine or human μ-opioid receptor
MRF	Morphine
FTL	Fentanyl
NTX	Naltrexone

1. Introduction

1.1. Background

1.1.1. G protein-coupled receptors are relevant targets for drugs

The footprint of human protein target classes across disease areas presents five enriched families accounting for the 70% of all FDA-approved drugs [1](Santos et al. 2017), [2](Hauser et al. 2017): G protein-coupled receptors (GPCRs), ion channels, protein kinases, nuclear hormone receptors and proteases. From these superfamilies, the most largely drug targeted one is the former, responsible for the therapeutic effect of approximately 33% of all drugs and representing the 12% of all human protein targets [1](Santos et al. 2017), [2](Hauser et al. 2017). GPCRs are membrane proteins with modest sequence similarity between them but high structural conservation. They are formed by seven transmembrane helices packed into a helical cylinder connected by three intracellular loops, three extracellular loops (ICLs and ECLs, respectively, Figure 1), an extracellular N-terminus and an intracellular C-terminus [3](Zou et al. 2019),[4](Weis et al. 2018). This GPCR superfamily can be classified into five families or classes: rhodopsin (class A), secretin (class B1), adhesion (class B2), glutamate (class C) and frizzled/taste (class F) [5](Alexander et al. 2021). GPCRs mediate many physiological responses through the binding of a wide range of molecules, namely neurotransmitters, hormones, odorants, tastants, amino acids, polypeptides, nucleotides, lipids, ions and even photons. In addition to these ligand-receptor interactions through the orthosteric binding site, allosteric modulations by receptor-receptor interactions, membrane lipids, ions and synthetic molecules may occur. Propagation of the GPCR activation message is mainly determined by the intracellular binding of various transducer proteins: guanine nucleotide-binding proteins (G-proteins), G protein-coupled receptor kinases (GRKs) or arrestins, thus activating different signalling pathways. New biochemical and pharmacological findings associated with allosterism, receptor oligomerization, and multiple signalling pathways have led to new paradigms in GPCR chemical biology. These have widened the chemical space for drug discovery, as demonstrated by the high number of new drug targets and research efforts in GPCR structural biology, pharmacology and modelling [2](Hauser et al. 2017). Consequently, these receptors are among the most successful targets for therapeutic development of central nervous system

(CNS) disorders including Alzheimer's disease, dementia, Parkinson's disease, Huntington's disease, schizophrenia, pain and addiction [6](Huang et al. 2017),[7](Foster et al. 2017).

The understanding of structural and functional properties of GPCRs may greatly facilitate the rational design of active compounds. In order to obtain conformational pictures of GPCRs, two main experimental techniques are used: i) X-ray crystallography and ii) nuclear magnetic resonance spectroscopy (NMR). X-ray crystallography is based on the processing of diffraction patterns obtained when a purified crystallized sample at high concentration is exposed to an X-ray beam, which through a map of electron density permits the building of an accurate thermodynamically favoured conformation of the molecular structure [8](Smyth et al. 2000). X-ray crystallography provides a high-resolution static molecular snapshot of GPCRs [8](Smyth et al. 2000). Conversely, NMR relies upon the quantum mechanical properties of the nuclear spins of atoms, which, when placed in a magnetic field, show different energy levels at specific resonance frequencies [9](Tikhonova et al. 2009), [10](Puthenveetil et al. 2019). Using the three-dimensional position of each atom type with respect to its neighbors, this technique allows the generation of the protein structure [10](Puthenveetil et al. 2019). NMR, differently from X-ray crystallography, generates flexible and dynamic pictures of receptor structures, offering insights into the molecular mechanisms by sacrificing resolution to a certain degree [9](Tikhonova et al. 2009), [10](Puthenveetil et al. 2019). As GPCR crystallization is challenging, computational techniques such as homology modelling, protein-protein docking and long-timescale molecular dynamics (MD) simulations can shed light onto the functional significance of GPCR conformational landscape at an atomic level.

1.1.2. GPCR homo- or hetero-oligomerization

Until the last couple of decades, GPCRs were generally believed to function as monomeric complexes. However, recent data support the idea that GPCRs can physically interact with other protomers of the same or different type (homo- or hetero- complexes) thus forming dimers, trimers, tetramers or even higher oligomeric complexes [11](Barreto et al. 2020). Despite class C GPCRs constitutively forming dimers, a growing number of studies have shown the relevance of such complexes in class A GPCRs [11](Barreto et al. 2020). Physical

interactions between GPCRs are established through particular interfaces between transmembrane (TM) helical regions. Several interfaces have been widely described in GPCRs with the most frequently formed being: i) TM helix 1 and 7 (TM1-TM7), ii) TM4-TM5, and iii) TM5-TM6 interfaces [11](Barreto et al. 2020). Recent data support a dynamic equilibrium between monomeric and oligomeric complexes in the cell membrane as a response to environmental factors, such as ligand binding [11](Barreto et al. 2020). The effect one protomer exerts on the other in the oligomerization process is not yet fully understood. However, it can be categorized as: i) allosteric modulation of the orthosteric pocket of the opposite protomer, ii) conformational changes of the intracellular pockets of the protomers, and iii) the formation of new allosteric binding sites [11](Barreto et al. 2020). The existence of direct cross-talk and mutual regulation between GPCRs protomers, in addition to the physiological relevance that rely on the formation of such complexes, contributes to the development of new therapeutic approaches and oligomer-targeting drug design [11](Barreto et al. 2020), [12](Ferré et al. 2008), [13](Botta et al. 2020), [14](González-Maeso 2011).

1.1.3. GPCR activation

In a timescale of nanoseconds to milliseconds, GPCRs can conformationally change from an inactive- to an active-like state, which allows the intracellular binding of G proteins and GRKs or β-arrestin, leading to G protein-dependent and G protein-independent pathways, respectively [15](Gurevich et al. 2017), [16](Tan et al. 2018). The conformational equilibrium of GPCRs is not shifted towards single inactive or active conformations, and instead multiple energetic stable conformations exist covering a whole spectrum with different intermediate states of the receptor [15](Gurevich et al. 2017). GPCRs present constitutive activation, which can be modulated by endogenous or exogenous ligands. Therefore, ligands can modulate the response of the receptor acting as: i) full agonists (the system yields the maximal response of the receptor), ii) partial agonists (lower efficacy than full agonists: the asymptotic response at high ligand concentrations is lower than that of full agonists), iii) neutral antagonists (ligands that occupy the receptor binding site without changing the basal response, iv) partial inverse agonists (partially reducing the fraction of constitutively active receptor states or partially reducing the basal response) or iv) full inverse agonists (totally abolishing the presence of receptor active states meaning no response is

observed) [17](Berg et al. 2018). Structural and biophysical studies indicate that specific active-like conformations of GPCRs are required for the different binding of each intracellular partner [15](Gurevich et al. 2017). The differential activation of the signalling cascades associated with these transducer couplings may present beneficial or negative therapeutic effects, which differ between GPCRs. Most ligands are able to activate all the different signal cascades of a GPCR (balanced or unbiased agonists). However, a wide range of studies have attempted to identify ligands that induce or select, by particular ligand-receptor interactions, partner-specific conformational changes (i.e. biased agonists) [16](Tan et al. 2018). Experimental studies, such as for instance mutagenesis, crystallization of GPCR structures and molecular dynamics simulations, have shown that some activation mechanisms of GPCRs present common features in each family.

1.1.3.1. Class A GPCR activation

Class A is one of the largest families of GPCRs, and includes several receptors present in this thesis such as: serotonin 2A receptor (5-HT$_{2A}$R), adenosine 2A receptor (A2AR), angiotensin receptor type 1 (AT1R), dopamine D2 receptor (D2R) and μ-opioid receptor (MOR). Different ligands targeting Class A GPCRs identify an orthosteric binding pocket at the extracellular side of the transmembrane domains (TMD), which directly interacts with sidechains that induce or select conformational changes of particular residues and TM helices, thus transmitting the signal to the intracellular side of the receptor [18](Dalton et al. 2015), [19](Zhou et al. 2019). During the activation of Class A GPCRs, TM6 noticeably separates from TM3 undergoing an outward movement by decreasing interactions (ionic, H-bonding, hydrophobic) between these helices [18](Dalton et al. 2015). The loss of these interactions is compensated by an increase of TM5-TM6 H-bonding, followed by an inward movement of TM5 [18](Dalton et al. 2015). In parallel, the outward movement of TM6 permits TM7 to move inward, towards the protein core, and an upward translocation of TM3 from its inactive position [18](Dalton et al. 2015), [20](Lans et al. 2015). These significant conformational changes of TM helices are accompanied by common activation microswitches, from the extracellular to the intracellular side: i) CWxP (including the so-called Trp toggle switch) [19](Zhou et al. 2019), [21](Olivella et al. 2013), ii) Na+ binding pocket [18](Dalton et al. 2015), [21](Olivella et al. 2013), [22](Vickery et al. 2018), iii) P-I-F

(also known as core triad) [19](Zhou et al. 2019), [23](White et al. 2018), [24](Bruzzese et al. 2018), iv) NPxxY [19](Zhou et al. 2019), [23](White et al. 2018) and v) E/DRY (also known as ionic-lock) [19](Zhou et al. 2019), [23](White et al. 2018), [25](Fleetwood et al. 2020), where "x" represents any residue.

The binding of ligands in the orthosteric pocket of the receptor elicits a conformational change of the residue of TM6: $Trp^{6.48}$ of the CWxP motif (superscript numbers refer to the Ballesteros and Weinstein generic numbering scheme [26](Ballesteros et al. 1995)), [19](Zhou et al. 2019), [21](Olivella et al. 2013). A rotation from *gauche+* to *trans* conformation of $Trp^{6.48}$ is proposed to occur in switching and repacking of hydrophobic interactions in the receptor core that favour the outward movement of TM6 [19](Zhou et al. 2019), [21](Olivella et al. 2013). The inactive states of class A GPCRs commonly display a Na^+ ion buried in the receptor core and in contact with the conserved $Asp^{2.50}$, which is disconnected from the cytosol by a hydrophobic layer of residues below it [19](Zhou et al. 2019), [22](Vickery et al. 2018), [23](White et al. 2018). During activation, conformational changes induced in the receptor allow the formation of a continuous water network through the core of the GPCR, which solvates and possibly protonates $Asp^{2.50}$ and facilitates the transfer of the Na^+ ion to the intracellular side [19](Zhou et al. 2019), [22](Vickery et al. 2018), [23](White et al. 2018). Therefore, in the active state of class A GPCRs the presence of Na+ ions differs with respect to the inactive state [19](Zhou et al. 2019), [22](Vickery et al. 2018), [23](White et al. 2018). In addition to $Trp^{6.48}$ and Na^+ pocket, in the transmembrane core of class A GPCRs a highly conserved triad between TM3, TM5 and TM6, formed by $Ile^{3.40}$, $Pro^{5.50}$ and $Phe^{6.44}$ (core triad or P-I-F motif), leads to a conformational change during receptor activation [19](Zhou et al. 2019), [23](White et al. 2018), [24](Bruzzese et al. 2018). This hydrophobic cluster rearranges in the active state relative to the inactive state of the receptor, which induces or selects the conformational changes associated with their respective helices [19](Zhou et al. 2019), [23](White et al. 2018), [24](Bruzzese et al. 2018).

In addition to the microswitches present in the receptor core, is has been widely described that the highly conserved NPxxY motif located in the intracellular side of TM7 is required for GPCR activation [19](Zhou et al. 2019), [23](White et al. 2018), in agreement with

mutational studies [27](Galés et al. 2000). Rearrangement of this motif, in accordance with the inward movement of TM7 with respect to the receptor core, facilitates TM5 interactions and the formation of a hydrogen-bonded water network, which are necessary for the binding of intracellular partners [18](Dalton et al. 2015), [19](Zhou et al. 2019), [23](White et al. 2018). Finally, the E/DRY motif (ionic-lock) is located in the intracellular side of TM3, where the highly conserved $Arg^{3.50}$ forms different interactions in the active or inactive states of the receptor [19](Zhou et al. 2019), [23](White et al. 2018), [25](Fleetwood et al. 2020). While the inactive state is stabilized by a strong electrostatic interaction between $Arg^{3.50}$ and the negatively charged carboxylate located at position 6.30 on TM6, forming a "lock" that prevents water permeation of the intracellular cavity and TM6 outward movement, during receptor activation this interaction is broken, thus increasing TM6 flexibility and allowing the binding of intracellular partners [19](Zhou et al. 2019), [23](White et al. 2018), [25](Fleetwood et al. 2020).

1.1.3.2. Metabotropic glutamate receptor activation

One of the receptors included in the present thesis is metabotropic glutamate receptor subtype 2 (mGlu2R), a receptor belonging to GPCR class C. Metabotropic glutamate receptors (mGluRs) are characterized by two features: i) in addition to the TMD, they present a large extracellular domain known as the venus fly trap (VFT), responsible for the recognition of the orthosteric ligands (differently from class A where the orthosteric binding sites are positioned in between the TM helices) [28](Chun et al. 2012), [29](Møller et al. 2017), and ii) they form constitutive dimers thus establishing an interface between two copies of the VFT to activate the receptor [28](Chun et al. 2012), [29](Møller et al. 2017). Docking poses located in between the TMs are reserved for allosteric modulators of the receptor [28](Chun et al. 2012). Therefore, activation of mGlu receptors sequentially progress from agonist binding in a dimer complex, which conformationally changes an open VFT conformation towards a closed one, which in turn transduces the activation signal to the TMDs through the rigid cysteine-rich domains (CRDs) that connect the VFT and TMD in each protomer [28](Chun et al. 2012), [29](Møller et al. 2017), [30](Pin et al. 2016).

The conformational activation transmitted to the TMDs compromises the interactions

between both protomers established in the inactive state of the receptor dimer [29](Møller et al. 2017), [31](Levitz et al. 2016), [32](Lans et al. 2020). It has been described that during activation of some class C GPCRs such as mGlu2R a switch from TM4-TM5 to TM6-TM6 interface is induced by a rotation of the protomers [33](Xue et al. 2015). These conformational changes modulate receptor intracellular pockets, which allows the binding of G-proteins or β-arrestin. In addition, the release of TM4 and TM5 allow the formation of new protein-protein interactions with the respective TM helices of other GPCRs.

Importantly and in contrast to class A GPCRs, mGluR activation does not involve the outward movement of TM6 on any of the protomers within the homodimer to facilitate the binding of the G protein, as shown by recent crystallographic studies [34](Seven et al. 2021). The same happens with another class C receptor: the heterodimeric GABA$_B$ receptor, as also revealed by crystallographic data [35](Shen et al. 2021). These experimental results confirm previous computational studies from our group showing differences in the activation modes between class A and class C receptors [32](Lans et al. 2020), [36](Dalton et al. 2017). It is tempting to propose that receptor dimerization redefines the activation mode of GPCRs by widening the structure-function space.

1.2. Motivation

GPCRs have become one of the most relevant targets for treating a wide range of diseases and have been shown proficient in target-specific drug design. Therefore, understanding their functionality and signal transmission is fundamental for therapeutic purposes. Despite GPCRs having been widely studied, the precise mechanisms by which a specific ligand induces receptor coupling to a specific intracellular partner still remains elusive. Computational techniques such as molecular modelling and molecular dynamics have demonstrated to be useful for the study of GPCRs, permitting investigation of these receptors at the atomic level. These techniques enhance the study of GPCRs further than static crystal structures by adding a time-dependent dimension to the conformational implications of ligand-protein and protein-protein interactions.

In this direction, this thesis studies the modulation of several GPCRs by means of four

different research lines:

1. We examined the growing experimental evidence [37](Navarro et al. 2016) that suggests that GPCRs, specifically angiotensin-1 receptor (AT1R) and adenosine A2A receptor (A2AR), may function as oligomeric complexes potentially forming dimers and tetramers; either interacting with the same (homo-) or different (hetero-) receptors. This work was published in [38](Oliveira et al. 2017).

2. We studied the protein-protein interactions between serotonin 2A receptor (5-HT$_{2A}$R) and metabotropic glutamate receptor 2 (mGlu2R), specifically, the demonstrated negative reciprocal influence between 5-HT$_{2A}$R-mediated Gq/11-signalling and mGlu2R-mediated Gi-signalling in vivo [39](Fribourg et al. 2011), [40](Moreno et al. 2016), [41](Delille et al. 2012), [42](Baki et al. 2016), through oligomer formation. In silico, a highly stable conformational complex was used to determine the direct cross-talk between 5-HT$_{2A}$R and mGlu2R within the oligomeric complex, thus identifying possible interface interaction points to assist mutational experimental studies.

3. We analyzed how two different D2R antagonists: clozapine and spiperone, yield differences in the formation of D2R homodimers. Experimental studies have demonstrated that the formation of D2R homodimers is significantly decreased by 40–60% after incubation with the D2R antagonist spiperone, but not with other D2R antagonists such as clozapine [43](Wouters et al. 2019). This work was published in *International Journal of Molecular Science* [43](Wouters et al. 2019).

4. We tackled the difference in potency and efficacy between morphine and fentanyl MOR agonists. MOR is the molecular target for opiate-mediated analgesia, which treats chronic pain, a major public health problem with a high prevalence and impact on quality of life [44](Steglitz et al. 2012). Fentanyl has appeared to be 50-100 times more potent than morphine [45](O'Donell et al. 2017), and at the same time has been implicated in an increase of opioid-overdose deaths [46](Mounteney et al. 2015). In order to study morphine and fentanyl potency differences, we modelled human activated and inactive MOR (hMOR) from murine crystal structures [47](Manglik et al. 2012), [48](Huang et al. 2015) thus generating four different systems: i)

morphine-bound active-hMOR, ii) morphine-bound inactive-hMOR, iii) fentanyl-bound active-hMOR, and iv) fentanyl-bound inactive-hMOR; each of them run in triplicate throughout MD simulations (3μs-length each replica). In addition, binding and MD simulations of naltrexone bound in the inactive or activated hMOR model were performed as a negative control. This work was published in *International Journal of Chemical Information and Modeling* [49](Ricarte et al. 2021).

1.3. Aim

The aim of this thesis focuses on a deep-comprehension of the activation of GPCRs by ligands, bound in their respective orthosteric pockets, or the allosteric modulation elicited by oligomerization with other GPCRs, either "homo-" (same receptors) or "hetero-" (different receptors). Therefore, this study explores a wide range of receptors, including AT1R, A2AR, 5-HT$_{2A}$R, mGlu2R, D2R and MOR, which provides useful knowledge for better understanding GPCRs and target-specific drug design.

1.4. Research questions

In order to achieve a better understanding of the activation mechanisms of GPCRs we have employed computational techniques that bring an atomic level perspective. Therefore, making use of modelling, molecular dynamics simulations and visual molecular dynamics software we tried to find answers to the following questions, which are related with the receptor systems presented above:

1. Is the conformational stability of AT1R and A2AR homodimers increased when these two receptors form a higher hetero-oligomeric complex (AT1R/A2AR heterotetramer)?

2. Is the formation of a 5-HT$_{2A}$R-mGlu2R heterotrimer (including a TM6-TM6 interaction within the mGlu2R homodimer and a TM4-TM5 interface between the serotonin and glutamate receptors) feasible?

3. Can spiperone reduce D2R homodimerization relative to clozapine? Which conformational differences induce the ligands that can potentially enhance or decrease protein–protein interactions in D2R homodimers?

4. Do fentanyl and morphine show differences in their binding within the orthosteric pocket of hMOR? How are these interactions related with the conformational changes observed in the receptor core and water network modulation? And, how can these, in turn, differently affect the intracellular pocket and ultimately be an indication of their different potency?

2. Methods

2.1. Homology modelling

All the computational work performed in this thesis has been made using 3D atomic models of GPCRs generated from homologous crystal structures with Chimera v1.11 [50](Pettersen et al. 2004) and Modeller v9.16 [51](Webb et al. 2014) programs. Therefore, conformations of hMOR (activated and inactive), inactive D2R, inactive AT1R, inactive A2AR, inactive 5-HT$_{2A}$R and active mGlu2R were homology modelled from respective crystal structures of activated and inactive states of murine MOR (PDB ids: 5C1M [48](Huang et al. 2015) and 4DKL [47](Manglik et al. 2012), D2R (PDB id: 6CM4) [52](Wang et al. 2018), AT1R (PDB id: 4ZUD) [53](Zhang et al. 2015), A2AR (PDB id: 4EIY) [54](Liu et al. 2012), 5-HT$_{2B}$R (PDB id: 4IB4) [55](Wacker et al. 2013) and 5-HT$_{1B}$R (PDB id: 4IAQ) [137](Yin et al. 2018), and mGlu1R (PDB id: 4OR2) [56](Wu et al. 2014). In cases where non-native fusion protein, camelid G-protein mimetic nanobodies and cocrystallized ligands were present, prior removal of such crystal elements was performed before subsequent homology or ab initio modelling. We homology modelled the wt-sequence of these GPCRs (extracted from Uniprot database [57](The Uniprot Consortium 2018)). For hMOR, D2R, AT1R and A2AR, missing residues of non-crystallized N-terminus and intracellular (ICL) and extracellular loop (ECL) sections were built ab initio using Modeller v9.16 [51](Webb et al. 2014), and mutated or non-conserved residues between species were converted to human wild-type using the Dunbrack 2010 rotamer library [58](Shapovalov et al. 2011) within Chimera v1.11 [50](Pettersen et al. 2004) where the rotamer with highest probability and fewest steric conflicts was selected where appropriate. Conversely, human 5-HT$_{2A}$R and mGlu2R were completely homology modelled from homologous crystal structure templates: primarily 5-HT$_{2B}$R (PDB id: 4IB4 [55](Wacker et al. 2013)) with secondary assistance of 5-HT$_{1B}$R (PDB id: 4IAQ [137](Yin et al. 2018)) to model 5-HT$_{2A}$R N-terminus, the extracellular region of TM1, and ICL3; or mGlu1R (PDB id: 4IB4 [55](Wacker et al. 2013), respectively, following the sequence alignments shown in Supplementary Figure 1 and 2, which were generated with the web-server PROMALS-3D [59](Pei et al. 2008). The 5-HT$_{2A}$R/5-HT$_{1B}$R/5-HT$_{2B}$R multiple sequence alignment (MSA) was manually refined where appropriate with the sequence alignment editing software Jalview [60](Waterhouse et al.

2009), and unaligned loop residues (i.e. gaps in alignments) were modelled ab initio using Modeller v9.16 [51](Webb et al. 2014). From each structural template, 50 different homology models were generated using Modeller v9.16 [51](Webb et al. 2014) ranked by positional criteria and zDOPE score [61](Shen et al. 2012), a statistical potential score that assesses the energy of each model by satisfying atomic distance-dependent potentials derived from crystallographic structures. We explored the possible existence of secondary structures within non-crystallized loop regions through secondary structure predictions of whole receptor sequences, made using the web-service PSIpred [62](Jones 1999), PSSPred [63](Yan et al. 2013) and JPred [64](Drozdetskiy et al. 2015). For all systems, complete GPCR homology models were subsequently energy minimized in the AMBER14SB force-field [65](Maier et al. 2015) using Chimera v1.11 in vacuum conditions [50](Pettersen et al. 2004).

2.2. Ligand docking

Structures of ligands of interest were extracted from Pubchem [66](Kim et al. 2016) and energy minimized in the AMBER14SB force-field using Chimera v1.11 [50](Pettersen et al. 2004) in vacuum conditions and then docked into the respective homology models with Autodock4.2.6 [67](Morris et al. 2009). Specifically, **i)** morphine, fentanyl and naltrexone (a MOR antagonist taken as a reference for comparison with agonists) were prepared by protonating their amino group, which is consistent with physiological pH. This protonation state allowed ligand binding into both activated and inactive hMOR models in accordance with cocrystallized μ-opioid ligands and related structural data [47](Manglik et al. 2012), [48](Huang et al. 2015), [68](Koehl et al. 2018), [69](Spahn et al. 2017). **ii)** Spiperone and clozapine were docked into monomeric inactive D2R. **iii)** Antagonist losartan and istradefylline were docked into AT1R and A2AR, respectively, in accordance with binding modes of relevant cocrystallized antagonists [53](Zhang et al. 2015), [70](Doré et al. 2011). In all cases, docking grid points were extended to cover their corresponding total orthosteric pocket volumes. The selected docked conformation of each ligand in each receptor state represents the top hit identified by best predicted affinity (nM) in the largest docking cluster. Subsequent docked ligand-receptor complexes were additionally energy-minimized in the AMBER14SB force-field [65](Maier et al. 2015) using Chimera v1.11 [50](Pettersen et al. 2004) in vacuum conditions to optimize protein-ligand interactions.

2.3. Protein-protein docking

In studies involving i) two D2R protomers, ii) the combination of AT1R and A2AR, or iii) the combination of 5-HT$_{2A}$R and mGlu2R, the homo- or hetero-oligomeric complexes were respectively generated. For the construction of a D2R homodimer model, where two protomers of D2R interact via a symmetrical TM5/TM6-TM6/TM5 interface, two D2R monomers without bound antagonist were initially superimposed onto the respective protomers of the MOR homodimer crystal structure (PDB id: 4DKL) [47](Manglik et al. 2012). Conversely, for generating homodimers of respective receptors: AT1R and A2AR with bound antagonists, two MD-generated receptor-ligand monomers (see MD methods) of either AT1R or A2AR, in each case, were superimposed onto the A2AR homodimer arrangement as displayed in the full unit cell of the crystal structure (PDB id: 4EIY) [54](Liu et al. 2012), yielding an initial homodimer-ligand model. Finally, for the construction of 5-HT$_{2A}$R and mGlu2R heteroligomer, we first generated an activated mGlu2R homodimer alone by superimposing two monomeric mGlu2R homology models onto the respective protomers of the MOR homodimer crystal structure (PDB id: 4DKL) [47](Manglik et al. 2012). All initial homodimer models were then submitted to the ROSIE Web server [71](Lyskov et al. 2013) for protein–protein docking using default parameters, i.e. perturbation of 3 Å between proteins, 8° of tilt, and 360° rotation around protein centres, with generation of 1000 docking solutions per case. The best docked homodimer was identified by three factors: best possible ROSETTA interface score (I_sc), lowest possible root mean square deviation (RMSD) in relation to the initial model, and acceptable membrane-compatible orientation. For the construction of an AT1R-A2AR heterotetramer, two initial tetrameric arrangements were manually generated by combining respective MD-generated AT1R and A2AR homodimers (see MD section) in alternative ways: (i) where homodimers are arranged side-to-side in a rectangular-like configuration, where each homodimer subunit interacts with a subunit of the other homodimer (by respective TM1/2–5/6 helices), (ii) where homodimers are partially displaced with respect to one another creating a parallelogram-like configuration, where both subunits of one homodimer interact with a single subunit of the other homodimer (by respective TM4/5 helices). Similarly, conformations of 5-HT$_{2A}$R monomer and mGlu2R homodimer achieved after respective MD simulations (see MD section) were used to model the mGlu2R-5-HT$_{2A}$R heteromeric complex modelled by superimposing them onto the

protomers of the A2AR homodimer unit cell arrangement (PDB id: 4EIY) [54](Liu et al. 2012). These alternative configurations were submitted to the ROSIE webserver [71](Lyskov et al. 2013) for identification of the best possible tetrameric and trimeric arrangements, respectively, according to the same criteria implemented previously. All oligomeric models were energy minimized without restraints with Chimera v1.11 [50](Pettersen et al. 2004) in the AMBER14SB force-field [65](Maier et al. 2015) to optimize protein–protein interactions.

2.4. Molecular dynamics systems setup

The complexes included in each study were the following: **i)** six systems of hMOR with either morphine, fentanyl or naltrexone bound into the activated or inactive states of the receptor, **ii)** five systems for AT1R and A2AR with antagonists losartan and istradefylline, respectively (two in monomeric and homodimeric complexes and one in the heteroterameric form), **iii)** three systems of D2R either monomeric with bound spiperone or clozapine or homodimeric without bound antagonists, and **iv)** three systems of 5-HT$_{2A}$R monomer, and mGlu2R homodimer either alone or forming an heterotrimer with 5-HT$_{2A}$R. These systems were respectively embedded into 1-Palmitoyl-2-oleoylphosphatidylcholine (POPC) membrane using the CHARMM-GUI web-based interface [72](Jo et al. 2008) and solvated with TIP3P water molecules. All models were oriented in the membrane according to the OPM database [73](Lomize et al. 2006) entry of **i)** activated mMOR crystal structure (id: 5C1M) [48](Huang et al. 2015), **ii)** A2AR crystal structure (id: 4EIY) [54](Liu et al. 2012), **iii)** D2R crystal structure (id: 6CM4) [52](Wang et al. 2018) or mMOR homodimer crystal structure (PDB id: 4DKL) [47](Manglik et al. 2012) for monomer and homodimer models, respectively, and **iv)** 5-HT$_{2B}$R crystal structure (PDB id: 4IB4) [55](Wacker et al. 2013) and mGlu1R crystal structure (PDB id: 4OR2) [56](Wu et al. 2014), mMOR homodimer crystal structure (PDB id: 4DKL) [47](Manglik et al. 2012) or A2AR crystal structure (PDB id: 4EIY) [54](Liu et al. 2012) for monomer 5-HT$_{2A}$R, mGlu2R homodimer alone and mGlu2R and 5-HT$_{2A}$R heterotrimer, respectively. GPCRs disulfide bonds were maintained in all systems and charge neutralizing ions (0.15 M KCl) were introduced in order to make a net system charge of 0. CHARMM-GUI [72](Jo et al. 2008) automatically generated the membrane, water and protein parameters according to the CHARMM36 force-field [74](Huang et al. 2013) and ligand parameters in accordance to CHARMM General Force

14

Field (CGenFF) v.1.0.0 [75](Vanommeslaeghe et al. 2010).

2.5. Molecular dynamics simulations

MD simulations of each membrane-embedded complex were performed using the CHARMM36 force-field [74](Huang et al. 2013) with ACEMD [76](Harvey et al. 2009) on specialized GPU-computer hardware. Number of replicas of each system and their time-length extension depended on the requirements and limitations of each study. MD simulations require an equilibration step to stabilize the system, therefore all systems were energy-minimized for 2000 steps, followed by 28 ns of equilibration at 300 K and 1 atm, with positional harmonic restraints on protein and ligand heavy atoms progressively released over the first 8 ns of equilibration, thereafter continued without restraints, except AT1R/A2AR homodimers and heterotetramer, which instead were equilibrated for 50 ns under the same conditions. After equilibration, different unbiased continuous production runs under the same conditions were performed for each study. In the MOR study, three replicas of 3 μs each were run starting from each of the six different systems generated, making a total additive simulation time of 54 μs. AT1R and A2AR monomers were subjected to production runs of 250 ns and 500 ns, respectively, whereas AT1R and A2AR homodimers were subjected to respective runs of 750 ns and 1.5 μs. In addition, the AT1R/A2AR heterotetramer was subjected to an unbiased production run of 2 μs, thus totaling 5 μs across systems. The D2R monomer, with bound spiperone or clozapine, and the D2R homodimer were subjected to 3 μs production runs. Finally, 5-HT_{2A}R monomer, mGlu2R homodimer alone and 5-HT_{2A}R-mGlu2R heterotrimer were subjected to respective runs of 5 μs each.

2.6. Molecular dynamics simulation analysis

The analysis of the MD simulation trajectories was performed using VMD software v1.9.2 [77](Humphrey et al. 1996). In the hMOR study, the three microsecond trajectories were analyzed with the following protocol: i) ligand positional stability in inactive and activated hMOR models and ii) analysis of respective stable binding poses; iii) comparison between ligand-mediated hMOR orthosteric pocket conformational changes and their correlation with a) TM helical movement, b) intracellular receptor conformational state and d) conformational

changes of the rest of the receptor; iv) water-network differences associated with different receptor states. The evaluation of receptor conformational stability was measured by the analysis of the two last microseconds of each replica of the generated systems, whereas the residue-specific conformational changes were studied considering the entire simulation time-length. In detail, RMSD measurements of fentanyl or morphine in their respective MD simulations were used to monitor ligand positional stability. A list of residues contacted by either morphine or fentanyl (<3.5 Å) in each replica of each system and their frequency were extracted making use of a custom-made TCL script [78](Saam 2005) executed in VMD [77](Humphrey et al. 1996). Electrostatic, van der Waals and hydrophobic interactions between ligand and residues with frequencies ≥20.0% in two or more replicas were analyzed for energetics using NAMD-Energy plugin v1.4 [79](Phillips et al. 2005) within VMD [77](Humphrey et al. 1996). RMSD analysis of hMOR TM domain was performed with respect to the receptor starting conformation or the fully active mMOR cryo-EM structure [68](Koehl et al. 2018) to assess conformational stability and receptor (in)activation. A threshold of ±3.5 Å from initial receptor state was used to determine significant receptor conformational changes, considering the conformational divergence of activated and inactive crystals from the fully active cryo-EM structure [68](Koehl et al. 2018) equal 1.4 Å and 3.0 Å, respectively. Intracellular receptor conformational changes associated with activation/deactivation were analyzed by making use of VMD software v1.9.2 [77](Humphrey et al. 1996) in terms of movement with respect to protein centre of: i) TM3, ii) intracellular tip of TM5, iii) intracellular tip of TM6 and iv) NPxxY motif on TM7, in addition to v) distance between alpha carbons of residues Arg167$^{3.50}$ and Thr281$^{6.34}$. The TM3 upward axial movement was measured by Z-axis offset difference between TM3 and protein centres of mass (COM). Helix tips were defined according to second and third-last intracellular helical turns (TM5: residues 251-261, TM6: 274-284) and distances measured relative to protein COM. Taking into consideration differences between crystal structures [47](Manglik et al. 2012), [48](Huang et al. 2015), [68](Koehl et al. 2018) in their positions of TM3, TM5 and TM6, as well as MD simulations with the antagonist naltrexone, relevant internal distances were normalized with respect to the inactive crystal [47](Manglik et al. 2012), with respective distances thresholds of +0.3 Å, -0.8 Å and +1.7 Å, which were used to classify active or inactive helix conformations. Active- or inactive-like conformations of

intracellular metrics such as NPxxY motif and Arg167[3.50]-Thr281[6.34] interaction were defined by their distance from protein COM (using -0.8 Å threshold) or by +10.0 Å for Arg167[3.50]-Thr281[6.34] inter-residue distance. Residues showing differences in their potential energy (P.E). of interaction between bound fentanyl and morphine were analyzed according to: i) sidechain $\chi1$ dihedral angle; ii) $\chi2$ dihedral angle; iii) P.E. of interaction with nearby residues; iv) distribution with respect to conformational changes of other residues; and v) correlation with intracellular receptor conformational changes. Sidechain dihedral angles were classified according to a threshold between predominantly observed $\chi1$ and $\chi2$ dihedral angle conformations. Thus, a ±115.0º value was used as a threshold for classifying Asp149[3.32] $\chi1$ dihedral angle conformation (*gauche-* and *trans* conformations), ±90.0º threshold for Met153[3.36] $\chi1$ dihedral angle (*gauche-* or alternative conformations), and ±240.0º threshold for Lys235[5.39] and Gln126[2.60] $\chi2$ dihedral angles (predominant *cis* and *trans* conformations of 300.0º and 180.0º, respectively). Electrostatic inter-sidechain or ligand-sidechain interactions were specified according to ±4.5 Å distance threshold. Close H-bonding between morphine, fentanyl or naltrexone with Asp149[3.32] was selected according to a threshold of ±2.5 Å. Distances/H-bonding was measured between: i) fentanyl, morphine or naltrexone amino group and Asp149[3.32] gamma carbon (considered as centre of Asp149[3.32] carboxylate group), ii) fentanyl, morphine or naltrexone oxygen acceptor atoms (a single carbonyl group in the former or one ether and two hydroxyl groups in morphine or one ether, one hydroxyl group and one carbonyl group in naltrexone) and Tyr150[3.33] hydroxyl group or Lys235[5.39] amino group, iii) Asp149[3.32] gamma carbon and Tyr328[7.43] hydroxyl group, and iv) Trp295[6.48] indole NH group and Ala242[5.46] backbone carbonyl group. The distance between residues Trp295[6.48] and Ala242[5.46] was measured between their respective sidechain COMs. Water density maps were created using VolMap within VMD [77](Humphrey et al. 1996) by calculating weighted atomic density of water molecules averaged over the last two microseconds of each MD replica. Conversely, the analyses of MD simulations of D2R monomer, with bound spiperone or clozapine, and D2R homodimer without bound antagonist were performed by measuring RMSD of the backbone of the TMD of D2R to observe receptor conformational changes with respect to the initial D2R monomeric crystal structure (PDB id: 6CM4) [52](Wang et al. 2018) or initial D2R homodimer model. Likewise, RMSD measurements of either clozapine or spiperone in their respective MD simulations were used to monitor ligand positional

stability in the orthosteric pocket of the D2R monomer. Residues in close contact (protein-ligand distance <3.5 Å) with cocrystallized ligand risperidone were compared, in terms of RMSD with MD conformations of D2R monomer with bound stable clozapine or spiperone to observe differences between the induced fits of both ligands. Similarly, residues frequently close-contacted by either clozapine or spiperone in respective MD simulations, within simulation time-periods where ligands remain stable, were identified with a TCL script [78](Saam 2005) executed in VMD [77](Humphrey et al. 1996), thus defining ligand-specific D2R orthosteric pockets. After visual comparisons of the D2R monomer, with bound spiperone or clozapine, and D2R homodimer conformations, we performed an analysis of Tyr199$^{5.48}$ and Phe390$^{6.52}$ χ1 dihedral angle conformations using an in-house custom TCL script executed in VMD [77](Humphrey et al. 1996). A threshold of 240° was selected to classify Tyr199$^{5.48}$ and Phe390$^{6.52}$ χ1 dihedral angle *cis* or *trans*-conformation (> or <240°, respectively). Subsequently, the proportion of each conformation was measured. Distance analyses of the interface of D2R homodimer were performed using the TCL script executed in VMD [77](Humphrey et al. 1996). An energy analysis of the D2R homodimer TM5/TM6-TM6/TM5 interface was performed with FoldX v.4 [80](Schymkowitz et al. 2005). Alanine scanning of D2R homodimer Tyr199$^{5.48}$ and Phe390$^{6.52}$, generating Y199A and F390A mutations, followed by energy analysis with FoldX v.4 [80](Schymkowitz et al. 2005), was carried out to measure the contribution of these residues to the homodimer interface. Finally, analysis of interaction between 5-HT$_{2A}$R and mGlu2R was performed with the following protocol: i) analysis of 5-HT$_{2A}$R and mGlu2R receptor conformational stability; ii) calculation of helical, ionic-lock and ICL distances; and iii) analysis of proposed point mutations. In detail, protomer conformational change of each system was respectively measured by means of RMSD. Similarly, conformational stability of mGlu2R homodimer either alone or in complex with 5-HT$_{2A}$R, as well as respective ICL2, was analyzed by root mean square fluctuation (RMSF). Distance between each centres of mass (COM) of: i) mGlu2R protomers, ii) TM6-TM6 mGlu2R protomer #1-2; iii) ICL2 and ICL3, iv) Lys653$^{3.50}$ and Glu758$^{6.35}$ (ionic-lock) was measured in mGlu2R homodimer alone and mGlu2R-5-HT$_{2A}$R heterotrimer model, similarly, v) COM-COM distance was measured between each mGlu2R protomers and 5-HT$_{2A}$R in mGlu2R-5-HT$_{2A}$R heterotrimer model. Point mutation combinations found based on mGlu2R-5-HT$_{2A}$R heterotrimer complex were

proposed by visual exploration and computational analysis of alpha carbon distances between Tyr781$^{6.58}$ of each mGlu2R protomers and between pairs of mGlu2R-5-HT$_{2A}$R residues: i) Leu737$^{5.49}$ – Ile206$^{4.56}$; ii) Arg659$^{3.56}$ – Gln178$^{3.55}$; and iii) Gly730$^{5.42}$ – Ile237$^{5.41}$. Additional intracellular inter-receptor H-bond/electrostatic residue-residue distances determined by mGlu2R Arg659$^{3.56}$ amino group and either 5-HT$_{2A}$R Gln178$^{3.55}$ carbonyl group or 5-HT$_{2A}$R Glu264$^{5.68}$ carboxylate group were also measured making use of VMD software 1.9.2 [77](Humphrey et al. 1996).

2.7. Statistical analysis

In the hMOR study, Chi-square (Chi2) and Student's t-tests statistical analyses were performed to assess the statistical significance of the potential association between orthosteric pocket metrics (sidechain-sidechain Asp149$^{3.32}$-Tyr$^{7.43}$, Tyr150$^{3.33}$-ligand, Lys235$^{5.39}$-ligand and sidechain-backbone Trp295$^{6.48}$-Ala242$^{5.46}$ H-bond presence or absence, Met153$^{3.36}$ *gauche*- conformation selection, or Trp295$^{6.48}$-Ala242$^{5.46}$ distance, respectively) with the intracellular conformations achieved (active or inactive-like conformation of TM3, TM5, TM6, NPxxY and Arg167$^{3.50}$-Thr281$^{6.34}$ distance). To perform these analyses we used 50 representative snapshots of each replica, extracted every 40 ns from the last two microseconds of respective trajectories, independently of the initial state of the receptor or the ligand bound, thus making a total sample of 900 receptor-ligand conformations. This sample was considered sufficient to construct two-way contingency tables to evaluate Chi2 score and to perform Student's t-tests analysis for exploring general mechanistic trends. $P < 0.05$ was considered statistically significant. IBM SPSS Statistics 20.0.0 [81] was used for statistical analyses.

3. Studies performed

3.1. Oligomerization of GPCRs: modulation of receptor function through protein-protein interactions

3.1.1. Angiotensin 1 receptor and adenosine A2A receptor homodimers form functional heterotetramers

This study was performed in collaboration with Dr. Francisco Ciruela from Universitat de Barcelona. Our group was responsible for the computational work. The results of the study were published in *Scientific Reports* [38](Oliveira et al. 2017). The computational results supported, and structurally described, the findings observed by our experimental collaborators on the possible formation of a heterotetrameric interaction between AT1R and A2AR, revealing for the first time the existence of AT1R/A2AR oligomers in the striatum and its implications in tardive dyskinesia. The computational work was performed by Adrián Ricarte under the supervision and guidance of Dr. James Dalton and Dr. Jesús Giraldo.

3.1.1.1. Introduction to Angiotensin II type 1/adenosine A2AR oligomers: a novel target for tardive dyskinesia

The concept that cell surface receptors may physically interact forming oligomers appeared early in the eighties, while characterizing GPCR function through neurotransmitter action [82](Agnati et al. 1980), [83](Fuxe et al. 1983). Notably, striatal dopaminergic receptors in general, and D2R in particular, constitute the archetypal GPCR capable of forming receptor-receptor complexes with several GPCRs [84](Gomes et al. 2016), including A2AR [85](Ciruela et al. 2004) and AT1R [86](Martínez-Pinilla et al. 2015). These oligomers have a potential impact on the dopaminergic dysfunction that leads to the pathogenesis and progression of dopaminergic-related pathologies such as tardive dyskinesia (TD), Parkinson's disease (PD) or schizophrenia. The D2R-A2AR heteromer, located in GABAergic striatopallidal neurons [12](Ferré et al. 2008), has been defined as a potential pharmacological target for pathologies associated with dysfunctional dopaminergic signalling. Indeed, the A2AR antagonist istradefylline is used in Japan for treatment of PD

[87](Müller 2015).

AT1R is located in neuronal and glial cells [88](Garrido-Gil et al. 2013) supposing a key component of the renin-angiotensin system (RAS), which regulates blood pressure [89](Brunner et al. 1972). It has been postulated that RAS may be involved in dopaminergic degeneration. AT1R recognizes the endogenous peptidic hormone angiotensin II (AII) exerting a demonstrated role in in the control of stress reaction and cerebral circulation, and in the mechanisms leading to brain ischemia, neuronal injury and inflammation [90](Saavedra et al. 2005). AT1R blockade with selective antagonists has shown [91](Goa et al. 1996) effects in the treatment of hyperthensive patients by reducing brain inflammation responses [92](Saavedra et al. 2012) and involves microglial activation and neuroinflammation [93](Labandeira-García et al. 2014). Moreover, oligomerization of D2R and AT1R has been postulated to be formed in the striatum [86](Martínez-Pinilla et al. 2015).

As far as both AT1R-D2R and A2AR-D2R oligomeric complexes are supported by experimental and clinical data [87](Müller 2015), [86](Martínez-Pinilla et al. 2015), it seems plausible to consider the formation of an AT1R-A2AR heteromer. In detail, the effect produced by adenosine A1 receptor agonists is comparable to the antinociceptive effect of AII [94](Pechlivanova et al. 2002), and a synergistic AT1R-A2AR interaction is described in the peripheral RAS [95](Tchekalarova et al. 2000), [96](Thakur et al. 2010). In addition, several pieces of evidence regarding interactions between the adenosinergic system and RAS have been described during the last few decades [97](Lai et al. 2009), [98](Rongen et al. 1998). Therefore, in this study, we wanted to computationally validate the physical formation of an AT1R-A2AR heteroligomer for potentially targeting dopaminergic signalling disorders. Also, we sought to characterize the most likely heteromeric receptor arrangement through protein-protein docking and long-timescale MD simulations.

3.1.1.2. Computational construction of an AT1R/A2AR heterotetramer model

Both AT1R and A2AR are thought to form functional homodimers at the cell surface [99](Thévenin et al. 2005), [100](Canals et al. 2004), [101](Karip et al. 2007), [102](AbdAlla et al. 2004), [103](Hansen et al. 2004), [104](Fanelli et al. 2011), [105](Gracia et al. 2011).

21

Prior to investigating heteromeric interactions between the receptors, we needed to generate reliable homodimer models of the respective partners. In this direction, using computational modelling, protein-protein docking, and MD simulations, we investigated the likely structure and behaviour of the respective homodimers with bound AT1R and A2AR antagonists (losartan and istradefylline, respectively). These ligands were initially docked in respective inactive crystal structures of these receptors [53](Zhang et al. 2015), [70](Doré et al. 2011) and then subjected to 250 ns and 500 ns MD runs, respectively. Losartan made H-bonds with Arg167[4.64] (superscripts indicate Ballesteros-Weinstein numbering [26](Ballesteros et al. 1995)) of AT1R in a similar manner to that of cocrystallized ligand olmesartan [53](Zhang et al. 2015) (Figure 1). Likewise, in A2AR, Asn253[6.55] formed an H-bond with istradefylline similar to cocrystallized A2AR xanthine antagonist [70](Doré et al. 2011) (Figure 1).
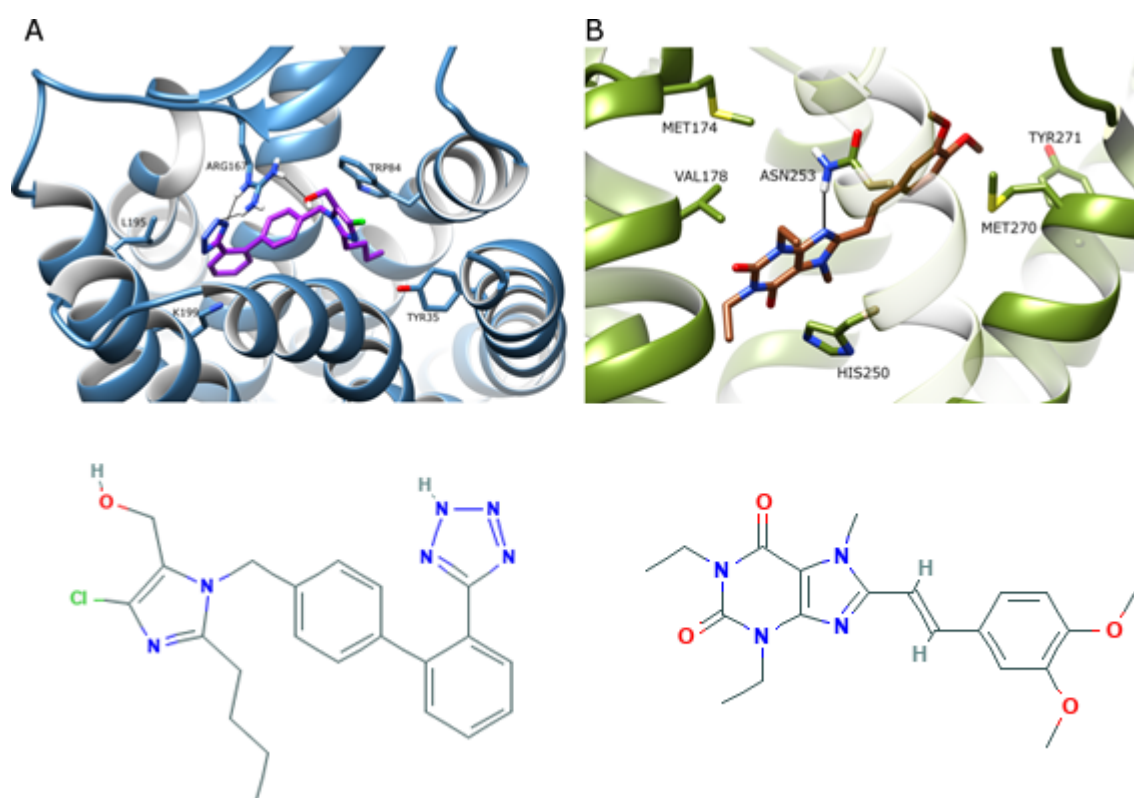
Figure 1. Binding poses after docking and MD simulations. a) Losartan (purple) in AT1R (PDB id: 4ZUD, blue ribbon) and b) istradefylline (KW6002, brown) in A2AR (PDB id: 4EIY, green ribbon). Selected residues are displayed and protein-ligand H-bonds are represented by black lines. 2D representations of the ligands are shown.

Homodimeric losartan-bound AT1R and istradefylline-bound A2AR models were generated by superposition of two copies of the respective monomeric conformations onto the A2AR homodimer crystal structure [54](Liu et al. 2012). This dimeric crystal structure is observed to contain an interface between TM4 and TM5 helices of each protomer, respectively interacting with either TM5 or TM4 of the other partner [54](Liu et al. 2012). Homodimer models were refined with protein-protein docking using ROSIE webserver [71](Lyskov et al. 2013). Following protein-protein docking, the A2AR and AT1R homodimers were subjected to further MD simulations of 1.5 μs and 750 ns, respectively. Results obtained throughout these MD simulations show the formation of significant interactions between TM4 and TM5 of each protomer of the homodimers, indicative of energetically stable dimers (Figure 2). In addition, the respective docked antagonists remained stably bound in each participating protomer, with all receptor subunits maintaining an inactive state. These results support the computational in-silico reliability of generating stable models of experimentally described AT1R and A2AR functional homodimers, including ligands of interest (losartan and istradefylline). Generated homodimer models made it possible to computationally analyse heteromeric interaction between these receptors.
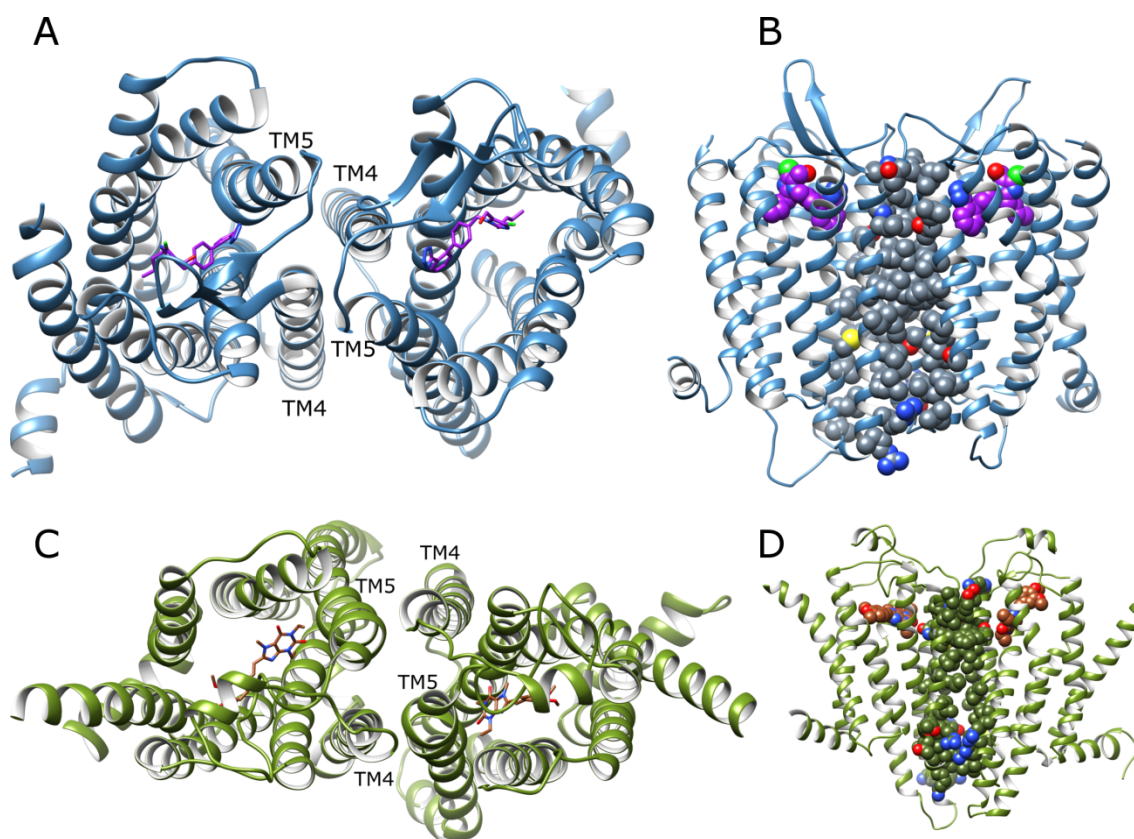
Figure 2. Conformations of homodimer models after protein-protein docking and MD simulations. a), b) homodimer of AT1R (blue ribbon) with bound losartan (purple), top and side view; **c), d)** homodimer of A2AR (green ribbon) with bound istradefylline (brown), top and side view. In **b)** and **d)**, selected residues are displayed to show contact interfaces.

Conformations of A2AR and AT1R homodimers, physically stable during respective MD simulations, were fit into a heterotetramer arrangement similar to previously described models for other GPCRs [37](Navarro et al. 2016), [106](Bonaventura et al. 2015). Therefore, a tetrameric model was generated through extensive protein-protein docking to finally find the most optimal conformation allowing mutual cross-talk and involving two complementary TM5/TM6-TM1/TM2 interfaces between protomers of different receptor types (Figure 3). The generated heterotetramer model was subjected to an unbiased 2 µs MD run, which progressively shows a remarkable degree of conformational stability after initial rearrangements in inter-receptor interfaces (RMSD plot in Supplementary Figure 3). This rearrangement enhances the interaction between A2AR and AT1R homodimers whilst maintaining its original tetrameric configuration (Figure 3). In addition to heterotetramer stability, the respective A2AR and AT1R homodimers within the tetramer remain stable and unperturbed in their inactive state throughout the MD simulation. These results suggest that

the formation of a heterotetrameric interaction between A2AR and AT1R is physically plausible and compatible with losartan- and istradefylline-bound antagonists.
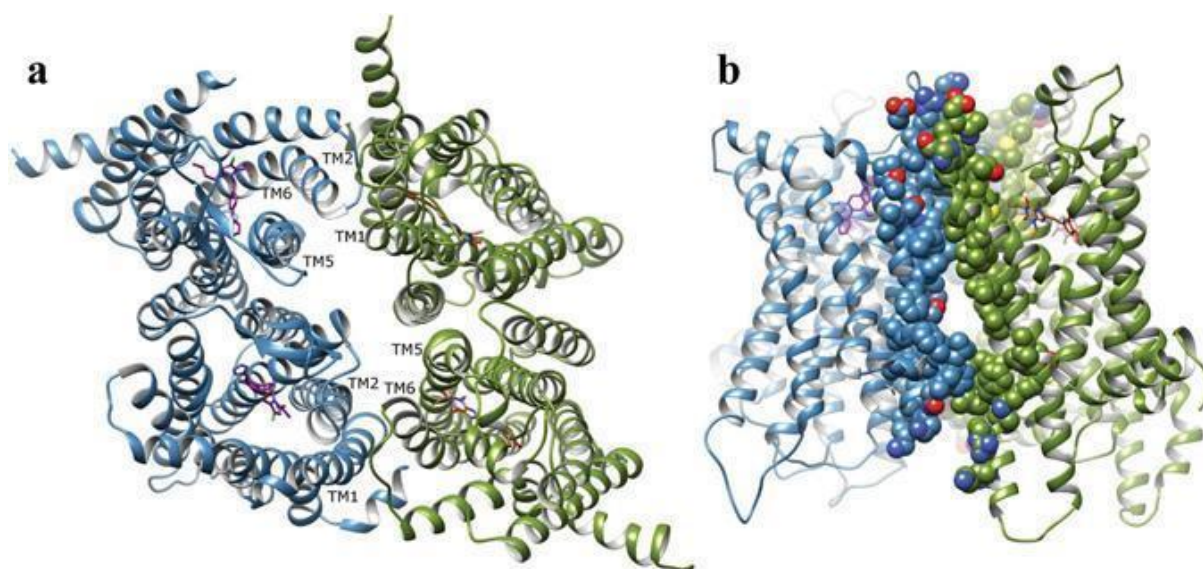
Figure 3. Conformational arrangement of AT1R/A2AR heterotetramer. Model generated after protein-protein docking and 2 µs MD simulation. **a)** Top view of tetramer (AT1R in blue, A2AR in green, losartan in purple and istradefylline in brown). **b)** Side view of the interaction between A2AR and AT1R homodimers.

3.1.1.3. Does the AT1R/A2AR heteromer formation suggest a new framework for drug design?

TD is a serious motor side effect associated with long-term treatment with neuroleptics [107](Andreassen et al. 2000). Motor function control has been associated with the ability of D2R to oligomerize with other GPCRs [108](Fuxe et al. 2014), in particular, with A2AR [12](Ferré et al. 2008), [109](Ferré et al. 2011), [110](Fuxe et al. 2007), thus making it a relevant target for TD treatment. In addition, dopaminergic neurotransmission has been described to be modulated by the signalling of AII through AT1R [111](Mendelsohn et al. 1993), [112](Brown et al. 1996). Therefore, dopamine receptors in the striatum and the substantia nigra are functionally modulated by their direct heteromeric interaction with A2AR and AT1R [86](Martínez-Pinilla et al. 2015), [113](Villar-Cheda et al. 2010), [114](Villar-Cheda et al. 2014). In agreement with these proposals, we decided to explore the formation of a direct interaction between AT1R and A2AR. This idea was considered plausible because of the direct cross-talk both these receptors establish with D2R.

25

Computational results revealed for the first time the conformational stability of an AT1R/A2AR heterotetramer, which may have implications for TD in striatum.

The data collected by our experimental collaborators demonstrated that A2AR and AT1R form heteromers which are targetable by the antagonists losartan and istradefylline, respectively. The hypothesis of receptor heteromers allows for the proposal of multimodal pharmacological approaches in which a combination of drugs targeting each of the heteromer partners can be used instead of a single drug. This multimodal pharmacological approach displayed an unprecedented synergism on the control of involuntary mandibular movements induced by reserpine in an animal model of TD, thus suggesting an attractive solution. Our *in silico* study, strengths the validation of the hypothesis of this heteromeric interaction by showing the conformational stability of an A2AR/AT1R heterotetramer over 2 μs of an unbiased MD simulation. The "best" receptor-receptor arrangement involves a TM4 and TM5 interface between each protomer of the respective A2AR or AT1R homodimers [108](Fuxe et al. 2014), [115](Borroto-Escuela et al. 2010) and two TM1/TM6-TM1/TM2 interfaces between protomers of different receptor types.

The renin-angiotensin and the adenosinergic systems play an important role in controlling the striatal function including motor and non-motor functions [116](Ferré et al. 2010), [117](Yager et al. 2015). Therefore, the ability of A2AR and AT1R to form oligomeric complexes in the striatum might envisage a potential drug target for motor dysfunctions including TD. Both A2AR and AT1R have previously been described to regulate dopaminergic neurotransmission through their ability to heteromerize with D2R [86](Martínez-Pinilla et al. 2015), [118](Parsons et al. 1995), [119](Bishnoi et al. 2006), [120](Ivanova et al. 2012), [121](Muñoz et al. 2015), [122](Fernández-Dueñas et al. 2015). However, it could be speculated that AT1R and A2AR might control D2R function through functional AT1R/D2R/A2AR-containing complexes in GABAergic neurons. A number of facts support this last statement: i) the high and selective coexpression of AT1R, D2R and A2AR in these particular cells; ii) the demonstration of A2AR/D2R, AT1R/D2R and AT1R/A2AR heteromers; and iii) the existence of strong multiple interactions between the three receptors.

Although in this study AT1R/A2AR oligomerization experimentally showed functional consequences, further work is needed to elucidate the precise molecular mechanism underlying this complex. Moreover, from an *in silico* point of view, a putative AT1R/D2R/A2AR oligomer can be considered for further analysis, including the determination of new TM-TM contacts and receptor rearrangements defining the AT1R/D2R/A2AR oligomer stoichiometry. Overall, this information is expected to be extremely valuable when assessing potential pathologies in which these receptors play a key role through multimodal pharmaco-therapeutic interventions based on drug combinations targeting A2AR and AT1R.

3.1.2. Serotonin 2A receptor forms higher-oligomers with metabotropic glutamate receptor 2

This study, which was performed in collaboration with Dr. Jean-Philippe Pin and Dr. Philippe Rondard from Institut de Génomique Fonctionnelle (IGF) – Université de Montpellier, is in its ending phase and close to publication. Therefore, description of experimental results will be largely limited to preserve their confidentiality. In this study, we explored the viability of 5-HT$_{2A}$R and mGlu2R heterotrimeric direct interaction, which allowed us to perform a prospective exploration of essential residues involved in such receptor cross-talk. Results obtained by this computational work (presented below) led to the identification of three point mutation candidates that further facilitated experimental studies performed by our collaborators with positive results. Computational work was performed by Adrián Ricarte under the supervision of Dr. James Dalton and Dr. Jesús Giraldo.

3.1.2.1. Introduction to 5-HT$_{2A}$R and mGlu2R cross-talk

The theory of classical GPCR activation states that the coupling to intracellular heterotrimeric G-protein [4](Weis et al. 2018) or β-arrestin [123](Jean-Charles et al. 2017) is influenced by the conformational changes prompted by agonist binding [18](Dalton et al. 2015). However, it has recently been widely described that the formation of oligomeric GPCRs complexes exhibit distinct signalling behaviour compared to monomeric receptors [38](Oliveira et al. 2017), [39](Fribourg et al. 2011), [124](Gonzalez-Maeso 2011), [125](Ferré et al. 2014), enhancing the possibilities of rational drug design [126](Lee et al. 2018) targeting the

pathophysiology of several diseases like psychotic states [127](Komatsu et al. 2019). Recently, a negative reciprocal influence of serotonin 2A receptor (5-HT$_{2A}$R)-mediated Gq/11-signalling on metabotropic glutamate receptor 2 (mGlu2R)-mediated Gi-signalling has been described *in vivo* [39](Fribourg et al. 2011), [40](Moreno et al. 2016), [128](Delille et al. 2014). Therefore, formation of a 5-HT$_{2A}$R and mGlu2R heteromeric receptor complex would establish an optimal Gi-Gq balance in response to endogenous ligands: glutamate and serotonin [39](Fribourg et al. 2011). Strong agonists and inverse agonists targeting one of the receptors could modulate the balance by controlling their counterpart receptor. Experimentally, it has been described that the disruption that some psychedelics exert over 5-HT$_{2A}$R-mediated Gq/11-signalling and mGlu2R-mediated Gi-signalling [39](Fribourg et al. 2011), can be reversed with the use of 5-HT$_{2A}$R inverse agonists and strong mGlu2R agonists [39](Fribourg et al. 2011). Although this interaction between mGlu2R and 5-HT$_{2A}$R signalling has previously been suggested to involve direct physical receptor cross-talk in mammalian brain cells [40](Moreno et al. 2016), no published experimental results have unequivocally addressed this issue.

In literature, mGluRs have been widely described to form constitutive homodimers [129](Rondard et al. 2010), [33](Xue et al. 2015). During activation of mGlu2R homodimers the interface switches from TM4-TM5 to TM6-TM6 [33](Xue et al. 2015). Therefore, locking a specific conformation and interface stabilizes either the inactive or active state of mGlu2R homodimers [33](Xue et al. 2015). Although this rearrangement seems to be unique to Class C GPCRs (where mGlu2R is classified), the interfaces involved share similarities to other Class A GPCRs dimers which typically display TM4-TM5 or TM5-TM6 interactions [33](Xue et al. 2015), [47](Manglik et al. 2012), [130](Liu et al. 2012). 5-HT$_{2A}$R belongs to the Class A GPCR family and is predicted to make interactions with mGlu2R via its TM4 [40](Moreno et al. 2016), supported by a mutation-based study [131](Moreno et al. 2012). The literature therefore suggests that a heteroligomeric complex can be formed between an active mGlu2 homodimer and 5-HT$_{2A}$R through its exposed TM4-TM5 interface.

The aim of the computational part of this study was to generate a reliable atomistic model of this mGlu2R and 5-HT$_{2A}$R heteromeric complex and explore key interaction features

throughout unbiased MD simulations. The simplest oligomeric biological unit was proposed as the study model, consisting of a trimer formed by one mGlu2R homodimer interacting with one 5-HT$_{2A}$R monomer. Initial homology models of these components were deemed sensible starting points. As there was no published crystal structure of an mGluR homodimer at the time of this study, only crystals of monomeric mGlu1R (PDB id: 4OR2) [56](Wu et al. 2014), which was used as a template, and mGlu5 (PDB ids: 4OO9, 5CGC, 5CGD, 6FFH, 6FFI) [132](Doré et al. 2014), [133](Christopher et al. 2015), [134](Christopher et al. 2019), the homology modelling of an mGlu2R homodimer might be considered speculative. However, validation of our mGlu2R homodimer model was achieved by recent publication of an mGlu5 homodimer crystal in both its inactive and active configurations (PDB ids: 6N51, 6N52) [135](Koehl et al. 2019). Similarly to mGlu2R, no 5-HT$_{2A}$R crystal structure was available at the time of the study, only crystals of monomeric 5-HT$_{1B}$R (PDB ids: 4IAR, 4IAQ, 5V54, 6G79) [136](Wang et al. 2018), [137](Yin et al. 2018), [138](García-Nafría et al. 2019), 5-HT$_{2B}$R (PDB ids: 4IB4, 4NC3, 5TVN, 5TUD, 6DRX, 6DRY, 6DS0) [55](Wacker et al. 2013), [139](Liu et al. 2013), [140](Wacker et al. 2017), [141](Ishchenko et al. 2017), [142](McCorvy et al. 2018), and 5-HT$_{2C}$R (6BQG, 6BQH) [143](Peng et al. 2018) were published. From these potential templates we considered 5-HT$_{2B}$R (PDB id: 4IB4) [55](Wacker et al. 2013) as the best template candidate to model 5-HT$_{2A}$R, with the assistance of 5-HT$_{1B}$R (PDB id: 4IAQ) [137](Yin et al. 2018) to help model N-terminus, TM1 and ICL3. These crystal structures have an overall sequence identity of 53.1 % and 33.3 % with 5-HT$_{2A}$R, respectively. Therefore, we homology modelled 5-HT$_{2A}$R following an MSA manually refined in specific positions, including N-terminus, TM4, ECL2, ICL3, ECL3 and C-terminus (Supplementary Figure 2). However, conformational similarity between our 5-HT$_{2A}$R model and the recently released inactive 5-HT$_{2A}$R crystal structures (PDB ids: 6A93, 6A94) [144](Kimura et al. 2019) validates our homology model. Representative conformations of the mGlu2R homodimer and 5-HT$_{2A}$R monomer were extracted from respective MD simulations (see below) and used to make the mGlu2R-5-HT$_{2A}$R complex of interest, which was then used to describe inter- and intra-receptor conformational changes that could reflect a direct cross-talk between these receptors and could lead experimental studies.

3.1.2.2. Receptor homology models and heteromeric complex show stable conformations

The structural viability of the proposed interaction between mGlu2R and 5-HT$_{2A}$R was based on the modelling of an mGlu2R homodimer, which was constructed from two copies of a monomeric mGlu2R homology model (based on inactive mGlu1R crystal structure [56](Wu et al. 2014) whose TM domain shares a sequence identity of 50 % with mGlu2R, and following the sequence alignment showed in Supplementary Figure 1) superposed on MOR homodimer crystal structure [47](Manglik et al. 2012), and a homology model of inactive 5-HT$_{2A}$R primarily constructed from the crystal structure of monomeric inactive 5-HT$_{2B}$R [55](Wacker et al. 2013). After protein-protein interaction refinement, a TM6-TM6 interface was established for the mGlu2R homodimer and a TM4-TM5 interface was formed between one protomer of mGlu2R and monomeric 5-HT$_{2A}$R (Figure 4), thus simultaneously maintaining two different interfaces [33](Xue et al. 2015). The interface between mGlu2R and 5-HT$_{2A}$R was based on superposition of these units onto the A2AR homodimer crystal structure [54](Liu et al. 2012). Unbiased 5 μs MD simulations were first performed for monomeric 5-HT$_{2A}$R and independent mGlu2R homodimer, in order to obtain relaxed conformations suitable for subsequent heteromeric interaction modelling and generation of the 5-HT$_{2A}$R-mGlu2R heterotrimeric model. Results observed during the MD simulation of an mGlu2R homodimer alone showed that the initial position of the interface, which involved interaction between TM5 and TM6, rotated towards a more markedly TM6-TM6 interface, and was maintained until the end of the simulation (Figure 4). This mode of interaction is in agreement with experimental data of an activated mGlu2R state [33](Xue et al. 2015), as well as the recently published activated mGlu5 homodimer crystal structure [135](Koehl et al. 2019). In addition, the TMD backbone showed high conformational stability of each individual protomer with respect to their initial conformation (RMSD <2.5 Å; average RMSDs of 2.3 Å, 2.0 Å and 2.1 Å for mGlu2R protomer 1 and 2, and 5-HT$_{2A}$R monomer, respectively, Figure 5). This conformational stability supported the use of these models for generating a reliable mGlu2R-5-HT$_{2A}$R heterotrimeric model.

A long-timescale unbiased MD simulation performed on the whole mGlu2R–5-HT$_{2A}$R heterotrimeric complex indicated its structural stability and functional cross-talk. In detail, the conformation of mGlu2R protomers in the heterotrimer displays similar RMSDs to that

observed in the independent mGlu2R homodimer (average RMSDs of 2.0 Å and 1.8 Å for mGlu2R protomers which interact or not with 5-HT$_{2A}$R, respectively, Figure 5). Similarly, 5-HT$_{2A}$R also displays conformationally stable behaviour throughout MD simulations, either in the mGlu2R-5-HT$_{2A}$R heterotrimeric complex or by itself (average RMSDs of 2.0 Å [max. 2.6 Å] and 2.1 Å [max. 2.8 Å], respectively, Figure 5). Interestingly, the conformational fluctuation (RMSF) of the mGlu2R-5-HT$_{2A}$R heterotrimeric model is relatively low and appears to be slightly reduced in comparison with the mGlu2R homodimer alone (average RMSFs of 1.8 Å and 1.9 Å [max. of 2.9 Å and 3.3 Å], respectively, Figure 5). These results, which suggest a greater conformational stability of protomers forming the mGlu2R–5-HT$_{2A}$R heterotrimeric complex compared with their isolated forms, indicate that not only is this a valid and physically reliable model but also that the formation of oligomeric complexes can enhance the conformational stability of particular receptors in a specific state. Therefore, our heterotrimeric model constitutes a suitable tool for studying inter- and intra-receptor functional effects and to propose cross-linking points for experimental purposes.
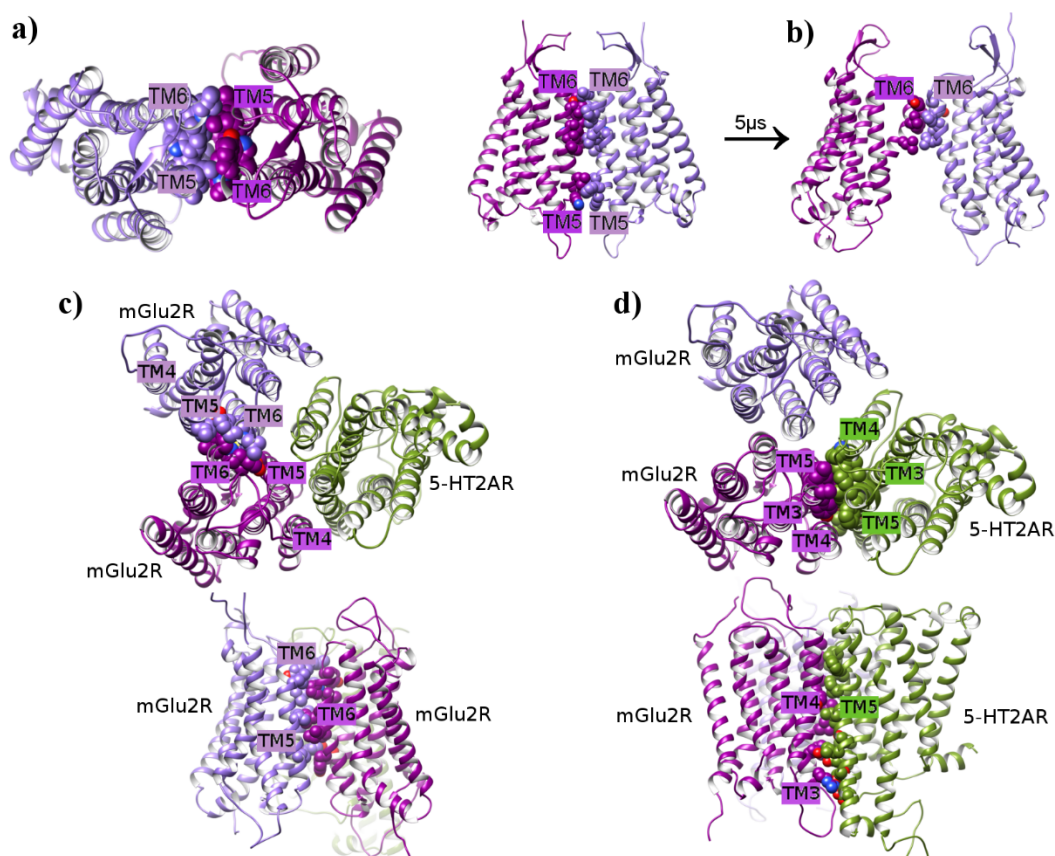
Figure 4. Structure of modelled mGlu2R homodimer and 5-HT$_{2A}$R-mGlu2R heterotrimer. a) Top and side view of initial homology model of mGlu2R homodimer alone with TM5-TM6 interface between protomers (purple and violet, respectively) with van der Waal radii of relevant atoms displayed. **b)** Side view of final conformation of mGlu2R homodimer alone after MD simulation with

TM6-TM6 interface. **c)** and **d)** Final conformation of 5-HT$_{2A}$R-mGlu2R heterotrimer after MD simulation, showing top and side views. In **c)** enhanced stabilization of TM6-TM6 interface between mGlu2R protomers (purple and violet, respectively) and in **d)** TM4-TM5 interface between one mGlu2R protomer (purple) and 5-HT$_{2A}$R (green).
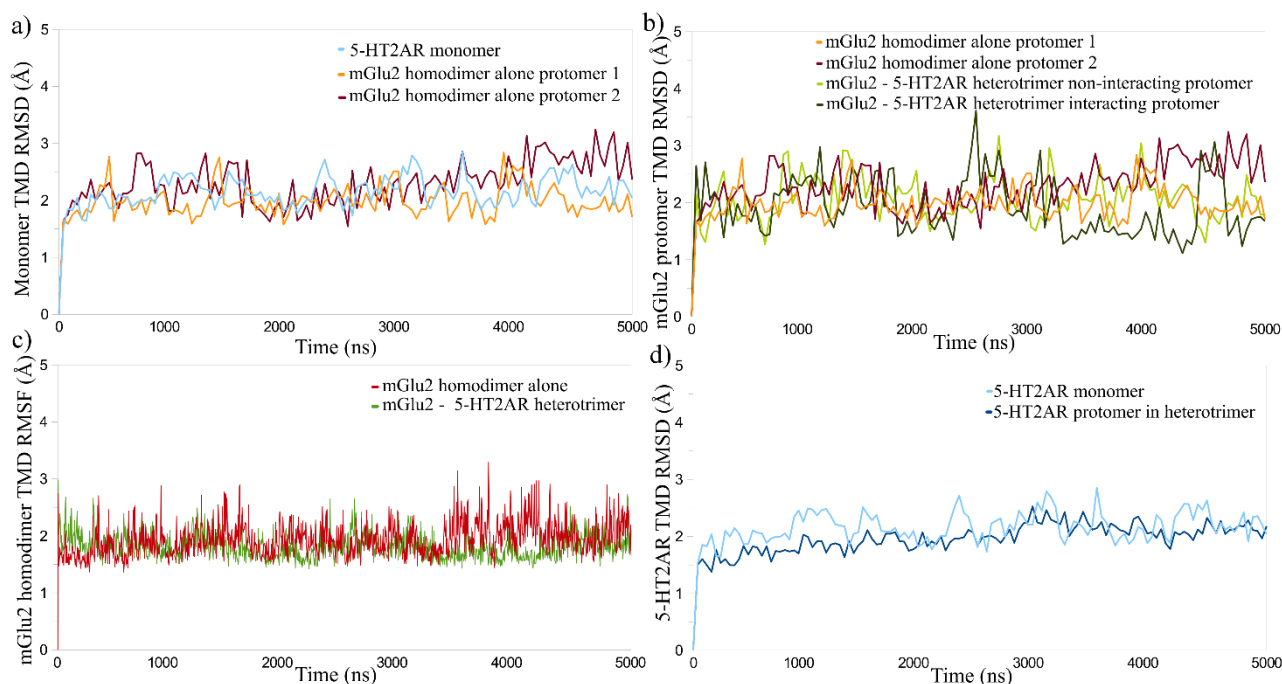
Figure 5. MD simulations showing conformational change of 5-HT$_{2A}$R-mGlu2R interaction. Backbone RMSD of respective **a)** and **b)** protomers #1-2 of mGlu2R homodimer alone (orange and dark red, respectively) compared to **a)** monomeric 5-HT$_{2A}$R (light blue) or **b)** mGlu2R protomer #1-2 of 5-HT$_{2A}$R-mGlu2R heterotrimer (non-interacting mGlu2R protomers, light and dark green, respectively). **c)** Backbone conformational fluctuation (RMSF) of TMD mGlu2R homodimer either by itself or forming a 5-HT2AR-mGlu2R heterotrimer (red or green, respectively). **d)** TMDs RMSD comparison between 5-HT$_{2A}$R as a monomer or as a protomer of 5-HT$_{2A}$R-mGlu2R heterotrimer (light or dark blue, respectively).

3.1.2.3. Receptor heteromerization enhances conformational stability of active mGlu2R homodimer and determines different inter- and intra-receptor functional effects

As reported by previous studies [39](Fribourg et al. 2011), [40](Moreno et al. 2016), [42](Baki et al. 2016), [128](Delille et al. 2014), formation of mGlu2R-5-HT$_{2A}$R oligomers establishes an optimal Gi-Gq balance in response to endogenous ligands: glutamate and 5-HT [39](Fribourg et al. 2011). Despite our mGlu2R-5-HT$_{2A}$R heterotrimer model not containing either bound glutamate, 5-HT or G-protein, the physical stabilization of mGlu2R protomers in their active configuration is consistent with experimental data [129](Rondard et al. 2010),

[33](Xue et al. 2015), and adds further understanding to how Gi-Gq balance might occur. Study of inter- and intra-subunit conformational changes was performed to assess how the cross-talk may occur in this complex, suggesting explanations for the functionality of mGlu2R and 5-HT$_{2A}$R interactions.

Despite the conformational stability of mGlu2R protomers either in an isolated mGlu2R homodimer or forming an mGlu2R-5-HT$_{2A}$R heterotrimer being similar, the spatial arrangements differ between models. In particular, the distance between the centres of mGlu2R protomers becomes noticeably larger in the mGlu2R homodimer alone than when it is forming the heterotrimer (final distances of 40.0 Å and 32.0 Å, respectively, Figure 6). This result indicates that the presence of the 5-HT$_{2A}$R monomer interacting with the mGlu2R homodimer through a TM4-TM5 interface involves the establishment of a closer and more extensive TM6-TM6 interface between mGlu2R protomers. Indeed, the distances between the interacting TM6s of mGlu2R are shorter in mGlu2R-5-HT$_{2A}$R heterotrimer than in the mGlu2R homodimer alone (average TM6-TM6 distances of 12.5 Å (6.5 SD) and 18.2 Å (1.1 SD), respectively, Figure 4 and 6). This enhanced interface between mGlu2R protomers, which physically stabilizes the mGlu2R homodimer active state may provide an explanation for the functional experimentally-observed mGlu2R-5-HT$_{2A}$R cross-talk [39](Fribourg et al. 2011), [40](Moreno et al. 2016), [128](Delille et al. 2014), [129](Rondard et al. 2010).

Despite the interface between mGlu2R protomers being increased when the mGlu2R homodimer interacts with 5-HT$_{2A}$R as compared with its isolation, no sustained breakage (>4.5 Å) of the mGlu2R ionic-lock is observed (Figure 6) [32](Lans et al. 2020), [36](Dalton et al. 2017), [145](Binet et al. 2007), a feature essential for mGlu2R activation if the canonical activation mode of class A GPCRs applies. However, an occasional break in the ionic-lock was observed more frequently in the heterotrimer model than in the mGlu2R homodimer alone (ionic-lock breakage frequency of 7.6% or 2.8%, respectively, Figure 6). Initially, we speculated that intra-subunit activation of either mGlu2R protomer in our MD simulations was absent because of the lack of mGlu2R extracellular domains and a bound G-protein. Now, we know, from crystal structures of full dimeric mGlu2R and GABA$_B$ receptors [34] Seven et al. 2021), [35](Shen et al. 2021), that activation of class C GPCRs

does not require the outward displacement of TM6 and, therefore, complete breakage of the ionic lock does not seem to be a required condition for activation. These experimental results, which may be connected to the dimeric nature of these receptors, confirm previous computational studies from our group showing differences in the activation modes between class A and class C receptors [32](Lans et al. 2020), [36](Dalton et al. 2017). Other subtle intra-subunit conformational differences could be observed in ICL2, where lower conformational fluctuation in the mGlu2R-5-HT$_{2A}$R heterotrimer model resulted in a more stable ICL1-ICL2 distance than compared to the mGlu2R homodimer alone (average ICL1-ICL2 distance between mGlu2R protomers of 19.1 Å (1.3 SD) with associated average RMSF of 1.6 Å (0.6 SD) or 20.0 Å (2.6 SD) with associated average RMSF of 2.6 Å (1.1 SD), respectively, Figure 6). These results can be associated with the interaction with 5-HT$_{2A}$R in its heteromeric interface (Figure 4), which may stabilize mGlu2R ICLs in a conformation more suitable to coupling with an intracellular G-protein, especially as intracellular loops are known to influence mGluR activity [36](Dalton et al. 2017).
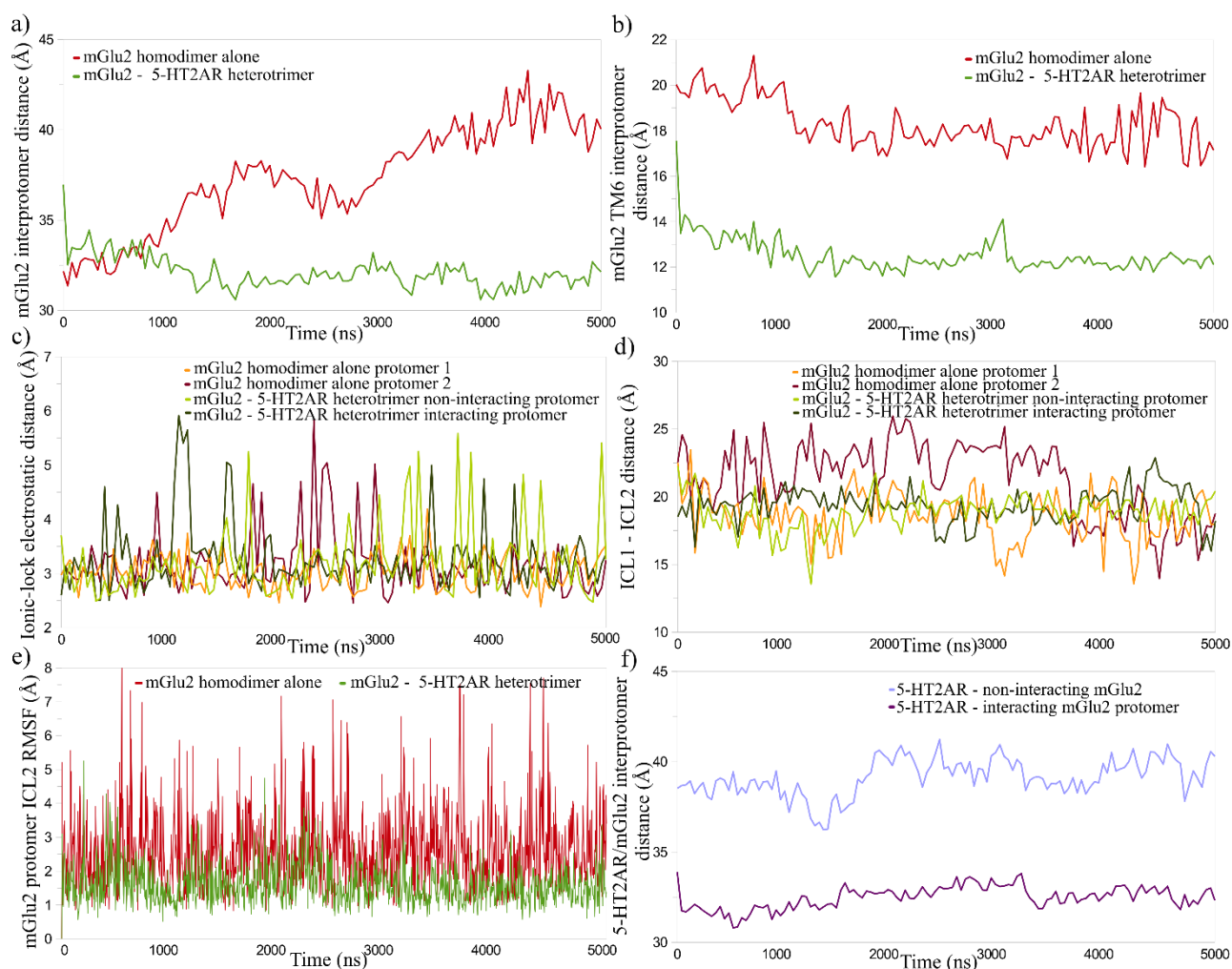
Figure 6. Conformational change of key structural features in mGlu2R homodimer alone or in 5-HT$_{2A}$R-mGlu2R heteromeric complex. Comparison of **a)** mGlu2R inter-protomer distance and **b)** mGlu2R-mGlu2R TM6-TM6 distance of mGlu2R homodimer alone or in 5-HT$_{2A}$R-mGlu2R heterotrimer (red or green, respectively). Comparison of **c)** ionic-lock distance and **d)** intracellular loops (ICL) 1 and 2 distance between mGlu2R protomers #1-2 of the mGlu2R homodimer alone or in 5-HT$_{2A}$R-mGlu2R heterotrimer (orange/dark red or light/dark green, respectively). **e)** ICL2 conformational fluctuation of protomer #1 of mGlu2R homodimer alone or in 5-HT$_{2A}$R-mGlu2R heterotrimer (interacting mGlu2R protomer, red or green, respectively). **f)** Distance between 5-HT$_{2A}$R protomer and either interacting or non-interacting mGlu2R protomers (dark magenta or violet, respectively).

Similarly to the TM6-TM6 interface between mGlu2R protomers, the cross-talking TM4-TM5 interface with 5-HT$_{2A}$R also retains its physical integrity. Distance between centres of 5-HT$_{2A}$R and the interacting mGlu2R protomer remains mostly close and invariable throughout the MD simulation (average distance of 32.4 Å (1.0 SD), Figure 6), comparable to that observed between mGlu2R protomers (Figure 6). Likewise, as might be expected, a larger distance is observed between 5-HT$_{2A}$R and the mGlu2R protomer that does

not interact with 5-HT$_{2A}$R, which despite some observed fluctuation, begins and finishes at a similar point (average distance of 39.1 Å (0.6 SD), Figure 6). The physical stability of both TM4-TM5 and TM6-TM6 interfaces in the mGlu2R-5-HT$_{2A}$R heterotrimer model suggests a conformationally stable complex. These results may indicate a cooperative conformational stabilization of active mGlu2R and inactive 5-HT$_{2A}$R states, which can be associated with the *in vivo* previously described predominance of mGlu2R signalling in mGlu2R-5-HT$_{2A}$R oligomer interactions [39](Fribourg et al. 2011), [40](Moreno et al. 2016), [128](Delille et al. 2014), [129](Rondard et al. 2010).

3.1.2.4. Exploration of cross-linking in the mGlu2R-5-HT$_{2A}$R heterotrimer complex

In order to assist experimental studies, we analyzed the final MD-generated conformation of the mGlu2R-5-HT$_{2A}$R heterotrimer model to find potential point mutations that could be used to coprecipitate mGlu2R–5-HT$_{2A}$R oligomer *in vitro*. A maximum number of three mutations (two on mGlu2R and one on 5-HT$_{2A}$R) were considered sensible to achieve the cross-linking of the complex without excessively compromising either receptor structure. In accordance with the described TM6-TM6 mGlu2R-mGlu2R interface and TM4-TM5 mGlu2R-5-HT$_{2A}$R interface [40](Moreno et al. 2016), [131](Moreno et al. 2012), we proposed different combinations of point mutations (Figure 7 and 8) involving mGlu2R helices: TM3, TM5 and TM6 (TM3 partially participates at an intracellular level in the TM4-TM5 interface); and 5-HT$_{2A}$R helices: TM3, TM4 and TM5. Mutations on TM4 of mGlu2R are specifically avoided, as this might incorrectly cross-link the mGlu2R homodimer in its inactive state, which would probably not be able to heteromerize with 5-HT$_{2A}$R.

3.1.2.5. Prospective cross-linking between active mGlu2R protomers in mGlu2R homodimer alone or in mGlu2R-5-HT$_{2A}$R heterotrimer model

During MD simulation of either mGlu2R homodimer alone or forming a heterotrimer with 5-HT$_{2A}$R, Tyr781$^{6.58}$ residues on TM6 extracellular regions of both mGlu2R protomers close-contacted each other (Figure 8). This heteromeric interaction establishes a close Cα–Cα distance up to 5.5 Å, which either remains stable or transitory throughout MD simulations of mGlu2R-5-HT$_{2A}$R heterotrimeric model or the mGlu2R homodimer alone, respectively (Figure 7). Differences in interaction stability rely on the effect that 5-HT$_{2A}$R exerts on the

active state of the mGlu2R homodimer. In addition to extracellular $Tyr781^{6.58}$-$Tyr781^{6.58}$ interaction, the presence of 5-HT$_{2A}$R involves a tightening of the whole TM6-TM6 interface between mGlu2R protomers (Figure 6). Therefore, this residue represents a single TM6 point mutation that allows cross-linking of the mGlu2R homodimer in its active state, which is ideal to avoid cross-linking of mGlu2R in its inactive state. As such, residue $Tyr781^{6.58}$ appears optimal for mutation in all cross-linking scenarios (Figure 7 and 8).

3.1.2.6. Prospective cross-linking between 5-HT$_{2A}$R and interacting mGlu2R protomer in mGlu2R-5-HT$_{2A}$R heterotrimer model

In addition to $Tyr781^{6.58}$ point mutation, three complementary possible pair of residues were proposed to coprecipitate mGlu2R-5-HT$_{2A}$R heterotrimer (Figures 7 and 8): i) $Leu737^{5.49}$-$Ile206^{4.56}$, ii) $Arg659^{3.56}$-$Gln178^{3.55}$ and iii) $Gly730^{5.42}$ – $Ile237^{5.41}$. Of these, the interaction between mGlu2R: $Gly730^{5.42}$ and 5-HT$_{2A}$R: $Ile237^{5.41}$ shows the closest and most stable Cα-Cα distance in our MD simulation (average Cα-Cα distance of 6.2 Å, Figure 7c), thus indicating a pervasive TM5-TM5 interface between mGlu2R and 5-HT$_{2A}$R at the extracellular side of the receptor. As such, the proposed double mutation of $Gly730^{5.42}$-$Ile237^{5.41}$, in combination with mutation of previously described mGlu2R:$Tyr781^{6.58}$ (Figure 8), resulted in the best predicted cross-linking for the mGlu2R-5-HT$_{2A}$R heterotrimeric complex *in vitro*. These TM5-TM5 point mutations are reinforced by inter-receptor TM3/TM5 interactions at the intracellular level (Figure 7), which are primarily electrostatic in nature and likely help to stabilize the heteromeric complex at the water-membrane boundary. These intracellular interactions mostly involve close contact between sidechains of mGlu2R:$Arg659^{3.56}$ and both 5-HT$_{2A}$R: $Gln178^{3.55}$ and $Glu264^{5.68}$ (average $Arg659^{3.56}$–$Gln178^{3.55}$ amino–carbonyl and $Arg659^{3.56}$–$Glu264^{5.68}$ amino–carboxylate distances of 4.0 Å and 4.3 Å, respectively, Figure 7). These electrostatic interactions seem to be key features in the formation of the heteromeric TM4-TM5 mGlu2R-5-HT$_{2A}$R interface at the intracellular level [39](Fribourg et al. 2011), [40](Moreno et al. 2016), [128](Delille et al. 2014), [129](Rondard et al. 2010), making them less suitable for mutation.
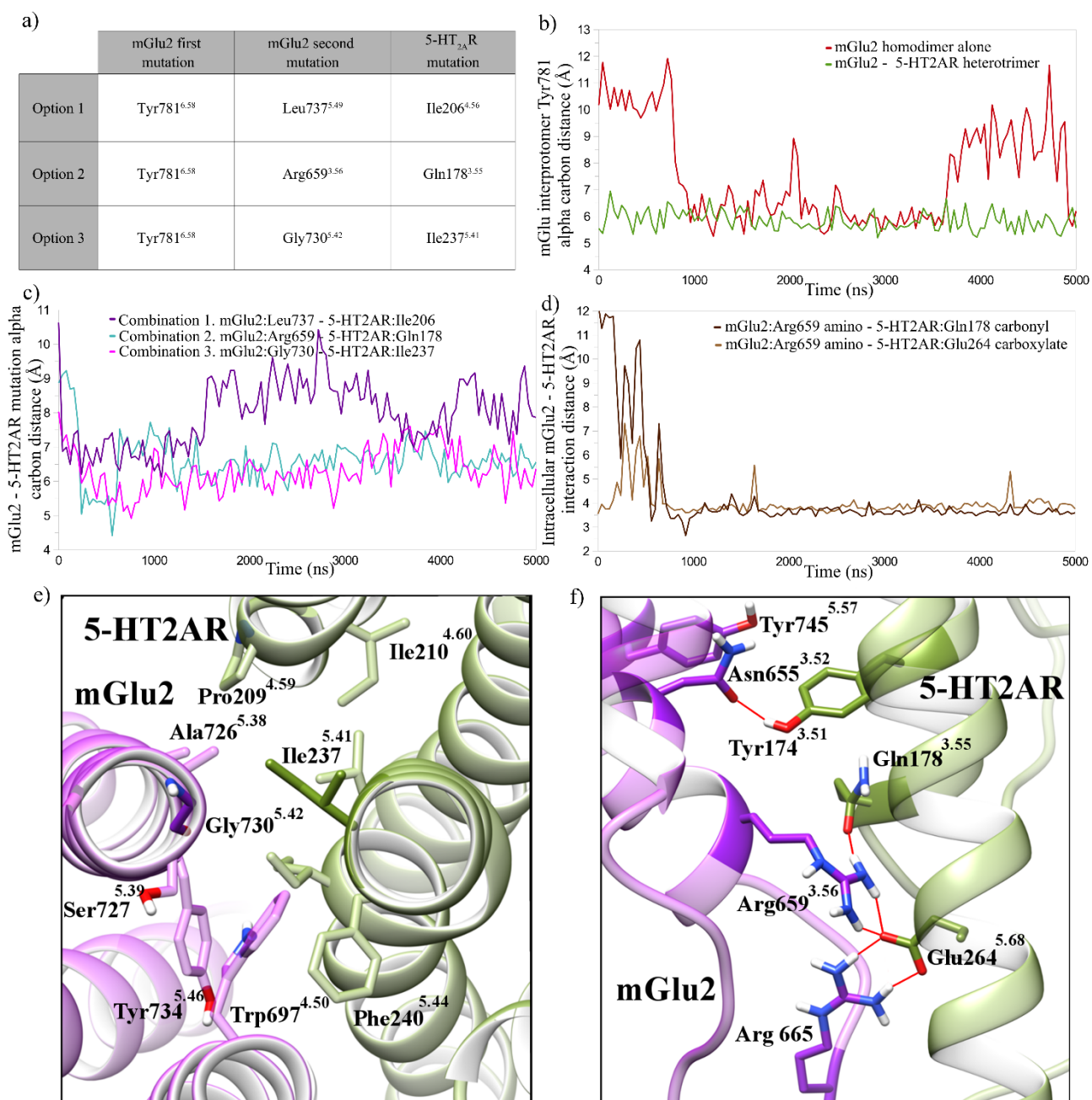
Figure 7. Analysis of mGlu2R-5HT$_{2A}$R interface during MD simulation of heteromeric complex.
a) Table summarizing triple mutation combinations for stabilizing 5-HT$_{2A}$R-mGlu2R heteromeric complex. **b)** and **c)** Cα-Cα distances between proposed mutation points of a) mGlu2R – mGlu2R: Tyr781$^{6.58}$ - Tyr781$^{6.58}$, in mGlu2R homodimer alone or in 5-HT$_{2A}$R-mGlu2R heterotrimer (red or green, respectively), and **b)** mGlu2R - 5-HT$_{2A}$R: Leu737$^{5.49}$ - Ile206$^{4.56}$, Arg659$^{3.56}$ - Gln178$^{3.55}$ and Gly730$^{5.42}$ - Ile237$^{5.41}$ of 5-HT$_{2A}$R-mGlu2R heterotrimer (purple, turquoise or pink, respectively). **d)** Intracellular inter-receptor H-bond/electrostatic residue-residue distances of mGlu2R Arg659$^{3.56}$ amino group and either 5-HT$_{2A}$R Gln178$^{3.55}$ carbonyl group or 5-HT$_{2A}$R Glu264$^{5.68}$ carboxylate group (dark or light brown, respectively). **e)** and **f)** Final MD-generated conformation of 5-HT$_{2A}$R-mGlu2R heteromeric interface from **e)** extracellular and **f)** intracellular sides.
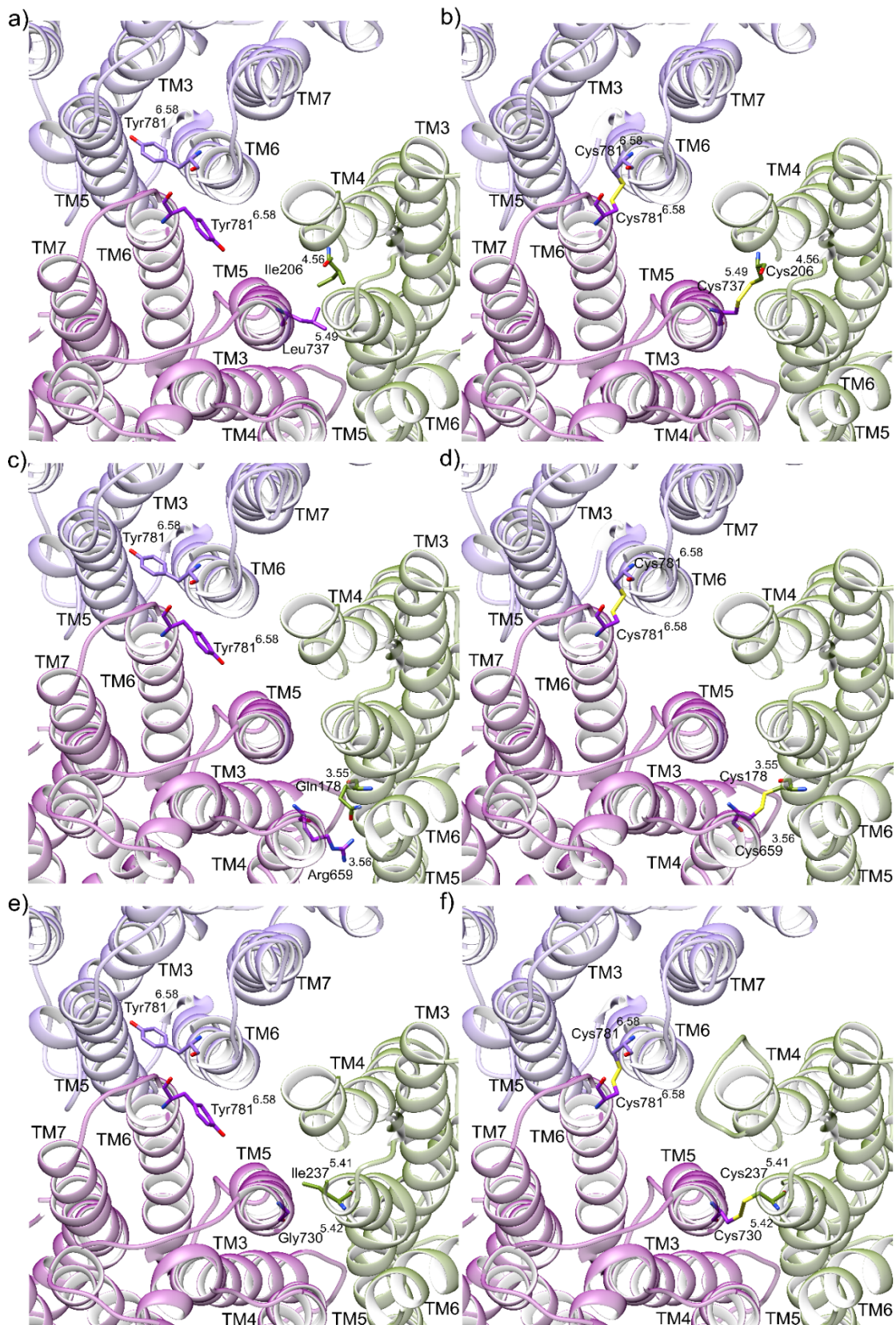
Figure 8. Point mutations. Structural view on the left of **a)**, **c)** and **e)** mutation combinations #1-3 (see Figure 7a) for mGlu2R (violet and purple, non-interacting and interacting mGlu2R, respectively) and 5-HT$_{2A}$R (green) cross-linking. On the right, **b), d)** and **e)** show respective cysteine disulphide-linked mutant models.

3.1.2.7. Comparison of modelled systems against novel crystals of active-state mGlu5 homodimer and monomeric inactive-state 5-HT$_{2A}$R

Our initial mGlu2R-5-HT$_{2A}$R heterotrimer model was limited by the crystal structures available at the time of its modelling. However, posterior comparison with new crystal structures of an mGlu5 homodimer either in its active or inactive states (PDB ids: 6N51 and 6N52, respectively) [135](Koehl et al. 2019), showed some differences in the exact initial position of mGluR protomers forming our mGlu2R homodimer (Figure 9). The novel mGlu5 homodimer crystal structure shows a pure TM6-TM6 interface in comparison with our initial modelled mGlu2R interface, which in addition to TM6 also involved TM5 (lateral translation of 8.2 Å of one mGlu2R protomer compared to the equivalent protomer in mGlu5, Figure 9). This is in accordance with previously published data which stated that, during activation, mGlu2R homodimer switches from a TM4-TM5 interface to a pure TM6-TM6 interface [33](Xue et al. 2015). Despite our initial model not representing a completely activated position, results obtained during MD simulations, which show movements of the mGlu2R protomers towards a pure TM6-TM6 interface (largely shown when 5-HT$_{2A}$R interacts with mGlu2R homodimer), supports the idea that our mGlu2R–5-HT$_{2A}$R interface is good enough to ensure the conformational stability of the higher-order mGlu2R-5-HT$_{2A}$R oligomer. In addition, structural alignment of active mGlu5 crystal protomers over our MD-generated mGlu2R protomers in the mGlu2R–5-HT$_{2A}$R heterotrimer shows very little individual protomer conformational change (max TMD RMSD of 2.1 Å, Figure 9). We can speculate that as our model perhaps represents an activating configuration of the mGlu2R–5-HT$_{2A}$R oligomer, instead of a fully active one, it may assist experimental coprecipitation of the oligomeric complex because only partial mGlu2R activation would be required.

In addition to the mGlu5 homodimer crystal structure, recent structures of 5-HT$_{2A}$R have been released with either bound antipsychotic risperidone or zotepine (PDB ids: 6A93, 6A94) [144](Kimura et al. 2019), which behave as antagonists causing 5-HT$_{2A}$R to adopt an inactive conformation. Despite our monomeric 5-HT$_{2A}$R model being homology modelled from 5-HT$_{2B}$R, very few conformational differences are observed with respect to the newly crystallized 5-HT$_{2A}$R structure (max TMD RMSDs of 2.5 Å and 2.1 Å, respectively, in monomeric form or as part of the heterotrimer). However, intracellular and extracellular

loops present larger conformational changes because of their greater intrinsic flexibility. Nevertheless, this result indicates that our 5-HT$_{2A}$R homology model adopts a reliable conformation for studying transmembrane interactions with the mGlu2R homodimer.
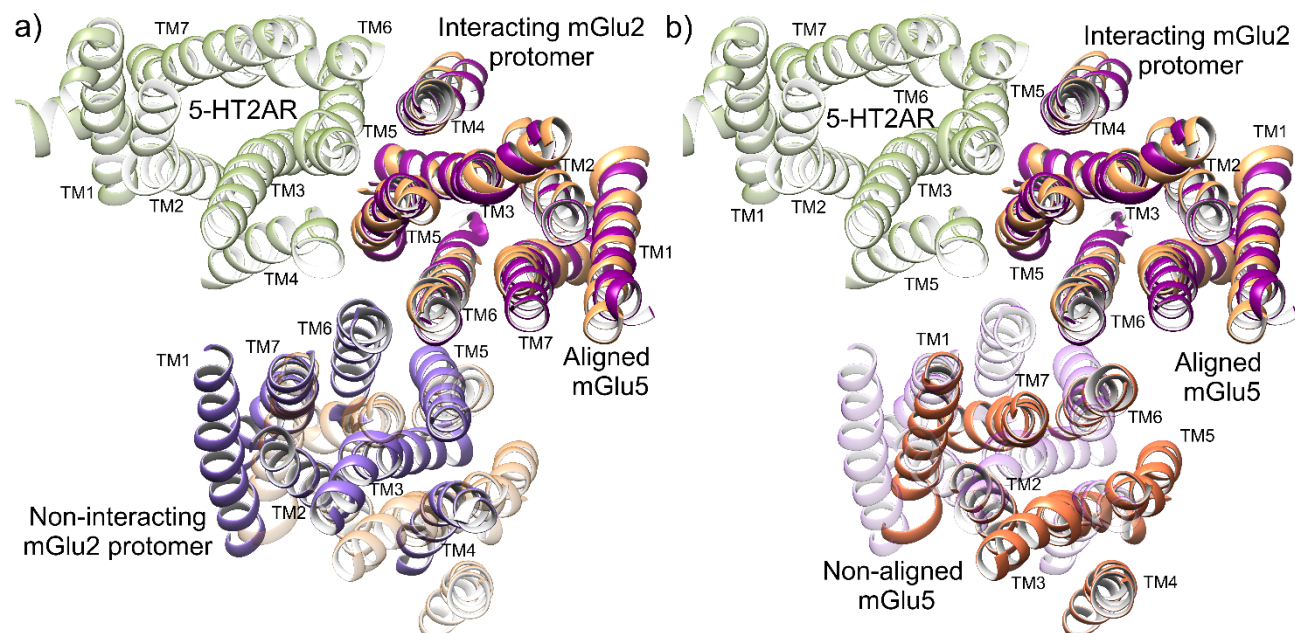
Figure 9. TMD mGlu2R homodimer homology model validation. Superposition of crystallized active mGlu5 homodimer (light or dark orange, aligned or non-aligned mGlu5 protomer, respectively) and MD-generated conformation of mGlu2R – 5-HT$_{2A}$R heterotrimer (non- or interacting [aligned] mGlu2R protomers in violet and magenta, respectively, 5-HT$_{2A}$R in green). **a)** mGlu2R-mGlu2R TM6-TM5/6 interface of our heterotrimer and **b)** mGlu5-mGlu5 pure TM6-TM6 interface observed in crystal.

3.1.2.8. Concluding remarks

The recent experimentally described negative reciprocal influence of 5-HT$_{2A}$R-mediated Gq/11-signalling on mGlu2R-mediated Gi-signalling [39](Fribourg et al. 2011), [40](Moreno et al. 2016), [128](Delille et al. 2014), [129](Rondard et al. 2010), raises special interest in how these two receptors can directly form an oligomeric complex in cell membranes. However, lack of coprecipitation studies with presence of such a complex leads to the need for better understanding. In this context, atomistic computational techniques can help to better comprehend the arrangement and stability of a possible mGlu2R-5-HT$_{2A}$R heterotrimeric complex.

The mGlu2R receptor has been described to form constitutive homodimers with an interface that switches from TM4-TM5 to TM6-TM6 during activation, releasing the TM4-TM5 interface which can potentially interact with other receptors [33](Xue et al. 2015). In addition, 5-HT$_{2A}$R is predicted to make interactions through its TM4 interface with mGlu2 within the hetero-oligomer [40](Moreno et al. 2016), which leads us to consider the formation of a rational oligomeric complex between mGlu2R and 5-HT$_{2A}$R, with an mGlu2R–5-HT$_{2A}$R heterotrimer the simplest oligomeric unit. Because of the lack of crystal structures of both mGlu2R and 5-HT$_{2A}$R at the time of starting this study, we respectively homology modelled them from mGlu1R and 5-HT$_{2B}$R crystals [56](Wu et al. 2014), [55](Wacker et al. 2013), further validating them with recently released active mGlu2R homodimer and inactive 5-HT$_{2A}$R crystals [135](Koehl et al. 2019), [144](Kimura et al. 2019). The results obtained in this study depend on the reliability of the mGlu2R–5-HT$_{2A}$R heterotrimer model and the interactions formed between protomers during a long-timescale unbiased MD simulation. As such, protomers of our modelled mGlu2R–5-HT$_{2A}$R heterotrimer, similarly to those in the isolated mGlu2R homodimer and 5-HT$_{2A}$R monomer, present little conformational change across the entire simulation time. Similarly, both mGlu2R-mGlu2R TM6-TM6 and mGlu2R–5-HT$_{2A}$R TM4-TM5 interfaces remain physically stable throughout the heterotrimer MD simulation in comparison to the slightly lower stability found in the TM6-TM6 interface of mGlu2R homodimer alone. Therefore, we suggest that the presence of 5-HT$_{2A}$R facilitates the stabilization of the active conformation of the mGlu2R homodimer. These results show that our modelled mGlu2R–5-HT$_{2A}$R heterotrimer represents a highly stable complex which can be considered reliable enough to study inter- and intra-receptor conformational effects associated with experimental evidence [39](Fribourg et al. 2011), [40](Moreno et al. 2016), [128](Delille et al. 2014), [129](Rondard et al. 2010).

In this direction, the mGlu2R–5-HT$_{2A}$R heterotrimer model was used for identifying point mutation candidates following a structure-based approach [146](Popov et al. 2018), where close contacting pairs of residues might be replaced with cysteines (point mutations) in order to form inter-protomer disulfide bonds. These covalent bonds can help to restrict the conformational flexibility [146](Popov et al. 2018) of the mGlu2R–5-HT$_{2A}$R oligomeric

complex *in vivo* and improve its stability in order to be coprecipitated. The best candidates predicted involve mGlu2R Gly730$^{5.42}$ and Tyr781$^{6.58}$ and 5-HT$_{2A}$R Ile237$^{5.41}$ residues. In addition, several mGlu2R-5-HT$_{2A}$R residue-residue intracellular electrostatic interactions (Arg659$^{3.56}$ – Gln178$^{3.55}$/Glu264$^{5.68}$, respectively) were suggested to play a key role in the stabilization of the mGlu2R–5-HT$_{2A}$R heterotrimer by stabilizing the TM4-TM5 interface at its intracellular side. Additionally, higher conformational stability of ICL2 and slightly more frequent ionic-lock breakage was observed in the mGlu2R–5-HT$_{2A}$R heterotrimer as compared to the mGlu2R homodimer alone, which may indicate selective oligomeric G-protein binding, especially as intracellular loops are known to influence mGluR activity [36](Dalton et al. 2017).

3.1.3. Dopamine D2 receptor forms homodimeric complexes

The work described in this section was performed in collaboration with the group of Dr. Christophe Stove, from the Faculty of Pharmaceutical Sciences at Ghent University, and published in *International Journal of Molecular Sciences* [43](Wouters et al. 2019). In this study, we provided a structural explanation of the results found by our experimental collaborators where the binding of spiperone and clozapine to D2R induced different homodimerization rates of the receptor. The computational work as well as the writing of the computational section of the manuscript was performed by Adrián Ricarte under the supervision of Dr. James Dalton and Dr. Jesús Giraldo.

3.1.3.1. Dopamine D2 receptor antagonists differentially impact D2 receptor oligomerization

Dopamine receptors have been demonstrated to be involved in the coordination of motor control, cognitive function, memory and reward [147](Rangel-Barajas et al. 2015), [148](Missale et al. 1998). These class A GPCRs, classified in two subfamilies: D1-like, including the D1 and D5 subtypes, and D2-like, including the D2, D3, and D4 subtypes [149](Baulieu et al. 2011), have been proposed to interact with other GPCRs, thus fine-tuning their activation process and function [150](Ferré et al. 2014), [151](Farran 2017), [152](Fiorentini et al. 2010), [153](Blasiak et al. 2017), [154](O'Dowd el al. 2013), [155](Van Craenenbroeck et al. 2014). More specifically, the D2 sub-type receptor (D2R) has

been the target of extensive studies because of its key role in the regulation of physiological actions of the neurotransmitter dopamine, as well as its influence in some diseases such as schizophrenia, Parkinson's disease, depression, attention deficit hyperactivity, stress, nausea, and vomiting [156](Nakawara et al. 2008), [157](Pan et al. 2015), [158](Roccheti et al. 2015), [159](Tozzi et al. 2018), [160](Urs et al. 2017), [161](Weber et al. 2018), [162](Weinstein et al. 2018).

The D2R was first reported to form homodimers in 1996 by Ng et al. [163] by co-immunoprecipitation (co-IP). Further evidence for homodimerization of this receptor has been provided by studies using a wide variety of biochemical techniques such as co-IP, ligand binding [164](Armstrong et al. 2001), fluorescence resonance energy transfer (FRET) [165](Wurch et al. 2001), single-molecule tracking [166](Kasai et al. 2018), and protein–protein docking [167](Kaczor et al. 2016), [168](Kaczor et al. 2016). Heteromeric interactions of D2R with other GPCRs have also been extensively documented such as A2AR-D2R [169](Borroto-Escuela et al. 2018), [170](Canals et al. 2003), β2-D2R [171](Niewiarowska-Sendo et al. 2017), and CB1-D2R [172](Kearn et al. 2005), [173](Pinna et al. 2014). Different TM interfaces formed in the D2R homodimer have been reported based on the incubation of receptors with peptides targeting TM6, which dissociate oligomeric complexes into monomers [163](Ng et al. 1996), [174](Pulido et al. 2018). The importance of this helix was also assessed by Guitart et al. in 2014 [175]. In addition, mutation and cysteine cross-linking studies revealed the relevance of hydrophobic interactions in TM4, a helix that forms part of a TM4-TM5 interface [86](Martínez-Pinilla et al. 2015), [106](Bonaventura et al. 2015), [176](Ferre et al. 2018), [177](Navarro et al. 2018), [178](Qian et al. 2018). This interface, in addition to a TM5-TM6 interface, has been described to establish interactions with other class A GPCRs [38](Oliveira et al. 2017), [86](Martínez-Pinilla et al. 2015), [106](Bonaventura et al. 2015), [176](Ferre et al. 2018), [177](Navarro et al. 2018). Collectively, these reported features support the hypothesis of multiple oligomerization interfaces [179](Kasai et al. 2014), wherein GPCRs undergo multiple cycles of interconversion between monomer and dimer forms, suggesting transient dimer formation with different interfaces [166](Kasai et al. 2018), [180](Tabor et al. 2016), [179](Kasai et al. 2014), [181](Hern et al. 2010), [182](Kasai et al. 2011), [183](Calebiro et al. 2013).

Therefore, there is a growing interest in better understanding the crosstalk between dopamine receptors from a structural point of view.

The emerging evidence on transient dynamics of class A GPCR dimers, characterized by fast association and dissociation events, adds a layer of complexity to the understanding of these phenomena and suggests a functional relevance of receptor oligomerization. Indeed, an increase in D2R homodimer formation has been correlated with the pathophysiology of schizophrenia [184](Wang et al. 2010). Therefore, targeting D2R oligomeric complexes can lead to the identification of potential therapeutic targets and an increase in knowledge of the pathophysiology associated with this receptor. To this end, in the present study, we computationally analyzed the conformational modulation of specific clinically-used D2R antagonists/inverse-agonists and their relevance in D2R homodimerization by using unbiased atomistic long-timescale MD simulations.

3.1.3.2. Spiperone and clozapine achieve stable binding poses in D2R across MD simulations

To computationally approach the modulation of D2R homodimerization by the action of two D2R antagonists of interest, clozapine and spiperone, we first docked them into the monomeric form of D2R crystal structure (PDB id: 6CM4) [52](Wang et al. 2018). Clozapine is an atypical antipsychotic drug, which despite targeting the dopaminergic receptors, has lower affinity and occupancy for them and instead shows a higher degree of occupancy for 5-HT$_{2A}$R [185](Dazzan et al. 2005). Conversely, spiperone belongs to the typical antipsychotic class which exerts its effect through the blocking of D2R [185](Dazzan et al. 2005). During respective 3 μs unbiased MD simulations, both spiperone and clozapine achieved stable binding poses from 0.4 and 1.8 μs onwards, with an RMSD below 2.5 Å (average RMSD of 1.5 Å (0.5 SD) for clozapine and 1.9 Å (1.0 SD) for spiperone, Figure 10). The observed initial conformational changes are expected because of an initial accommodation of the ligand in the orthosteric pocket of the receptor (Supplementary Figure 4). Relatively higher conformational fluctuations observed with spiperone can be attributed to its greater flexibility, mainly due to its central alkyl chain (Supplementary Figure 4). In addition to ligand positional stability, the conformation of the D2R monomer with either

clozapine or spiperone bound remains stable throughout the entire MD simulation time, with final backbone RMSDs of 2.5 Å and 2.2 Å, respectively (Supplementary Figure 4B). In terms of the ligand-protein interactions, both spiperone and clozapine commonly close-contact (<3.5 Å) orthosteric pocket residues: Asp114$^{3.32}$, Val115$^{3.33}$, Ile184^{ECL2}, and Ser193$^{5.42}$ (Figure 10 and Table 1, superscript numbers refer to the Ballesteros and Weinstein generic numbering scheme [26](Ballesteros et al. 1995)). Asp114$^{3.32}$ is a highly conserved residue in class A GPCRs, where several ligands have been found to form a stable electrostatic interaction through their protonated amine group. Differentially, clozapine establishes several distinct contacts with TM5 and TM6, whereas spiperone more frequently interacts with sidechains on TM2 and TM3. These observed interactions are in accordance with the residues in close contact with cocrystallized risperidone [52](Wang et al. 2018), which involve sidechains located on extracellular loop 1 (ECL1), TM3, TM5, and TM6 (Table 1 and Supplementary Figure 5). Noteworthy, these differences between residues may indicate a different mode of signalling through the D2R orthosteric pocket.
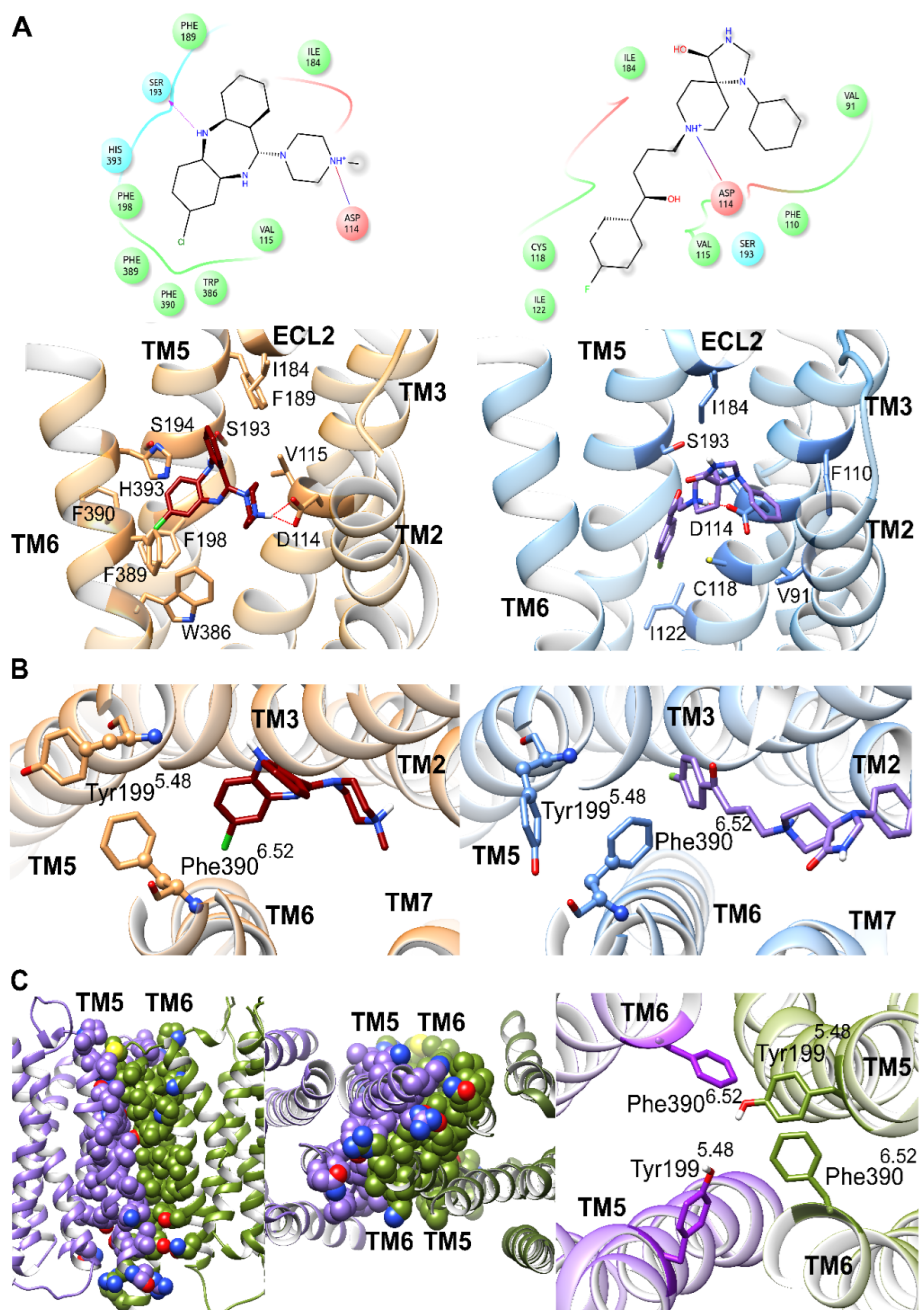
Figure 10. The D2R monomer and homodimer complex. a) 2D and 3D (top and bottom, respectively) stable ligand binding poses including residues in close contact throughout MD simulations (<3.5 Å) with clozapine and spiperone (dark red and purple, respectively) bound to respective D2R monomers (left and right, orange and blue, respectively). **b)** *Trans* and *cis* conformations of Tyr199[5.48] and Phe390[6.52] according to χ1 dihedral angle selected by bound clozapine or spiperone (dark red and purple, respectively) bound to D2R monomers (left and right, orange and blue, respectively). **c)** From left to right, lateral and intracellular views of TM5–TM6/TM6–TM5 D2R homodimer model interface, which generates aromatic interactions between Tyr199[5.48] and Phe390[6.52] of both D2R protomers during an MD simulation (purple or green, respectively).

47

Table 1. Protein–ligand interactions (<3.5 Å) of cocrystallized risperidone, and stably bound clozapine and spiperone throughout MD simulations. (i) Common residues in contact with all ligands; (ii) common residues in contact with risperidone and clozapine; (iii) common residues in contact with risperidone and spiperone; (iv) common residues in contact with clozapine and spiperone.

Ligand	Unique Interactions	Common Interactions	
Risperidone	Trp100^{ECL1}	Asp114$^{3.32}$	(I)
	Ser197$^{5.48}$	Cys118$^{3.36}$	(III)
	Phe382$^{6.44}$	Ile122$^{3.40}$	(III)
	Tyr416$^{7.43}$	Trp386$^{6.48}$	(II)
		Phe389$^{6.51}$	(II)
Clozapine	Phe189$^{5.38}$	Asp114$^{3.32}$	(I)
	Ser193$^{5.42}$	Val115$^{3.33}$	(IV)
	Phe198$^{5.47}$	Ile184^{ECL2}	(IV)
	Phe390$^{6.52}$	Ser193$^{5.42}$	(IV)
	His393$^{6.55}$	Trp386$^{6.48}$	(II)
		Phe389$^{6.51}$	(II)
Spiperone	Val91$^{2.61}$	Asp114$^{3.32}$	(I)
	Phe110$^{3.28}$	Val115$^{3.33}$	(IV)
		Cys118$^{3.36}$	(III)
		Ile122$^{3.40}$	(III)
		Ile184^{ECL2}	(IV)
		Ser193$^{5.42}$	(IV)

3.1.3.3. Spiperone and clozapine select different sidechain conformations in D2R TM5 and TM6

Residue-level analysis of the MD-generated D2R conformation shows that spiperone and clozapine do not induce/select conformational changes in TM residues with the exception of TM5 and TM6, more specifically residues Tyr199$^{5.48}$ and Phe390$^{6.52}$, which showed different χ1 dihedral angle conformations. In general terms, two different semi-stable conformations can be observed in our MD simulations for these two aromatic residues, a *cis* and a *trans* χ1 dihedral angle of 300° and 180°, respectively (Figure 10). In the D2R crystal [52](Wang et al. 2018), both Tyr199$^{5.48}$ and Phe390$^{6.52}$ present *cis* conformations. Throughout our MD simulations, the *trans* conformation of these sidechains occurs more frequently with bound clozapine than with bound spiperone (Figure 11). Specifically, considering only time periods where clozapine and spiperone present stable binding poses (respectively from 0.4 and 1.8 μs onwards), clozapine preferentially selects Tyr199$^{5.48}$ and Phe390$^{6.52}$ χ1 *trans* conformations

99% of the time, which lead them to adopt an outward orientation (towards the membrane). This "double" $\chi 1$ *trans* conformation may potentially encourage protein–protein interactions through the formation of aromatic contacts with other GPCRs, in general, and D2R homodimers in particular [186](Madhusudan Makwana et al. 2015). Conversely, spiperone induces rapid fluctuations between $\chi 1$ *cis* and *trans* conformations of Tyr199[5.48], with the *cis* selected 25% of the time, whereas the *cis* conformation of Phe390[6.52] is exclusively maintained. In comparison with clozapine, the spiperone-mediated *cis* conformation of Tyr199[5.48] and Phe390[6.52] leads to a more inward sidechain orientation, away from the membrane, which may conceivably discourage protein–protein interactions (Figure 10).

3.1.3.4. Aromatic interactions stabilize D2R homodimer model interface throughout MD simulation

In order to evaluate the different implications that the conformational changes exerted by spiperone and clozapine in a D2R monomer can have in a D2R homodimer, we modelled the latter, using protein-protein docking on two copies of the D2R crystal structure without bound antagonist and following a TM5-TM6 interface (in line with experimental evidence by Pulido, 2018 [174]). The resulting D2R homodimer has a highly favourable interface docking score of −9.7 (on a scale of 0 to −10, where lower than −5.0 was considered satisfactory [71](Lyskov et al. 2013); see Methods) and was considered as a sensible starting point to run 3 μs unbiased MD simulations (Figure 10). During this period of time, the interface maintains a close interaction between TM5 and TM6 of each protomer of the D2R homodimer, experiencing a moderate backbone conformational change of 3.2 Å, which enhances hydrophobic interactions with an average interaction energy of −11.7 kcal/mol (3.2 SD, Supplementary Figure 4).

To ascertain the relevance of residues Tyr199[5.48] and Phe390[6.52] in the interactions involved in the interface between TM5 and TM6, we performed an analysis of the $\chi 1$ dihedral angles (Figure 10). In both protomers of the D2R homodimer, a *cis* to *trans* conformational change rapidly occurred for Phe390[6.52] $\chi 1$ dihedral angle, selecting this conformation in 90% and 93% of total MD simulation time, respectively (Figure 10 and 11). Conversely, only one of the protomers presented the selection of Tyr199[5.48] *trans* conformation over 94% of simulation time, whereas no significant conformational change of Tyr199[5.48] was observed for

the second protomer (Figure 10 and 11). The overall outward conformation of Tyr199[5.48] and Phe390[6.52] achieved in the D2R homodimer enables the formation of an aromatic interaction network as well as transient H-bond formation between Tyr199[5.48] sidechains (H-bond occupancy of 4%). As a result, the average minimum distance between Tyr199[5.48]/Phe390[6.52] residues of each protomer was 5.5 Å (1.5 SD, Supplementary Figure 4C). From an energetic point of view, alanine scanning of Tyr199[5.48] and Phe390[6.52] confirmed the relevance of these residues in the D2R homodimer interface, where removal of these interactions resulted in a less favourable average interface energy of −8.6 kcal/mol (2.8 SD). These results suggest that the aromatic interaction network formed between Tyr199[5.48] and Phe390[6.52] contributes an average energy of −3.1 kcal/mol at the homodimer interface.
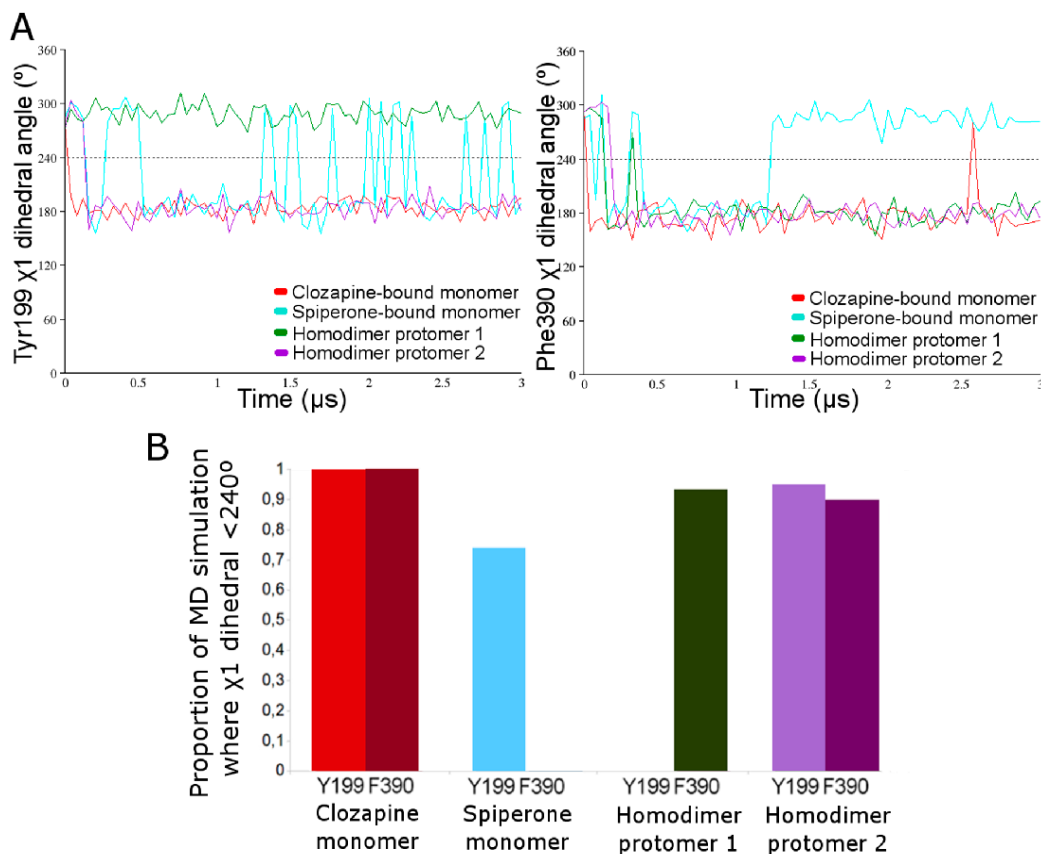
Figure 11. Conformational change of Tyr199[5.48] and Phe390[6.52] $\chi 1$ dihedral angles. a) Time-dependent plots of Tyr199[5.48] and Phe390[6.52] $\chi 1$ dihedral angle induction/selection (left and right graph, respectively) of D2R monomer with bound clozapine or spiperone, and protomer 1 or 2 of D2R homodimer (red, blue, green and purple, respectively) throughout their respective MD simulations. Black dotted line indicates cis/trans conformation threshold. **b)** Proportion of selected $\chi 1$ dihedral angle conformation <240º in D2R monomer with bound stable clozapine or spiperone, and protomer 1 and 2 of D2R homodimer (red, blue, green and purple, respectively).

50

3.1.3.5. Discussion

Over the past few decades, it has been widely suggested that GPCRs are able to form dimers and higher-order oligomers [187](Rossi et al. 2017). These oligomeric forms of GPCRs represent a novel possible target for pathophysiological processes related to the alteration of signalling cascades. Specifically, a significant increase in D2R dimerization has been associated with schizophrenia [184](Wang et al. 2010). Although significant knowledge has been gathered concerning dimer formation of D2R in the cell membrane [166](Kasai et al. 2018), [180](Tabor et al. 2016), [179](Kasai et al. 2014), [181](Hern et al. 2010), [182](Kasai et al. 2011), [183](Calebiro et al. 2013), key questions about the biological mechanisms and their physiological relevance still remain unanswered. In particular, and making the study more difficult, multiple oligomerization interfaces have been proposed that may be part of the homodimerization process [179](Kasai et al. 2014), with recent interest on TM5 and TM6 [174](Pulido et al. 2018), [178](Qian et al. 2018), [175](Guitart et al. 2014). In the present study, we have addressed the reliability of this dimeric interface and its implication in the D2R homodimer by means of computational techniques including unbiased microsecond-length MD simulations. In addition, we have evaluated the effect that different antagonists: clozapine and spiperone exert on the ability of D2R to form GPCR-GPCR interactions by modulating the conformation of interacting sidechains. The oligomeric modulation of GPCRs induced by ligands is a topic which has previously been debated [188](Ilien et al. 2009), [189](Milligan 2004), [190](Saenz del Burgo et al. 2010), with arguments for and against. In the present study, we further elaborated on this topic and demonstrated the ability of spiperone to alter the dynamic equilibrium between D2R monomers and dimers, with a clear preference towards monomers, in comparison to clozapine.

From an experimental point of view, our collaborators found that the typical D2R antipsychotic antagonist spiperone could significantly decrease the level of D2R dimers by 40%–60% in real-time and after long-term incubation, in comparison to atypical antipsychotic antagonists like clozapine. Computational techniques such as MD simulations have shown promising potential for studying GPCRs, such as D2R, and their associated signalling transmission mechanisms [168](Kaczor et al. 2016). Our study therefore made use

of computational resources to describe noticeable differences between orthosteric binding poses of spiperone and clozapine in a D2R monomer. Different binding poses led to different conformations of Tyr199[5.48] and Phe390[6.52] sidechains located in TM5 and TM6. Briefly, spiperone induces/selects an inward position of Tyr199[5.48] and Phe390[6.52] in a D2R monomer, compared with bound clozapine, which exposes them toward the membrane, being able to interact with other elements such another D2R monomer. In addition, outward conformations of Tyr199[5.48] and Phe390[6.52] are present in our modelled D2R homodimer, establishing aromatic interactions between them and occasional H-bonding between Tyr199[5.48] of both protomers. This result may be indicative of the relevance of these two residues in the establishment of a TM5–TM6 interface and their role in the homodimerization process. This TM5-TM6 interface, followed in our model in accordance with a previously published D2R–mGlu5 heterodimer model presented by Qian et al. (2018) [178], is physically stable during microsecond-length MD simulations. In addition to this homodimeric interface, it has been widely described that D2R heteromerizes through a TM4–TM5 interface with other class A GPCRs, such as A2AR and AT1R [38](Oliveira et al. 2017), [86](Martínez-Pinilla et al. 2015), [106](Bonaventura et al. 2015), [176](Ferre et al. 2018), [177](Navarro et al. 2018). Our experimental collaborators found that spiperone, while reducing D2R homodimer formation, preserves the effect on A2AR–D2R heterodimer formation. The fact that the conformational change occurring in Tyr199[5.48] and Phe390[6.52] would affect the TM5-TM6 interface without compromising the TM4-TM5 interface, may explain the experimental difference between D2R homodimer and A2AR-D2R heterodimer formation. Altogether, these results indicate that the interfaces involved in homodimerization of D2R may differ from the interfaces involved in heterodimerization processes with other class A GPCRs, which could also differ between different GPCR classes, in agreement with the hypothesis of multiple oligomerization interfaces presented by Kaisai et al. (2014) [179].

Interestingly, Ng et al. (1996) [163](Ng et al. 1996) postulated that spiperone favours binding to the monomer over the dimer, whereas risperidone (atypical antipsychotic) binds to monomers as well as dimers. In light of our findings, one might hypothesize that spiperone does not necessarily favour binding to monomers, but simply reduces the number of dimers, as observed in this study. On the contrary, Armstrong et al. (2001) [164](Armstrong et al.

2001) reported quite opposite data obtained from ligand binding experiments. These authors proposed a model wherein D2R can form dimeric units with two orthosteric binding sites, one in each protomer, which allows allosteric cooperativity between the two units. Within the mindset of this proposed model by Armstrong et al. [164](Armstrong et al. 2001), spiperone binds to the D2R dimer, and although no negative effect on affinity due to cooperativity was observed by the authors, from our data we would suggest that conformational changes within the dimer upon spiperone binding might lead to dissociation of the dimer into its monomers. Based on the present understanding, further research to study the effect of the D2R antagonist spiperone on the D2R homodimer is required.

3.2. Ligands induce conformational changes in GPCRs conditioning their activation mechanism. Ligand-protein interactions

3.2.1. Fentanyl activates the mu-opioid receptor (MOR) differently than morphine

The following study was published including Adrián Ricarte as first-author in *Journal of Chemical Information and Modeling* [49](Ricarte et al. 2021). The study shows the binding pose differences between fentanyl and morphine, which differently affect the MOR orthosteric pocket conformation and resulting TM3, TM5, TM6 and TM7 conformations. Here we describe that fentanyl has a stronger effect on TM6 and TM7 conformation, while morphine preferentially affects TM3 and TM5. As conformational change in TM6 is critical for GPCR activation and G protein binding, this likely explains the enhanced receptor activity elicited by fentanyl in vivo and its associated higher potency. All the computational work was performed by Adrián Ricarte under the supervision and guidance of Dr. James Dalton and Dr. Jesús Giraldo.

3.2.1.1. Chronic pain and MOR pharmacology: getting knowledge from morphine and fentanyl agonists

Chronic pain is a major public health problem with a high prevalence and impact on quality of life [44](Steglitz et al. 2012), [191](Breivik et al. 2006). Opiate-mediated analgesia has shown to be the most efficacious treatment for chronic pain [192](O'Brien et al. 2017), which primarily targets the MOR, a class A GPCR encoded by the Oprm1 gene [193](Wang et al.

1994). Upon binding of opioid analgesics, ligand-specific conformational changes occur in the MOR [48](Huang et al. 2015), which lead to activation of the receptor and coupling with intracellular heterotrimeric Gi protein or β-arrestin [48](Huang et al. 2015), thus mediating the propagation of the receptor message through different signalling pathways. It remains elusive precisely how ligand−receptor interactions at the binding site influence MOR conformational dynamics and hence different signal transmissions. While the therapeutic effect of opioid analgesics is mainly attributed to MOR activation through Gi protein signalling [48](Huang et al. 2015), [194](Roeckel et al. 2017), [195](Kapoor et al. 2017), [196](Raehal et al. 2005) their side effects, opioid-induced hyperalgesia, constipation, respiratory depression, and analgesic tolerance, have mostly been linked to β-arrestin signalling [48](Huang et al. 2015), [194](Roeckel et al. 2017), [195](Kapoor et al. 2017), [196](Raehal et al. 2005). Thus, agonists biased toward the Gi protein pathway would be ideal to be considered for drug development as potential future medications. Following this research direction, high expectations were generated by preclinical in vivo studies on the MOR Gi protein-biased agonist TRV130 (oliceridine) [197](DeWire et al. 2013), [198](Schneider et al. 2016). Oliceridine has been recently approved (August 2020) by the US Food and Drug Administration (FDA) under the trade name Olinvyk for short-term intravenous use in hospitals and other controlled settings [199](FDA news release web site). Moreover, in the prescribing information leaflet, it is stated that oliceridine is a full opioid agonist and is relatively selective for the MOR. It is also recognized that, depending on the dose used, adverse reactions, including respiratory, and CNS depression may appear. Importantly, it is also stated that the precise mechanism of the analgesic action is unknown although specific CNS opioid receptors are thought to play a role in the analgesic effects of the drug [200](Olinvyk web site), [201](Lambert et al. 2020). Thus, although drug discovery programs based on biased agonism seem to be a promising strategy, in particular for the MOR, they still need further knowledge and experimentation both at the molecular and quantitative pharmacology levels [202](Gurevich et al. 2020), [203](Wingler et al. 2020), [204](Kenakin et al. 2013), [205](Hall et al. 2018), [206](Gillis et al. 2020). In this regard, following the strategy of MOR biased agonism, several studies have examined how agonists targeting the MOR interact with specific residues to selectively regulate coupling of Gi protein or β-arrestin [207](Manglik et al. 2016), [208](Azzam et al. 2019),

[209](Piekielna-Ciesielska et al. 2018), [210](Pasquinucci et al. 2019), [211](Schmid et al. 2017), which in some cases have led to the discovery of new analgesics with reduced negative side effects [207](Manglik et al. 2016), [212](Grim et al. 2020). Yet, although some structural studies of varying MOR agonist efficacy have been addressed [213](de Waal et al. 2020), [214](Lipiński et al. 2019), there is still a lack of complete understanding of the precise nature of ligand−MOR interactions responsible for observed pharmacological profiles. In this regard, further studies at the atomic level including agonists with different efficacies can shed light on MOR activation mechanisms. This was the reason for selecting morphine and fentanyl for the present study. Fentanyl is a high-efficacy MOR agonist, whereas morphine is a lower efficacy MOR agonist, which, depending on the assay performed, can behave as a partial agonist [215](Morgan et al. 2011), [216](Kelly et al. 2013). It is expected that the generated knowledge can be later incorporated into drug discovery programs with a view to avoiding ligands with unwanted effects yet conserving the analgesic capacity of the most powerful drugs.

Biophysical studies of the MOR have led to the determination of three different crystal structures of the receptor: inactive [47](Manglik et al. 2012), activated [48](Huang et al. 2015), and fully active [68](Koehl et al. 2018) structures of the murine MOR (mMOR). In 2012, the inactive crystal structure of the mMOR [47](Manglik et al. 2012) was obtained by X-ray crystallography, cocrystallized with the morphine-like antagonist β-FNA covalently bound to Lys233$^{5.39}$ (superscript numbers refer to the Ballesteros and Weinstein generic numbering scheme [26](Ballesteros et al. 1995)). This structure provided the first high-resolution insight of the MOR [47](Manglik et al. 2012), which enabled the application of structure-based computational approaches: rational targeted drug design [217](Filizola et al. 2012), [218](Carroll et al. 2014), [219](Yuan et al. 2013), receptor oligomerization studies with other GPCRs [220](Fujita et al. 2014), [221](Lee et al. 2013), and study of the mechanism by which sodium ions prevent large-scale movement of transmembrane (TM) helix 6 away from TM3, which inhibits receptor activation [222](Shang et al. 2014), [223](Livingston et al. 2014). In 2015, an activated crystal structure of the mMOR bound to the morphine-like agonist BU-72, with intracellular binding of a G protein mimetic camelid antibody fragment (Nb39), was resolved by X-ray crystallography [48](Huang et al. 2015). G

protein mimetic nanobodies have been shown to be of great utility for stabilization of active-like states of GPCRs [224](Rasmussen et al. 2011), [225](Ring et al. 2013), [226](Kruse et al. 2013). The crystal structure of the activated mMOR shed light on the structural features of MOR activation that are responsible for the efficacy of most therapeutic analgesics. In addition, it allowed the description of an extensive reorganization of the protein−water polar network, required in the full activation process [48](Huang et al. 2015), which is associated with an efficient allosteric coupling between the receptor orthosteric pocket and Gi protein-coupling interface [48](Huang et al. 2015), [227](Sounier et al. 2015). However, it was not until 2018 that a structure of the fully active state of the mMOR was achieved by cryo-electron microscopy [68](Koehl et al. 2018). This receptor structure with bound peptide agonist DAMGO and human Gi protein has provided new insights into the mechanism of intracellular binding to the MOR [68](Koehl et al. 2018).

Computational techniques such as MD simulations have shown promise in further understanding the complexities of MOR signalling mechanisms. For example, several MD simulation studies of the MOR [48](Huang et al. 2015), [195](Kapoor et al. 2017), [207](Manglik et al. 2016), [213](de Waal et al. 2020), [214](Lipiński et al. 2019), [68](Koehl et al. 2018) initialized from inactive [47](Manglik et al. 2012) and activated [48](Huang et al. 2015) mMOR crystal structures, have been worthy in assessing some relevant features of the activation process. Briefly, the activated mMOR crystal structure presents, compared to the inactive crystal structure, (i) large outward movement of TM6 relative to TM3, (ii) smaller inward movements of TM5 and TM7, (iii) breakage of the H-bond between Arg165$^{3.50}$ and Thr279$^{6.34}$ (equivalent of the classical Arg3.50−Asp/Glu6.30 GPCR ionic lock, which involves an acidic amino acid at position 6.30 that is lacking in the MOR) [228](Huang et al. 2002) and formation of a H-bond between Arg165$^{3.50}$ and Tyr252$^{5.58}$, (iv) inward movement of the N$^{7.49}$PXXY$^{7.53}$ motif on TM7 towards TM5 [48](Huang et al. 2015), [195](Kapoor et al. 2017), [207](Manglik et al. 2016), [68](Koehl et al. 2018) and (v) upward axial movement of TM3 [18](Dalton et al. 2015). In general, previous MD studies were performed by removing non-native Nb39 and T4 lysozyme, as well as bound ligands BU-72 and β-FNA, from activated and inactive states of the mMOR, respectively [48](Huang et al. 2015), [47](Manglik et al. 2012), [68](Koehl et al. 2018). In

particular, a model was provided to show how efficacy depends on small chemical differences in structurally similar morphine-like ligands [48](Huang et al. 2015). A shared feature of bound opioid ligands revealed in these studies [48](Huang et al. 2015), [195](Kapoor et al. 2017), [207](Manglik et al. 2016), [47](Manglik et al. 2012), [68](Koehl et al. 2018), [229](Kaserer et al. 2016) is the protonation of their tertiary amine, which is necessary to form a conserved salt bridge with Asp147$^{3.32}$ on TM3 in the orthosteric pocket. This residue is also located within the H-bond distance with Tyr326$^{7.43}$ on TM7 in the mMOR [230](Mansour et al. 1997), thus favouring interaction between TM3 and TM7 and activation of the receptor [18](Dalton et al. 2015), [231](Xu et al. 2008), [232](Li et al. 1999), [233](Befort et al. 1996). This can be observed in activated and inactive crystal structures of the mMOR [48](Huang et al. 2015), [47](Manglik et al. 2012), where the distance between these residues is closer in the activated crystal structure than in the inactive one. In addition, computational studies of the mMOR have reported specific protein−ligand interactions such as the plausible existence of two possible tautomers of His297$^{6.52}$, which can have relevance in ligand function [207](Manglik et al. 2016), as well as Tyr326$^{7.43}$ and Gln124$^{2.60}$ H-bonding interactions, which may also determine ligand activity [194](Roeckel et al. 2017), [230](Mansour et al. 1997). However, computational techniques are yet to satisfactorily explain varying MOR agonist efficacy and potency.

Opioid analgesics, the prototypical pain killers, differ from each other in their structural scaffold and potency. Of all of them, the naturally occurring compound morphine has been considered the reference MOR agonist to which other opioid analgesics are compared [234](James et al. 2020). In the last decade, fentanyl, a synthetic opioid 50−100 times more potent than morphine [45](O'Donell et al. 2017), [46](Mounteney et al. 2015), [235](Vardanyan et al. 2014), and fentanyl analogs have been related to a rapid increase in the number of opioid overdose deaths because of legal (such as transdermal patches, which led to an increase in deaths up to 2010 [236](Grissinger et al. 2010), [237](Schifano et al. 2019)) or illicit manufacture [45](O'Donell et al. 2017), [46](Mounteney et al. 2015), [235](Vardanyan et al. 2014), [238](Lyons et al. 2015), [239](Warner et al. 2016). This has contributed to what is called the opioid epidemic, which has affected mainly the United States and Canada and, to a lower degree, Europe [240](Skolnick et al. 2018), [241](Verhamme et

al. 2019). Fentanyl differs from morphine primarily in its pharmacokinetic properties [234](James et al. 2020), constituting a highly lipid-soluble drug compared to low lipid solubility of morphine, allowing it to penetrate the blood−brain barrier faster [234](James et al. 2020), [235](Vardanyan et al. 2014). Therefore, fentanyl has a faster onset but shorter duration of action than morphine [234](James et al. 2020), [235](Vardanyan et al. 2014). Following receptor activation, differences in morphine and fentanyl structural scaffolds determine specific ligand-dependent receptor internalization processes [242](Anselmi et al. 2013). It has been described [242](Anselmi et al. 2013) that high-efficacy opiates like fentanyl induce rapid MOR phosphorylation and internalization compared to morphine. However, 50−100 times potency difference [45](O'Donell et al. 2017), [46](Mounteney et al. 2015), [235](Vardanyan et al. 2014) between fentanyl and morphine has been widely discussed by in vitro studies [211](Schmid et al. 2017), [243](Zheng et al. 2008), [244](Mori et al. 2017), [245](Kovoor et al. 1998), [246](Burgueño et al. 2017) and its potential relation with fentanyl β-arrestin-biased behaviour has not been clearly established. In this regard, a recent literature [247](Vasudevan et al. 2020) study supports that both fentanyl and morphine work as unbiased agonists [248](Kalvass et al. 2007), [249](Bobeck et al. 2012), [250](Trescot et al. 2008) toward Gi protein and β-arrestin signalling pathways [243](Zheng et al. 2008), [244](Mori et al. 2017), [245](Kovoor et al. 1998). Apparently, contradictory conclusions on biased signalling may depend not only on the variety of biological assays used but also on the mathematical models and parameters employed. Thus, while the Emax/EC50 sigmoidal-fitting parameter was chosen in [247](Vasudevan et al. 2020), a comparison between operational τ/KA and τ parameters was made in [246](Burgueño et al. 2017). In the latter study, while fentanyl was found to be G protein-biased under the τ/KA parameter, an opposite bias toward the β-arrestin signalling pathway was found when using the τ parameter [246](Burgueño et al. 2017). Moreover, it has been shown, by measuring the antinociceptive and respiratory depressant effects of some MOR agonists, that the low intrinsic efficacy of some opioid ligands can explain their improved side effect profile [251](Gillis et al. 2020). Additionally, a strong correlation between measures of efficacy for receptor activation, G protein coupling, and β-arrestin recruitment was found for some MOR agonists, including those that had previously been described as biased [251](Gillis et al. 2020). A detailed review on the relationship between agonist efficacy, biased agonism, and therapeutic window can be

found in [206] Gillis et al. 2020. This issue is still under debate as can be seen in [252] Stahl et al. 2021.

From the above data, it can be concluded that the mechanisms of MOR activation and signal transduction are not yet fully understood. Although downstream signalling events occur after a number of steps following the initial drug-receptor interactions at the receptor binding site, a chemical connection is expected to be present between initial and final signalling states. Thus, understanding of the distinct receptor conformational changes induced by high- and low-efficacy MOR agonists, and their differential involvement in the activation of the receptor, can be informative to identify the structural features that cause different MOR functionalities. This knowledge is crucial for the rational design of safer but not weaker drugs.

The experimentally observed functional MOR response to morphine and fentanyl is a consequence of molecular events that occur first in the receptor as a result of the interactions established by these ligands with residues of the receptor binding pocket, which are then transmitted from the extracellular to the intracellular side of the cell membrane. In this context, in the present study, we performed unbiased μs-length MD simulations to complete a detailed atomic level study of the receptor conformational space induced or selected in the MOR by morphine and fentanyl in order to explain the variations seen in opiate efficacy [215](Morgan et al. 2011). Receptor activation by either induction or selection of receptor active states has been recurrently under debate [253](Changeux et al. 2011) though they may coexist and be part of the same thermodynamic cycle [254](Giraldo et al. 2004). Here, both models are considered, which will allow noteworthy structural comparisons. Despite human and murine MOR sequences being highly similar (94 %), we consider that in order to understand how opioid analgesics transmit their molecular signal and generate effects in humans, it is appropriate to perform our study in the native human MOR (hMOR) and across multiple independent MD trajectories. Our results show that fentanyl displays a completely different binding pose from morphine, which leads to divergent effects on the orthosteric pocket conformational arrangement. The fact that both morphine and fentanyl could activate both Gi protein and β-arrestin signalling pathways raises the question of which signalling

pathway corresponds to the receptor conformational changes found computationally. This is a question for which there is not a definite answer with the present knowledge. Nevertheless, to avoid speculations, structural comparison of computational structures was made with the current MOR crystal structures [48](Huang et al. 2015), [47](Manglik et al. 2012), [68](Koehl et al. 2018), which are related to the Gi signalling pathway. Our results show that extracellular conformational changes of the receptor compromise the ability of its intracellular side to consistently reach (induce) or maintain (select) the Gi protein-signalling fully active state [68](Koehl et al. 2018).
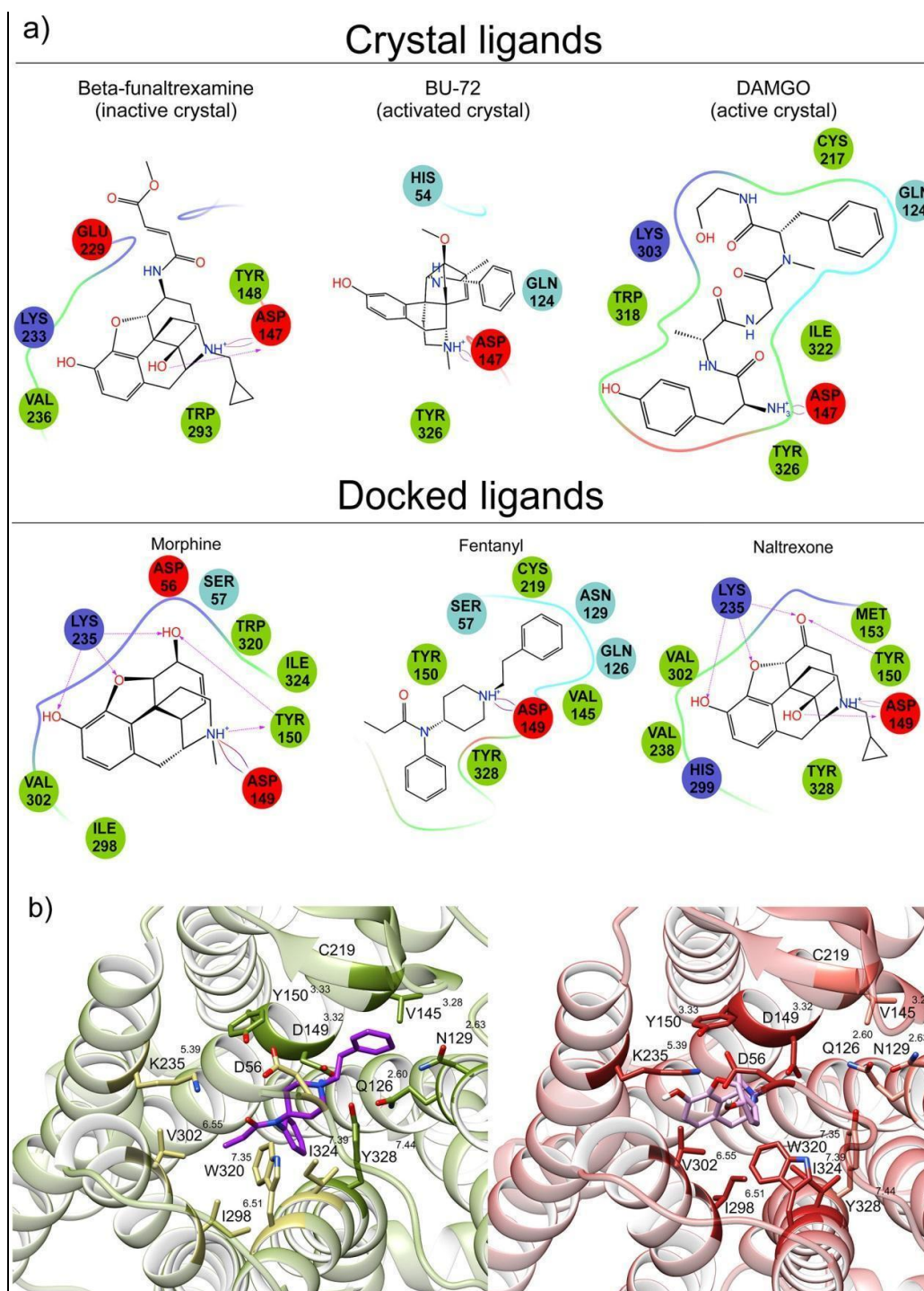
Figure 12. Crystal and docked ligands. Morphine and fentanyl binding poses. a) 2D binding poses of respective inactive, activated, and fully active cocrystallized ligands: β-FNA, BU-72, and DAMGO, and docked ligands of interest: morphine, fentanyl, and naltrexone. **b)** 3D conformation of fentanyl and morphine representative stable binding poses observed during MD simulations (purple and pink, left and right, respectively). Residues of the hMOR in close contact with fentanyl or morphine (<3.5 Å) are coloured in dark green or dark red, respectively. Residues coloured in light green or light red, respectively, are not in close contact but displayed for comparison purposes.

3.2.1.2. Homology models of the hMOR remain conformationally stable in control MD simulations

Native activated and inactive hMOR homology models were generated from respective activated and inactive mMOR crystals [48](Huang et al. 2015), [47](Manglik et al. 2012) by renumbering sequences, mutating non-conserved residues, and adding non-crystallized segments of the inactive hMOR N-terminus, inactive hMOR intracellular loop, and activated hMOR C-terminus. In order to validate the accuracy of activated and inactive hMOR models, we performed two control replicas of 2 μs-length unbiased MD simulations with cocrystallized agonist BU-72 [48](Huang et al. 2015) and three control replicas of 3 μs-length with docked antagonist naltrexone, respectively. As cocrystallized antagonist β-FNA of the inactive mMOR [47](Manglik et al. 2012) is covalently bound to Lys233$^{5.39}$, it is not an ideal control antagonist for our purposes here, but because of high similarity between the molecular structures of naltrexone and β-FNA (Figure 12), β-FNA can be easily substituted for naltrexone. Therefore, in order to test docking accuracy, BU-72 was re-docked into our hMOR active model, while naltrexone was docked into our inactive hMOR model and compared to cocrystallized β-FNA. Docking results reveal a top-ranked BU-72 binding pose with a RMSD of 0.4 Å from its cocrystallized position and a top-ranked naltrexone binding pose with a RMSD of 0.7 Å compared to the common heavy atoms of cocrystallized β-FNA. Trajectories of the hMOR with bound BU-72 and naltrexone show stable receptor conformations (average RMSDs of 1.8 Å (0.4 SD) and 2.8 Å (0.2 SD), respectively (Supplementary Figure 6 and 7) and ligand binding poses (average RMSDs of 1.7 Å (0.6 SD) and 2.2 Å (0.6 SD), respectively (Supplementary Figure 6 and 7). These results indicate that both activated and inactive hMOR models remain near their initial conformation throughout long-timescale MD trajectories, which supports their use as reliable starting points to evaluate the binding effect of ligands of interest: morphine and fentanyl.

3.2.1.3. The binding poses of morphine and fentanyl differ

In order to computationally examine the MOR efficacy differences between fentanyl and morphine at the atomic level, we first docked each ligand into our models of activated and inactive hMOR models. Starting from these protein−ligand systems, we performed three replicas of 3 μs-length unbiased MD simulations to allow for ligand-dependent receptor

conformational changes. From the respective morphine- and fentanyl-bound MD trajectories, we identified one stable binding pose for each ligand (Figure 12), consistent across all replicas and predominantly selected over other alternative temporary poses (Supplementary Figure 7). According to RMSD across MD simulations (Supplementary Figure 7), and considering a threshold of ±2.5 Å to define ligand positional stability, we observe that both morphine and fentanyl are stable after the first microsecond of simulation time and until the end of each trajectory, independently of the initial receptor state (average ligand RMSDs of 1.3 Å (0.5 SD) and 2.2 Å (0.5 SD), respectively). Notable initial ligand instability, limited to the first microsecond of replicas starting from the receptor activated state with bound fentanyl and replicas #1 and #2 starting from the receptor inactive state with bound morphine, can be explained by receptor−ligand relaxation and adaptation (Supplementary Figure 7). Therefore, both ligands are bound in a stable fashion, and any differences in ligand positional stability in the activated state are probably a result of better fit of the mMOR crystal structure for morphine-like ligands, as well as differences in the molecular scaffold between morphine and fentanyl (Figure 12). On the other hand, the difference of size between cocrystallized morphine-like ligands of activated [48](Huang et al. 2015) and inactive [47](Manglik et al. 2012) mMOR models, BU-72 (smaller) and β-FNA (larger), respectively, creates a wider orthosteric pocket in the inactive hMOR model. This may allow ligands larger than morphine, like fentanyl, to obtain its preferred binding pose faster in this receptor state. Nevertheless, irrespective of initial receptor conformation, both morphine and fentanyl reach consistent stable poses in the orthosteric pocket over replicated trajectories, which indicate satisfactory docking accuracy (Figure 12). Differences are not only observed in the conformation of morphine and fentanyl but also in orthosteric pocket residues that are in close contact with them (ligand−residue distance <3.5 Å). The distribution of residues most frequently making contact, summarized in Table 2, indicates that morphine establishes its most stable interactions with the N-terminus, extracellular regions of TM5, TM6, and TM7, and a section of TM3 facing TM5 (Figure 12 and Supplementary Figure 8). On the other hand, fentanyl establishes more frequent contact with ECL2, extracellular regions of TM2 and TM7, and a section of TM3 facing TM2 (Figure 12 and Supplementary Figure 8). Interestingly, fentanyl comes into contact with $Cys219^{ECL2}$, which is directly involved in an important structural disulfide bond with $Cys142^{3.25}$, which may have implications for

conformational changes in TM3 [20](Lans et al. 2015), especially as this helix has previously been described to undergo an upward axial movement in receptor activation of class A GPCRs [18](Dalton et al. 2015), [255](Tehan et al. 2014). In addition to fentanyl and morphine, we have performed in the present study three additional replicas of 3 μs-length unbiased MD simulations with the MOR-bound antagonist naltrexone starting from the activated hMOR state, which supports the comparison between morphine and fentanyl. Naltrexone, similar to morphine and fentanyl, overall maintains a stable disposition in the binding pocket across replicas (Supplementary Figure 7). However, when compared to control replicas where naltrexone is bound in the inactive hMOR state, it presents a slightly worse receptor accommodation (average RMSDs of 2.6 Å compared to 2.2 Å, Supplementary Figure 7) as might be expected for its antagonist condition. Similarities between naltrexone and morphine scaffolds lead to similar interaction environments (Figure 12 and Table 2). Thus, contact between naltrexone and the hMOR is similarly and frequently formed with TM5, TM6, TM7, and a section of TM3 facing TM5 (Table 2 and Supplementary Figure 8). However, differently from morphine, naltrexone comes into close contact with Tyr328[7.43], a residue also involved in the interaction between fentanyl and the receptor in our MD simulations. As these interactions with Tyr328[7.43] are common to both a potent agonist and an antagonist, it could be speculated that they are apparently associated with affinity rather than with efficacy. However, a detailed analysis of the simulations reveals a fine structural tuning of this residue, which allows the functional distinction between agonists and antagonists (see below).

Table 2. Crystal ligands, Morphine, Fentanyl, and Naltrexone Protein-Ligand interactions[α]

ligand	unique interactions		common interactions	
crystal ligands				
beta-funaltrexamine	mTyr148[3.33]		mAsp147[3.32]	
(inactive crystal)	mGlu229[5.35]			
	mLys233[5.39]			
	mVal236[5.42]			
	mTrp293[6.48]			
BU-72 (activated crystal)	mPro59[N-ter]		mAsp147[3.32]	
	mLeu129[2.65]		mTyr326[7.43]	
DAMGO (active crystal)	mGln124[2.60]		mAsp147[3.32]	
	mCys217[ECL2]		mTyr326[7.43]	
	mLys303[6.58]			
	mTrp318[7.35]			
	mIle322[7.39]			
docked ligands				
morphine	hAsp56[N-term]		hSer57[N-term]	
	hLys235[5.39]	(i)	hAsp149[3.32]	(i) (ii) (iii)
	hIle298[6.51]		hTyr150[3.33]	(i)
	hVal302[6.55]			
	hTrp320[7.35]	(iii)		
	hIle324[7.39]			
fentanyl	hGln126[2.60]	(iii)	hSer57[N-term]	
	hAsn129[2.63]		hAsp149[3.32]	(i) (ii) (iii)
	hVal145[3.28]		hTyr150[3.33]	(i)
	hCys219[ECL2]	(iii)		
	hTyr328[7.43]	(ii) (iii)		
naltrexone	hMet153[3.36]		hAsp149[3.32]	(i) (ii) (iii)
	hLys235[5.39]	(i)	hTyr150[3.33]	(i)
	hVal238[5.42]	(i)		
	hHis299[6.52]			
	hVal302[6.55]			
	hTyr328[7.43]	(ii) (iii)		

[α]Residues in close contact (<3.5 Å) listed with respective murine (m) or human (h) numbering following the Ballesteros and Weinstein generic scheme,[31] for crystal structures and MD systems, respectively. Residues interacting with morphine, fentanyl, and naltrexone are included when frequency of contact is >20% of trajectory time during at least two MD simulation replicas, independent of the initial state of the receptor. Similarity between residues in contact across crystals and MD simulations are labeled as common to the (i) inactive crystal, (ii) activated crystal, and (iii) fully active crystal.

3.2.1.4. Fentanyl and morphine induce different receptor activation patterns

According to RMSD of the TMD, the hMOR experiences varying degrees of backbone conformational changes across our MD simulations (Supplementary Table 1 and Supplementary Figure 9). This is an expected result as the MOR is known to be a highly dynamic protein [48](Huang et al. 2015), [195](Kapoor et al. 2017), [47](Manglik et al. 2012), [68](Koehl et al. 2018), as shown when comparing both activated and inactive crystal structures [48](Huang et al. 2015), [47](Manglik et al. 2012) with the fully active crystal

structure [68](Koehl et al. 2018) (TMD RMSDs of 1.4 and 3.0 Å, respectively). Making use of a threshold of ±3.5 Å, calculated from TMD RMSD of crystal structures, we quantified the conformational changes between active and inactive states with respect to either its initial state or fully active crystal. In general terms, the receptor conformation is relatively stable (≤ 3.5 Å) in all replicas starting from the activated state with the bound agonist (morphine or fentanyl) with an average TMD RMSD of 3.2 Å (0.4 SD) from its initial state and 2.2 Å (0.4 SD) from the fully active crystal [68](Koehl et al. 2018) (Supplementary Table 1 and Supplementary Figure 9). On the contrary, in MD simulations starting from the inactive state with the bound agonist (morphine or fentanyl), TMD conformations remain mostly inactive-like with an average TMD RMSD of 2.8 Å (0.3 SD) from its initial state and distant (>3.5 Å) from the fully active crystal [68](Koehl et al. 2018) (TMD RMSD of 3.6 Å (0.4 SD), Supplementary Table 1 and Supplementary Figure 9). However, the receptor in replicas #2 and #3 with bound fentanyl or replica #2 with bound morphine starting from the inactive state presents occasional TMD RMSDs of 2.8 and 2.9 Å or 2.6 Å from the fully active crystal [68](Koehl et al. 2018), respectively, which indicate transient receptor activation toward active-like states (≤3.5 Å, and Supplementary Figure 9). Larger conformational changes in simulations starting from the activated state than those starting from the inactive state are explained by the lack of an intracellular partner in our models. In more detail, computational results also suggest that both activated and inactive crystal structures [48](Huang et al. 2015), [47](Manglik et al. 2012) (and the models generated from them) are better adapted to morphine than fentanyl because of the similarity between morphine and the cocrystallized ligand scaffolds, which implies that the receptor has to undergo bigger conformational changes to properly bind fentanyl. TMD conformational changes can be compared with those observed when the antagonist naltrexone is bound, where a clear tendency toward inactivation is observed when starting from the activated state (average RMSD of 3.9 Å (0.3 SD) from the initial state, Supplementary Table 1) and a preservation of the inactive conformation is found in control replicas starting from the inactive state (average RMSD of 2.8 Å (0.2 SD) from the initial state, Supplementary Table 1). Surprisingly, when comparing naltrexone-bound receptor simulations with the fully active crystal [68](Koehl et al. 2018), the average RMSD achieved is only 3.0 Å (0.4 SD) or 3.7 Å (0.3 SD) in trajectories starting from activated or inactive states, respectively (Supplementary Table 1). In order to better

describe receptor intracellular conformational changes involved in receptor activation, four metrics were employed relative to the protein centre, considering only the two last microseconds of MD simulations: (i) TM3, which moves upward, (ii) intracellular tips of TM5 and (iii) TM6, which move inward and outward, respectively; and (iv) NPxxY motif of TM7 [228](Huang et al. 2002), which rotates toward the core of the helical bundle. Meanwhile, a fifth metric was used for assessing intracellular separation between TM3 and TM6: the distance between residues Arg167$^{3.50}$ and Thr281$^{6.34}$ (Arg−Thr), which is equivalent to the ionic lock in class A GPCRs [228](Huang et al. 2002), [256](Rosenbaum et al. 2009), [257](Trzaskowski et al. 2012), [258](Vogel et al. 2008). Thresholds for these metrics were based on fully active [68](Koehl et al. 2018), activated [48](Huang et al. 2015), and inactive [47](Manglik et al. 2012) crystal structures (normalized according to the inactive crystal structure), with a representative sign, which represents the movement involved with respect to the receptor centre (inward or outward movement, or downward or upward movement, "−" or "+" sign, respectively): +0.3 Å for TM3, −0.8 Å for TM5 and NPxxY, +1.7 Å for TM6, and +10.0 Å for Arg−Thr distance as utilized in a previous study [195](Kapoor et al. 2017). These thresholds were fine-tuned with naltrexone-bound MD simulation results to classify active- or inactive-like conformations of the five intracellular metrics.

Upward axial movement of TM3 (Figure 13 and 14, Supplementary Table 1, and Supplementary Figure 10) is a key indicator of receptor activation, as shown previously in other GPCRs [259](Díaz et al. 2019), [260](Bruzzese et al. 2020). Comparison between mMOR crystal structures shows that TM3 adopts a more upward position when the receptor is activated: by distances of +0.2 Å and +0.6 Å in activated [48](Huang et al. 2015) and fully active [68](Koehl et al. 2018) crystals with respect to the inactive one [47](Manglik et al. 2012), respectively. Based on these differences and antagonist-bound MD simulations (average movement of +0.1 Å (0.2 SD) and +0.3 Å (0.2 SD) in replicas starting from activated or inactive states, respectively), we considered a threshold value of +0.3 Å. Our trajectories show that replicas #2 and #3 starting from the activated hMOR with bound fentanyl present an average TM3 upward axial movement of +0.6 Å (0.2 SD), more upward than the initial receptor activated state and adopting a conformation similar to the fully active crystal [68](Koehl et al. 2018) (Figure 14, Supplementary Table 1, and Supplementary Figure

10). In replica #1, the receptor maintains an average active-like position of +0.3 Å (0.2 SD, Figure 14, Supplementary Table 1, and Supplementary Figure 10). In comparison, all replicas starting from the activated state with bound morphine, despite transient active-like TM3 conformations, show an average less active-like TM3 position of only +0.2 Å (0.2 SD, Figure 14, Supplementary Table 1, and Supplementary Figure 10). Surprisingly, the tendency observed in replicas starting from the activated state, where fentanyl selects for more upward conformations of TM3 than morphine, is not conserved in replicas starting from the inactive hMOR. Under this condition, 2/3 trajectories with bound morphine (replicas #1 and #3) induce an active-like average shift of +0.3 Å (0.2 SD), while replica #2 shows an even larger average of +0.6 Å (0.2 SD), in accordance with the fully active crystal [68](Koehl et al. 2018) (Figure 14, Supplementary Table 1, and Supplementary Figure 10). On the contrary, none of
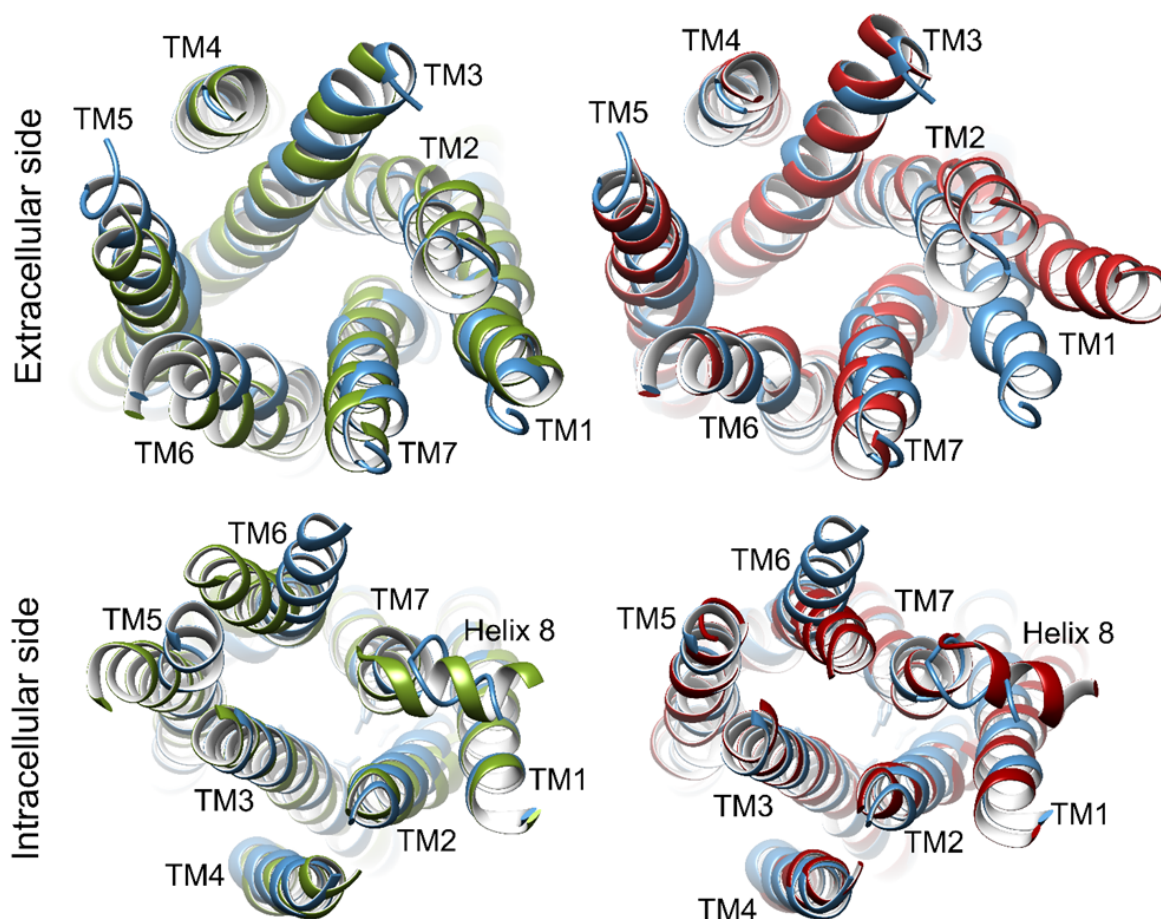
Figure 13. Conformational change of the TM domain in MD simulations of the inactive hMOR. Extracellular (top) or intracellular (bottom) views of representative receptor conformations from replicas #3 and #1 starting from the inactive state with bound fentanyl (left, in green) or morphine (right, in red), respectively, compared with the fully active crystal structure (blue).

the replicas starting from the inactive state with bound fentanyl presents average TM3 movements ≥ +0.3 Å, resulting in mostly selecting an inactive-like TM3 conformation (Figure 14, Supplementary Table 1, and Supplementary Figure 10). Interestingly, under these conditions, replica #3 shows a downward TM3 movement of −0.4 Å (0.2 SD, Figure 14, Supplementary Table 1, and Supplementary Figure 10), which suggests that the specific contact fentanyl establishes with Cys219[ECL2] does not reliably invoke TM3 upward axial movement, at least when starting from the inactive state. Rather, direct interactions between the ligand and TM3 appear more influential, as evidenced by the numerous interactions morphine makes with TM3 relative to fentanyl. In terms of other TM helices, the distance between the protein centre and intracellular tip of TM5 decreases in activated [48](Huang et al. 2015) or fully active crystal structures [68](Koehl et al. 2018) with respect to the inactive structure [47](Manglik et al. 2012) by −1.5 Å or −2.1 Å, respectively. Considering these crystal movements and naltrexone-bound MD simulations (average movement of +0.5 Å (0.6 SD) and +0.2 Å (0.5 SD) in replicas starting from activated or inactive states, respectively), a threshold of −0.8 Å can therefore be established for determining active- or inactive-like conformations of TM5. In MD simulations starting from the activated hMOR with either fentanyl or morphine bound, as expected, TM5 stabilizes (selects) the active-like conformation with normalized distances mostly between −0.8 Å and − 2.1 Å (Figure 14, Supplementary Table 1, and Supplementary Figure 10). An exception is replica #3 with bound morphine, where TM5 fails to reliably select an active-like conformation and instead permits a change toward an inactive-like conformation with a maximum of +0.7 Å at 2.8 μs (Supplementary Figure 10). Likewise, in trajectories starting from the inactive state with bound fentanyl or morphine, TM5 does not obtain an active-like conformation and remains inactive (Figure 14, Supplementary Table 1, and Supplementary Figure 10). Moreover, in replica #3, TM5 undergoes an average change of +1.7 Å with a maximum of +2.9 Å (Supplementary Figure 10), which places TM5 in a more outward conformation with respect to the receptor core (Figure 13 and 14, Supplementary Table 1, and Supplementary Figure 10). This may be the result of an outward movement of TM6 (see below), which temporarily influences TM5 through their mutual interhelical contact, an effect observed in active-like crystal structures [48](Huang et al. 2015), [68](Koehl et al. 2018). Exceptionally, replicas #1 and #2 when morphine is bound in MD simulations starting from the inactive state, present

transient or sustained inward TM5 movement induction with maximum and average displacements of −1.7 Å and −1.5 Å (0.8 SD), respectively (Supplementary Figure 10). Altogether, these results indicate that TM5 generally remains in an active-like conformation if the receptor begins in that state, or if initially inactive, morphine is more effective than fentanyl at inducing active-like conformations of TM5 (Figure 13 and 14, Supplementary Table 1, and Supplementary Figure 10). Similarly, activated [48](Huang et al. 2015) and fully active [68](Koehl et al. 2018) crystal structures present a more outward TM6 intracellular tip conformation (see Methods) relative to the inactive crystal [47](Manglik et al. 2012), with TM6 respectively moving +2.1 Å and +2.0 Å away from the protein centre. Based on these differences and naltrexone-bound MD simulations (average movement of +0.8 Å (0.5 SD) and +0.6 Å (0.4 SD) in replicas starting from activated or inactive states, respectively), a distance threshold of +1.7 Å can therefore be used for defining active- or inactive-like conformations of TM6. This helix selects an active-like outward conformation with an average distance of +3.5 Å (0.6 SD) in trajectories starting from the activated hMOR, independent of the agonist bound (Figure 14, Supplementary Table 1, and Supplementary Figure 11). However, a transient deactivation of TM6 occurs when it falls into an inactive-like conformation in replica #1 with bound morphine at 1.8 μs, recording a distance of +1.4 Å (Supplementary Figure 11). Likewise, in all replicas starting from the inactive hMOR with bound morphine, TM6 does not demonstrate any outward movement, maintaining only an average distance of +0.4 Å (0.4 SD) with respect to the inactive crystal and below the +1.7 threshold (Figure 14, Supplementary Table 1, and Supplementary Figure 11). However, with bound fentanyl, active-like conformations of TM6 are induced in replicas #2 and #3 with maximum values of +2.3 Å and +3.2 Å, respectively (Figure 13 and 14, Supplementary Table 1, and Supplementary Figure 11). While in replica #2 these conformational changes are observed transiently, a more sustained conformational change occurs in replica #3 with an average TM6 movement of +1.9 Å (0.6 SD) over the last microsecond. Altogether, these results indicate that while both fentanyl and morphine are able to select an active-like conformation of TM6 in simulations starting from the activated state, uniquely fentanyl is able to induce TM6 activation when starting from the inactive state, which leads TM6 to adopt conformations more similar to activated and fully active crystals [48](Huang et al. 2015), [68](Koehl et al. 2018) (Figure 13 and 14, Supplementary

Table 1, and Supplementary Figure 11). This may represent an indication of the greater efficacy of fentanyl relative to morphine.

Rearrangement of TM helices during receptor activation leads to specific intracellular conformational changes such as the NPxxY motif on TM7 and Arg167$^{3.50}$−Thr281$^{6.34}$ interaction (Figure 14). The fully active crystal structure of the mMOR [68](Koehl et al. 2018) allows a better understanding of the conformational changes adopted by these regions when the intracellular Gi protein partner is bound to the receptor. Interestingly, in the fully active crystal [68](Koehl et al. 2018), the NPxxY motif adopts an alternative conformation closer to the inactive crystal structure [47](Manglik et al. 2012) than to the activated crystal structure [48](Huang et al. 2015). This difference may be due to the non-native binding of Nb39 to the receptor. In these crystal structures, the NPxxY position can be described according to the protein centre. As such, activated [48](Huang et al. 2015) and fully active [68](Koehl et al. 2018) crystals present more inward positions of the NPxxY motif than the inactive crystal [47](Manglik et al. 2012) (−1.7 and −0.8 Å, respectively). Consequently, in addition to antagonist-bound MD simulations (average movement of −0.8 Å (0.6 SD) and +0.1 Å (0.3 SD) in replicas starting from activated or inactive states, respectively), a threshold of −0.8 Å can be defined and applied for determining active- or inactive-like conformations of this intracellular region (Figure 14, Supplementary Table 1, and Supplementary Figure 11). Because of computational limitations, our MD simulations do not include bound Gi protein; therefore, it might be expected that activated-like NPxxY conformations could be selected or induced over fully active conformations. During MD simulations starting from the activated state, NPxxY is broadly selected in its original conformation with an average distance of −2.5 Å (0.5 SD), independent of the agonist bound (Figure 14, Supplementary Table 1, and Supplementary Figure 11). On the other hand, all replicas starting from the inactive state with bound fentanyl induce a conformational change so that NPxxY achieves a stable active-like position (average of −1.4 Å, 0.6 SD), which is the greatest in replica #3 (average of −1.8 Å, 0.7 SD, Figure 14, Supplementary Table 1, and Supplementary Figure 11). Conversely, when morphine is bound, only replica #1 starting from the inactive state induces an active-like position that crosses the −0.8 Å threshold (average of −1.5 Å, 0.3 SD, Supplementary Figure 11), whereas other replicas select an

inactive-like conformation. These results suggest that fentanyl consistently induces active-like conformations of both TM7 and the NPxxY motif stronger than morphine (Figure 14). The intracellular distance between $Arg167^{3.50}$ and $Thr281^{6.34}$, equivalent to the ionic lock in class A GPCRs [228](Huang et al. 2002), [256](Rosenbaum et al. 2009), [257](Trzaskowski et al. 2012), [258](Vogel et al. 2008), can be classified as being in an active- or inactive-like conformation by applying a threshold value of +10.0 Å, as used previously [195](Kapoor et al. 2017). The Arg−Thr distance is broadly selected in its original state in respective MD simulations starting from activated or inactive states, independent of the agonist bound, resulting in respective averages of 13.0 Å (0.9 SD) and 6.5 Å (0.5 SD, Figure 14, Supplementary Table 1, and Supplementary Figure 12). However, in replica #3 when starting from the inactive state with bound fentanyl, this interaction is seen to transiently break at 1.8 μs when the distance reaches 10.1 Å (Supplementary Figure 12). In the replicas where naltrexone is bound, $Arg167^{3.50}$ and $Thr281^{6.34}$ reach and stabilize distances <10 Å over the entire two last microseconds of MD simulations, started from either control inactive or activated states, as expected by the antagonist nature of naltrexone, contrary to the overall active-like states selected by agonists when starting from the activated state (Figure 14, Supplementary Table 1, and Supplementary Figure 12). Similarly, naltrexone induces an inward movement of TM6, in parallel to an outward movement of TM5 and the NPxxY region, in simulations starting from the activated state, thus adopting, as expected, inactive-like conformations of these metrics (Figure 14, Supplementary Table 1, and Supplementary Figure 12). This result indicates that the threshold used clearly differentiates between active- or inactive-like states of this interaction. Altogether our results strongly indicate that receptor activation by means of TM6 outward movement (Figure 13 and 14, Supplementary Table 1, and Supplementary Figure 10-12) is more frequently observed with bound fentanyl, which is uniquely able to initiate in a μs time period, than with morphine. Therefore, in addition to conformational changes of helical regions mentioned above, the different frequency of activation of these intracellular metrics is consistent with the difference experimentally observed in efficacy between morphine and fentanyl.
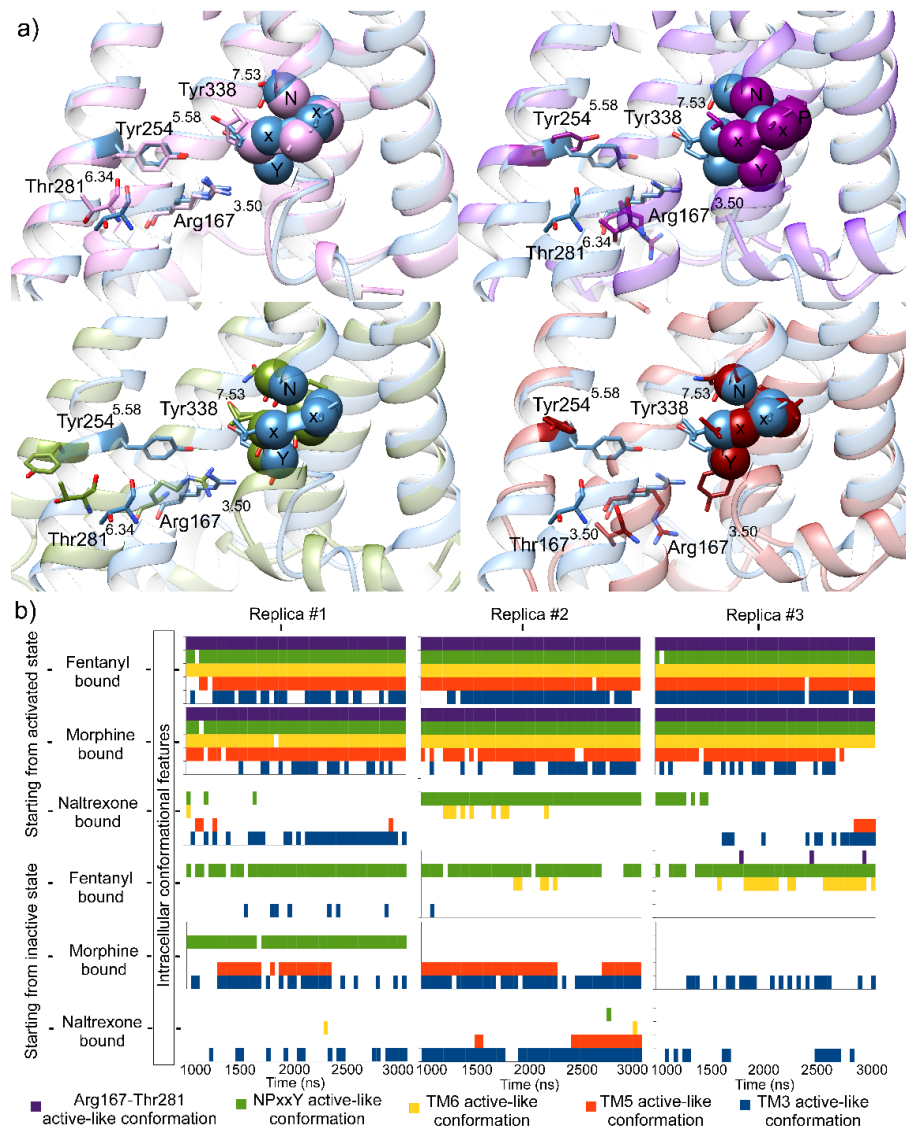
Figure 14. Intracellular conformation in MD replicas defined by the Arg167[3.50]−Thr281[6.34] distance, vertical TM3 movement, and lateral NPxxY motif, TM5, and TM6 movements. a) Structural comparison between the fully active crystal (blue) and either activated or inactive crystals (top, pink or purple, left or right, respectively), or representative conformation of MD-generated replicas #3 and #1 starting from the inactive state with bound fentanyl or morphine, respectively (bottom, green or red, left or right, respectively). As a function of time, **b)** active- or inactive-like states of the five different activation-related intracellular features of each replica starting from the activated or inactive hMOR with bound fentanyl, morphine, or naltrexone (active-like conformations of: Arg167[3.50]−Thr281[6.34], NPxxY, intracellular TM6, intracellular TM5, and TM3, in purple, green, yellow, orange, or blue, respectively). White gaps represent inactive-like conformations of each respective metric. See the Methods section for thresholds used to define active- or inactive-like states of intracellular features and Supplementary Figure 10 and 11 for respective metric individual time-dependent analysis.

73

All these TMs and intracellular metric movements (average tendencies summarized in Supplementary Table 1) observed during receptor (in)activation are indicative of conformational changes at the intracellular side of the receptor in system dynamics starting either from activated or inactive states. As shown in Figure 14, some of these activation features coexist in time. Therefore, their simultaneous presence represents a highly active conformation of the receptor. However, the activation of one feature prior to another can be an indication of the exploration of a certain process or pathway of receptor activation. Our results indicate that all active-like conformational intracellular metrics are mostly preserved in MD simulations starting from the activated agonist-bound receptor state, which is biologically reasonable because morphine and fentanyl are both agonists. However, agonist-specific differences are consistently observed during receptor activation from the inactive state. While with bound morphine, the hMOR largely presents an upward axial movement of TM3 and exclusively induced TM5 active-like conformations, with bound fentanyl, the hMOR shows specific activation of TM6 and stronger activation of the NPxxY motif on TM7 (Figure 14). Interestingly, replica #3 starting from the inactive state with bound fentanyl, which most frequently presents active-like conformations of TM6 and the NPxxY motif, is the only replica that yields transient active-like $Arg167^{3.50}-Thr281^{6.34}$ distances (Figure 14). The non-preservation of this $Arg167^{3.50}-Thr281^{6.34}$ separation may be a result of the absence of TM3 upward axial movement, which, in addition to TM6 outward movement, is required to properly break intracellular TM3−TM6 interactions. Altogether, these results are indicative of different receptor activation patterns induced by morphine (TM3 and TM5) and fentanyl (TM6 and TM7).

It has been widely discussed if fentanyl acts as a β-arrestin biased agonist or behaves as a balanced agonist [206](Gillis et al. 2020), [211](Schmid et al. 2017), [243](Zheng et al. 2008), [244](Mori et al. 2017), [245](Kovoor et al. 1998), [246](Burgueño et al. 2017), [247](Vasudevan et al. 2020), [248](Kalvass et al. 2007), [249](Bobeck et al. 2012), [250](Trescot et al. 2008). As done for other GPCRs [259](Díaz et al. 2019), [260](Bruzzese et al. 2020), we performed a density map (Figure 15) of the receptor intracellular state achieved considering two of the main representative intracellular metrics, which conformationally differ more between morphine and fentanyl: (i) outward movement of the

intracellular side of TM6 and (ii) conformation of NPxxY with respect to the protein centre. This representation (Figure 15) suggests that in our MD simulations, we reach a common active-like state with either fentanyl or morphine bound. It should be considered that our models starting from the activated hMOR were modelled from its respective crystal [48](Huang et al. 2015), which contains a G protein mimetic camelid nanobody subsequently removed in our model. Therefore, the conformations achieved in our trajectories can be conditioned by the initial crystal used, which may limit the observations of other alternative conformations. However, in a timescale of three microseconds, our simulations have not identified receptor conformational regions consistent with biased agonism, in agreement with a recent experimental study [247](Vasudevan et al. 2020). It is worth noting that conclusions on biased agonism from experimental functional studies may depend on the parameter used for its quantification, where the proposed $\Delta\Delta\log(\tau/KA)$, $\Delta\Delta\log(\tau)$, or $\Delta\Delta\log(Emax/EC50)$ bias factors have led to different biased profiles when applied to fentanyl, with Gi protein bias, and β-arrestin with and without bias, respectively [211](Schmid et al. 2017), [247](Vasudevan et al. 2020). Interestingly, density maps of simulations starting from the inactive state show that fentanyl reaches more intermediate intracellular states than morphine, the latter presenting a larger density closer to the inactive crystal conformation [47](Manglik et al. 2012) (Figure 15). This result may suppose an additional indication of the differences in efficacy observed between both ligands [45](O'Donell et al. 2017), [46](Mounteney et al. 2015), [235](Vardanyan et al. 2014). On the other hand, the possibility that the higher trend of fentanyl of generating intermediate states may facilitate the generation of receptor conformations more prone to β-arrestin binding is a speculation to be considered in further studies.
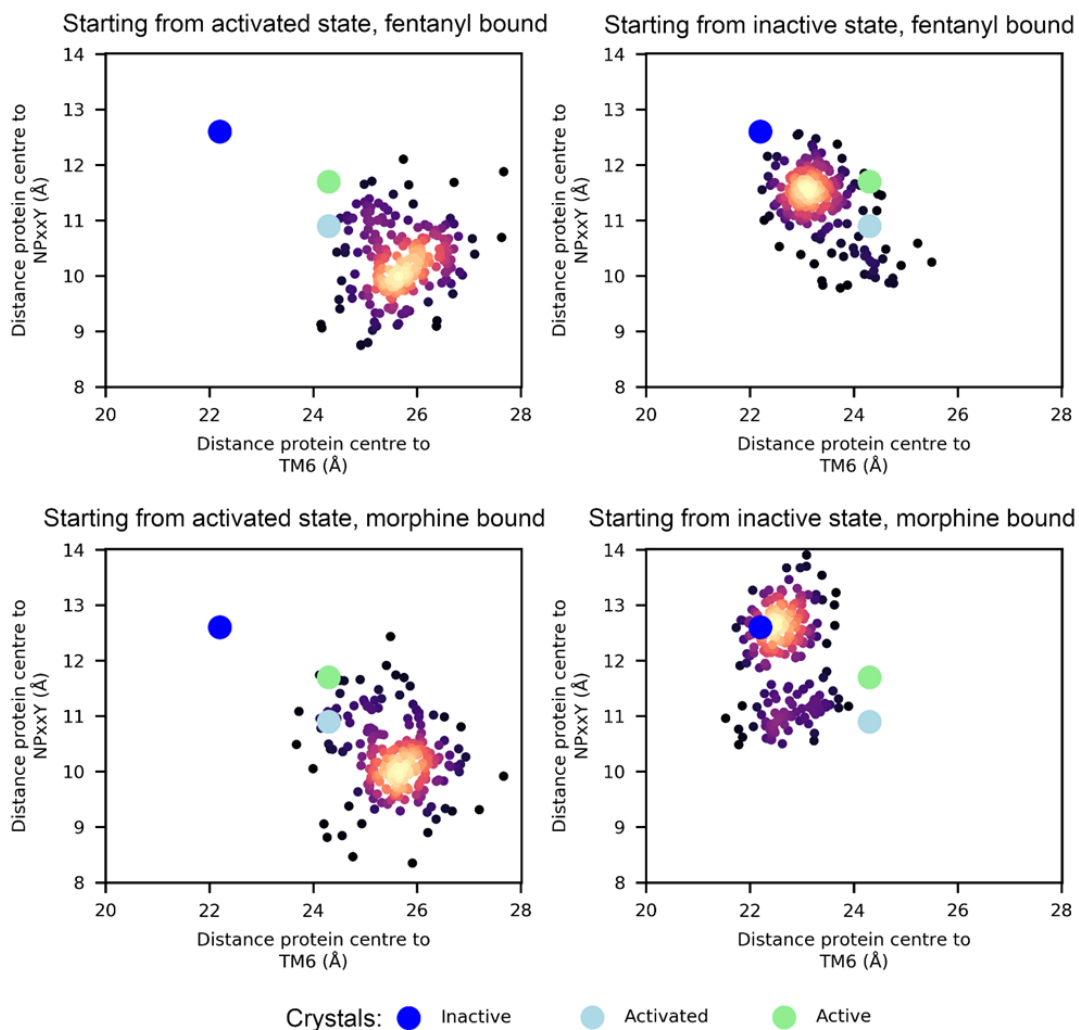
Figure 15. Density maps of the outward movement of TM6 and conformation of the NPxxY motif with respect to the protein centre. Density maps of fentanyl or morphine (top or bottom row, respectively) of the three replicas started from activated or inactive states (left or right column, respectively). Inactive, activated, and fully active crystals are represented for comparison by dark blue, light blue, or green, respectively. Density maps show conformations more or less frequently induced, represented with a hot to cold colour gradient.

Figure 16. Orthosteric pocket conformational changes of the hMOR in MD simulations. a) and
b) Predominant *trans* (~180.0°) or *cis* conformation (~300.0°) of **a)** Gln126$^{2.60}$ χ2 dihedral angle or **b)**
Lys235$^{5.39}$ χ2 dihedral angle, in representative MD conformations with bound fentanyl or morphine
(purple or pink, hMOR residues in green or red, left and right, respectively). Structural images also
show different Asp149$^{3.32}$ χ1 dihedral angle *cis* and *trans* conformations selected, and
Asp149$^{3.32}$−ligand, Tyr150$^{3.33}$−ligand, or Asp149$^{3.32}$−Tyr328$^{7.43}$ H-bond formation. **c)** Conformation
frequency of the Asp149$^{3.32}$ *trans* χ1 dihedral angle or Gln126$^{2.60}$ and Lys235$^{5.39}$ *cis* χ2 dihedral angle
selected with bound fentanyl, morphine, or naltrexone, independent of the initial state of the receptor
(green, red, or purple, respectively). **d)** H-bond occupancy of Asp149$^{3.32}$−Tyr328$^{7.43}$,
Lys235$^{5.39}$−ligand, or Tyr150$^{3.33}$−ligand interaction of simulations with bound fentanyl, morphine, or
naltrexone, independent of the initial state of the receptor (green, red, or purple, respectively). **e)**
Structural comparison of Met153$^{3.36}$ conformation between the fully active crystal (blue) and either
replica #3 starting from the inactive state with bound morphine or fentanyl (red or green, left or right,
respectively). **f)** Frequency of Met153$^{3.36}$ *gauche−* conformation in trajectories with bound fentanyl,
morphine, or naltrexone, starting from activated or inactive states (green, red, or purple, respectively).

3.2.1.5. Morphine and fentanyl mediate different orthosteric pocket conformational changes

To ascertain which conformational changes in the orthosteric pocket, induced or selected by morphine and fentanyl (see Figure 12), are most responsible for observed intracellular conformational differences, we performed an energetic analysis of residues in close contact with each ligand (Supplementary Figure 13). Accordingly, from residues in close contact with both ligands (summarized in Table 2), fentanyl makes stronger energetic interaction with Asp56[N-term], Gln126[2.60], Cys219[ECL2], and Tyr328[7.43], whereas morphine makes stronger interactions with Tyr150[3.33] and Lys235[5.39] (Supplementary Figure 13). Both ligands establish the highly energetic and conserved MOR-opiate salt bridge with Asp149[3.32], as previously identified in other studies [48](Huang et al. 2015), [195](Kapoor et al. 2017), [207](Manglik et al. 2016), [47](Manglik et al. 2012), [68](Koehl et al. 2018), [229](Kaserer et al. 2016). From a conformational perspective, we observe (i) H-bonds (either direct or water-mediated) between the ligand and Asp149[3.32] or Tyr150[3.33] and between residues Asp149[3.32] and Tyr328[7.43], (ii) specific χ1 dihedral angles of Asp149[3.32] and Met153[3.36] (directly determined by conformational changes of Tyr150[3.33]), and (iii) specific χ2 dihedral angle selections of Gln126[2.60] and Lys235[5.39] sidechains (Figure 16 and Figure S9−S12). Taking these metrics one by one, morphine and fentanyl have both been described to make a highly conserved MOR-opiate electrostatic interaction with Asp149[3.32], a residue located on TM3 [48](Huang et al. 2015), [195](Kapoor et al. 2017), [207](Manglik et al. 2016), [47](Manglik et al. 2012), [68](Koehl et al. 2018), [229](Kaserer et al. 2016). In our MD simulations, this interaction between the ligand and Asp149[3.32] is highly energetically favourable with bound fentanyl but even greater with bound morphine, independent of the initial receptor state (average interaction energy of −78.1 or −94.9 kcal/mol, respectively, Supplementary Figure 13). Despite this energetic difference between morphine and fentanyl, both ligands maintain a stable interaction (<4.5 Å) over three microseconds between their amine group and Asp149[3.32] (Figure 16 and Supplementary Figure 14). In addition, Asp149[3.32] presents different χ1 dihedral angle conformations when morphine or fentanyl is bound in the hMOR (Figure 16 and Supplementary Figure 14). Two different Asp149[3.32] conformations are observable in our MD simulations: (i) a *trans* conformation (χ1 dihedral angle >115.0°), predominantly induced in 5/6 trajectories with bound fentanyl (average frequency of 89.2%,

Figure 16 and Supplementary Figure 14), which positions the sidechain closer to TM2 and (ii) a *gauche−* conformation ($\chi 1$ dihedral angle <115.0°) induced by morphine in all trajectories (average frequency of 93.7%, Figure 16 and Supplementary Figure 14), which positions the sidechain away from TM2. Similar to morphine-bound replicas, when the antagonist naltrexone is bound to the hMOR, an overall Asp149[3.32] *gauche−* conformation is induced, independent of the initial state of the receptor (Figure 16 and Supplementary Figure 14). Under this condition, conformational change from *gauche−* to *trans* conformation is only observed in replica #3 starting from the inactive state at 2.2 μs. As a result of the *trans* conformation predominantly observed with bound fentanyl, Asp149[3.32] is within closer H-bonding distance with Tyr328[7.43] located on TM7 [230](Mansour et al. 1997). Activated and fully active crystal structures [48](Huang et al. 2015), [68](Koehl et al. 2018) show closer Asp149[3.32]−Tyr328[7.43] interaction distances than the inactive crystal structure [47](Manglik et al. 2012) (3.2 Å and 3.4 Å, respectively), and this interaction also differs in our MD simulations with either bound morphine or fentanyl (Figure 16 and Supplementary Figure 14). Throughout 4/6 trajectories with bound fentanyl, independent of the initial receptor state, Asp149[3.32]−Tyr328[7.43] maintains a closer interaction (<4.5 Å) with an H-bond occupancy of 89.5% (36.1 SD, Figure 16 and Supplementary Figure 14). Conversely, across all trajectories with bound morphine, only transient interactions between Asp149[3.32] and Tyr328[7.43] are observed with a H-bond occupancy of 24.1% (22.4 SD, Figure 16 and Supplementary Figure 14). Similarly, the *gauche−* conformation overall selected when naltrexone is bound leads to an Asp149[3.32]−Tyr328[7.43] H-bond occupancy of 41.1%, independent of the starting receptor state (19.5 SD, Figure 16 and Supplementary Figure 14). These results are supported by the low H-bond occupancy observed when the antagonist naltrexone is bound into the orthosteric pocket of the receptor (Asp149[3.32]−Tyr328[7.43] H-bond occupancy of 41.6% across all replicas, Figure 16), which, despite being in close contact with Tyr328[7.43] like fentanyl, presents larger Asp149[3.32]−Tyr328[7.43] distances. Therefore, fentanyl mediates a stronger Asp149[3.32]-Tyr328[7.43] H-bond than morphine in the orthosteric pocket.

In addition to Asp149[3.32]−ligand interaction, greater energetic interactions can also be observed between Tyr150[3.33] and morphine with respect to bound fentanyl (average potential energy (P.E.) of −5.6 kcal/mol (2.4 SD) or −1.9 kcal/mol (2.7 SD), respectively,

Supplementary Figure 13). Differences in the energetic landscape between fentanyl and morphine relate to their different scaffold, which presents a single oxygen group in the former (carbonyl group) and three oxygen groups in the latter (one ether and two hydroxyl groups, Figure 12). This distinction translates to a different H-bond occupancy (either direct or water-mediated) between $Tyr150^{3.33}$ and fentanyl or morphine with average occupancies of 32.2% (7.2 SD) or 89.2% (9.4 SD), respectively (Figure 16). In the case of the antagonist naltrexone, which presents a scaffold similar to morphine (Figure 12), it adopts a $Tyr150^{3.33}$−naltrexone H-bond occupancy of 56.1% (9.6 SD, Figure 16). $Tyr150^{3.33}$ and morphine or naltrexone hydroxyl/carbonyl groups are considered either donors or acceptors when evaluating $Tyr150^{3.33}$−ligand H-bond presence/absence. The higher H-bond occupancy between morphine and $Tyr150^{3.33}$ enhances upward axial movement of TM3 (Figure 14, Supplementary Table 1, and Supplementary Figure 10) and exerts a stabilizing effect in the bottom of the receptor orthosteric pocket, as observed with the conformation of $Met153^{3.36}$ (Figure 16 and Supplementary Figure 15). In MD simulations starting from the activated state, independent of the agonist bound, the $Met153^{3.36}$ χ1 dihedral angle generally adopts a *gauche−* conformation (~60.0°). Likewise, in MD simulations starting from the inactive state with bound morphine, $Met153^{3.36}$ *gauche−* conformation is selected with a frequency of 93.2% (8.8 SD, Figure 16 and Supplementary Figure 15). However, when fentanyl is bound, alternative conformations of $Met153^{3.36}$ (χ1 >90.0°) are more frequently induced with a frequency of 65.3% (4.9 SD, Figure 16 and Supplementary Figure 15). Interestingly, in naltrexone-bound conditions, $Met153^{3.36}$ *gauche−* conformation is overall selected only with a frequency of 58.3% (24.5 SD, Figure 16 and Supplementary Figure 15), which indicates that this residue conformationally fluctuates more with bound naltrexone than when fentanyl or morphine is bound in the hMOR, probably as a result of the direct contact naltrexone makes with this sidechain (Table 2 and Supplementary Figure 8). Selection of χ1 *gauche−* appears to be associated with aforementioned active-like conformations of TM3 (Figure 14, Supplementary Table 1, and Supplementary Figure 10). This process can be linked with fentanyl-mediated TM6 activation where the receptor core undergoes reorganization and becomes more flexible. Once this transition ends, the stability of the core can be recovered, as indicated by trajectories starting from the activated state (Figure 16 and Supplementary Figure 15). Conversely to the low H-bond occupancy between fentanyl and $Tyr150^{3.33}$ in

80

TM3, which conditions the conformation of Met153$^{3.36}$, an energetically favourable interaction with Gln126$^{2.60}$ on TM2 is established with an average P.E. of −3.0 kcal/mol (4.4 SD). This contrasts with an unfavourable average P.E. of +2.7 kcal/mol (2.2 SD) displayed by morphine (Supplementary Figure 13). Subsequently, Gln126$^{2.60}$ shows conformational differences when morphine or fentanyl is bound in the hMOR (Figure 16 and Supplementary Figure 16). In general, two different Gln126$^{2.60}$ χ2 dihedral angles are observed in our MD simulations: (i) a *cis* and (ii) *trans* (~300.0° and ~ 180.0°, respectively). By using a threshold of ±240°, Gln126$^{2.60}$ can be categorized according to these two conformations (Figure 16 and Supplementary Figure 16). Although both conformations are observable with each ligand, its frequency is noticeably different from one to another. Systems with bound fentanyl predominantly induce the *trans* conformation 86.0% of the time (10.5 SD, Figure 16 and Supplementary Figure 16), which positions Gln126$^{2.60}$ toward the orthosteric pocket, allowing a three-way sidechain interaction with Tyr328$^{7.43}$ and Asp149$^{3.32}$ and supporting closer Asp−Tyr interaction (Figure 16 and Supplementary Figure 18). By contrast, morphine selects the Gln126$^{2.60}$ *cis* conformation with a frequency of 80.5% (13.5 SD, Figure 16 and Supplementary Figure 16), which positions it toward the membrane and negatively affects the Asp−Tyr interaction (Figure 16 and Supplementary Figure 18). Similar to morphine, naltrexone selects the Gln126$^{2.60}$ *cis* conformation with a frequency of 87.3% (10.0 SD, Figure 16 and Supplementary Figure 16).

Finally, Lys235$^{5.39}$−agonist interaction is the only one established between morphine and TM5 and is present at least 20.0% of the time in 5/6 trajectories (Table 2 and Supplementary Figure 7). This interaction shows differences in energy between morphine and fentanyl with an average P.E. of +6.1 kcal/mol (6.9 SD) or +16.5 kcal/mol (3.8 SD), respectively (Supplementary Figure 12). Similar to Tyr150$^{3.33}$, the Lys235$^{5.39}$ amino group establishes an interaction with any of morphine's oxygen groups (ether, hydroxyl groups #1 and #2) with a H-bond occupancy of 63.5% (13.2 SD) but generally avoids interaction with fentanyl's carbonyl group (H-bond occupancy of 7.2% (6.9 SD), Figure 16 and Supplementary Figure 17). When naltrexone is bound, which shares a similar scaffold with morphine (Figure 12), Lys235$^{5.39}$ H-bonds naltrexone with an occupancy of 43.9% (18.6 SD). In this specific interaction, ligand oxygen groups are only considered as acceptors. Accordingly, Lys235$^{5.39}$

displays two different χ2 dihedral angles, either adopting a *cis* or *trans* conformation (~300.0° or ~ 180.0°, respectively) where a threshold of ±240° can be used to categorize these two sidechain conformations (Figure 16 and Supplementary Figure 17). Independent of the bound ligand, the *trans* conformation is most commonly selected, with the sidechain interacting with the extracellular solvent rather than with the ligand. However, different rates of *cis* conformation are induced between fentanyl, morphine, and naltrexone, with average percentages of 11.5% (5.1 SD), 38.0% (13.9 SD), and 40.0% (14.9 SD), respectively (Figure 15 and Supplementary Figure 17). In this case, the *cis* conformation permits interaction with the bound ligand. This indicates that morphine mediates different conformational dynamics of Lys235[5.39] (Supplementary Figure 18), which, accordingly, helps to stabilize the binding pose of morphine inside the orthosteric pocket of the receptor.

3.2.1.6. Conformational changes of Trp295[6.48] inducing different bottom-orthosteric pocket receptor interactions are relevant in TM5−TM6 packing

During activation of the MOR, TM6 moves outward, which, together with conformational rearrangement of TM3, TM5, and TM7, creates solvation of the intracellular cavity [48](Huang et al. 2015) and conformational changes in specific residues on TM6, such as Trp295[6.48] [48](Huang et al. 2015). By classifying sidechain conformation by dihedral angles, *gauche−* (0−120°), *trans* (120−240°), or *gauche+* (240−360°) in mMOR crystals, Trp295[6.48] χ2 changes from *gauche−* to *trans* to *gauche+* in inactive, activated, and fully active crystals, respectively (values of 78.6°, 121.3°, and 342.9°, respectively). In our MD simulations, we observe two stable Trp295[6.48] conformations (Figure 17 and Supplementary Figure 19): (i) an activated-like *trans* conformation at 225.6° (6.9 SD) and (ii) an inactive-like *gauche−* conformation at 97.1° (4.1° SD). We do not observe the *gauche+* conformation probably because, due to computational limitations, we have not included an interacting Gi protein in our simulations. In all trajectories starting from the activated hMOR state, independent of the agonist bound, the Trp295[6.48] *trans* conformation is stabilized within 1250 ns (Figure 17 and 18 and Supplementary Figure 19). This enables a novel H-bond between Trp295[6.48] and Ala242[5.46] (sidechain amino group and backbone carbonyl group, respectively) with an average occupancy of 97.7% (1.1 SD), which is beneficial for maintaining active conformations of TM5 and TM6 (Figure 18). Conversely, all replicas starting from the

inactive state with bound fentanyl, as well as replicas #2 and #3 where morphine is bound, select an inactive-like Trp295[6.48] *gauche−* conformation (Figure 17 and Supplementary Figure 19). This conformation enables H-bonding with the adjacent residue on TM7, Asn330[7.45], which enhances TM6−TM7 interaction and avoids the interaction of this residue with water molecules, thus inhibiting TM6 activation (Figure 18). Interestingly, in replica #1 starting from the inactive state with bound morphine, the activated-like *trans* conformation is induced at 400 ns, which is the only replica in this category where the NPxxY motif yields an active-like conformation, observed from 200 ns onward (Supplementary Figure 11). This enables sidechain−backbone Trp295[6.48]-Ala242[5.46] H-bonding between TM5−TM6 with an occupancy of 68.0%, which assists TM5 activation after 500 ns (Supplementary Figure 10), even though TM6 activation is not observed. Despite active-like conformations of the NPxxY motif being present in all replicas starting from the inactive state with bound fentanyl, only replica #3 transiently induces the *trans* conformation of Trp295[6.48] during the first 500 ns before returning to *gauche−* (Supplementary Figure 19). This conformational change results in only 6% Trp−Ala H-bonding occupancy, but repeated sidechain switching is enough to trigger the gradual activation of TM6, which is observed more strongly later in this trajectory (Supplementary Figure 11). Indeed, Trp295[6.48] and Ala242[5.46] mostly interact via hydrophobic contact for the rest of the trajectory (closest distance: 4.7 Å, Supplementary Figure 19) rather than H-bonding because Trp295[6.48] remains in its *gauche−* conformation. This suggests that although bound morphine is capable of eliciting similar conformational changes in Trp295[6.48], switching from *gauche−* to *trans*, its effect can be different depending on other residues, such as Met153[3.36].

In particular, it is noticeable in replica #3 with bound fentanyl that Met153[3.36] $\chi2$ conformational switching occurs at the same time as Trp295[6.48] (Figure S10 and S13) with these switches in Met153[3.36] conformation becoming more frequent as TM6 moves outward. Despite these differences, closer interactions between Trp295[6.48] and Ala242[5.46] are observed with active-like conformations of TM5, TM6, and the NPxxY motif (Figure 18), which demonstrates the importance of rearrangements in TM5−TM6 packing. For comparison purposes, naltrexone-bound trajectories induced or selected *gauche−* conformations from respective activated or inactive states with percentages of 74.6 and 88.8%, respectively, with

the closest Trp295[6.48]−Ala242[5.46] distance of 8.4 Å achieved in control simulations starting from the inactive state. This distance, larger than that observed in fentanyl-bound trajectories, suggests a lack of TM5−TM6 packing, which favours the inactive state of the receptor. In addition, we observe different distributions between Asp149[3.32]−Tyr328[7.43] H-bonding in the orthosteric pocket and Trp295[6.48]−Ala242[5.46] interaction, where average Trp−Ala distances of 3.7 Å (1.8 SD) or 6.8 Å (3.0 SD) are reported when the Asp−Tyr H-bond is formed or broken, respectively (Supplementary Figure 18). This demonstrates the interconnectivity of residue−residue interactions in the orthosteric pocket, which may have different implications for intracellular receptor conformations.
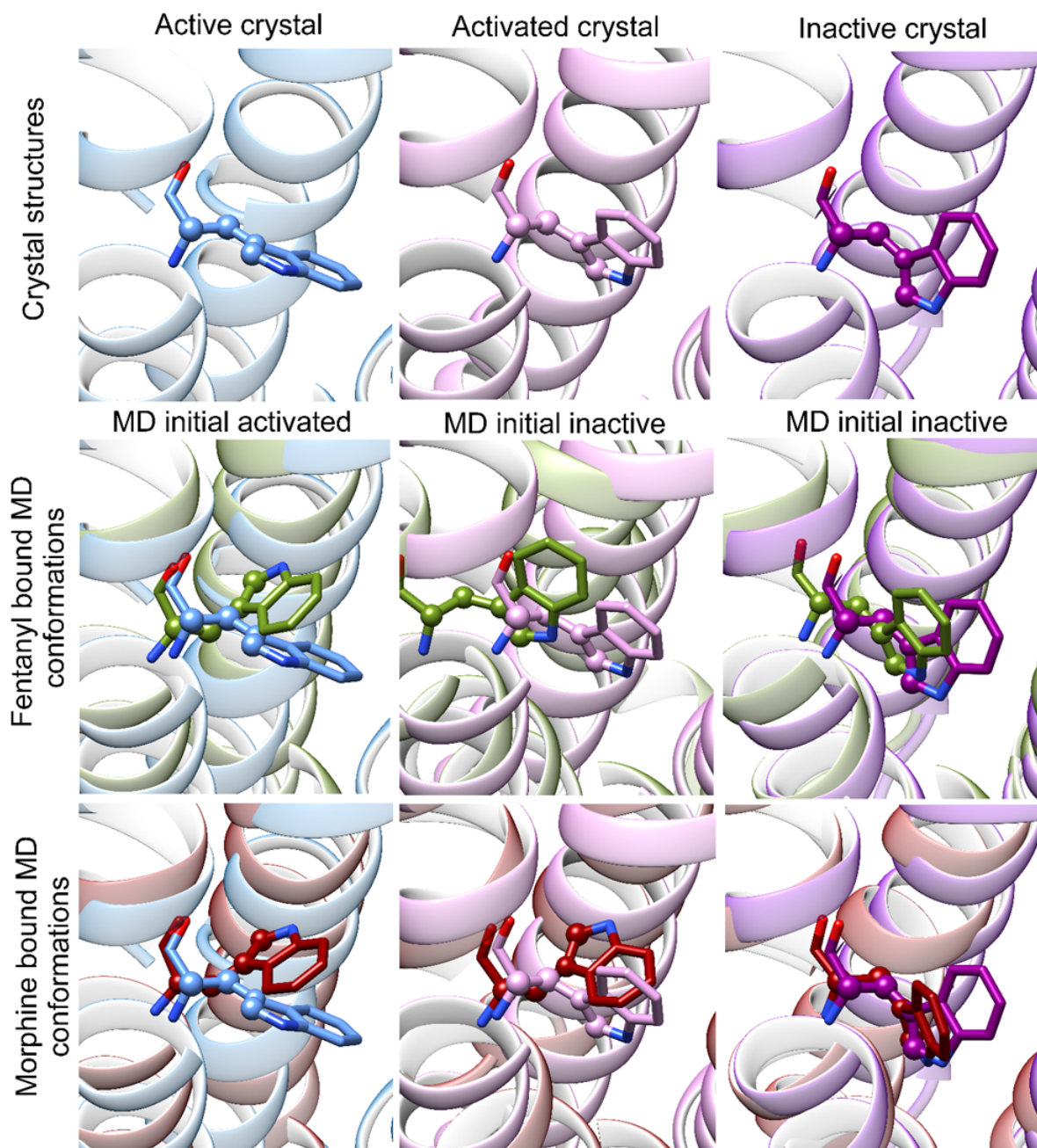
Figure 17. Trp295[6.48] conformational changes in MD simulations with respect to MOR crystals. Comparison between different conformations of Trp295[6.48] ($\chi 2$ dihedral angle represented by spheres) of fully active, activated, and inactive crystals (salmon, blue and purple, respectively) and (i) representative MD-generated hMOR conformations with bound fentanyl (green, middle row) of replica #2 starting from the activated state, replicas #3 and #2 starting from the inactive state (from left to right, respectively) or, ii) with bound morphine (red, bottom row), replica #3 starting from the activated state, or replicas #1 and #2 starting from the inactive state (from left to right, respectively).
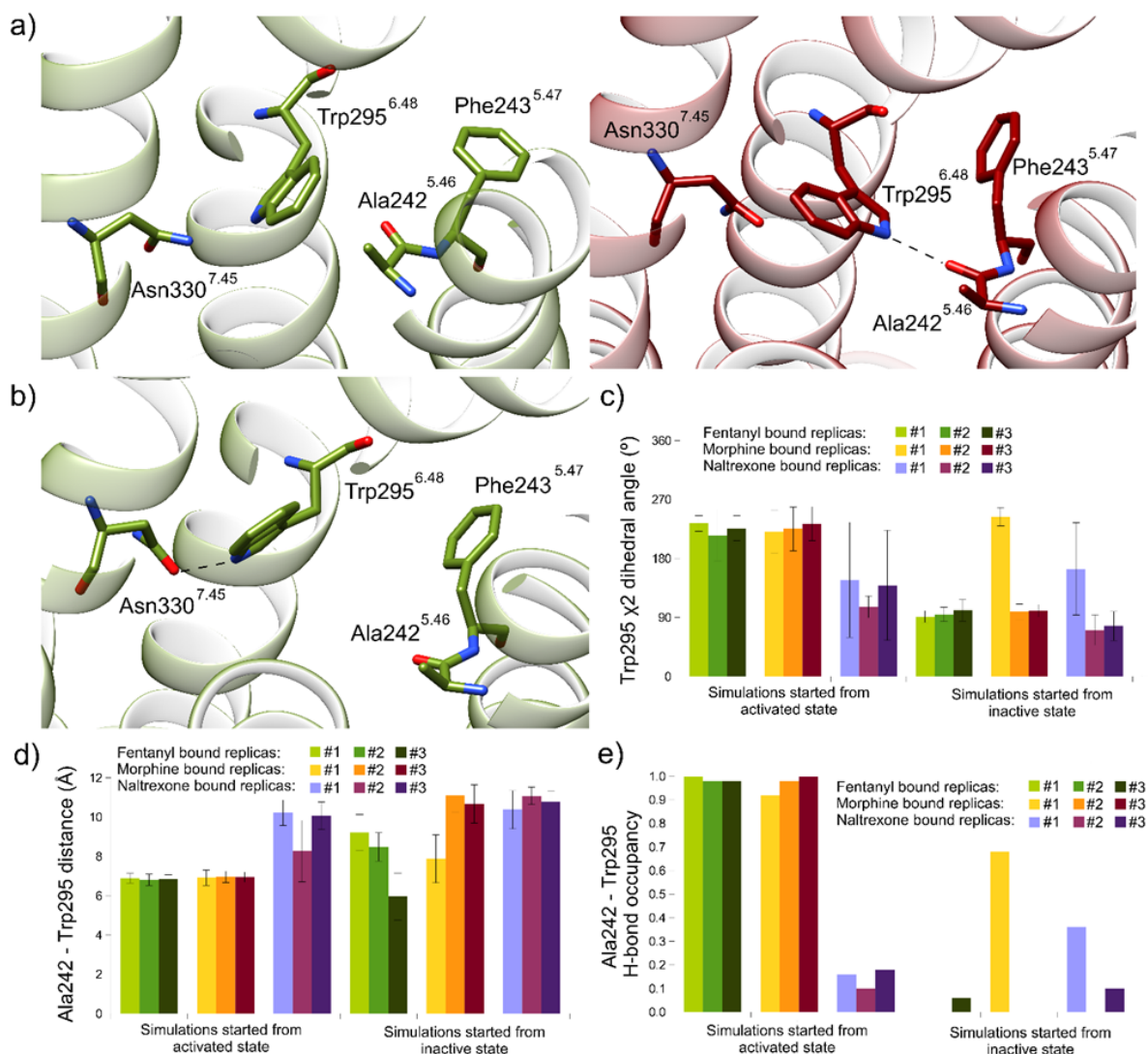
Figure 18. TM5−TM6 interactions in MD simulations: Trp295[6.48] and Ala242[5.46]. MD-generated receptor structures showing the interaction of Trp295[6.48] with Ala242[5.46] or Asn330[7.45], in **a)** replica #3 or #2 starting from inactive or activated states with bound fentanyl or morphine, respectively (left or right, green or red, respectively) or **b)** replica #2 starting from the inactive state with bound fentanyl (green). **(c−e)** Per replica average **c)** Trp295[6.48] χ2 dihedral angle, **d)** Trp295[6.48]−Ala22[5.46] distance, and **e)** Trp295[6.48]−Ala242[5.46] H-bond occupancy (shades of green, red, or purple for replicas #1−3 with bound fentanyl, morphine, or naltrexone, respectively).

3.2.1.7. Intracellular conformational changes correlate with ligand-specific conformational changes in the receptor orthosteric pocket

In order to elucidate how ligand-specific orthosteric pocket conformational changes determine intracellular receptor conformations, we performed a number of statistical analyses (Figure S15 and S16) with respect to (in)activation of specific intracellular receptor metrics: TM3 upward-, TM5 inward-, TM6 outward-, and NPxxY motif inward-movement and Arg167$^{3.50}$–Thr281$^{6.34}$ distance. The chi-square (chi2) test was chosen to examine the association between these intracellular metrics and orthosteric pocket metrics: sidechain-sidechain Asp149$^{3.32}$–Tyr328$^{7.43}$, Lys235$^{5.39}$–ligand or Tyr150$^{3.33}$–ligand, sidechain-backbone Trp295$^{6.48}$–Ala242$^{5.46}$ H-bond formation and Met153$^{3.36}$ *gauche−* conformation. The chi2 analyses involve two-way frequency tables of binary variables (presence/absence of H-bonds or Met153$^{3.36}$ *gauche−* conformation and active/inactive state of each intracellular metric, Figure S15 and S16). In addition, the potential association between the Trp295$^{6.48}$-Ala242$^{5.46}$ distance and active- or inactive-like state of the selected intracellular metrics was measured using Student's t-tests (Supplementary Figure 21). All these statistical analyses were performed independently of the initial state of the receptor and the ligand bound. Our objective was not to find differences between ligands but to detect general mechanistic trends of receptor activation. Because we are combining data from different ligands and MD simulations with different starting states, we should take these tests as exploratory rather than confirmatory of the statistical hypotheses. Nevertheless, the consistency found in the results suggests these analyses are valuable to realize the apparent relationships between the selected structural features. Chi2 tests show that differences exist between active- and inactive-like intracellular receptor conformations and Asp149$^{3.32}$–Tyr328$^{7.43}$, Tyr150$^{3.33}$–ligand, Lys235$^{5.39}$–ligand, Trp295$^{6.48}$–Ala242$^{5.46}$ H-bond formation and Met153$^{3.36}$ *gauche−* conformation (p <0.05 in all cases, Figure S15 and S16). The absence of statistical significance was found for the association between Tyr150$^{3.33}$–ligand H-bond formation and the intracellular TM6 state (p = 0.051, Supplementary Figure 20) and between Lys235$^{5.39}$–ligand H-bond formation and either TM3 or TM5 movements (p = 0.9 or 0.7, respectively, Supplementary Figure 20). Interestingly, the fact that this last H-bond formation is not associated with movements of TM5 (Supplementary Figure 20) suggests that Lys235$^{5.39}$ affects the position of the ligand in the

orthosteric pocket, which in turn determines the conformation of other residues (such as Asp149[3.32]), rather than directly transmitting the signal through TM5. Large chi2 values observed in the association between the sidechain−backbone Trp295[6.48]−Ala242[5.46] H-bond and intracellular metrics (values between 252.7 and 582.9, which are extremely significant because 2×2 contingency tables contain 1 degree of freedom and significant $P < 0.05$ values are reached if chi2 > 3.841, Supplementary Figure 21) highlight the relevance of this interaction in the (in)activation of the hMOR. Similarly, Student's t-tests show that the Trp295[6.48]−Ala242[5.46] distance statistically differentiates between active and inactive TM3, TM5, TM6, and NPxxY motif conformational states and the Arg167[3.50]−Thr281[6.34] distance state ($p < 0.001$ in all cases, Supplementary Figure 21), showing overall Trp295[6.48]−Ala242[5.46] closer distances in active- than inactive-like states. Close Trp295[6.48]−Ala242[5.46] distances, which are mainly attributed to helical rearrangement, enhance the establishment of hydrophobic contact between both residues. These results highlight the importance of these two residues becoming physically close irrespective of their H-bonding status.

Altogether, these results indicate that, independent of the ligand bound and the starting conformation of the receptor for MD simulations, mostly all orthosteric metrics studied in this study statistically reveal significant differences between active and inactive-like states of the intracellular metrics used, thus establishing an (in)activation communication connection mechanism through the entire receptor. The differences found between agonists in their propensity to select or induce specific receptor conformations through these mechanistic structural features may explain the differences in efficacy observed experimentally [45](O'Donell et al. 2017), [46](Mounteney et al. 2015), [215](Morgan et al. 2011), [235](Vardanyan et al. 2014).

3.2.1.8. Internal receptor polar-water network differs between morphine and fentanyl

A polar network mediated by water molecules has been described to be involved in signal transmission from the extracellular to the intracellular side of the mMOR [48](Huang et al. 2015). An average water density map of the hMOR reveals differences in this network between activated/inactive states in morphine/fentanyl-bound MD simulations (Figure 19). As might be expected, the different molecular size and binding pose of fentanyl compared to

morphine affects the number of water molecules that can enter the orthosteric pocket. Therefore, we observe more waters when morphine is bound than with fentanyl, independent of the initial receptor state (Figure 19). In terms of the receptor core or intracellular regions, two different water clusters can be identified: (i) between Trp295$^{6.48}$ and Asn330$^{7.45}$ on TM6 and TM7, respectively, and (ii) adjacent to the intracellular N$^{7.49}$PxxY$^{7.53}$ motif on TM7. In MD simulations with bound fentanyl, greater solvation is observed at both these regions, in particular near the NPxxY motif, which has previously been described as important for active conformations of the mMOR or class A GPCRs, in general [48](Huang et al. 2015), [261](Yuan et al. 2014), [262](Tomobe et al. 2017), [263](Venkatakrishnan et al. 2019). This is consistent with stabilization of an active-like receptor conformation or receptor activation from the inactive state, which is observed in replica #3 with bound fentanyl (Figure 19). On the contrary, with bound morphine, these same water clusters are less pronounced, even with greater solvation in the orthosteric pocket, which suggests comparatively reduced receptor activation or increased destabilization of the active state. This is the case even when an active-like *trans* conformation of Trp295$^{6.48}$ is induced, which allows sidechain−backbone H-bonding with Ala242$^{5.46}$ (Figure 19), as observed in replica #1 when starting from the inactive state. Furthermore, in this same replica, despite corresponding activation of the NPxxY motif (Figure 14), the lack of TM6 conformational change as a whole allows fewer water molecules to access this region compared to simulations with bound fentanyl. In the same direction, when the antagonist naltrexone is bound, solvation of the two aforementioned regions is reduced even in simulations starting from the activated state, which facilitates hydrophobic interactions, TMD rearrangements, and inactivation of the receptor (Figure 19). This indicates that proper conformational movements of both TM6, most importantly through Trp295$^{6.48}$, and the NPxxY motif are necessary for formation of a water column in the receptor core, which is thought to be necessary for activation of the MOR [48](Huang et al. 2015), [261](Yuan et al. 2014), [262](Tomobe et al. 2017), [263](Venkatakrishnan et al. 2019).
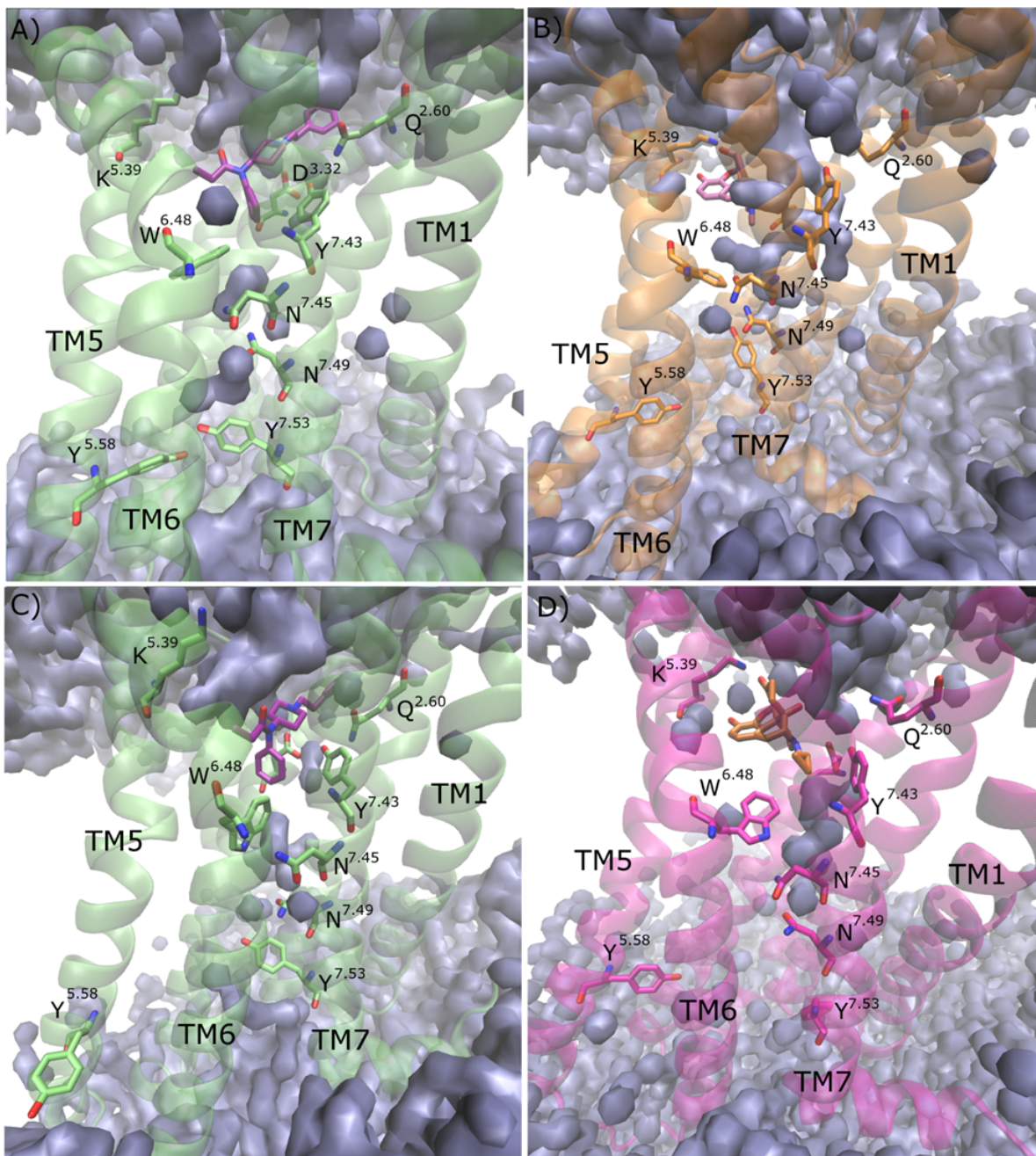
Figure 19. Polar water network in MD simulations. Comparison of the water network connecting extracellular and intracellular sides of the hMOR with bound fentanyl or morphine (green or orange, respectively). Receptor conformations from replicas #1 and #1 starting from the activated hMOR (snapshots at 2.4 µs and 3.0 µs, respectively) with **a)** fentanyl and **b)** morphine and replicas #3 and #1 starting from the inactive hMOR (pictures at 2.2 µs and 1.8 µs, respectively) with **c)** fentanyl and **d)** naltrexone.

3.2.1.9. A general discussion on morphine and fentanyl activation patterns

The recent spate of deaths from fentanyl and its derived compounds [45](O'Donell et al. 2017), [46](Mounteney et al. 2015), [235](Vardanyan et al. 2014), [238](Lyons et al. 2015), [239](Warner et al. 2016) raises special interest in how these high efficacy agonists interact with the hMOR compared to lower efficacy agonists such as morphine. Questions about potential differences between morphine- and fentanyl-based signalling lead to the need for better understanding of how these two ligands modulate MOR conformation and function and how this could instigate stronger responses from the receptor [45](O'Donell et al. 2017), [46](Mounteney et al. 2015), [235](Vardanyan et al. 2014) or even stimulate different downstream pathways [213](de Waal et al. 2020), [246](Burgueño et al. 2017). There are conflicting experimental data about whether fentanyl is a biased agonist or not. It was proposed through in vitro studies that fentanyl is more biased toward β-arrestin activation than morphine [211](Schmid et al. 2017), [213](de Waal et al. 2020), [246](Burgueño et al. 2017), but the recent literature [247](Vasudevan et al. 2020) did not find significant bias of neither fentanyl nor a collection of fentanyl analogues toward Gi protein or β-arrestin signalling pathways. Interestingly, opposite bias profiles were obtained for fentanyl depending on the model parameter used for bias quantification: Gi protein bias or β-arrestin bias when τ/KA or τ parameters were respectively chosen [246](Burgueño et al. 2017). MD simulations cannot give a definite answer to this problem. GPCR-dependent β-arrestin signalling involves the phosphorylation of particular serine or threonine residues at the intracellular regions of the receptor by GPCR kinases (GRKs). In a recent study on the dopamine D1 receptor [264](Kaya et al. 2020), it was found that intracellular loop 3 (ICL3) phosphorylation affects arrestin binding and activation through various phosphorylation patterns, which direct the signalling to either one effector or another. This bar-coded phosphorylation signalling indirectly affects G protein coupling because arrestin- and G protein-coupled receptor populations coexist and the increase of one population decreases the other [264](Kaya et al. 2020). However, phosphorylation patterns may vary between GPCRs, in particular for the MOR. For this receptor, it was found that a single threonine (T180) in ICL2 is fundamental for agonist-dependent receptor phosphorylation and subsequent arrestin binding, activation, and signalling [265](Celver et al. 2001). In the present study, the examination of MD simulations of the hMOR with either fentanyl or morphine bound did not

find differences with respect to T180. It is worth noting that with present computational means, it is not possible to assess which active receptor conformations are more prone to be phosphorylated, which ultimately lead to β-arrestin signalling. However, at the timescales and starting models used, our MD simulations suggest the presence of a single common active like receptor state stabilized by both morphine and fentanyl, in comparison to multiple conformations observed in other GPCRs such as the A2AR [260](Bruzzese et al. 2020). This leads us to consider an unbiased behaviour of both morphine and fentanyl, where both ligands achieve a common active-like receptor state by differently activating ligand-specific conformations of the receptor. Nevertheless, it cannot be completely discarded that the higher propensity of fentanyl to induce receptor intermediate states could facilitate the generation of conformations predisposed to β-arrestin binding. In addition, it is worth noting that reliable quantification of biased agonism needs the use of proper parameters, and in this regard, the following has been proposed: the use of operational efficacy (τ) versus the transduction coefficient (τ/KA) in the case of comparing ligands producing different maximum responses or, in other words, when partial agonism is present [246](Burgueño et al. 2017) or, moreover, the inclusion of constitutive receptor activity in the mathematical modelling in those cases where basal receptor response is observed [205](Hall et al. 2018), [266](Zhou et al. 2019). On the contrary, other authors have applied the Emax/EC50 parameter for bias calculation of μ-opioid agonists [247](Vasudevan et al. 2020). Thus, it may happen that the mathematical models used for agonist bias quantification, in particular in those systems where pharmacological complexity either at the ligand (partial agonism) or receptor (constitutive activity) levels is present, may have permitted the occurrence of conflicting results in some cases. Nevertheless, a connection between functional experimental results yielded by ligands from particular receptors and the molecular interactions of these ligands with the residues in the receptor binding pocket is expected. The observed functional response is a consequence of molecular events that occur first within the receptor and are later propagated to the effector system.

The results obtained in this study greatly depend on the interactions established by morphine and fentanyl in the MOR orthosteric pocket, which to be properly determined requires a sufficiently accurate initial docking pose, as has been previously demonstrated in MD

simulations of other GPCR-ligand complexes [267](Söldner et al. 2019). In this regard, our accurate docking of cocrystallized ligands (or their close analogues) gives us reason to have confidence in our docking protocol. We consider that, in order to properly characterize the efficacy of fentanyl and morphine in humans, it is important to study the hMOR instead of the mMOR, thus avoiding protein−ligand interactions with non-conserved residues. At the time our models were generated, only crystals of the activated [48](Huang et al. 2015) and inactive [47](Manglik et al. 2012) mMOR were available. Models of activated or inactive receptor, with bound control ligands: BU-72 and naltrexone, were conformationally stable in MD simulations. However, a third mMOR crystal structure [68](Koehl et al. 2018) was later released, which details the fully active receptor conformation coupled to human Gi protein. Despite not providing data of the β-arrestin signalling pathway, it supposes a novel point of reference for comparison with our MD simulations in terms of Gi protein signalling. Therefore, this crystal structure was used as an independent positive control, which, in addition to the use of cocrystallized BU-72-bound activated hMOR and naltrexone-bound inactive hMOR, allows us to quantify different conformational changes induced or selected in the hMOR by fentanyl or morphine. The question arises which is the proper reference state for the system. Both the apo receptor [268](Bruzzese et al. 2020) and an antagonist-bound receptor may, in principle, be suitable for this purpose. We chose the latter condition because of the high stability of an antagonist-bound inactive receptor state, as well as the potential to deactivate an active receptor state to the inactive. However, utilizing the apo receptor to investigate the apparently low reported basal activity of the hMOR [269](Seifert et al. 2002) is an interesting area for future study, in particular regarding potential allosteric modulation by anionic phospholipids as has been reported for other homologous class A GPCRs [259](Díaz et al. 2019), [260](Bruzzese et al. 2020), [24](Bruzzese et al. 2018). Under the simple framework of the two-state model of receptor activation: $R \overset{L}{\leftrightarrow} R^*$, with R and R*, the inactive and active receptor states and L, the interconversion equilibrium constant L = [R*]/[R], the agonist intrinsic efficacy α can be seen either through the induction branch $AR \overset{\alpha L}{\Leftrightarrow} AR^*$ or through the selection branches: $A + R \overset{K}{\leftrightarrow} AR$ and $A + R^* \overset{K/\alpha}{\leftrightarrow} AR^*$ of the thermodynamic cycle, where K is the dissociation equilibrium constant. Thus, induction and selection approaches are equivalent in terms of intrinsic efficacy α within the context of four receptor species in equilibrium. However, the situation can be more complex when

receptor states include ensembles of protein conformations. Conversion of AR into AR* may involve different intermediates with different kinetics. The kinetic component can be a limiting factor in some cases, making more complex the correspondence between induction and selection approaches. Considering that the inactive receptor R is, normally, the major species in the absence of an agonist, it is expected that an agonist making "easier" the conversion of AR into AR* will reflect this molecular feature onto its pharmacological profile. Our simulations suggest that this could be the case in the comparison between morphine and fentanyl. Therefore, in the present study, receptor activation by either induction or selection of receptor active states has been considered. This has been possible because both inactive and active MOR structures were available. Therefore, when starting from a specific simulation initial state (activated or inactive hMOR) if the receptor achieves the opposite state (inactive- or active-like conformations, respectively) the induced-fit approach is followed, otherwise, if the initial state is preserved, we can state that a selection approach occurs. This makes the dynamic structural analysis more robust and reliable. It should be taken into account that because we are using receptor states obtained for particular ligands, there is a bias toward these states for those ligands structurally resembling the crystallized ones (BU72 and β-FNA). In this regard, the morphine binding pose is widely known [227](Sounier et al. 2015), [270](Serohijos et al. 2011), [271](Berríos-Cárcamo et al. 2017) because of its similarity with the morphine-like scaffold of agonist BU-72 and antagonist β-FNA in the activated or inactive mMOR [48](Huang et al. 2015), [47](Manglik et al. 2012), respectively. Conversely, the native fentanyl binding pose is still unclear, with previously proposed binding poses differing in their orientation [69](Spahn et al. 2017), [214](Lipiński et al. 2019), [271](Berríos-Cárcamo et al. 2017), [272](Subramanian et al. 2000), [273](Jarończyk et al. 2017), [274](Ellis et al. 2018), [275](Dosen-Micovic et al. 2006), [276](Gentilucci et al. 2012), and no consensus having been reached. Mutagenesis-based studies [230](Mansour et al. 1997), [277](Xu et al. 1999) first characterized the binding landscape of fentanyl and fentanyl derivatives involving Asp149$^{3.32}$, Tyr150$^{3.33}$, Asn152$^{3.35}$, Trp320$^{7.35}$, His321$^{7.36}$, and Tyr328$^{7.43}$. During the last two decades, the use of computational techniques has revealed new details in fentanyl binding, identifying different residues that might potentially interact [69](Spahn et al. 2017), [213](de Waal et al. 2020), [214](Lipiński et al. 2019), [276](Gentilucci et al. 2012). Despite fentanyl being more

94

prone to change in its initial conformation during our MD simulations compared to morphine, the same stable binding mode of fentanyl is reached in the first microsecond of all replicas, especially in the inactive receptor state. This is interesting because a recent report investigating fentanyl binding in MD simulations of the mMOR failed to obtain a stable binding pose in the inactive state unless sodium ions (a known negative allosteric modulator) were cobound [214](Lipiński et al. 2019). Such ions are not required in our study. As fentanyl and morphine are both agonists, it might be expected that they should favour binding of the activated state over the inactive; however, tight induced-fit of the activated crystal structure for its cocrystallized morphine-like agonist BU-72 [48](Huang et al. 2015) appears to enable precise docking of morphine but partially hinders fentanyl. Conversely, the larger size of cocrystallized antagonist β-FNA in the inactive crystal [47](Manglik et al. 2012) may favour a faster stabilization of fentanyl in this state compared to the activated one. Nevertheless, once stable ligand binding is reached within our MD simulations starting from activated or inactive states, morphine and fentanyl make different ligand−receptor interactions. In particular, morphine interacts more frequently with the N-terminus, TM5, TM6, and TM7, coming into contact with residues: $Asp56^{N-ter}$, $Lys235^{5.39}$, $Ile298^{6.51}$, $Val302^{6.55}$, $Trp320^{7.35}$, and $Ile324^{7.39}$, while fentanyl interacts with ECL2, TM2, and TM7, coming into contact with $Gln126^{2.60}$, $Asn129^{2.63}$, $Val145^{3.28}$, $Cys219^{ECL2}$, and $Tyr328^{7.43}$. However, there are similarities as both morphine and fentanyl interact with $Ser57^{N-ter}$, $Tyr150^{3.33}$, and $Asp149^{3.32}$.

The different molecular scaffolds of morphine and fentanyl lead to different binding modes, which are associated with different conformational arrangements in the orthosteric pocket and which may be related to their different pharmacological efficacies. The widely described [48](Huang et al. 2015), [195](Kapoor et al. 2017), [205](Hall et al. 2018), [47](Manglik et al. 2012), [68](Koehl et al. 2018), [229](Kaserer et al. 2016) electrostatic interaction with $Asp149^{3.32}$ has been observed as essential for binding of MOR ligands, and the $Asp149^{3.32}$ conformation resulting from it plays a direct role in receptor (in)activation as shown by mutagenesis experiments [214](Lipiński et al. 2019), [232](Li et al. 1999), [233](Befort et al. 1996). Likewise, H-bonding between $Asp149^{3.32}$ and $Tyr328^{7.43}$ in the orthosteric pocket has been shown to be relevant for MOR activation [214](Lipiński et al. 2019). Further experimental studies [214](Lipiński et al. 2019), [230](Mansour et al. 1997),

[275](Dosen-Micovic et al. 2006) have shown that Tyr328[7.43] has a significant effect on ligand potency and agonist-induced receptor activation, specifically for fentanyl, and is conserved and functional in δ- and κ-opioid receptors as demonstrated by mutagenesis [278](Yan et al. 2005). Other mutagenesis studies have identified Tyr150[3.33] to be relevant for agonist binding affinity [275](Dosen-Micovic et al. 2006), [277](Xu et al. 1999), including fentanyl. In addition, mutation of the conserved residue Tyr139[3.33] in the κ-opioid receptor alters ligand potency [278](Yan et al. 2005). Likewise, a mutagenesis study [279](Zhang et al. 1999) showed that Cys219[ECL2] likely comes into contact with fentanyl and is relevant in its binding but does not affect receptor activation. This is an interesting result because it implies a molecular separation between the affinity and efficacy concepts, which is difficult if not impossible to obtain by parameter estimation from functional studies as the estimated binding constants in operational models include the receptor activation component [280](Roche et al. 2016). Therefore, our morphine binding pose is in accordance with previously described binding modes [227](Sounier et al. 2015), [270](Serohijos et al. 2011), [271](Berríos-Cárcamo et al. 2017), cocrystallized BU-72 [48](Huang et al. 2015) and β-FNA, [47](Manglik et al. 2012) and side-directed mutagenesis, which determined Val302[6.55] or Trp320[7.35] to be crucial for the decrease [281](Sader et al. 2018) or increase [47](Manglik et al. 2012) of morphine affinity, respectively. Despite this, to our knowledge, no mutagenesis studies have been performed for residues: Asp56[N-ter], Lys235[5.39], and Ile324[7.39], even though they have been implicated in morphine binding before [227](Sounier et al. 2015), [271](Berríos-Cárcamo et al. 2017). On the other hand, the fentanyl binding pose presented in our study, which presents protein−ligand interactions similar to those shown previously [69](Spahn et al. 2017), [213](de Waal et al. 2020), is in agreement with the first point mutation experiments [229](Kaserer et al. 2016), [230](Mansour et al. 1997), [277](Xu et al. 1999) involving residues Asp149[3.32], Tyr150[3.33], and Tyr328[7.43] but not Asn152[3.35], Trp320[7.35], and His321[7.36]. As far as we are aware, no experimental mutagenesis has been performed on Gln126[2.60] and Asn129[2.63], which we predict to interact with fentanyl. The relative stability of our observed binding poses of morphine and fentanyl, irrespective of receptor conformation, leads us to conclude that they are sufficiently accurate. As an extra validation of the fentanyl binding pose, we docked fentanyl to the new DAMGO-bound fully active crystal structure of the mMOR [68](Koehl et al. 2018), which might be expected to

yield greater accuracy. This results in a similar docking pose to that obtained with our hMOR models and MD simulations (Supplementary Figure 22), thus adding an extra layer of confidence.

Conformational dispositions in the orthosteric pocket lead to alteration of other receptor residues such as Met153[3.36] and Trp295[6.48], which assist receptor activation [214](Lipiński et al. 2019), [282](Della Longa et al. 2018), [283](Fowler et al. 2004). More specifically, different conformations of Met153[3.36] have been associated with a specific ligand-dependent micro switch for MOR β-arresting signalling [213](de Waal et al. 2020). Although in our results we have not found multiple active-like states, we observe different conformations of Met153[3.36] more frequently induced when either fentanyl or morphine is bound into the receptor orthosteric pocket. In addition, Trp295[6.48] has previously been observed to rotate during activation of the mMOR [214](Lipiński et al. 2019), [283](Fowler et al. 2004) and class A GPCRs, in general [256](Rosenbaum et al. 2009), and has been commonly named a "toggle switch". Such "toggling" can result in different H-bonding between TM5, TM6, and TM7 and solvation of the receptor core [214](Lipiński et al. 2019), [283](Fowler et al. 2004). In particular, it has been described that fentanyl stabilizes different rotameric states of Trp295[6.48] compared to morphine or the apo receptor [214](Lipiński et al. 2019). In our study, we identify ligand-specific orthosteric pocket changes in (i) ligand interactions with Gln126[2.60], Asp149[3.32], Tyr150[3.33], and Lys235[5.39] including concomitant sidechain rotameric changes, (ii) interhelical Asp149[3.32]−Tyr328[7.43] H-bonding, (iii) sidechain rotameric changes in Trp295[6.48] and Met153[3.36] (influenced by conformational change of Tyr150[3.33]), and (iv) proximity and interhelical H-bonding between Trp295[6.48]−Ala242[5.46] (influenced by conformational change in Trp295[6.48]). In terms of how these conformational changes are connected, we observe that morphine and fentanyl engage with Asp149[3.32] via different *gauche−* or *trans* sidechain conformations, respectively. As *trans* Asp149[3.32] is within the H-bonding distance with Tyr328[7.43], as expected, we find higher Asp149[3.32]−Tyr328[7.43] H-bond occupancy with bound fentanyl. Likewise, a *trans* sidechain conformation of Gln126[2.60], which is induced predominantly when fentanyl is bound, interacts with Tyr328[7.43], further stabilizing Asp149[3.32]−Tyr328[7.43] H-bonding through a three-way sidechain interaction thus favouring receptor activation [18](Dalton et al. 2015), [231](Xu et al. 2008). In

comparison, the Gln126[2.60] *cis* sidechain conformation, predominantly selected by morphine, shows lower Asp149[3.32]−Tyr328[7.43] H-bonding and less favourable receptor activation [18](Dalton et al. 2015), [231](Xu et al. 2008). Differences in Gln126[2.60] conformation with fentanyl and morphine and their influence on Asp149[3.32]−Tyr328[7.43] H-bonding may partly explain their difference in efficacy [45](O'Donell et al. 2017), [46](Mounteney et al. 2015), [235](Vardanyan et al. 2014), [238](Lyons et al. 2015), [239](Warner et al. 2016). The sidechain conformation of Asp149[3.32], which is dictated by the different binding poses of morphine and fentanyl, is further dictated by different interactions the ligands make with Lys235[5.39]. As both ligands contain an oxygen acceptor group(s), the sidechain amino group of Lys235[5.39] can theoretically interact with either. In relevant crystals, Lys235[5.39] covalently binds antagonist β-FNA [47](Manglik et al. 2012), does not interact with agonist BU-72 [48](Huang et al. 2015), and makes an H-bond with agonist DAMGO [68](Koehl et al. 2018). Differences in the molecular scaffold between ligands lead to higher Lys235[5.39]−ligand H-bond occupancy with bound morphine, which results in different conformations of Lys235[5.39]. Accordingly, Lys235[5.39]−ligand H-bonding is related to enhanced stabilization of morphine relative to fentanyl in the orthosteric pocket, thus leading Asp149[3.32] to adopt a *gauche−* sidechain conformation when morphine is bound. Therefore, our results indicate that Asp149[3.32]−Tyr328[7.43] H-bonding, previously described to be essential for MOR activation [18](Dalton et al. 2015), [231](Xu et al. 2008), is determined by ligand interactions with Asp149[3.32] and Gln126[2.60] and by its position in the orthosteric pocket influenced by its interaction with Lys235[5.39].

Oxygen H-bond acceptor groups on morphine and fentanyl not only establish interactions with TM5 but also make H-bonds with Tyr150[3.33] on TM3, either directly or through a water molecule. Similar to Lys235[5.39], morphine has a higher Tyr150[3.33]−ligand H-bond occupancy than fentanyl, which may enhance TM3 activation and exert a stabilizing effect on the receptor orthosteric pocket. This includes the crystal *gauche* sidechain conformation of Met153[3.36], which is largely induced in simulations starting from the activated state and when morphine is bound. This conformation stabilizes hydrophobic interactions that occur at the bottom of the orthosteric pocket restricting the transition from one state to the other. In this respect, signal transmission along TM3 from Tyr150[3.33] to Met153[3.36] of the hMOR is similar

to that of other GPCRs such as the nociceptin receptor [282](Della Longa et al. 2018). On the contrary, selection of the Met153$^{3.36}$ *trans* conformation by fentanyl when the receptor is in an inactive-like state suggests a destabilization of the hydrophobic interactions, which supports transition from an inactive receptor state to a more active one by disconnecting TM3 from TM6. These results indicate that fentanyl has a facility to change Met153$^{3.36}$ from an inactive to active-like conformation more frequently than morphine. In addition to Asp149$^{3.32}$-Tyr328$^{7.43}$ and Tyr150$^{3.33}$−ligand H-bonding and associated conformational change of Met153$^{3.36}$, the conformational toggling of Trp295$^{6.48}$ has previously been described in the activation of the MOR [214](Lipiński et al. 2019) and δ-opioid receptor [284](Tryoen-Tóth et al. 2005). The Trp295$^{6.48}$ sidechain also adopts different conformations in inactive [47](Manglik et al. 2012), activated [48](Huang et al. 2015), and fully active crystals of the mMOR. [68](Koehl et al. 2018) In our MD simulations with either bound morphine or fentanyl, Trp295$^{6.48}$ adopts an inactive-like *gauche* or an activated-like *trans* conformation depending on the receptor state and ligand bound. The *trans* position resembles the conformation observed in the fully active crystal structure [68](Koehl et al. 2018), adopting a perpendicular orientation to TM6 but with the indole NH pointing toward TM5 instead of TM7. This conformation is in general agreement with a recent study implementing MD simulations of the mMOR with docked fentanyl but differs from those observed with docked morphine [214](Lipiński et al. 2019). The reason for this discrepancy over morphine is unclear but could be due to differences between mouse and human receptor models or cobound sodium ions, which might negate agonist activity [214](Lipiński et al. 2019). In our simulations starting from the inactive hMOR, the *trans* conformation of Trp295$^{6.48}$ is only obtained twice, once with bound morphine and the other more transiently with fentanyl. This shows that activation of the hMOR, in particular TM6 conformational change, is a relatively difficult process to capture in a microsecond period. This contrasts with the relative ease of receptor activation observed in MD simulations of other class A GPCRs, such as CB1 [259](Díaz et al. 2019) or A2AR [260](Bruzzese et al. 2020). In some respects, this fits with the low constitutive activity displayed by the hMOR in pharmacological experiments [269](Seifert et al. 2002), which suggests a highly stable inactive state. When Trp295$^{6.48}$ adopts the *trans* conformation, it allows interhelical H-bonding with Ala242$^{5.46}$, a position which has been shown to be relevant for TM5 flexibility in class A GPCRs

[263]([Venkatakrishnan et al. 2019]). Conversely, the *gauche* conformation of Trp295[6.48] H-bonds Asn330[7.45] when whole TM6 movement is not present and the distance between Trp295[6.48] and Ala242[5.46] is large. As a result, conformational change and activation of TM5 and TM6 are highly related to close Trp295[6.48]−Ala242[5.46] interaction, either by H-bond formation or helical rearrangement. Together with Asp149[3.32]−Tyr328[7.43] and Tyr150[3.33]−ligand H-bonding, as well as Met153[3.36] conformational change in the receptor orthosteric pocket, these are the factors that most strongly govern intracellular receptor conformation and where differences between morphine and fentanyl are most clear.

In our MD simulations, conformational changes of TM helices occur differently with bound morphine or fentanyl. While morphine largely induces or selects conformational activation changes of TM3 and TM5, fentanyl more frequently achieves active-like conformations of TM6 and TM7. Conformational rearrangements of these TM helices are reflected in changes in specific intracellular regions such as Arg167[3.50]−Thr281[6.34] interaction between TM3 and TM6 and the NPxxY motif on TM7. However, in the most part, we observe that the distance between Arg167[3.50] and Thr281[6.34] and conformation of the NPxxY motif remain constant when the receptor is already in the activated state with bound fentanyl or morphine, which means that both agonists generally sustain the active receptor state, which is consistent with their agonist character. However, activation of the receptor from the inactive state through breakage of Arg167[3.50]−Thr281[6.34] interaction and conformational change of the NPxxY motif is more frequently observed with bound fentanyl than with morphine. This suggests that fentanyl more strongly induces conformational changes in the NPxxY motif through enhanced Asp149[3.32]−Tyr328[7.43] H-bonding and enables TM3−TM6 separation through disruption of Met153[3.36] conformation and Trp295[6.48]−Ala242[5.46] transient H-bonding and further close contact. This may be indicative of its higher efficacy observed at the experimental level [45]([O'Donell et al. 2017]), [46]([Mounteney et al. 2015]), [235]([Vardanyan et al. 2014]) and also reflects the allosteric communication that operates between the orthosteric pocket and intracellular regions of the hMOR. Nearly all orthosteric metrics analyzed in this study have shown a statistically significant association with the state of intracellular metrics studied, independent of the ligand bound and receptor starting state. This communication has been proposed to operate, at least in part, through a polar network

mediated by water molecules, which changes depending on the receptor state [48](Huang et al. 2015), [261](Yuan et al. 2014), [262](Tomobe et al. 2017), [263](Venkatakrishnan et al. 2019). Here, we have identified two water clusters, which differ between active- and inactive-like states or between morphine/fentanyl bound systems: (i) intracellular solvation near the NPxxY region on TM7 and (ii) solvation in the receptor core between Asn330[7.45] and Trp295[6.48]. In particular, the former has been described to occur during activation of the hMOR and class A GPCRs in general [48](Huang et al. 2015), [235](Vardanyan et al. 2014), [263](Venkatakrishnan et al. 2019). This is partly because TM6 conformational change involved in the transition from the inactive to near-active receptor state, as observed more with bound fentanyl, leads to greater solvation in intracellular receptor regions, including the NPxxY motif, as well as the receptor core near Trp295[6.48]. On the contrary, the smaller size of morphine allows greater solvation of the orthosteric pocket, which may negatively affect its binding stability in the inactive receptor state. Furthermore, the energetic state of these waters and how fentanyl potentially displaces more of them in the orthosteric pocket relative to morphine can be the topic of future study.

In summary, our dynamics of the hMOR are determined by ligand binding to activated [48](Huang et al. 2015) and inactive [47](Manglik et al. 2012) receptor models, based on mMOR crystal structures, including extracellular/intracellular loops and modelled N-termini. The recently published fully active mMOR cryo-EM structure [68](Koehl et al. 2018) allows for an independent positive control of MD-generated receptor structures. In addition, MD simulations with the antagonist naltrexone bound represent a negative control that allows us to better describe differences between fentanyl and morphine. Likewise, the constitution of the geometry of our hMOR models is validated by the mutual ligand and receptor conformational stability in control systems with BU-72 or naltrexone bound, respectively, to activated or inactive states. Two different physically stable binding poses of morphine and fentanyl in the hMOR mediate different sets of protein−ligand interactions (in particular involving Gln126[2.60], Lys235[5.39], Asp149[3.32], Lys235[5.39], and Tyr150[3.33]), which differentially change orthosteric pocket conformation (in particular Asp149[3.32]−Tyr328[7.43] H-bonding, Met153[3.36] orientation, and Trp295[6.48]−Ala242[5.46] interaction). These result in different intracellular TM3, TM5, TM6, and TM7 conformational changes, including movement of the

NPxxY motif and Arg167$^{3.50}$−Thr281$^{6.34}$ separation. Fentanyl has a stronger effect on TM6 and TM7 conformation, while morphine preferentially affects TM3 and TM5. As conformational change in TM6 is critical for GPCR activation and G protein binding in particular, this likely explains the enhanced receptor activity elicited by fentanyl in vivo, which has 50−100-fold higher potency than morphine [45](O'Donell et al. 2017), [46](Mounteney et al. 2015), [235](Vardanyan et al. 2014), [238](Lyons et al. 2015), [239](Warner et al. 2016). The structural insights gained in the present study can be used in future work with a spread of MOR targeting drugs, to identify those interactions and conformational changes associated with particular ligand efficacy and the disjunction between signalling networks through the receptor, which probably determine the proficiency in modulation of the receptor intracellular pocket and Gi protein or β-arrestin recognition.

4. Conclusions

We hope that the results made from the work included in the present thesis can be useful to other studies and help to perform accurate target-specific drug design. For each respective research line we conclude:

1. AT1R and A2AR form stable higher-order oligomeric complexes (AT1R/A2AR heterotetramer) constituted by respective receptor homodimers in their inactive state. We observed that the "best" receptor-receptor interface identified for this complex involves TM5 and TM6 of one receptor and TM1 and TM2 of the other, and vice versa, while in the respective homodimers a TM4-TM5 interface is formed between their protomers. This cross-talk increases the stability of both receptors with respect to their monomeric forms, which not only suggests protein-protein allosteric cross-regulation, but also involves a general lower fluctuation of the system which allows bound antagonists to remain more stable in the orthosteric pocket of the receptors. The demonstration of their simultaneous physical interaction will be extremely valuable when assessing potential multimodal tardive dyskinesia pharmacotherapeutic interventions based on cotreatment with AT1R and A2AR antagonists.

2. The direct contact between a 5-HT$_{2A}$R protomer in its inactive state and an activated mGlu2R homodimer forms a 5-HT$_{2A}$R/mGlu2R heterotrimer that remains physically stable throughout MD simulations. This modelled complex presents a TM6-TM6 interface between mGlu2R protomers and a TM4-TM5 interface between interacting mGlu2R and 5-HT$_{2A}$R. The direct contact that 5-HT$_{2A}$R establishes with the interacting mGlu2R protomer seems to stabilize the active configuration of the mGlu2R homodimer. Our high-accuracy mGlu2R/5-HT$_{2A}$R heterotrimer model was considered reliable enough to be used as the starting point for defining point mutation candidates following a structure-based approach, where close contacting pairs of residues might be replaced with cysteines (point mutations) in order to form inter-protomer disulfide bonds. Making use of our generated model, we were able to identify three point mutation candidates, with the 'best' being: Gly730$^{5.42}$ and Tyr781$^{6.58}$ on mGlu2R, together with Ile237$^{5.41}$ on 5-HT$_{2A}$R. This prediction led our

experimental collaborators to coprecipitate mGlu2R/5-HT$_{2A}$R heterooligomers by means of cysteine disulphide linkages. In addition, our model shows that the TM4-TM5 interface between interacting protomers is established across the entire helical region, including intracellular electrostatic interactions between both receptors (Arg659[3.56] – Gln178[3.55]/Glu264[5.68], respectively).

3. Conformational change of residues Tyr199[5.48] and Phe390[6.52], observed by means of MD simulations, may give an atomic level explanation of the different D2R homodimerization rates, following a TM5–TM6 interface, when the antagonists spiperone and clozapine are bound in the orthosteric pocket of the receptor. Experimentally, using complementation-based assays, it was experimentally observed that spiperone could significantly decrease the level of D2R dimers by 40%–60% compared to other atypical antipsychotics like clozapine. From a computational point of view, after generation of a stable D2R homodimer, we observed that while bound spiperone induces inward conformations of Tyr199[5.48] and Phe390[6.52], clozapine positions them more outwardly, thus favouring interaction with the complementary D2R protomer. These residues, placed on the external side of TM5 and TM6, show clear aromatic interactions between Tyr199[5.48] and Phe390[6.52] during MD simulations, as well as occasional H-bonding between Tyr199[5.48] of both protomers of the D2R homodimer model. This conformational difference highlights its relevance in the homodimerization process and the formation of a TM5-TM6 interface.

4. Computational techniques shed light onto the mechanistic understanding of the *in vivo* 50-100 fold higher potency of the MOR agonist fentanyl, compared to the reference agonist morphine. Differences in the protein-ligand interactions established between both ligands and a human MOR model, lead to different conformational changes induced/selected in the orthosteric pocket of the receptor, in particular Asp149[3.32], Gln126[2.60], Met153[3.36] and Lys235[5.39] dihedral angles. Our results indicate that Asp149[3.32]-Tyr328[7.43] H-bonding, previously described to be essential for MOR activation, is determined by ligand interactions with Asp149[3.32], Gln126[2.60], and by its position in the orthosteric pocket, which is influenced by its interaction with Lys235[5.39]. These conformational changes are transmitted to the core of the receptor, more specifically to the conformation of Trp295[6.48] and its interaction with Asn330[7.45]

or Ala242$^{5.46}$. Conformational dispositions in the orthosteric pocket lead to alteration of TM3, TM5, TM6 and TM7 positions, which indicates a transmission of the signal to the intracellular side of the receptor moving NPxxY motif and separating Arg167$^{3.50}$-Thr281$^{6.34}$ to different degrees. From our computational results, it is observed that fentanyl has a stronger effect on TM6 and NPxxY conformation, by decreasing the distance between Trp295$^{6.48}$ and Ala242$^{5.46}$ due to a TM6 rearrangement, essential for GPCR activation and G$_i$-protein binding in particular. Conversely, morphine preferentially affects TM3 and TM5, activating the receptor by inducing a dihedral conformational change in Trp295$^{6.48}$ which establishes an H-bond with Ala242$^{5.46}$. Specific ligand-receptor interactions and conformational changes differently induced/selected by morphine and fentanyl in MOR, raise structural insights for better understanding the effect of ligands on modulation of the receptor intracellular pocket and the resulting functional response. Results presented in this study can be considered reliable enough because of the relative stability of our observed binding poses of morphine and fentanyl, irrespective of receptor conformation, and comparison with the new DAMGO-bound fully active crystal structure of mMOR, together with the antagonist naltrexone-bound system additionally generated.

5. Acknowledgements

6. Bibliography

1. Santos R, Ursu O, Gaulton A, Bento AP, Donadi RS, Bologa CG, Karlsson A, Al-Lazikani B, Hersey A, Oprea TI, Overington JP. A comprehensive map of molecular drug targets. Nat Rev Drug Discov. 2017;16(1):19-34.

2. Hauser AS, Attwood MM, Rask-Andersen M, Schiöth HB, Gloriam DE. Trends in GPCR drug discovery: new agents, targets and indications. Nat Rev Drug Discov. 2017;16(12):829-842.

3. Zou Y, Ewalt J, Ng HL. Recent Insights from Molecular Dynamics Simulations for G Protein-Coupled Receptor Drug Discovery. Int J Mol Sci. 2019;20(17):4237.

4. Weis WI, Kobilka BK. The Molecular Basis of G Protein-Coupled Receptor Activation. Annu Rev Biochem. 2018;87:897-919.

5. Alexander SP, Christopoulos A, Davenport AP, Kelly E, Mathie A, Peters JA, Veale EL, Armstrong JF, Faccenda E, Harding SD, Pawson AJ, Southan C, Davies JA, Abbracchio MP, Alexander W, Al-Hosaini K, Bäck M, Barnes NM, Bathgate R, Beaulieu JM, Bernstein KE, Bettler B, Birdsall NJM, Blaho V, Boulay F, Bousquet C, Bräuner-Osborne H, Burnstock G, Caló G, Castaño JP, Catt KJ, Ceruti S, Chazot P, Chiang N, Chini B, Chun J, Cianciulli A, Civelli O, Clapp LH, Couture R, Csaba Z, Dahlgren C, Dent G, Singh KD, Douglas SD, Dournaud P, Eguchi S, Escher E, Filardo EJ, Fong T, Fumagalli M, Gainetdinov RR, Gasparo M, Gerard C, Gershengorn M, Gobeil F, Goodfriend TL, Goudet C, Gregory KJ, Gundlach AL, Hamann J, Hanson J, Hauger RL, Hay DL, Heinemann A, Hollenberg MD, Holliday ND, Horiuchi M, Hoyer D, Hunyady L, Husain A, IJzerman AP, Inagami T, Jacobson KA, Jensen RT, Jockers R, Jonnalagadda D, Karnik S, Kaupmann K, Kemp J, Kennedy C, Kihara Y, Kitazawa T, Kozielewicz P, Kreienkamp HJ, Kukkonen JP, Langenhan T, Leach K, Lecca D, Lee JD, Leeman SE, Leprince J, Li XX, Williams TL, Lolait SJ, Lupp A, Macrae R, Maguire J, Mazella J, McArdle CA, Melmed S, Michel MC, Miller LJ, Mitolo V, Mouillac B, Müller CE, Murphy P, Nahon JL, Ngo T, Norel X, Nyimanu D, O'Carroll AM, Offermanns S, Panaro MA, Parmentier M, Pertwee RG, Pin JP, Prossnitz ER, Quinn M, Ramachandran R, Ray M, Reinscheid RK, Rondard P, Rovati GE, Ruzza C, Sanger GJ, Schöneberg T, Schulte G, Schulz S, Segaloff DL, Serhan CN, Stoddart LA, Sugimoto Y, Summers R, Tan VP, Thal D, Thomas WW, Timmermans PBMWM, Tirupula K, Tulipano G, Unal H, Unger T, Valant C, Vanderheyden P, Vaudry D, Vaudry H, Vilardaga JP, Walker CS, Wang JM, Ward DT, Wester HJ, Willars GB, Woodruff TM, Yao C, Ye RD. THE CONCISE GUIDE TO PHARMACOLOGY 2021/22: G protein-coupled receptors. Br J Pharmacol. 2021;178 Suppl 1:S27-S156.

6. Huang Y, Todd N, Thathiah A. The role of GPCRs in neurodegenerative diseases: avenues for therapeutic intervention. Curr Opin Pharmacol. 2017;32:96-110.

7. Foster DJ, Conn PJ. Allosteric Modulation of GPCRs: New Insights and Potential Utility for Treatment of Schizophrenia and Other CNS Disorders. Neuron. 2017 May 3;94(3):431-446.

8. Smyth MS, Martin JH. x ray crystallography. Mol Pathol. 2000;53(1):8-14.

9. Tikhonova IG, Costanzi S. Unraveling the structure and function of G protein-coupled receptors through NMR spectroscopy. Curr Pharm Des. 2009;15(35):4003-16.

10. Puthenveetil R, Vinogradova O. Solution NMR: A powerful tool for structural and functional studies of membrane proteins in reconstituted environments. J Biol Chem. 2019;294(44):15914-15931.

11. Barreto CAV, Baptista SJ, Preto AJ, Matos-Filipe P, Mourão J, Melo R, Moreira I. Prediction and targeting of GPCR oligomer interfaces. Prog Mol Biol Transl Sci. 2020;169:105-149.

12. Ferré S, Quiroz C, Woods AS, Cunha R, Popoli P, Ciruela F, Lluis C, Franco R, Azdad K, Schiffmann SN. An update on adenosine A2A-dopamine D2 receptor interactions: implications for the function of G protein-coupled receptors. Curr Pharm Des. 2008;14(15):1468-74.

13. Botta J, Appelhans J, McCormick PJ. Continuing challenges in targeting oligomeric GPCR-based drugs. Prog Mol Biol Transl Sci. 2020;169:213-245.

14. González-Maeso J. GPCR oligomers in pharmacology and signaling. Mol Brain. 2011;4(1):20.

15. Gurevich VV, Gurevich EV. Molecular Mechanisms of GPCR Signaling: A Structural Perspective. Int J Mol Sci. 2017;18(12):2519.

16. Tan L, Yan W, McCorvy JD, Cheng J. Biased Ligands of G Protein-Coupled Receptors (GPCRs): Structure-Functional Selectivity Relationships (SFSRs) and Therapeutic Potential. J Med Chem. 2018;61(22):9841-9878.

17. Berg KA, Clarke WP. Making Sense of Pharmacology: Inverse Agonism and Functional Selectivity. Int J Neuropsychopharmacol. 2018;21(10):962-977.

18. Dalton JA, Lans I, Giraldo J. Quantifying conformational changes in GPCRs: glimpse of a common functional mechanism. BMC Bioinformatics. 2015;16(1):124.

19. Zhou Q, Yang D, Wu M, Guo Y, Guo W, Zhong L, Cai X, Dai A, Jang W, Shakhnovich EI, Liu ZJ, Stevens RC, Lambert NA, Babu MM, Wang MW, Zhao S. Common activation mechanism of class A GPCRs. Elife. 2019;8:e50279.

20. Lans I, Dalton JAR, Giraldo J. Helix 3 acts as a conformational hinge in Class A GPCR activation: An analysis of interhelical interaction energies in crystal structures. J Struct Biol. 2015;192(3):545-553.

21. Olivella M, Caltabiano G, Cordomí A. The role of Cysteine 6.47 in class A GPCRs. BMC Struct Biol. 2013;13:3.

22. Vickery ON, Carvalheda CA, Zaidi SA, Pisliakov AV, Katritch V, Zachariae U. Intracellular Transfer of Na+ in an Active-State G-Protein-Coupled Receptor. Structure. 2018;26(1):171-180.e2.

23. White KL, Eddy MT, Gao ZG, Han GW, Lian T, Deary A, Patel N, Jacobson KA, Katritch V, Stevens RC. Structural Connection between Activation Microswitch and Allosteric Sodium Site in GPCR Signaling. Structure. 2018;26(2):259-269.e5.

24. Bruzzese A, Gil C, Dalton JAR, Giraldo J. Structural insights into positive and negative allosteric regulation of a G protein-coupled receptor through protein-lipid interactions. Sci Rep. 2018;8(1):4456.

25. Fleetwood O, Matricon P, Carlsson J, Delemotte L. Energy Landscapes Reveal Agonist Control of G Protein-Coupled Receptor Activation via Microswitches. Biochemistry. 2020;59(7):880-891.

26. Ballesteros JA, Weinstein H. [19] Integrated methods for the construction of three-dimensional models and computational probing of structure-function relations in G protein-coupled receptors. Methods in Neurosciences. 1995;25:366-428.

27. Galés C, Kowalski-Chauvel A, Dufour MN, Seva C, Moroder L, Pradayrol L, Vaysse N, Fourmy D, Silvente-Poirot S. Mutation of Asn-391 within the conserved NPXXY motif of the cholecystokinin B receptor abolishes Gq protein activation without affecting its association with the receptor. J Biol Chem. 2000 Jun 9;275(23):17321-7.

28. Chun L, Zhang WH, Liu JF. Structure and ligand recognition of class C GPCRs. Acta Pharmacol Sin. 2012;33(3):312-23.

29. Møller TC, Moreno-Delgado D, Pin JP, Kniazeff J. Class C G protein-coupled receptors: reviving old couples with new partners. Biophys Rep. 2017;3(4):57-63.

30. Pin JP, Bettler B. Organization and functions of mGlu and GABAB receptor complexes. Nature. 2016;540(7631):60-68.

31. Levitz J, Habrian C, Bharill S, Fu Z, Vafabakhsh R, Isacoff EY. Mechanism of Assembly and Cooperativity of Homomeric and Heteromeric Metabotropic Glutamate Receptors. Neuron. 2016 Oct 5;92(1):143-159.

32. Lans I, Díaz Ó, Dalton JAR, Giraldo J. Exploring the Activation Mechanism of the mGlu5 Transmembrane Domain. Front Mol Biosci. 2020 Mar 6;7:38.

33. Xue L, Rovira X, Scholler P, Zhao H, Liu J, Pin JP, Rondard P. Major ligand-induced rearrangement of the heptahelical domain interface in a GPCR dimer. Nat Chem Biol. 2015;11(2):134-140.

34. Seven AB, Barros-Álvarez X, de Lapeyrière M, Papasergi-Scott MM, Robertson MJ, Zhang C, Nwokonko RM, Gao Y, Meyerowitz JG, Rocher JP, Schelshorn D, Kobilka BK, Mathiesen JM, Skiniotis G. G-protein activation by a metabotropic glutamate receptor. Nature. 2021;595(7867):450-454.

35. Shen C, Mao C, Xu C, Jin N, Zhang H, Shen DD, Shen Q, Wang X, Hou T, Chen Z, Rondard P, Pin JP, Zhang Y, Liu J. Structural basis of GABAB receptor-Gi protein coupling. Nature. 2021;594(7864):594-598.

36. Dalton JAR, Pin J, Giraldo J. Analysis of positive and negative allosteric modulation in metabotropic glutamate receptors 4 and 5 with a dual ligand. Sci Rep. 2017;7(1): 4944.

37. Navarro G, Cordomí A, Zelman-Femiak M, Brugarolas M, Moreno E, Aguinaga D, Perez-Benito L, Cortés A, Casadó V, Mallol J, Canela EI, Lluís C, Pardo L, García-Sáez AJ, McCormick PJ, Franco R. Quaternary structure of a G-protein-coupled receptor heterotetramer in complex with Gi and Gs. BMC Biol. 2016;14:26.

38. Oliveira PA, Dalton JAR, López-Cano M, Ricarte A, Morató X, Matheus FC, Cunha AS, Müller CE, Takahashi RN, Fernández-Dueñas V, Giraldo J, Prediger RD, Ciruela F. Angiotensin II type 1/adenosine A 2A receptor oligomers: a novel target for tardive dyskinesia. Sci Rep. 2017;7(1):1857.

39. Fribourg M, Moreno JL, Holloway T, Provasi D, Baki L, Mahajan R, Park G, Adney SK, Hatcher C, Eltit JM, Ruta JD, Albizu L, Li Z, Umali A, Shim J, Fabiato A, MacKerell AD Jr, Brezina V, Sealfon SC, Filizola M, González-Maeso J, Logothetis DE. Decoding the signalling of a GPCR Heteromeric Complex Reveals a Unifying Mechanism of Action of Antipsychotic Drugs. Cell. 2011;147(5):1011-1023.

40. Moreno JL, Miranda-Azpiazu P, García-Bea A, Younkin J, Cui M, Kozlenkov A, Ben-Ezra A, Voloudakis G, Fakira AK, Baki L, Ge Y, Georgakopoulos A, Morón JA, Milligan G, López-Giménez JF, Robakis NK, Logothetis DE, Meana JJ, González-Maeso J. Allosteric signalling through an mGlu2 and 5-HT2A heteromeric receptor complex and its potential contribution to schizophrenia. Sci signal. 2016;9(410):ra5.

41. Delille HK, Becker JM, Burkhardt S, Bleher B, Terstappen GC, Schmidt M, Meyer AH, Unger L, Marek GJ, Mezler M. Heterocomplex formation of 5-HT2A-mGlu2 and its relevance for cellular signaling cascades. Neuropharmacology. 2012;62(7):2184-91.

42. Baki L, Fribourg M, Younkin J, Eltit JM, Moreno JL, Park G, Vysotskaya Z, Narahari A, Sealfon SC, Gonzalez-Maeso J, Logothetis DE. Cross-signalling in metabotropic glutamate 2 and serotonin 2A receptor heteromers in mammalian cells. Pflugers Archiv: European journal of physiology. 2016;468(5):775-793.

43. Wouters E, Marín AR, Dalton JAR, Giraldo J, Stove C. Distinct Dopamine D₂ Receptor Antagonists Differentially Impact D₂ Receptor Oligomerization. Int J Mol Sci. 2019;20(7):1686.

44. Steglitz J, Buscemi J, Ferguson MJ. The future of pain research, education, and treatment: a summary of the IOM report "Relieving pain in America: a blueprint for transforming prevention, care, education, and research". Transl Behav Med. 2012;2(1):6-8.

45. O'Donnell JK, Halpin J, Mattson CL, Goldberger BA, Gladden RM. Deaths involving fentanyl, fentanyl analogs, and U-47700 - 10 States, July-December 2016. Morbidity and Mortality Weekly Report. 2017;66(43):1197-1202.

46. Mounteney J, Giraudon I, Denissov G, Griffiths P. Fentanyls: Are we missing the signs? Highly potent and on the rise in Europe. International Journal of Drug Policy. 2015;26:626-631.

47. Manglik A, Kruse AC, Kobilka TS, Thian FS, Mathiesen JM, Sunahara RK, Pardo L, Weis WI, Kobilka BK, Granier S. Crystal structure of the μ-opioid receptor bound to a morphinan antagonist. Nature. 2012;485(7398):321-326.

48. Huang W, Manglik A, Venkatakrishnan AJ, Laeremans T, Feinberg EN, Sanborn AL, Kato HE, Livingston KE, Thorsen TS, Kling RC, Granier S, Gmeiner P, Husbands SM, Traynor JR, Weis WI, Steyaert J, Dror RO, Kobilka BK. Structural insights into μ-opioid receptor activation. Nature. 2015;524(7565):315-21.

49. Ricarte A, Dalton JAR, Giraldo J. Structural Assessment of Agonist Efficacy in the μ-Opioid Receptor: Morphine and Fentanyl Elicit Different Activation Patterns. J Chem Inf Model. 2021;61(3):1251-1274.

50. Pettersen EF, Goddard TD, Huang CC, Couch GS, Greenblatt DM, Meng EC, Ferrin TE. UCSF Chimera--a visualization system for exploratory research and analysis. Journal of Computational Chemistry. 2004;25(13):1605-1612.

51. Webb B, Sali A. Protein structure modeling with MODELLER. Methods Mol Biol. 2014;1137:1–15.

52. Wang S, Che T, Levit A, Shoichet BK, Wacker D, Roth BL. Structure of the D2 dopamine receptor bound to the atypical antipsychotic drug risperidone. Nature. 2018;555:269–273.

53. Zhang H, Unal H, Desnoyer R, Han GW, Patel N, Katritch V, Karnik SS, Cherezov V,

Stevens RC. Structural Basis for Ligand Recognition and Functional Selectivity at Angiotensin Receptor. J Biol Chem. 2015;290(49):29127-39.

54. Liu W, Chun E, Thompson AA, Chubukov P, Xu F, Katritch V, Han GW, Roth CB, Heitman LH, IJzerman AP, Cherezov V, Stevens RC. Structural basis for allosteric regulation of GPCRs by sodium ions. Science. 2012;337(6091):232-6.

55. Wacker D, Wang C, Katritch V, Han GW, Huang XP, Vardy E, McCorvy JD, Jiang Y, Chu M, Siu FY, Liu W, Xu HE, Cherezov V, Roth BL, Stevens RC. Structural Features for Functional Selectivity at Serotonin Receptors. Science. 2013;340(6132):615-619.

56. Wu H, Wang C, Gregory KJ, Han GW, Cho HP, Xia Y, Niswender CM, Katritch V, Meiler J, Cherezov V, Conn PJ, Stevens RC. Structure of a class C GPCR metabotropic glutamate receptor 1 bound to an allosteric modulator. Science. 2014;344(6179):58-64.

57. The UniProt Consortium. UniProt: the universal protein knowledgebase. Nucleic Acids Research. 2018;46(5):2699.

58. Shapovalov MV, Dunbrack RL Jr. A smoothed backbone-dependent rotamer library for proteins derived from adaptive kernel density estimates and regressions. Structure. 2011, 19, pp. 844-58.

59. Pei J, Kim BH, Grishin N V. PROMALS3D: A tool for multiple protein sequence and structure alignments. Nucleic Acids Res. 2008;36:2295–300.

60. Waterhouse AM, Procter JB, Martin DMA, Clamp M, Barton GJ. Jalview Version 2-A multiple sequence alignment editor and analysis workbench. Bioinformatics. 2009;25:1189–91.

61. Shen MY, Sali A. Statistical potential for assessment and prediction of protein structures. Protein Sci. 2006;15:2507–24.

62. Jones DT. Protein secondary structure prediction based on position-specific scoring matrices. J Mol Biol. 1999;292:195–202. doi:10.1006/jmbi.1999.3091.

63. Yan R, Xu D, Yang J, Walker S, Zhang Y. A comparative assessment and analysis of 20 representative sequence alignment methods for protein structure prediction. Sci Rep. 2013;3:2619.

64. Drozdetskiy A, Cole C, Procter J, Barton GJ. JPred4: a protein secondary structure prediction server. Nucleic Acids Res. 2015;43:W389–94.

65. Maier JA, Martinez C, Kasavajhala K, Wickstrom L, Hauser KE, Simmerling C. ff14SB: Improving the accuracy of protein side chain and backbone parameters from ff99SB. Journal of Chemical Theory and Computation. 2015;11:3696-3713.

66. Kim S, Thiessen PA, Bolton EE, Chen J, Fu G, Gindulyte A, Han L, He J, He S, Shoemaker BA, Wang J, Yu B, Zhang J, Bryant SH. PubChem substance and compound databases. Nucleic Acids Research. 2016;44(D1):202-213.

67. Morris GM, Huey R, Lindstrom W, Sanner MF, Belew RK, Goodsell DS, Olson AJ. AutoDock4 and AutoDockTools4: Automated docking with selective receptor flexibility. Journal of Computational Chemistry. 2009;30(16):2785-2791.

68. Koehl A, Hu H, Maeda S, Zhang Y, Qu Q, Paggi JM, Latorraca NR, Hilger D, Dawson R, Matile H, Schertler GFX, Granier S, Weis WI, Dror RO, Manglik A, Skiniotis G, Kobilka BK. Structure of the μ-opioid receptor-Gi protein complex. Nature. 2018;558(7711):547-552.

69. Spahn V, Del Vecchio G, Labuz D, Rodriguez-Gaztelumendi A, Massaly N, Temp J, Durmaz V, Sabri P, Reidelbach M, Machelska H, Weber M, Stein C. A nontoxic pain killer designed by modeling of pathological receptor conformations. Science. 2017;355:966-969.

70. Doré AS, Robertson N, Errey JC, Ng I, Hollenstein K, Tehan B, Hurrell E, Bennett K, Congreve M, Magnani F, Tate CG, Weir M, Marshall FH. Structure of the adenosine A(2A) receptor in complex with ZM241385 and the xanthines XAC and caffeine. Structure. 2011;19(9):1283-93.

71. Lyskov S, Chou FC, Conchuir SO, Der BS, Drew K, Kuroda D, Xu J, Weitzner BD, Renfrew PD, Sripakdeevong P, Borgo B, Havranek JJ, Kuhlman B, Kortemme T, Bonneau R, Gray JJ, Das R. Serverification of molecular modeling applications: The Rosetta Online Server that Includes Everyone (ROSIE) PLoS ONE. 2013;8:e63906.

72. Jo S, Kim T, Iyer VG, Im W. CHARMM-GUI: a web-based graphical user interface for CHARMM. Journal of Computational Chemistry. 2008;29(11):1859-1865.

73. Lomize MA, Lomize AL, Pogozheva ID, Mosberg HI. OPM: orientations of proteins in membranes database. Bioinformatics. 2006;22(5):623-625.

74. Huang J, MacKerell ADJ. CHARMM36 all-atom additive protein force field: validation based on comparison to NMR data. Journal of Computational Chemistry. 2013;34(25):2135-2145.

75. Vanommeslaeghe K, Hatcher E, Acharya C, Kundu S, Zhong S, Shim J, Darian E, Guvench O, Lopes P, Vorobyov I, Mackerell AD Jr. CHARMM General Force Field (CGenFF): A force field for drug-like molecules compatible with the CHARMM All-Atom Additive Biological Force Fields. Journal of Computational Chemistry. 2010;31(4):671-690.

76. Harvey MJ, Giupponi G, De Fabritiis G. ACEMD: Accelerating biomolecular dynamics in the microsecond time scale. Journal of Chemical Theory and Computation. 2009;5(6):1632-1639.

77. Humphrey W, Dalke A, Schulten K. VMD: visual molecular dynamics. Journal of molecular graphics. 1996;14(1):33-38,27-28.

78. Saam J. Trajectory Smooth 1.1 TCL-script n.d. available at http://www.ks.uiuc.edu/Research/vmd/script_library/scripts/trajectory_smooth/.

79. Phillips JC, Braun R, Wang W, Gumbart J, Tajkhorshid E, Villa E, Chipot C, Skeel RD, Kalé L, Schulten K. Scalable molecular dynamics with NAMD. Journal of Computational Chemistry. 2005;26:1781-1802.

80. Schymkowitz J, Borg J, Stricher F, Nys R, Rousseau F, Serrano L. The FoldX web server: An online force field. Nucleic Acids Res. 2005;33:W382–W388.

81. IBM SPSS Statistics for Windows, version 20 (IBM Corp., Armonk, N.Y., USA).

82. Agnati LF, Fuxe K, Zini I, Lenzi P, Hökfelt T. Aspects on receptor regulation and isoreceptor identification. Med Biol. 1980;58(4):182-7.

83. Fuxe K, Agnati LF, Benfenati F, Celani M, Zini I, Zoli M, Mutt V. Evidence for the existence of receptor--receptor interactions in the central nervous system. Studies on the regulation of monoamine receptors by neuropeptides. J Neural Transm Suppl. 1983;18:165-79.

84. Gomes I, Ayoub MA, Fujita W, Jaeger WC, Pfleger KD, Devi LA. G Protein-Coupled Receptor Heteromers. Annu Rev Pharmacol Toxicol. 2016;56:403-25.

85. Ciruela F, Burgueño J, Casadó V, Canals M, Marcellino D, Goldberg SR, Bader M, Fuxe K, Agnati LF, Lluis C, Franco R, Ferré S, Woods AS. Combining mass spectrometry and pull-down techniques for the study of receptor heteromerization. Direct epitope-epitope electrostatic interactions between adenosine A2A and dopamine D2 receptors. Anal Chem. 2004;76(18):5354-63.

86. Martínez-Pinilla E, Rodríguez-Pérez AI, Navarro G, Aguinaga D, Moreno E, Lanciego JL, Labandeira-García JL, Franco R. Dopamine D2 and angiotensin II type 1 receptors form functional heteromers in rat striatum. Biochem Pharmacol. 2015;96(2):131-42.

87. Müller T. The safety of istradefylline for the treatment of Parkinson's disease. Expert Opin Drug Saf. 2015;14(5):769-75.

88. Garrido-Gil P, Valenzuela R, Villar-Cheda B, Lanciego JL, Labandeira-Garcia JL. Expression of angiotensinogen and receptors for angiotensin and prorenin in the monkey and human substantia nigra: an intracellular renin-angiotensin system in the nigra. Brain Struct Funct. 2013;218(2):373-88.

89. Brunner HR, Chang P, Wallach R, Sealey JE, Laragh JH. Angiotensin II vascular receptors: their avidity in relationship to sodium balance, the autonomic nervous system, and hypertension. J Clin Invest. 1972;51(1):58-67.

90. Saavedra JM. Brain angiotensin II: new developments, unanswered questions and therapeutic opportunities. Cell Mol Neurobiol. 2005;25(3-4):485-512.

91. Goa KL, Wagstaff AJ. Losartan potassium: a review of its pharmacology, clinical efficacy and tolerability in the management of hypertension. Drugs. 1996;51(5):820-45.

92. Saavedra JM. Angiotensin II AT(1) receptor blockers ameliorate inflammatory stress: a beneficial effect for the treatment of brain disorders. Cell Mol Neurobiol. 2012;32(5):667-81.

93. Labandeira-García JL, Garrido-Gil P, Rodriguez-Pallares J, Valenzuela R, Borrajo A, Rodríguez-Perez AI. Brain renin-angiotensin system and dopaminergic cell vulnerability. Front Neuroanat. 2014;8:67.

94. Pechlivanova DM, Georgiev VP. Interaction of angiotensin II and adenosine A1 and A2A receptor ligands on the writhing test in mice. Pharmacol Biochem Behav. 2002;72(1-2):23-8.

95. Tchekalarova J, Kambourova T, Georgiev V. Long-term theophylline treatment changes the effects of angiotensin II and adenosinergic agents on the seizure threshold. Brain Res Bull. 2000;52(1):13-6.

96. Thakur S, Du J, Hourani S, Ledent C, Li JM. Inactivation of adenosine A2A receptor attenuates basal and angiotensin II-induced ROS production by Nox2 in endothelial cells. J Biol Chem. 2010;285(51):40104-13.

97. Lai EY, Patzak A, Persson AE, Carlström M. Angiotensin II enhances the afferent arteriolar response to adenosine through increases in cytosolic calcium. Acta Physiol (Oxf). 2009;196(4):435-45.

98. Rongen GA, Brooks SC, Ando Si, Abramson BL, Floras JS. Angiotensin AT1 receptor blockade abolishes the reflex sympatho-excitatory response to adenosine. J Clin Invest.

1998;101(4):769-76.

99. Thévenin D, Lazarova T, Roberts MF, Robinson CR. Oligomerization of the fifth transmembrane domain from the adenosine A2A receptor. Protein Sci. 2005;14(8):2177-86.

100. Canals M, Burgueño J, Marcellino D, Cabello N, Canela EI, Mallol J, Agnati L, Ferré S, Bouvier M, Fuxe K, Ciruela F, Lluis C, Franco R. Homodimerization of adenosine A2A receptors: qualitative and quantitative assessment by fluorescence and bioluminescence energy transfer. J Neurochem. 2004;88(3):726-34.

101. Karip E, Turu G, Süpeki K, Szidonya L, Hunyady L. Cross-inhibition of angiotensin AT1 receptors supports the concept of receptor oligomerization. Neurochem Int. 2007;51(5):261-7.

102. AbdAlla S, Lother H, Langer A, el Faramawy Y, Quitterer U. Factor XIIIA transglutaminase crosslinks AT1 receptor dimers of monocytes at the onset of atherosclerosis. Cell. 2004;119(3):343-54

103. Hansen JL, Theilade J, Haunsø S, Sheikh SP. Oligomerization of wild type and nonfunctional mutant angiotensin II type I receptors inhibits galphaq protein signaling but not ERK activation. J Biol Chem. 2004;279(23):24108-15.

104. Fanelli F, Felline A. Dimerization and ligand binding affect the structure network of A(2A) adenosine receptor. Biochim Biophys Acta. 2011;1808(5):1256-66.

105. Gracia E, Pérez-Capote K, Moreno E, Barkešová J, Mallol J, Lluís C, Franco R, Cortés A, Casadó V, Canela EI. A2A adenosine receptor ligand binding and signalling is allosterically modulated by adenosine deaminase. Biochem J. 2011;435(3):701-9.

106. Bonaventura J, Navarro G, Casadó-Anguera V, Azdad K, Rea W, Moreno E, Brugarolas M, Mallol J, Canela EI, Lluís C, Cortés A, Volkow ND, Schiffmann SN, Ferré S, Casadó V. Allosteric interactions between agonists and antagonists within the adenosine A2A receptor-dopamine D2 receptor heterotetramer. Proc Natl Acad Sci U S A. 2015;112(27):E3609-18.

107. Andreassen OA, Jørgensen HA. Neurotoxicity associated with neuroleptic-induced oral dyskinesias in rats. Implications for tardive dyskinesia? Prog Neurobiol. 2000;61(5):525-41.

108. Fuxe K, Borroto-Escuela DO, Romero-Fernandez W, Palkovits M, Tarakanov AO, Ciruela F, Agnati LF. Moonlighting proteins and protein-protein interactions as neurotherapeutic targets in the G protein-coupled receptor field. Neuropsychopharmacology. 2014;39(1):131-55.

109. Ferré S, Quiroz C, Orru M, Guitart X, Navarro G, Cortés A, Casadó V, Canela EI, Lluis C, Franco R. Adenosine A(2A) Receptors and A(2A) Receptor Heteromers as Key Players in Striatal Function. Front Neuroanat. 2011;5:36.

110. Fuxe K, Marcellino D, Genedani S, Agnati L. Adenosine A(2A) receptors, dopamine D(2) receptors and their interactions in Parkinson's disease. Mov Disord. 2007;22(14):1990-2017.

111. Mendelsohn FA, Jenkins TA, Berkovic SF. Effects of angiotensin II on dopamine and serotonin turnover in the striatum of conscious rats. Brain Res. 1993;613(2):221-9.

112. Brown DC, Steward LJ, Ge J, Barnes NM. Ability of angiotensin II to modulate striatal

dopamine release via the AT1 receptor in vitro and in vivo. Br J Pharmacol. 1996;118(2):414-20.

113. Villar-Cheda B, Rodríguez-Pallares J, Valenzuela R, Muñoz A, Guerra MJ, Baltatu OC, Labandeira-Garcia JL. Nigral and striatal regulation of angiotensin receptor expression by dopamine and angiotensin in rodents: implications for progression of Parkinson's disease. Eur J Neurosci. 2010;32(10):1695-706.

114. Villar-Cheda B, Dominguez-Meijide A, Valenzuela R, Granado N, Moratalla R, Labandeira-Garcia JL. Aging-related dysregulation of dopamine and angiotensin receptor interaction. Neurobiol Aging. 2014;35(7):1726-38.

115. Borroto-Escuela DO, Romero-Fernandez W, Tarakanov AO, Gómez-Soler M, Corrales F, Marcellino D, Narvaez M, Frankowska M, Flajolet M, Heintz N, Agnati LF, Ciruela F, Fuxe K. Characterization of the A2AR-D2R interface: focus on the role of the C-terminal tail and the transmembrane helices. Biochem Biophys Res Commun. 2010;402(4):801-7.

116. Ferré S, Lluís C, Justinova Z, Quiroz C, Orru M, Navarro G, Canela EI, Franco R, Goldberg SR. Adenosine-cannabinoid receptor interactions. Implications for striatal function. Br J Pharmacol. 2010;160(3):443-53.

117. Yager LM, Garcia AF, Wunsch AM, Ferguson SM. The ins and outs of the striatum: role in drug addiction. Neuroscience. 2015;301:529-41.

118. Parsons B, Togasaki DM, Kassir S, Przedborski S. Neuroleptics up-regulate adenosine A2a receptors in rat striatum: implications for the mechanism and the treatment of tardive dyskinesia. J Neurochem. 1995;65(5):2057-64.

119. Bishnoi M, Chopra K, Kulkarni SK. Involvement of adenosinergic receptor system in an animal model of tardive dyskinesia and associated behavioural, biochemical and neurochemical changes. Eur J Pharmacol. 2006;552(1-3):55-66.

120. Ivanova SA, Al Hadithy AF, Brazovskaya N, Semke A, Wilffert B, Fedorenko O, Brouwers JR, Loonen AJ. No involvement of the adenosine A2A receptor in tardive dyskinesia in Russian psychiatric inpatients from Siberia. Hum Psychopharmacol. 2012;27(3):334-7.

121. Muñoz A, Garrido-Gil P, Dominguez-Meijide A, Labandeira-Garcia JL. Angiotensin type 1 receptor blockage reduces l-dopa-induced dyskinesia in the 6-OHDA model of Parkinson's disease. Involvement of vascular endothelial growth factor and interleukin-1β. Exp Neurol. 2014;261:720-32.

122. Fernández-Dueñas V, Taura JJ, Cottet M, Gómez-Soler M, López-Cano M, Ledent C, Watanabe M, Trinquet E, Pin JP, Luján R, Durroux T, Ciruela F. Untangling dopamine-adenosine receptor-receptor assembly in experimental parkinsonism in rats. Dis Model Mech. 2015;8(1):57-63.

123. Jean-Charles PY, Kaur S, Shenoy SK. G Protein-Coupled Receptor Signaling Through β-Arrestin-Dependent Mechanisms. J Cardiovasc Pharmacol. 2017;70(3):142–158.

124. Gonzalez-Maeso J. GPCR oligomers in pharmacology and signaling. Mol Brain. 2011;4(1):20.

125. Ferré S, Casadó V, Devi LA, Filizola M, Jockers R, Lohse MJ, Milligan G, Pin JP, Guitart X. G protein-coupled receptor oligomerization revisited: functional and pharmacological perspectives. Pharmacol Rev. 2014;66(2):413–434.

126.Lee Y, Basith S, Choi S. Recent Advances in Structure-Based Drug Design Targeting Class A G Protein-Coupled Receptors Utilizing Crystal Structures and Computational Simulations. J Med Chem. 2018;61(1):1-46.

127.Komatsu H, Fukuchi M, Habata Y. Potential Utility of Biased GPCR Signaling for Treatment of Psychiatric Disorders. Int J Mol Sci. 2019;20(13):pii:E3207.

128.Delille HK, Becker JM, Burkhardt S, Bleher B, Terstappen GC, Schmidt M, Meyer AH, Unger L, Marek GJ, Mezler M. Heterocomplex formation of 5-HT2A-mGlu2 and its relevance for cellular signalling cascades. Neuropharmacol. 2012;62(7):2184-2191.

129.Rondard P, Goudet C, Kniazeff J, Pin JP, Prézeau L. The complexity of their activation mechanism opens new possibilities for the modulation of mGlu and GABAB class C G protein–coupled receptors. Neuropharmacol. 2010;60:82–92.

130.Liu W, Chun E, Thompson AA, Chubukov P, Xu F, Katritch V, Han GW, Roth CB, Heitman LH, IJzerman AP, Cherezov V, Stevens RC. Structural basis for allosteric regulation of GPCRs by sodium ions. Science. 2012 Jul 13;337(6091):232-6.

131.Moreno JL, Muguruza C, Umali A, Mortillo S, Holloway T, Pilar-Cuéllar F, Mocci G, Seto J, Callado LF, Neve RL, Milligan G, Sealfon SC, López-Giménez JF, Meana JJ, Benson DL, González-Maeso J. Identification of three residues essential for 5-hydroxytryptamine 2A-metabotropic glutamate 2 (5-HT2A·mGlu2) receptor heteromerization and its psychoactive behavioral function. J Biol Chem. 2012;287(53):44301-44319.

132.Doré AS, Okrasa K, Patel JC, Serrano-Vega M, Bennett K, Cooke RM, Errey JC, Jazayeri A, Khan S, Tehan B, Weir M, Wiggin GR, Marshall FH. Structure of class C GPCR metabotropic glutamate receptor 5 transmembrane domain. Nature. 2014; 511(7511):557-562.

133.Christopher JA, Aves SJ, Bennett KA, Doré AS, Errey JC, Jazayeri A, Marshall FH, Okrasa K, Serrano-Vega MJ, Tehan BG, Wiggin GR, Congreve M. Fragment and Structure-Based Drug Discovery for a Class C GPCR: Discovery of the mGlu5 Negative Allosteric Modulator HTL14242 (3-Chloro-5-[6-(5-fluoropyridin-2-yl)pyrimidin-4-yl]benzonitrile). J Med Chem. 2015;58(16):6653-6664.

134.Christopher JA, Orgován Z, Congreve M, Doré AS, Errey JC, Marshall FH, Mason JS, Okrasa K, Rucktooa P, Serrano-Vega MJ, Ferenczy GG, Keserű GM. Structure-Based Optimization Strategies for G Protein-Coupled Receptor (GPCR) Allosteric Modulators: A Case Study from Analyses of New Metabotropic Glutamate Receptor 5 (mGlu5) X-ray Structures. J Med Chem. 2019;62(1):207-222.

135.Koehl A, Hu H, Feng D, Sun B, Zhang Y, Robertson MJ, Chu M, Kobilka TS, Laeremans T, Steyaert J, Tarrasch J, Dutta S, Fonseca R, Weis WI, Mathiesen JM, Skiniotis G, Kobilka BK. Structural insights into the activation of metabotropic glutamate receptors. Nature. 2019;566(7742):79-84.

136.Wang C, Jiang Y, Ma J, Wu H, Wacker D, Katritch V, Han GW, Liu W, Huang XP, Vardy E, McCorvy JD, Gao X, Zhou XE, Melcher K, Zhang C, Bai F, Yang H, Yang L, Jiang H, Roth BL, Cherezov V, Stevens RC, Xu HE. Structural basis for molecular recognition at serotonin receptors. Science. 2013;340(6132):610-4.

137.Yin W, Zhou XE, Yang D, de Waal PW, Wang M, Dai A, Cai X, Huang CY, Liu P, Wang

116

X, Yin Y, Liu B, Zhou Y, Wang J, Liu H, Caffrey M, Melcher K, Xu Y, Wang MW, Xu HE, Jiang Y. Crystal structure of the human 5-HT1B serotonin receptor bound to an inverse agonist. Cell Discov. 2018;4:12.

138. García-Nafría J, Nehmé R, Edwards PC, Tate CG. Cryo-EM structure of the serotonin 5-HT1B receptor coupled to heterotrimeric Go. Nature. 2018;558(7711):620-623.

139. Liu W, Wacker D, Gati C, Han GW, James D, Wang D, Nelson G, Weierstall U, Katritch V, Barty A, Zatsepin NA, Li D, Messerschmidt M, Boutet S, Williams GJ, Koglin JE, Seibert MM, Wang C, Shah ST, Basu S, Fromme R, Kupitz C, Rendek KN, Grotjohann I, Fromme P, Kirian RA, Beyerlein KR, White TA, Chapman HN, Caffrey M, Spence JC, Stevens RC, Cherezov V. Serial femtosecond crystallography of G protein-coupled receptors. Science. 2013;342(6165):1521-4.

140. Wacker D, Wang S, McCorvy JD, Betz RM, Venkatakrishnan AJ, Levit A, Lansu K, Schools ZL, Che T, Nichols DE, Shoichet BK, Dror RO, Roth BL. Crystal Structure of an LSD-Bound Human Serotonin Receptor. Cell. 2017;168(3):377-389.e12.

141. Ishchenko A, Wacker D, Kapoor M, Zhang A, Han GW, Basu S, Patel N, Messerschmidt M, Weierstall U, Liu W, Katritch V, Roth BL, Stevens RC, Cherezov V. Structural insights into the extracellular recognition of the human serotonin 2B receptor by an antibody. Proc Natl Acad Sci USA. 2017;114(31):8223-8228.

142. McCorvy JD, Wacker D, Wang S, Agegnehu B, Liu J, Lansu K, Tribo AR, Olsen RHJ, Che T, Jin J, Roth BL. Structural determinants of 5-HT2B receptor activation and biased agonism. Nat Struct Mol Biol. 2018;25(9):787-796.

143. Peng Y, McCorvy JD, Harpsøe K, Lansu K, Yuan S, Popov P, Qu L, Pu M, Che T, Nikolajsen LF, Huang XP, Wu Y, Shen L, Bjørn-Yoshimoto WE, Ding K, Wacker D, Han GW, Cheng J, Katritch V, Jensen AA, Hanson MA, Zhao S, Gloriam DE, Roth BL, Stevens RC, Liu ZJ. 5-HT2C Receptor Structures Reveal the Structural Basis of GPCR Polypharmacology. Cell. 2018;172(4):719-730.e14.

144. Kimura KT, Asada H, Inoue A, Kadji FMN, Im D, Mori C, Arakawa T, Hirata K, Nomura Y, Nomura N, Aoki J, Iwata S, Shimamura T. Structures of the 5-HT2A receptor in complex with the antipsychotics risperidone and zotepine. Nat Struct Mol Biol. 2019;26(2):121-128.

145. Binet V, Duthey B, Lecaillon J, Vol C, Quoyer J, Labesse G, Pin JP, Prézeau L. Common structural requirements for heptahelical domain function in class A and class C G protein-coupled receptors. J Biol Chem. 2007;282(16):12154-63.

146. Popov P, Peng Y, Shen L, Stevens RC, Cherezov V, Liu ZJ, Katritch V. Computational design of thermostabilizing point mutations for G protein-coupled receptors. Elife. 2018;7:e34729.

147. Rangel-Barajas C, Coronel I, Floran B. Dopamine Receptors and Neurodegeneration. Aging Dis. 2015;6:349–368.

148. Missale C, Nash SR, Robinson SW, Jaber M, Caron MG. Dopamine receptors: From structure to function. Physiol. Rev. 1998;78:189–225.

149. Beaulieu JM, Gainetdinov RR. The physiology, signaling, and pharmacology of dopamine receptors. Pharm. Rev. 2011;63:182–217.

150. Ferré S, Casadó V, Devi LA, Filizola M, Jockers R, Lohse MJ, Milligan G, Pin JP, Guitart X. G protein-coupled receptor oligomerization revisited: functional and

pharmacological perspectives. Pharmacol Rev. 2014 Feb 10;66(2):413-34.

151. Farran B. An update on the physiological and therapeutic relevance of GPCR oligomers. Pharmacol. Res. 2017;117:303–327.

152. Fiorentini C, Busi C, Spano P, Missale C. Dimerization of dopamine D1 and D3 receptors in the regulation of striatal function. Curr. Opin. Pharmacol. 2010;10:87–92.

153. Blasiak E, Lukasiewicz S, Szafran-Pilch K, Dziedzicka-Wasylewska M. Genetic variants of dopamine D2 receptor impact heterodimerization with dopamine D1 receptor. Pharmacol. Rep. 2017;69:235–241.

154. O'Dowd BF, Nguyen T, Ji X, George SR. D5 dopamine receptor carboxyl tail involved in D5-D2 heteromer formation. Biochem. Biophys. Res. Commun. 2013;431:586–589.

155. Van Craenenbroeck K, Borroto-Escuela DO, Skieterska K, Duchou J, Romero-Fernandez W, Fuxe K. Role of dimerization in dopamine D(4) receptor biogenesis. Curr. Protein Pept. Sci. 2014;15:659–665.

156. Nakagawa M, Kuri M, Kambara N, Tanigami H, Tanaka H, Kishi Y, Hamajima N. Dopamine D2 receptor Taq IA polymorphism is associated with postoperative nausea and vomiting. J. Anesth. 2008;22:397–403.

157. Pan YQ, Qiao L, Xue XD, Fu JH. Association between ANKK1 (rs1800497) polymorphism of DRD2 gene and attention deficit hyperactivity disorder: A meta-analysis. Neurosci. Lett. 2015;590:101–105.

158. Rocchetti J, Isingrini E, Dal Bo G, Sagheby S, Menegaux A, Tronche F, Levesque D, Moquin L, Gratton A, Wong TP, Rubinstein M, Giros B. Presynaptic D2 dopamine receptors control long-term depression expression and memory processes in the temporal hippocampus. Biol. Psychiatry. 2015;77:513–525.

159. Tozzi A, Tantucci M, Marchi S, Mazzocchetti P, Morari M, Pinton P, Mancini A, Calabresi P. Dopamine D2 receptor-mediated neuroprotection in a G2019S Lrrk2 genetic model of Parkinson's disease. Cell Death Dis. 2018;9:204.

160. Urs NM, Peterson SM, Caron MG. New Concepts in Dopamine D2 Receptor Biased Signaling and Implications for Schizophrenia Therapy. Biol. Psychiatry. 2017;81:78–85.

161. Weber MA, Graack ET, Scholl JL, Renner KJ, Forster GL, Watt MJ. Enhanced dopamine D2 autoreceptor function in the adult prefrontal cortex contributes to dopamine hypoactivity following adolescent social stress. Eur. J. Neurosci. 2018;48:1833–1850.

162. Weinstein JJ, van de Giessen E, Rosengard RJ, Xu X, Ojeil N, Brucato G, Gil RB, Kegeles LS, Laruelle M, Slifstein M, Abi-Dargham A. PET imaging of dopamine-D2 receptor internalization in schizophrenia. Mol. Psychiatry. 2018;23:1506–1511.

163. Ng GY, O'Dowd BF, Lee SP, Chung HT, Brann MR, Seeman P, George SR. Dopamine D2 receptor dimers and receptor-blocking peptides. Biochem. Biophys. Res. Commun. 1996;227:200–204.

164. Armstrong D, Strange PG. Dopamine D2 receptor dimer formation: Evidence from ligand binding. J. Biol. Chem. 2001;276:22621–22629.

165. Wurch T, Matsumoto A, Pauwels PJ. Agonist-independent and -dependent oligomerization of dopamine D(2) receptors by fusion to fluorescent proteins. FEBS Lett. 2001;507:109–113.

166. Kasai RS, Ito SV, Awane RM, Fujiwara TK, Kusumi A. The Class-A GPCR Dopamine

D2 Receptor Forms Transient Dimers Stabilized by Agonists: Detection by Single-Molecule Tracking. Cell Biochem. Biophys. 2018;76:29–37.

167. Kaczor AA, Jorg M, Capuano B. The dopamine D2 receptor dimer and its interaction with homobivalent antagonists: Homology modeling, docking and molecular dynamics. J. Mol. Model. 2016;22:203.

168. Kaczor AA, Rutkowska E, Bartuzi D, Targowska-Duda KM, Matosiuk D, Selent J. Computational methods for studying G protein-coupled receptors (GPCRs). Methods Cell Biol. 2016;132:359–399.

169. Borroto-Escuela DO, Rodriguez D, Romero-Fernandez W, Kapla J, Jaiteh M, Ranganathan A, Lazarova T, Fuxe K, Carlsson J. Mapping the Interface of a GPCR Dimer: A Structural Model of the A2A Adenosine and D2 Dopamine Receptor Heteromer. Front. Pharmacol. 2018;9:829.

170. Canals M, Marcellino D, Fanelli F, Ciruela F, de Benedetti P, Goldberg SR, Neve K, Fuxe K, Agnati LF, Woods AS, Ferré S, Lluis C, Bouvier M, Franco R. Adenosine A2A-dopamine D2 receptor-receptor heteromerization: Qualitative and quantitative assessment by fluorescence and bioluminescence energy transfer. J. Biol. Chem. 2003;278:46741–46749.

171. Niewiarowska-Sendo A, Polit A, Piwowar M, Tworzydlo M, Kozik A, Guevara-Lora I. Bradykinin B2 and dopamine D2 receptors form a functional dimer. Biochim. Biophys. Acta. 2017;1864:1855–1866.

172. Kearn CS, Blake-Palmer K, Daniel E, Mackie K, Glass M. Concurrent stimulation of cannabinoid CB1 and dopamine D2 receptors enhances heterodimer formation: A mechanism for receptor cross-talk? Mol. Pharmacol. 2005;67:1697–1704.

173. Pinna A, Bonaventura J, Farre D, Sanchez M, Simola N, Mallol J, Lluis C, Costa G, Baqi Y, Muller CE, Cortés A, McCormick P, Canela EI, Martínez-Pinilla E, Lanciego JL, Casadó V, Armentero MT, Franco R. L-DOPA disrupts adenosine A(2A)-cannabinoid CB(1)-dopamine D(2) receptor heteromer cross-talk in the striatum of hemiparkinsonian rats: Biochemical and behavioral studies. Exp. Neurol. 2014;253:180–191.

174. Pulido D, Casado-Anguera V, Perez-Benito L, Moreno E, Cordomi A, Lopez L, Cortes A, Ferre S, Pardo L, Casado V. Design of a True Bivalent Ligand with Picomolar Binding Affinity for a G Protein-Coupled Receptor Homodimer. J. Med. Chem. 2018;61:9335–9346.

175. Guitart X, Navarro G, Moreno E, Yano H, Cai NS, Sanchez-Soto M, Kumar-Barodia S, Naidu YT, Mallol J, Cortes A, Lluís C, Canela EI, Casadó V, McCormick PJ, Ferré S. Functional selectivity of allosteric interactions within G protein-coupled receptor oligomers: The dopamine D1-D3 receptor heterotetramer. Mol. Pharmacol. 2014;86:417–429.

176. Ferre S, Bonaventura J, Zhu W, Hatcher-Solis C, Taura J, Quiroz C, Cai NS, Moreno E, Casado-Anguera V, Kravitz AV, Thompson KR, Tomasi DG, Navarro G, Cordomí A, Pardo L, Lluís C, Dessauer CW, Volkow ND, Casadó V, Ciruela F, Logothetis DE, Zwilling D. Essential Control of the Function of the Striatopallidal Neuron by Pre-coupled Complexes of Adenosine A2A-Dopamine D2 Receptor Heterotetramers and Adenylyl Cyclase. Front. Pharmacol. 2018;9:243.

177. Navarro G, Cordomi A, Casado-Anguera V, Moreno E, Cai NS, Cortes A, Canela EI,

Dessauer CW, Casado V, Pardo L, Lluís C, Ferré S. Evidence for functional pre-coupled complexes of receptor heteromers and adenylyl cyclase. Nat. Commun. 2018;9:1242.

178. Qian M, Wouters E, Dalton JAR, Risseeuw MDP, Crans RAJ, Stove C, Giraldo J, Van Craenenbroeck K, Van Calenbergh S. Synthesis toward Bivalent Ligands for the Dopamine D2 and Metabotropic Glutamate 5 Receptors. J. Med. Chem. 2018;61:8212–8225.

179. Kasai RS, Kusumi A. Single-molecule imaging revealed dynamic GPCR dimerization. Curr. Opin. Cell Biol. 2014;27:78–86.

180. Tabor A, Weisenburger S, Banerjee A, Purkayastha N, Kaindl JM, Hubner H, Wei L, Gromer TW, Kornhuber J, Tschammer N, Birdsall NJ, Mashanov GI, Sandoghdar V, Gmeiner P. Visualization and ligand-induced modulation of dopamine receptor dimerization at the single molecule level. Sci. Rep. 2016;6:33233.

181. Hern JA, Baig AH, Mashanov GI, Birdsall B, Corrie JE, Lazareno S, Molloy JE, Birdsall NJ. Formation and dissociation of M1 muscarinic receptor dimers seen by total internal reflection fluorescence imaging of single molecules. Proc. Natl. Acad. Sci. USA. 2010;107:2693–2698.

182. Kasai RS, Suzuki KG, Prossnitz ER, Koyama-Honda I, Nakada C, Fujiwara TK, Kusumi A. Full characterization of GPCR monomer-dimer dynamic equilibrium by single molecule imaging. J. Cell Biol. 2011;192:463–480.

183. Calebiro D, Rieken F, Wagner J, Sungkaworn T, Zabel U, Borzi A, Cocucci E, Zurn A, Lohse MJ. Single-molecule analysis of fluorescently labeled G-protein-coupled receptors reveals complexes with distinct dynamics and organization. Proc. Natl. Acad. Sci. USA. 2013;110:743–748.

184. Wang M, Pei L, Fletcher PJ, Kapur S, Seeman P, Liu F. Schizophrenia, amphetamine-induced sensitized state and acute amphetamine exposure all show a common alteration: Increased dopamine D2 receptor dimerization. Mol. Brain. 2010;3:25.

185. Dazzan P, Morgan KD, Orr K, Hutchinson G, Chitnis X, Suckling J, Fearon P, McGuire PK, Mallett RM, Jones PB, Leff J, Murray RM. Different effects of typical and atypical antipsychotics on grey matter in first episode psychosis: the AESOP study. Neuropsychopharmacology. 2005;30(4):765-74.

186. Madhusudan Makwana K, Mahalakshmi R. Implications of aromatic-aromatic interactions: From protein structures to peptide models. Protein Sci. A Publ. Protein Soc. 2015;24:1920–1933.

187. Rossi M, Maggio R, Fasciani I, Scarselli M. Historical Perspectives: From Monomers to Dimers and Beyond, an Exciting Journey in the World of G Protein-Coupled Receptors. In: G-Protein-Coupled Receptor Dimers. Springer International Publishing; Cham, Switzerland. 2017:3–14.

188. Ilien B, Glasser N, Clamme JP, Didier P, Piemont E, Chinnappan R, Daval SB, Galzi JL, Mely Y. Pirenzepine promotes the dimerization of muscarinic M1 receptors through a three-step binding process. J. Biol. Chem. 2009;284:19533–19543.

189. Milligan G. G protein-coupled receptor dimerization: Function and ligand pharmacology. Mol. Pharmacol. 2004;66:1–7.

190. Saenz del Burgo L, Milligan G. Heterodimerisation of G protein-coupled receptors:

Implications for drug design and ligand screening. Expert Opin. Drug Discov. 2010;5:461–474.

191. Breivik H, Collett B, Ventafridda V, Cohen R, Gallacher D. Survey of chronic pain in Europe: prevalence, impact on daily life, and treatment. Eur J Pain. 2006;10(4):287-333.

192. O'Brien T, Christrup LL, Drewes AM, Fallon MT, Kress HG, McQuay HJ, Mikus G, Morlion BJ, Perez-Cajaraville J, Pogatzki-Zahn E, Varrassi G, Wells JC. European Pain Federation position paper on appropriate opioid use in chronic pain management. Eur J Pain. 2017;21(1):3-19.

193. Wang JB, Johnson PS, Persico AM, Hawkins AL, Griffin CA, Uhl GR. Human mu opiate receptor. cDNA and genomic clones, pharmacologic characterization and chromosomal assignment. FEBS Lett. 1994;338(2):217-22.

194. Roeckel LA, Utard V, Reiss D, Mouheiche J, Maurin H, Robé A, Audouard E, Wood JN, Goumon Y, Simonin F, Gaveriaux-Ruff C. Morphine-induced hyperalgesia involves mu opioid receptors and the metabolite morphine-3-glucuronide. Sci Rep. 2017;7(1):10406.

195. Kapoor A, Martinez-Rosell G, Provasi D, de Fabritiis G, Filizola M. Dynamic and Kinetic Elements of μ-Opioid Receptor Functional Selectivity. Sci Rep. 2017;7(1):11255.

196. Raehal KM, Walker JK, Bohn LM. Morphine side effects in beta-arrestin 2 knockout mice. J Pharmacol Exp Ther. 2005;314(3):1195-201.

197. DeWire SM, Yamashita DS, Rominger DH, Liu G, Cowan CL, Graczyk TM, Chen XT, Pitis PM, Gotchev D, Yuan C, Koblish M, Lark MW, Violin JD. A G protein-biased ligand at the μ-opioid receptor is potently analgesic with reduced gastrointestinal and respiratory dysfunction compared with morphine. J Pharmacol Exp Ther. 2013;344(3):708-17.

198. Schneider S, Provasi D, Filizola M. How Oliceridine (TRV-130) Binds and Stabilizes a μ-Opioid Receptor Conformational State That Selectively Triggers G Protein Signaling Pathways. Biochemistry. 2016;55(46):6456-6466.

199. FDA Approves New Opioid for Intravenous Use in Hospitals, Other Controlled Clinical Settings. FDA news release web site. https://www.fda.gov/news-events/press-announcements/fdaapproves-new-opioid-intrave nous-use-hospitals-ther-controlledclinical-settings (accessed Dec 3, 2020).

200. OLINVYK (oliceridine) injection, for intravenous use, CII. Olinvyk web site. https://olinvyk.com/docs/OLINVYK_Final_Label_Ver%20002_Nov2020_1103.pdf (accessed Dec 3, 2020).

201. Lambert D, Calo G. Approval of oliceridine (TRV130) for intravenous use in moderate to severe pain in adults. Br J Anaesth. 2020;125(6):e473-e474.

202. Gurevich VV, Gurevich EV. Biased GPCR signaling: Possible mechanisms and inherent limitations. Pharmacol Ther. 2020;211:107540.

203. Wingler LM, Skiba MA, McMahon C, Staus DP, Kleinhenz ALW, Suomivuori CM, Latorraca NR, Dror RO, Lefkowitz RJ, Kruse AC. Angiotensin and biased analogs induce structurally distinct active conformations within a GPCR. Science. 2020;367(6480):888-892.

204. Kenakin T, Christopoulos A. Signalling bias in new drug discovery: detection,

quantification and therapeutic impact. Nat Rev Drug Discov. 2013;12(3):205-16.

205. Hall DA, Giraldo J. A method for the quantification of biased signalling at constitutively active receptors. Br J Pharmacol. 2018;175(11):2046-2062.

206. Gillis A, Sreenivasan V, Christie MJ. Intrinsic Efficacy of Opioid Ligands and Its Importance for Apparent Bias, Operational Analysis, and Therapeutic Window. Mol Pharmacol. 2020;98(4):410-424.

207. Manglik A, Lin H, Aryal DK, McCorvy JD, Dengler D, Corder G, Levit A, Kling RC, Bernat V, Hübner H, Huang XP, Sassano MF, Giguère PM, Löber S, Da Duan, Scherrer G, Kobilka BK, Gmeiner P, Roth BL, Shoichet BK. Structure-based discovery of opioid analgesics with reduced side effects. Nature. 2016;537(7619):185-190.

208. Azzam AAH, McDonald J, Lambert DG. Hot topics in opioid pharmacology: mixed and biased opioids. Br J Anaesth. 2019;122(6):e136-e145.

209. Piekielna-Ciesielska J, Ferrari F, Calo' G, Janecka A. Cyclopeptide Dmt-[D-Lys-p-CF3-Phe-Phe-Asp]NH2, a novel G protein-biased agonist of the mu opioid receptor. Peptides. 2018;101:227-233.

210. Pasquinucci L, Turnaturi R, Calò G, Pappalardo F, Ferrari F, Russo G, Arena E, Montenegro L, Chiechio S, Prezzavento O, Parenti C. (2S)-N-2-methoxy-2-phenylethyl-6,7-benzomorphan compound (2S-LP2): Discovery of a biased mu/delta opioid receptor agonist. Eur J Med Chem. 2019;168:189-198.

211. Schmid CL, Kennedy NM, Ross NC, Lovell KM, Yue Z, Morgenweck J, Cameron MD, Bannister TD, Bohn LM. Bias Factor and Therapeutic Window Correlate to Predict Safer Opioid Analgesics. Cell. 2017;171(5):1165-1175.e13.

212. Grim TW, Acevedo-Canabal A, Bohn LM. Toward Directing Opioid Receptor Signaling to Refine Opioid Therapeutics. Biol Psychiatry. 2020;87(1):15-21.

213. de Waal PW, Shi J, You E, Wang X, Melcher K, Jiang Y, Xu HE, Dickson BM. Molecular mechanisms of fentanyl mediated β-arrestin biased signaling. PLoS Comput Biol. 2020;16(4):e1007394.

214. Lipiński PFJ, Jarończyk M, Dobrowolski JC, Sadlej J. Molecular dynamics of fentanyl bound to μ-opioid receptor. J Mol Model. 2019;25(5):144.

215. Morgan MM, Christie MJ. Analysis of opioid efficacy, tolerance, addiction and dependence from cell culture to human. Br J Pharmacol. 2011;164(4):1322-34.

216. Kelly E. Efficacy and ligand bias at the μ-opioid receptor. Br J Pharmacol. 2013;169(7):1430-46.

217. Filizola M, Devi LA. Structural biology: How opioid drugs bind to receptors. Nature. 2012;485(7398):314-7.

218. Carroll FI, Dolle RE. The discovery and development of the N-substituted trans-3,4-dimethyl-4-(3'-hydroxyphenyl)piperidine class of pure opioid receptor antagonists. ChemMedChem. 2014;9(8):1638-54.

219. Yuan Y, Zaidi SA, Elbegdorj O, Aschenbach LC, Li G, Stevens DL, Scoggins KL, Dewey WL, Selley DE, Zhang Y. Design, synthesis, and biological evaluation of 14-heteroaromatic-substituted naltrexone derivatives: pharmacological profile switch from mu opioid receptor selectivity to mu/kappa opioid receptor dual selectivity. J Med Chem. 2013;56(22):9156-69.

220. Fujita W, Gomes I, Devi LA. Revolution in GPCR signalling: opioid receptor heteromers as novel therapeutic targets: IUPHAR review 10. Br J Pharmacol. 2014;171(18):4155-76.

221. Lee CW, Ho IK. Pharmacological Profiles of Oligomerized μ-Opioid Receptors. Cells. 2013;2(4):689-714.

222. Shang Y, LeRouzic V, Schneider S, Bisignano P, Pasternak GW, Filizola M. Mechanistic insights into the allosteric modulation of opioid receptors by sodium ions. Biochemistry. 2014;53(31):5140-9.

223. Livingston KE, Traynor JR. Disruption of the Na+ ion binding site as a mechanism for positive allosteric modulation of the mu-opioid receptor. Proc Natl Acad Sci U S A. 2014;111(51):18369-74.

224. Rasmussen SG, Choi HJ, Fung JJ, Pardon E, Casarosa P, Chae PS, Devree BT, Rosenbaum DM, Thian FS, Kobilka TS, Schnapp A, Konetzki I, Sunahara RK, Gellman SH, Pautsch A, Steyaert J, Weis WI, Kobilka BK. Structure of a nanobody-stabilized active state of the β(2) adrenoceptor. Nature. 2011;469(7329):175-80.

225. Ring AM, Manglik A, Kruse AC, Enos MD, Weis WI, Garcia KC, Kobilka BK. Adrenaline-activated structure of β2-adrenoceptor stabilized by an engineered nanobody. Nature. 2013;502(7472):575-579.

226. Kruse AC, Ring AM, Manglik A, Hu J, Hu K, Eitel K, Hübner H, Pardon E, Valant C, Sexton PM, Christopoulos A, Felder CC, Gmeiner P, Steyaert J, Weis WI, Garcia KC, Wess J, Kobilka BK. Activation and allosteric modulation of a muscarinic acetylcholine receptor. Nature. 2013;504(7478):101-6.

227. Sounier R, Mas C, Steyaert J, Laeremans T, Manglik A, Huang W, Kobilka BK, Déméné H, Granier S. Propagation of conformational changes during μ-opioid receptor activation. Nature. 2015;524(7565):375-8.

228. Huang P, Visiers I, Weinstein H, Liu-Chen LY. The local environment at the cytoplasmic end of TM6 of the mu opioid receptor differs from those of rhodopsin and monoamine receptors: introduction of an ionic lock between the cytoplasmic ends of helices 3 and 6 by a L6.30(275)E mutation inactivates the mu opioid receptor and reduces the constitutive activity of its T6.34(279)K mutant. Biochemistry. 2002;41(40):11972-80.

229. Kaserer T, Lantero A, Schmidhammer H, Spetea M, Schuster D. μ Opioid receptor: novel antagonists and structural modeling. Sci Rep. 2016;6:21548.

230. Mansour A, Taylor LP, Fine JL, Thompson RC, Hoversten MT, Mosberg HI, Watson SJ, Akil H. Key residues defining the mu-opioid receptor binding pocket: a site-directed mutagenesis study. J Neurochem. 1997;68(1):344-53.

231. Xu W, Sanz A, Pardo L, Liu-Chen LY. Activation of the mu opioid receptor involves conformational rearrangements of multiple transmembrane domains. Biochemistry. 2008;47(40):10576-86.

232. Li JG, Chen C, Yin J, Rice K, Zhang Y, Matecka D, de Riel JK, DesJarlais RL, Liu-Chen LY. ASP147 in the third transmembrane helix of the rat mu opioid receptor forms ion-pairing with morphine and naltrexone. Life Sci. 1999;65(2):175-85.

233. Befort K, Tabbara L, Bausch S, Chavkin C, Evans C, Kieffer B. The conserved aspartate residue in the third putative transmembrane domain of the delta-opioid receptor is not the anionic counterpart for cationic opiate binding but is a constituent of the receptor binding

site. Mol Pharmacol. 1996;49(2):216-23.

234. James A, Williams J. Basic Opioid Pharmacology - An Update. Br J Pain. 2020;14(2):115-121.

235. Vardanyan RS, Hruby VJ. Fentanyl-related compounds and derivatives: current status and future prospects for pharmaceutical applications. Future Med Chem. 2014;6(4):385-412.

236. Grissinger M. Inappropriate Prescribing of Fentanyl Patches Is Still Causing Alarming Safety Problems. P T. 2010;35(12):653–4.

237. Schifano F, Chiappini S, Corkery JM, Guirguis A. Assessing the 2004-2018 Fentanyl Misusing Issues Reported to an International Range of Adverse Reporting Systems. Front Pharmacol. 2019;10:46.

238. Lyons PJ, Rivosecchi RM, Nery JP, Kane-Gill SL. Fentanyl-induced hyperalgesia in acute pain management. J Pain Palliat Care Pharmacother. 2015;29(2):153-60.

239. Warner M, Trinidad JP, Bastian BA, Minino AM, Hedegaard H. Drugs Most Frequently Involved in Drug Overdose Deaths: United States, 2010-2014. Natl Vital Stat Rep. 2016;65(10):1-15.

240. Skolnick P. The Opioid Epidemic: Crisis and Solutions. Annu Rev Pharmacol Toxicol. 2018;58:143-159.

241. Verhamme KMC, Bohnen AM. Are we facing an opioid crisis in Europe? Lancet Public Health. 2019;4(10):e483-e484.

242. Anselmi L, Jaramillo I, Palacios M, Huynh J, Sternini C. Ligand-induced μ opioid receptor internalization in enteric neurons following chronic treatment with the opiate fentanyl. J Neurosci Res. 2013;91(6):854-60.

243. Zheng H, Loh HH, Law PY. Beta-arrestin-dependent mu-opioid receptor-activated extracellular signal-regulated kinases (ERKs) Translocate to Nucleus in Contrast to G protein-dependent ERK activation. Mol Pharmacol. 2008;73(1):178-90.

244. Mori T, Kuzumaki N, Arima T, Narita M, Tateishi R, Kondo T, Hamada Y, Kuwata H, Kawata M, Yamazaki M, Sugita K, Matsuzawa A, Baba K, Yamauchi T, Higashiyama K, Nonaka M, Miyano K, Uezono Y, Narita M. Usefulness for the combination of G-protein- and β-arrestin-biased ligands of μ-opioid receptors: Prevention of antinociceptive tolerance. Mol Pain. 2017;13:1744806917740030.

245. Kovoor A, Celver JP, Wu A, Chavkin C. Agonist induced homologous desensitization of mu-opioid receptors mediated by G protein-coupled receptor kinases is dependent on agonist efficacy. Mol Pharmacol. 1998;54(4):704-11.

246. Burgueño J, Pujol M, Monroy X, Roche D, Varela MJ, Merlos M, Giraldo J. A Complementary Scale of Biased Agonism for Agonists with Differing Maximal Responses. Sci Rep. 2017;7(1):15389.

247. Vasudevan L, Vandeputte M, Deventer M, Wouters E, Cannaert A, Stove CP. Assessment of structure-activity relationships and biased agonism at the Mu opioid receptor of novel synthetic opioids using a novel, stable bio-assay platform. Biochem Pharmacol. 2020;177:113910.

248. Kalvass JC, Olson ER, Cassidy MP, Selley DE, Pollack GM. Pharmacokinetics and pharmacodynamics of seven opioids in P-glycoprotein-competent mice: assessment of

unbound brain EC50,u and correlation of in vitro, preclinical, and clinical data. J Pharmacol Exp Ther. 2007;323(1):346-55.

249. Bobeck EN, Haseman RA, Hong D, Ingram SL, Morgan MM. Differential development of antinociceptive tolerance to morphine and fentanyl is not linked to efficacy in the ventrolateral periaqueductal gray of the rat. J Pain. 2012;13(8):799-807.

250. Trescot AM, Datta S, Lee M, Hansen H. Opioid pharmacology. Pain Physician. 2008;11:133-53.

251. Gillis A, Gondin AB, Kliewer A, Sanchez J, Lim HD, Alamein C, Manandhar P, Santiago M, Fritzwanker S, Schmiedel F, Katte TA, Reekie T, Grimsey NL, Kassiou M, Kellam B, Krasel C, Halls ML, Connor M, Lane JR, Schulz S, Christie MJ, Canals M. Low intrinsic efficacy for G protein activation can explain the improved side effect profiles of new opioid agonists. Sci Signal. 2020;13(625):eaaz3140.

252. Stahl EL, Bohn LM. Low Intrinsic Efficacy Alone Cannot Explain the Improved Side Effect Profiles of New Opioid Agonists. Biochemistry. 2021, Sep 1.

253. Changeux JP, Edelstein S. Conformational selection or induced fit? 50 years of debate resolved. F1000 Biol Rep. 2011;3:19.

254. Giraldo J. Agonist induction, conformational selection, and mutant receptors. FEBS Lett. 2004;556(1-3):13-8.

255. Tehan BG, Bortolato A, Blaney FE, Weir MP, Mason JS. Unifying family A GPCR theories of activation. Pharmacol Ther. 2014;143(1):51-60.

256. Rosenbaum DM, Rasmussen SG, Kobilka BK. The structure and function of G-protein-coupled receptors. Nature. 2009;459(7245):356-63.

257. Trzaskowski B, Latek D, Yuan S, Ghoshdastider U, Debinski A, Filipek S. Action of molecular switches in GPCRs--theoretical and experimental studies. Curr Med Chem. 2012;19(8):1090-109.

258. Vogel R, Mahalingam M, Lüdeke S, Huber T, Siebert F, Sakmar TP. Functional role of the "ionic lock"--an interhelical hydrogen-bond network in family A heptahelical receptors. J Mol Biol. 2008;380(4):648-55.

259. Díaz Ó, Dalton JAR, Giraldo J. Revealing the Mechanism of Agonist-Mediated Cannabinoid Receptor 1 (CB1) Activation and Phospholipid-Mediated Allosteric Modulation. J Med Chem. 2019;62(11):5638-5654.

260. Bruzzese A, Dalton JAR, Giraldo J. Insights into adenosine A2A receptor activation through cooperative modulation of agonist and allosteric lipid interactions. PLoS Comput Biol. 2020;16(4):e1007818.

261. Yuan S, Filipek S, Palczewski K, Vogel H. Activation of G-protein-coupled receptors correlates with the formation of a continuous internal water pathway. Nat Commun. 2014;5:4733.

262. Tomobe K, Yamamoto E, Kholmurodov K, Yasuoka K. Water permeation through the internal water pathway in activated GPCR rhodopsin. PLoS One. 2017;12(5):e0176876.

263. Venkatakrishnan AJ, Ma AK, Fonseca R, Latorraca NR, Kelly B, Betz RM, Asawa C, Kobilka BK, Dror RO. Diverse GPCRs exhibit conserved water networks for stabilization and activation. Proc Natl Acad Sci U S A. 2019;116(8):3288-3293.

264. Kaya AI, Perry NA, Gurevich VV, Iverson TM. Phosphorylation barcode-dependent

signal bias of the dopamine D1 receptor. Proc Natl Acad Sci U S A. 2020;117(25):14139-14149.

265. Celver JP, Lowe J, Kovoor A, Gurevich VV, Chavkin C. Threonine 180 is required for G-protein-coupled receptor kinase 3- and beta-arrestin 2-mediated desensitization of the mu-opioid receptor in Xenopus oocytes. J Biol Chem. 2001;276(7):4894-900.

266. Zhou B, Hall DA, Giraldo J. Can Adding Constitutive Receptor Activity Redefine Biased Signaling Quantification? Trends Pharmacol Sci. 2019;40(3):156-160.

267. Söldner CA, Horn AHC, Sticht H. A Metadynamics-Based Protocol for the Determination of GPCR-Ligand Binding Modes. Int J Mol Sci. 2019;20(8):1970.

268. Bruzzese A, Dalton JAR, Giraldo J. Statistics for the analysis of molecular dynamics simulations: providing P values for agonist-dependent GPCR activation. Sci Rep. 2020;10(1):19942.

269. Seifert R, Wenzel-Seifert K. Constitutive activity of G-protein-coupled receptors: cause of disease and common property of wild-type receptors. Naunyn Schmiedebergs Arch Pharmacol. 2002;366(5):381-416.

270. Serohijos AW, Yin S, Ding F, Gauthier J, Gibson DG, Maixner W, Dokholyan NV, Diatchenko L. Structural basis for μ-opioid receptor binding and activation. Structure. 2011;19(11):1683-90.

271. Berríos-Cárcamo P, Quintanilla ME, Herrera-Marschitz M, Vasiliou V, Zapata-Torres G, Rivera-Meza M. Racemic Salsolinol and its Enantiomers Act as Agonists of the μ-Opioid Receptor by Activating the Gi Protein-Adenylate Cyclase Pathway. Front Behav Neurosci. 2017;10:253.

272. Subramanian G, Paterlini MG, Portoghese PS, Ferguson DM. Molecular docking reveals a novel binding site model for fentanyl at the mu-opioid receptor. J Med Chem. 2000;43(3):381-91.

273. Jarończyk M, Lipiński PFJ, Dobrowolski JC, Sadlej J. The FMO analysis of the molecular interaction of fentanyl derivatives with the μ-opioid receptor. Chem Pap. 2017;71:1429.

274. Ellis CR, Kruhlak NL, Kim MT, Hawkins EG, Stavitskaya L. Predicting opioid receptor binding affinity of pharmacologically unclassified designer substances using molecular docking. PLoS One. 2018;13(5):e0197734.

275. Dosen-Micovic L, Ivanovic M, Micovic V. Steric interactions and the activity of fentanyl analogs at the mu-opioid receptor. Bioorg Med Chem. 2006;14(9):2887-95.

276. Gentilucci L, Tolomelli A, De Marco R, Artali R. Molecular docking of opiates and opioid peptides, a tool for the design of selective agonists and antagonists, and for the investigation of atypical ligand-receptor interactions. Curr Med Chem. 2012;19(11):1587-601.

277. Xu H, Lu YF, Partilla JS, Zheng QX, Wang JB, Brine GA, Carroll FI, Rice KC, Chen KX, Chi ZQ, Rothman RB. Opioid peptide receptor studies, 11: involvement of Tyr148, Trp318 and His319 of the rat mu-opioid receptor in binding of mu-selective ligands. Synapse. 1999;32(1):23-8.

278. Yan F, Mosier PD, Westkaemper RB, Stewart J, Zjawiony JK, Vortherms TA, Sheffler DJ, Roth BL. Identification of the molecular mechanisms by which the diterpenoid

salvinorin A binds to kappa-opioid receptors. Biochemistry. 2005;44(24):8643-51.

279. Zhang P, Johnson PS, Zöllner C, Wang W, Wang Z, Montes AE, Seidleck BK, Blaschak CJ, Surratt CK. Mutation of human mu opioid receptor extracellular "disulfide cysteine" residues alters ligand binding but does not prevent receptor targeting to the cell plasma membrane. Brain Res Mol Brain Res. 1999;72(2):195-204.

280. Roche D, van der Graaf PH, Giraldo J. Have many estimates of efficacy and affinity been misled? Revisiting the operational model of agonism. Drug Discov Today. 2016;21(11):1735-1739.

281. Sader S , Anant K , Wu C . To probe interaction of morphine and IBNtxA with 7TM and 6TM variants of the human μ-opioid receptor using all-atom molecular dynamics simulations with an explicit membrane. Phys Chem Chem Phys. 2018;20(3):1724-1741.

282. Della Longa S, Arcovito A. "In silico" study of the binding of two novel antagonists to the nociceptin receptor. J Comput Aided Mol Des. 2018;32(2):385-400.

283. Fowler CB, Pogozheva ID, Lomize AL, LeVine H 3rd, Mosberg HI. Complex of an active mu-opioid receptor with a cyclic peptide agonist modeled from experimental constraints. Biochemistry. 2004;43(50):15796-810.

284. Tryoen-Tóth P, Décaillot FM, Filliol D, Befort K, Lazarus LH, Schiller PW, Schmidhammer H, Kieffer BL. Inverse agonism and neutral antagonism at wild-type and constitutively active mutant delta opioid receptors. J Pharmacol Exp Ther. 2005;313(1):410-21.

7. Supplementary Information

```
mGlu1     1 IPVRYLEWSNIESIIAIAFSCLGILVTLFVTLIFVLYRDTPVVKSSSRELCYIILAGIFL
mGlu2     1 LPQEYIRWGDAWAVGPVTIACLGALATLFVLGVFVRHNATPVVKASGRELCYILLGGVFL

mGlu1    61 GYVCPFTLIAKPTTTSCYLQRLLVGLSSAMCYSALVTKTNRIARILAGSKKKICTRKPRF
mGlu2    61 CYCMTFIFIAKPSTAVCTLRRLGLGTAFSVCYSALLTKTNRIARIFGGAREGA--QRPRF

mGlu1   121 MSAWAQVIIASILISVQLTLVVTLIIMEPPMPILSYPSI--KEVYLICNTSNLGVVAPLG
mGlu2   119 ISPASQVAICLALISGQLLIVVAWLVVEAPGTGKETAPERREVVTLRCNHRDASMLGSLA

mGlu1   179 YNGLLIMSCTYYAFKTRNVPANFNEAKYIAFTMYTTCIIWLAFVPIYFGSNY----KIIT
mGlu2   179 YNVLLIALCTLYAFKTRKCPENFNEAKFIGFTMYTTCIIWLAFLPIFYVTSSDYRVQTTT

mGlu1   235 TCFAVSLSVTVALGCMFTPKMYIIIAKPERNV
mGlu2   239 MCVSVSLSGSVVLGCLFAPKLHIILFQPQKNV
```

Supplementary Figure 1. Sequence alignment between mGlu1R-mGlu2R. Transmembrane domains (TMDs) of mGlu1R (template) and mGlu2R (target) have 50% sequence identity between them.
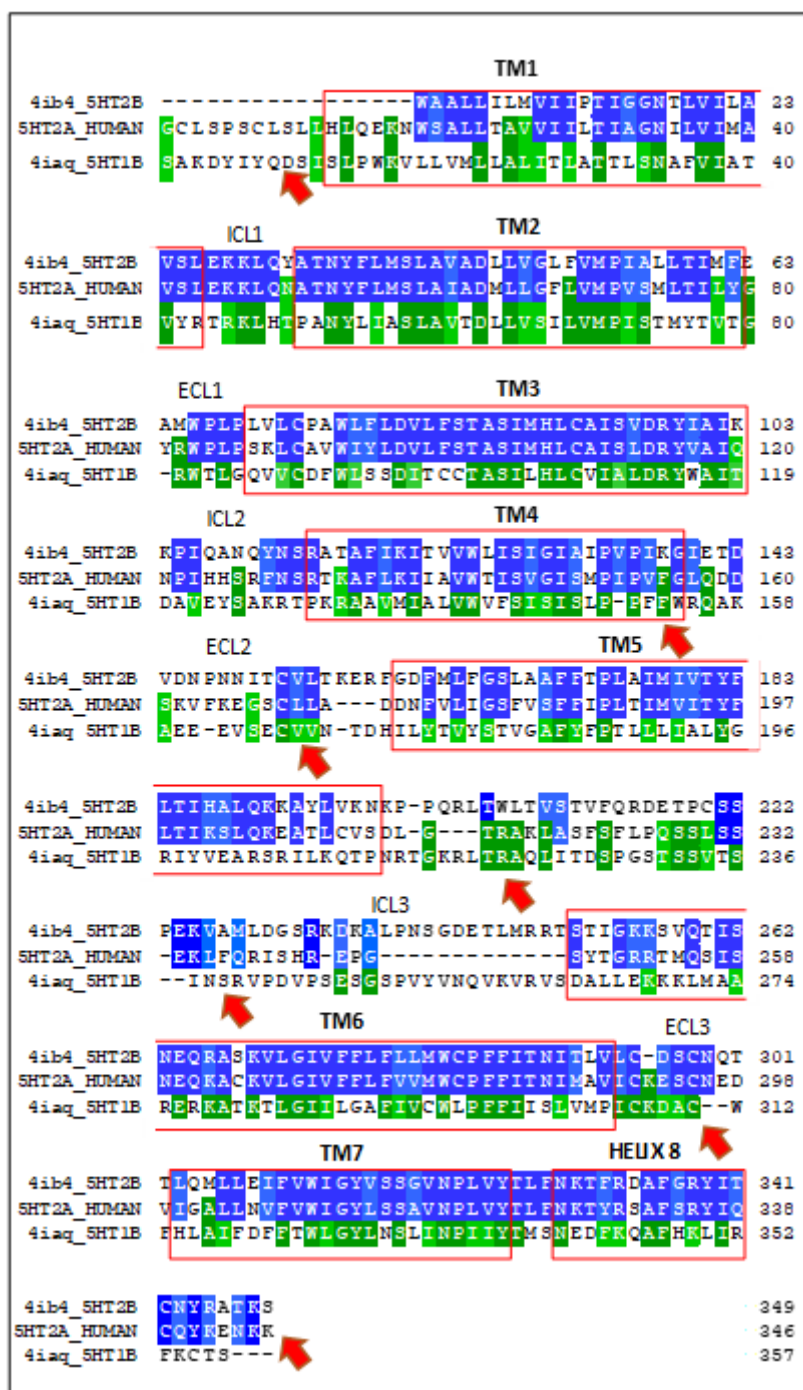
Supplementary Figure 2. Manually refined multiple sequence alignment of 5-HT$_{2A}$R. Identical residues are indicated with dark colours: dark blue for 5-HT$_{2B}$R receptor and dark-green for 5-HT$_{1B}$R receptor. Similar residues are marked with light colours: light blue for 5-HT$_{2B}$R receptor and light green for 5-HT$_{1B}$R receptor. TMs are shown with red boxes and areas requiring manual alignment (N-terminus, TM4, ECL2, ICL3, ECL3 and C-terminus) are indicated with red arrows.
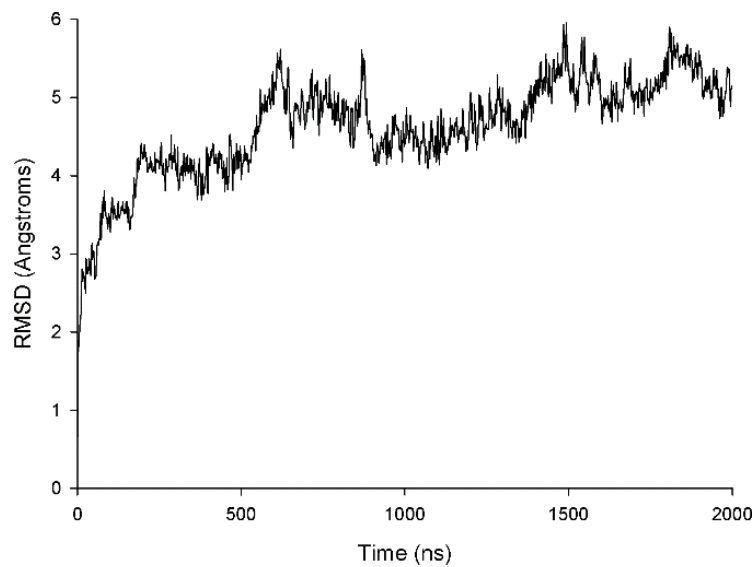
Supplementary Figure 3. RMSD of AT1R/A2AR heterotetramer (Cα atoms) over MD simulation.
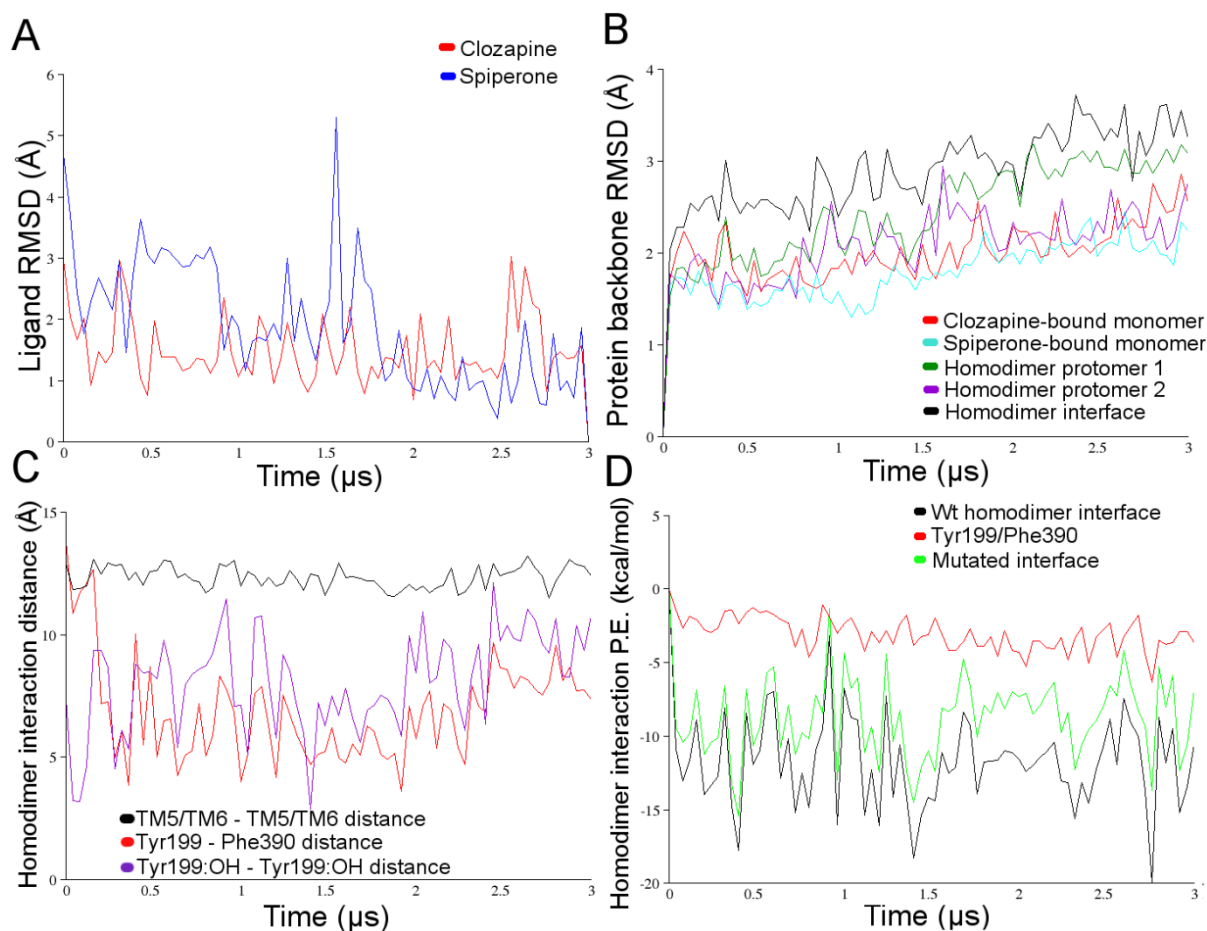
Supplementary Figure 4. a) Conformational stability of bound clozapine or spiperone (red and blue, respectively) in terms of RMSD compared against the last conformation achieved during MD simulations. b) Conformational change of the backbone of transmembrane domain of D2R monomer with bound clozapine or spiperone, and protomer 1 or 2 and TM5-TM6-TM5-TM6 interface of D2R homodimer (red, blue, purple, green and black, respectively) compared against initial conformation. c) Distance between centre of mass (COM) of interacting transmembrane hélices (TM5 and TM6, in black), closer distance between residues Tyr199$^{5.48}$ and Phe390$^{6.52}$ (in red), and distance between sidechain oxygen atoms of Tyr199$^{5.48}$ of both protomers (in purple). d) Energetic analysis of *wt* TM5-TM6-TM5- TM6 D2R homodimer interface, specific energetic contribution of interactions between Tyr199$^{5.48}$ and Phe390$^{6.52}$, and mutated D2R homodimer interface (Tyr199$^{5.48}$ and Phe390$^{6.52}$ replaced with alanine), coloured in black, red and green, respectively.
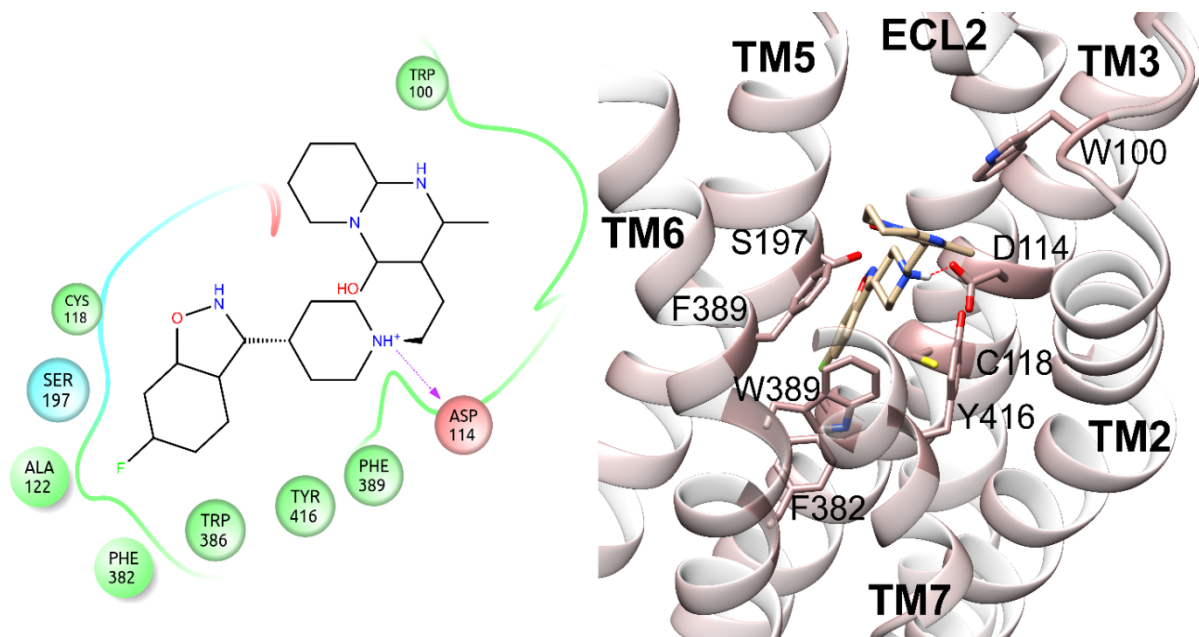
Supplementary Figure 5. Crystallized orthosteric binding pose of risperidone. 2D and 3D binding pose defined by residues close-contacted (<3.5 Å) by risperidone (tan) in D2R crystal structure (brown, PDBid: 6CM4).
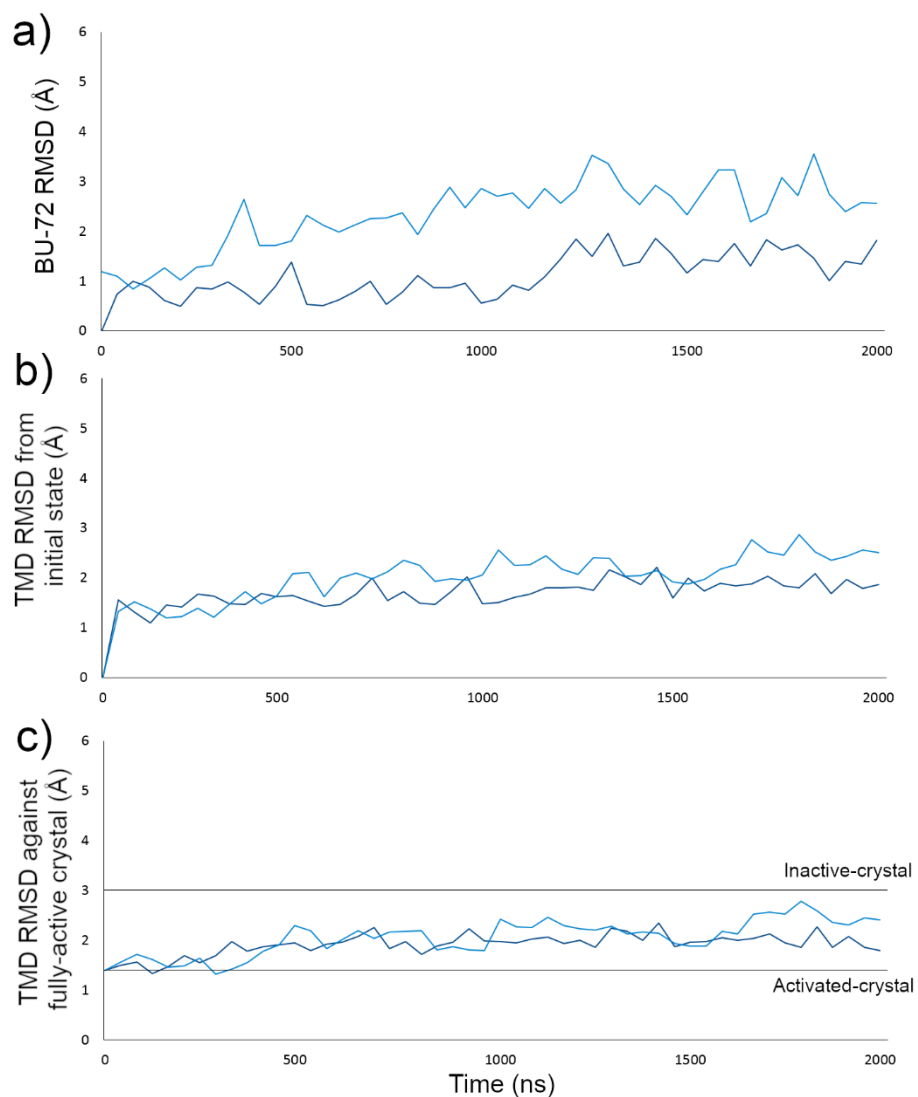
Supplementary Figure 6. Stability of BU-72 bound in activated hMOR model during control MD simulations. Plots showing stability in terms of RMSD of **a)** ligand, and TM domain with respect to: **b)** initial receptor conformation or c) fully-active crystal structure. Shades of blue represent replicas #1 and #2 of BU-72-bound activated hMOR state. Straight-lines indicate crystallized activated or inactive conformations with respect to fully-active crystal structure.
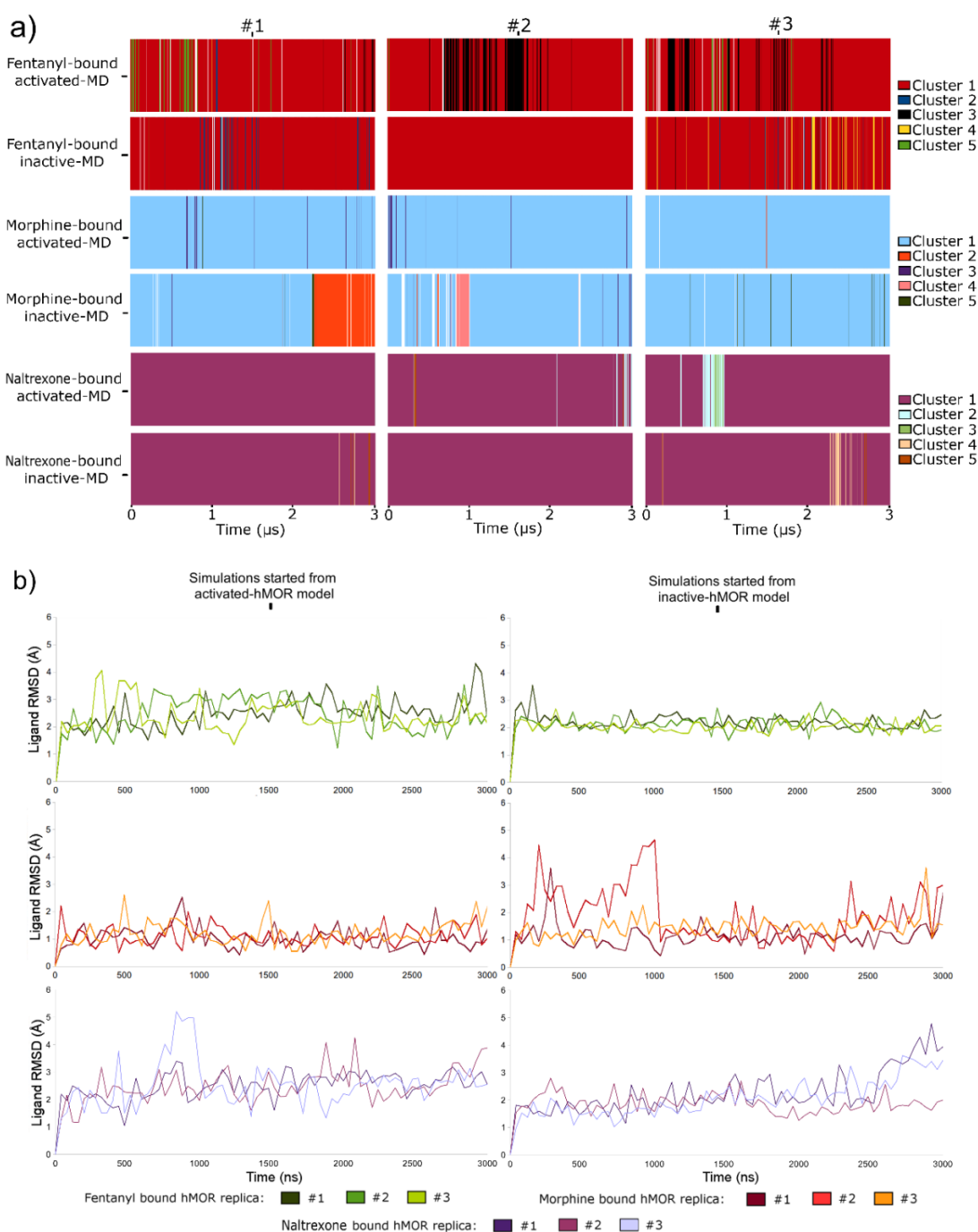
Supplementary Figure 7. Morphine, fentanyl and naltrexone conformational clustering and RMSD in MD simulations. **a)** Morphine, fentanyl and naltrexone poses observed over respective trajectories of each replica starting from activated or inactive receptor states with bound fentanyl, morphine or naltrexone, classified into 5 different clusters, using a cutoff of 2.0 Å between groups, with cluster 1 predominant in each case (fentanyl, morphine or naltrexone clusters #1-5 in: i) red, dark blue, black, yellow and light green, ii) light blue, orange, purple, salmon and dark green, or in iii) mauve, sky blue, pale green, khaki, brown; respectively). **b)** Plots showing ligand physical stability in terms of RMSD for replicas #1-3 of bound fentanyl, morphine or naltrexone (shades of green, red or purple, top, mid or bottom rows, respectively) starting from activated or inactive state (left or right, respectively).
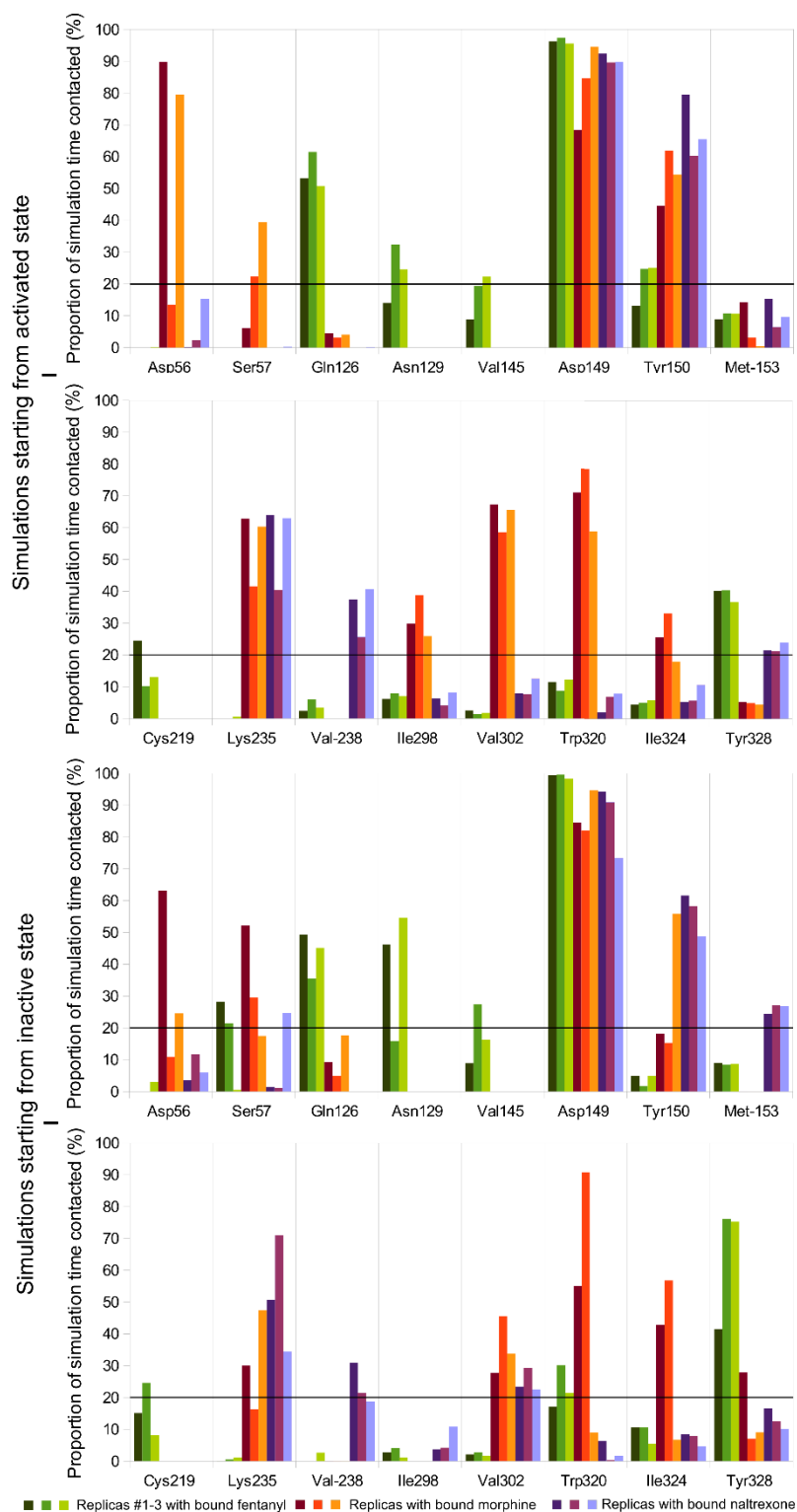
Supplementary Figure 8. Proportion of residues in close contact with morphine, fentanyl and naltrexone in MD simulations. Residues of hMOR orthosteric pocket closely contacted (<3.5 Å, with at least two trajectories with a contact frequency >20.0%, independently of the initial state) by fentanyl, morphine or naltrexone in replicas #1-3 (shades of green, red or purple, respectively) of MD simulations starting from activated or inactive state.

Supplementary Table 1. Average and SD of metrics: average protein RMSD from i) initial state or ii) with respect to fully active crystal, average iii) TM3 upward, iv) TM5 inward, v) TM6 outward or vi) NPxxY inward movement with respect to protein centre (normalized by inactive crystal structure), or vii) average distance between Arg167[3.50]-Thr281[6.34] of each replica #1-3 starting from activated or inactive receptor state with either fentanyl, morphine or naltrexone bound.

| Metric (threshold)	Replicas	Fentanyl bound	Morphine bound	Naltrexone bound
Average protein RMSD from initial state (±3.5 Å)				
Starting from activated hMOR	Replica #1	3.2 Å (0.2 SD)	3.5 Å (0.3 SD)	3.8 Å (0.2 SD)
	Replica #2	3.5 Å (0.4 SD)	3.1 Å (0.5 SD)	4.1 Å (0.3 SD)
	Replica #3	3.3 Å (0.2 SD)	3.1 Å (0.2 SD)	3.8 Å (0.3 SD)
Starting from inactive hMOR	Replica #1	3.1 Å (0.2 SD)	3.2 Å (0.3 SD)	3.0 Å (0.2 SD)
	Replica #2	2.9 Å (0.2 SD)	2.4 Å (0.2 SD)	2.5 Å (0.2 SD)
	Replica #3	2.8 Å (0.3 SD)	2.9 Å (0.2 SD)	3.0 Å (0.3 SD)
Average protein RMSD from fully active crystal (±3.0 Å)				
Starting from activated hMOR	Replica #1	2.9 Å (0.2 SD)	2.4 Å (0.2 SD)	2.8 Å (0.2 SD)
	Replica #2	2.9 Å (0.3 SD)	2.3 Å (0.2 SD)	3.4 Å (0.4 SD)
	Replica #3	2.4 Å (0.2 SD)	2.4 Å (0.4 SD)	2.9 Å (0.2 SD)
Starting from inactive hMOR	Replica #1	4.3 Å (0.2 SD)	4.0 Å (0.3 SD)	3.6 Å (0.2 SD)
	Replica #2	3.8 Å (0.5 SD)	3.5 Å (0.2 SD)	3.2 Å (0.2 SD)
	Replica #3	3.7 Å (0.3 SD)	4.0 Å (0.2 SD)	3.7 Å (0.3 SD)
Average TM3 upward movement (+0.3 Å)				
Starting from activated hMOR	Replica #1	+0.4 Å (0.2 SD)	+0.2 Å (0.2 SD)	+0.4 Å (0.2 SD)
	Replica #2	+0.5 Å (0.3 SD)	+0.3 Å (0.2 SD)	-0.5 Å (0.3 SD)
	Replica #3	+0.6 Å (0.2 SD)	+0.2 Å (0.3 SD)	+0.1 Å (0.2 SD)
Starting from inactive hMOR	Replica #1	+0.1 Å (0.2 SD)	+0.3 Å (0.2 SD)	+0.3 Å (0.2 SD)
	Replica #2	-0.1 Å (0.2 SD)	+0.6 Å (0.2 SD)	+0.6 Å (0.2 SD)
	Replica #3	-0.4 Å (0.3 SD)	+0.2 Å (0.2 SD)	+0.1 Å (0.2 SD)
Average TM5 inward movement (-0.8 Å)				
Starting from activated hMOR	Replica #1	-1.7 Å (0.5 SD)	-1.5 Å (0.4 SD)	-0.3 Å (0.4 SD)
	Replica #2	-1.4 Å (0.4 SD)	-1.3 Å (0.4 SD)	+1.8 Å (0.9 SD)
	Replica #3	-1.3 Å (0.2 SD)	-1.2 Å (0.6 SD)	+0.2 Å (0.6 SD)
Starting from inactive hMOR	Replica #1	+0.9 Å (0.4 SD)	-0.5 Å (0.9 SD)	+0.8 Å (0.4 SD)
	Replica #2	+0.8 Å (0.4 SD)	-1.5 Å (0.8 SD)	-0.4 Å (0.9 SD)
	Replica #3	+1.7 Å (0.4 SD)	+0.7 Å (0.5 SD)	+0.4 Å (0.5 SD)
Average TM6 outward movement (+1.7 Å)				
Starting from activated hMOR	Replica #1	+3.3 Å (0.8 SD)	+3.4 Å (0.6 SD)	+0.7 Å (0.5 SD)
	Replica #2	+3.7 Å (0.5 SD)	+3.6 Å (0.5 SD)	+1.2 Å (0.7 SD)
	Replica #3	+3.4 Å (0.5 SD)	+3.3 Å (0.6 SD)	+0.6 Å (0.5 SD)
Starting from inactive hMOR	Replica #1	+0.8 Å (0.4 SD)	+0.5 Å (0.5 SD)	+1.0 Å (0.4 SD)
	Replica #2	+1.0 Å (0.5 SD)	+0.5 Å (0.4 SD)	+0.4 Å (0.5 SD)
	Replica #3	+1.6 Å (0.7 SD)	+0.3 Å (0.4 SD)	+0.6 Å (0.5 SD)
Average NPxxY inward movement (-0.8 SD)				
Starting from activated hMOR	Replica #1	-2.9 Å (0.7 SD)	-2.6 Å (0.6 SD)	+0.0 Å (0.5 SD)
	Replica #2	-2.3 Å (0.3 SD)	-2.4 Å (0.3 SD)	-2.4 Å (0.6 SD)
	Replica #3	-2.4 Å (0.5 SD)	-2.8 Å (0.5 SD)	-0.2 Å (0.8 SD)
Starting from inactive hMOR	Replica #1	-1.3 Å (0.3 SD)	-1.5 Å (0.3 SD)	+0.2 Å (0.3 SD)
	Replica #2	-1.1 Å (0.3 SD)	-0.0 Å (0.3 SD)	-0.1 Å (0.3 SD)
	Replica #3	-1.9 Å (0.7 SD)	+0.3 Å (0.4 SD)	+0.4 Å (0.4 SD)
Average Arg-Thr distance (±10 Å)				
Starting from activated hMOR	Replica #1	12.2 Å (0.7 SD)	12.5 Å (0.8 SD)	7.4 Å (0.5 SD)
	Replica #2	13.6 Å (0.6 SD)	13.4 Å (0.7 SD)	6.3 Å (0.6 SD)
	Replica #3	13.3 Å (0.6 SD)	12.7 Å (1.0 SD)	6.3 Å (0.6 SD)
Starting from inactive hMOR	Replica #1	6.2 Å (0.5 SD)	6.6 Å (0.6 SD)	6.2 Å (0.4 SD)
	Replica #2	6.1 Å (0.3 SD)	6.6 Å (0.4 SD)	6.3 Å (0.4 SD)
	Replica #3	8.0 Å (1.1 SD)	6.0 Å (0.2 SD)	6.1 Å (0.3 SD)
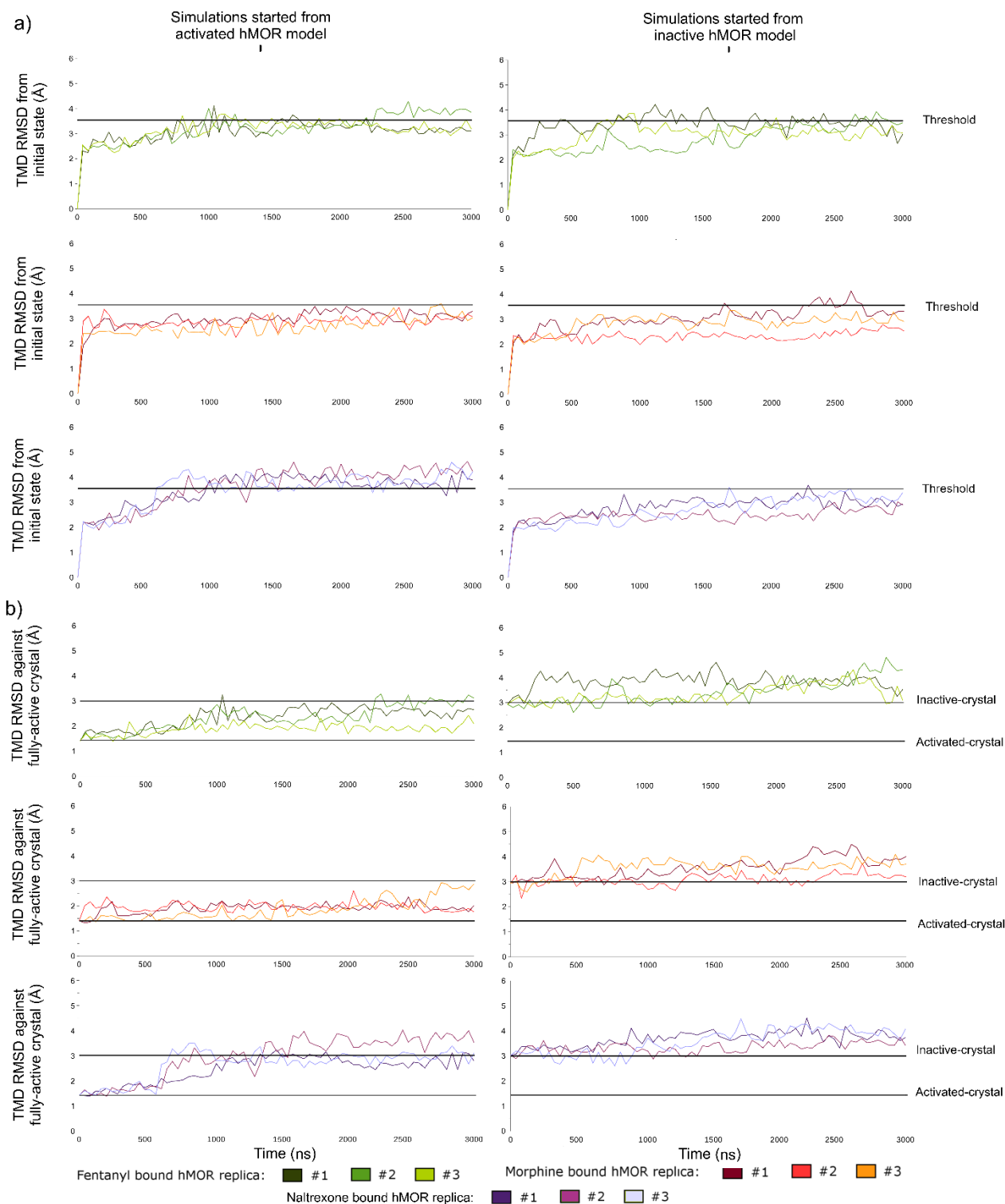
Supplementary Figure 9. Entire TMD receptor conformational change. TM domain RMSD with respect to: **a)** initial receptor conformation or **b)** fully-active crystal. Green, red or purple shades represent replicas #1-3 with bound fentanyl, morphine or naltrexone, respectively, in MD simulations starting from activated or inactive state (left or right columns, respectively). Straight-lines indicate 3.5 Å threshold of conformational change with respect to fully-active crystal or initial state of activated and inactive crystal structures.
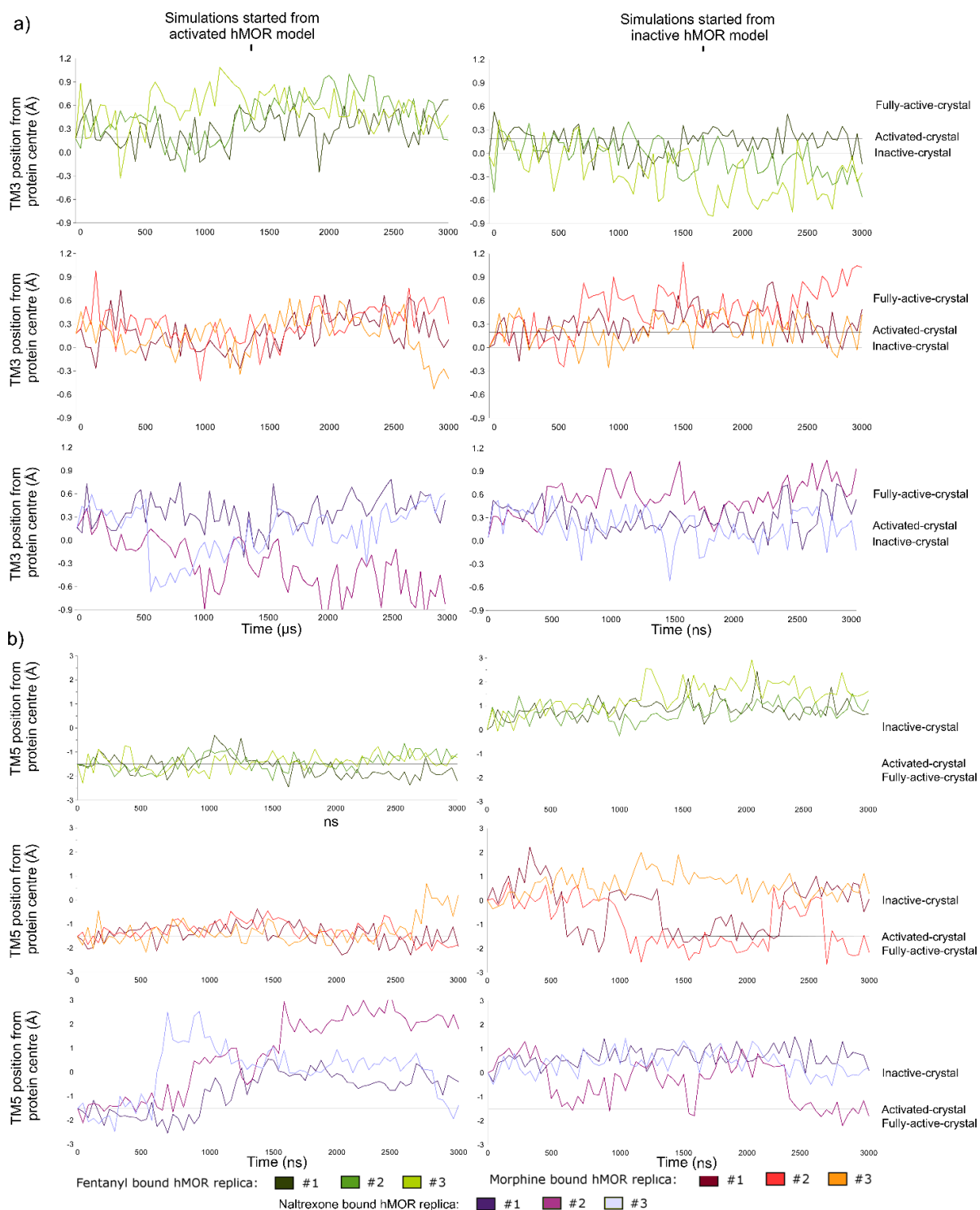
Supplementary Figure 10. TM helix movement with respect to protein centre in MD simulations I. As a function of time, and normalized by inactive crystal position, **a)** TM3 z-offset vertical movement, and **b)** distance between protein centre and intracellular tip of TM5, in replicas #1-3 with bound fentanyl, morphine or naltrexone (green, red or purple shades, respectively) starting from activated or inactive state (respective left or right columns). Flat-lines indicate respective metrics measured in fully-active, activated and inactive crystals.
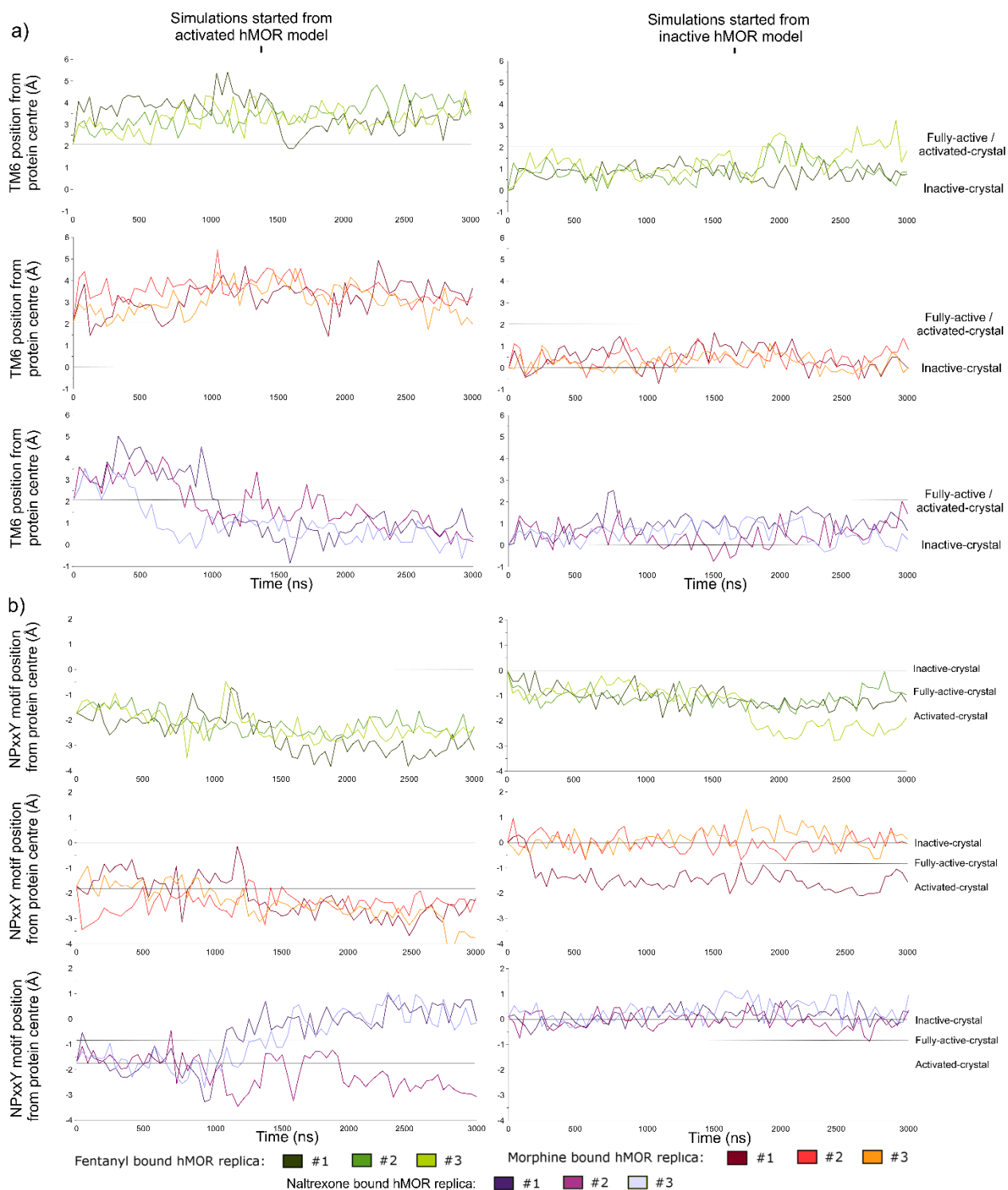
Supplementary Figure 11. TM helix movement with respect to protein centre in MD simulations II. As a function of time, and normalized by inactive crystal position, distance between protein centre and **a)** intracellular tip of TM6, or **b)** NPxxY motif, in replicas #1-3 with bound fentanyl, morphine or naltrexone (green, red or purple shades, respectively) starting from activated or inactive state (respective left or right columns). Flat-lines indicate respective metrics measured in fully-active, activated and inactive crystals.
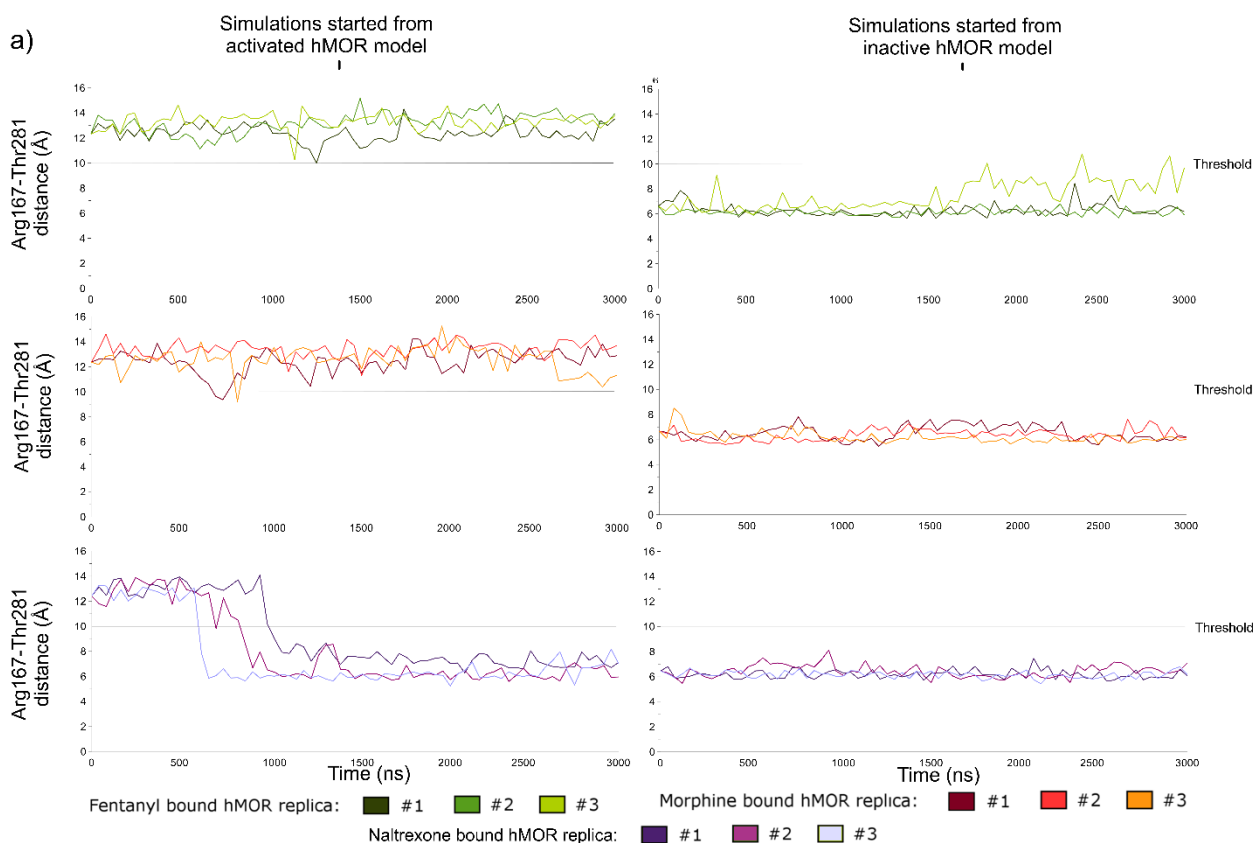
Supplementary Figure 12. Intracellular Arg167$^{3.50}$-Thr281$^{6.34}$ distance in MD simulations. As a function of time, **a)** intracellular Arg167$^{3.50}$-Thr281$^{6.34}$ distance in MD simulations starting from activated or inactive state (left or right columns, respectively). Green, red or purple shades represent replicas #1-3 with bound fentanyl, morphine or naltrexone, respectively. Straight lines indicate the thresholds dividing active- from inactive-like conformations.

140
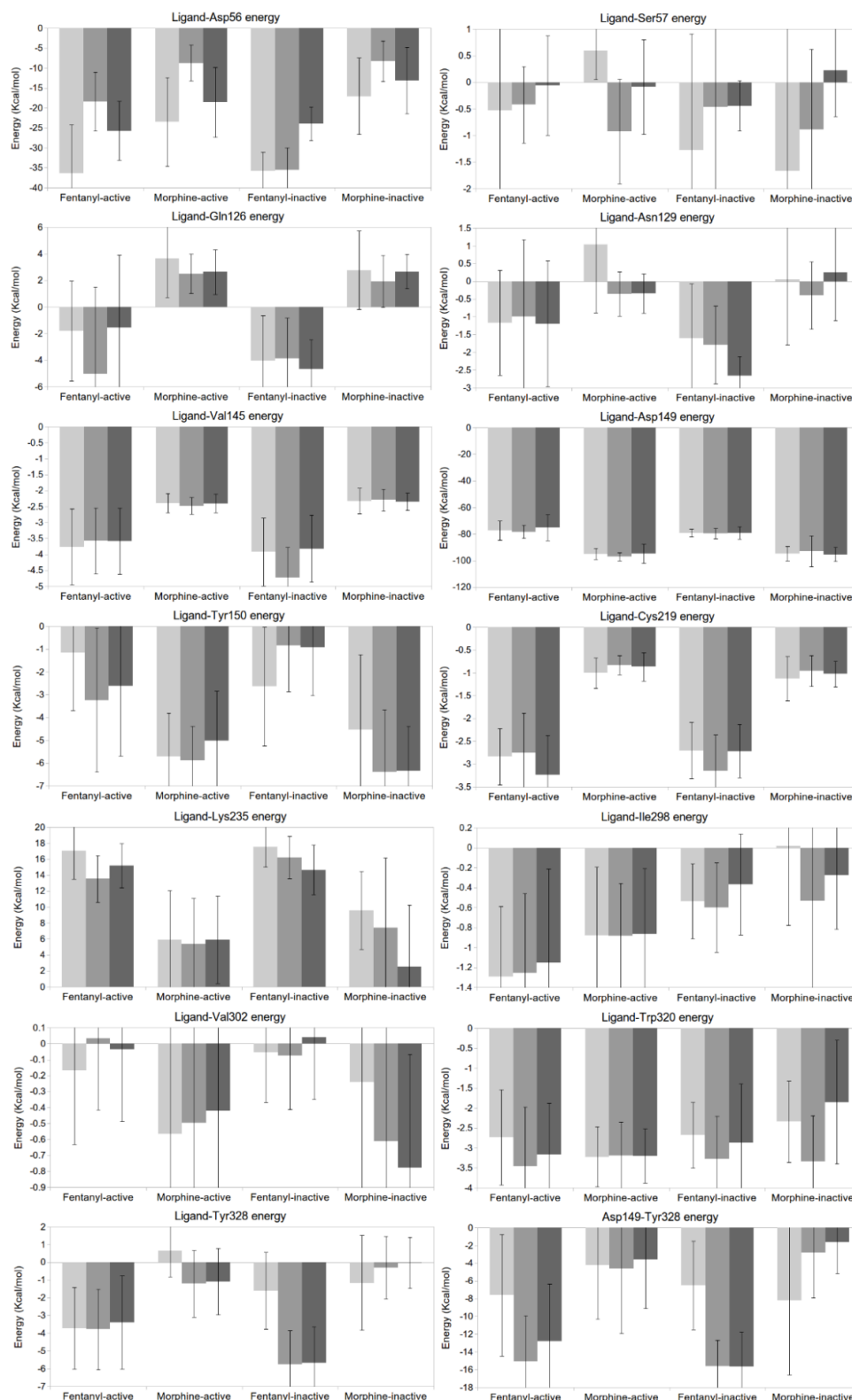
Supplementary Figure 13. Average potential energy per replica of protein-ligand and sidechain-sidechain interactions in MD simulations. Different shades of grey show average potential energy and standard deviation of relevant interactions closely contacted by fentanyl or morphine in replicas #1-3 starting from activated or inactive state, and the potential energy of Asp149[3.32]-Tyr328[7.43] interaction.
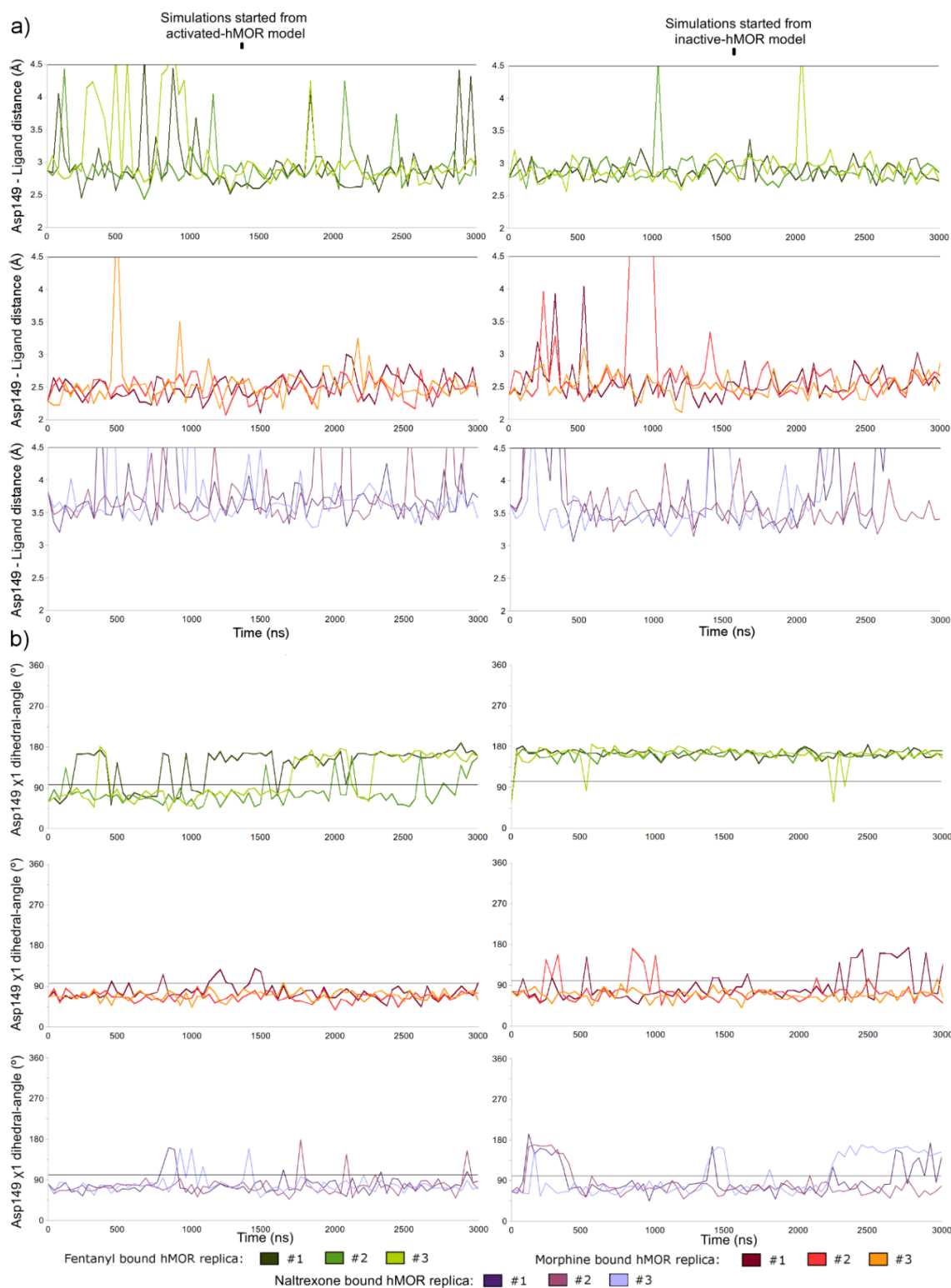
Supplementary Figure 14. Ligand-Asp149$^{3.32}$ and TM3-TM7 interaction in MD simulations. As a function of time, replicas #1-3 with bound fentanyl, morphine or naltrexone (shades of green, red or purple, respectively) starting from activated or inactive states of hMOR (left or right columns, respectively) showing **a)** interaction distance (<4.5 Å) between Asp149$^{3.32}$ and each ligand amine group, or **b)** Asp149$^{3.32}$ χ1 dihedral angle. Straight lines represent thresholds of interaction formation distance of 4.5 Å or Asp149$^{3.32}$ χ1 dihedral angle of 115º.

142
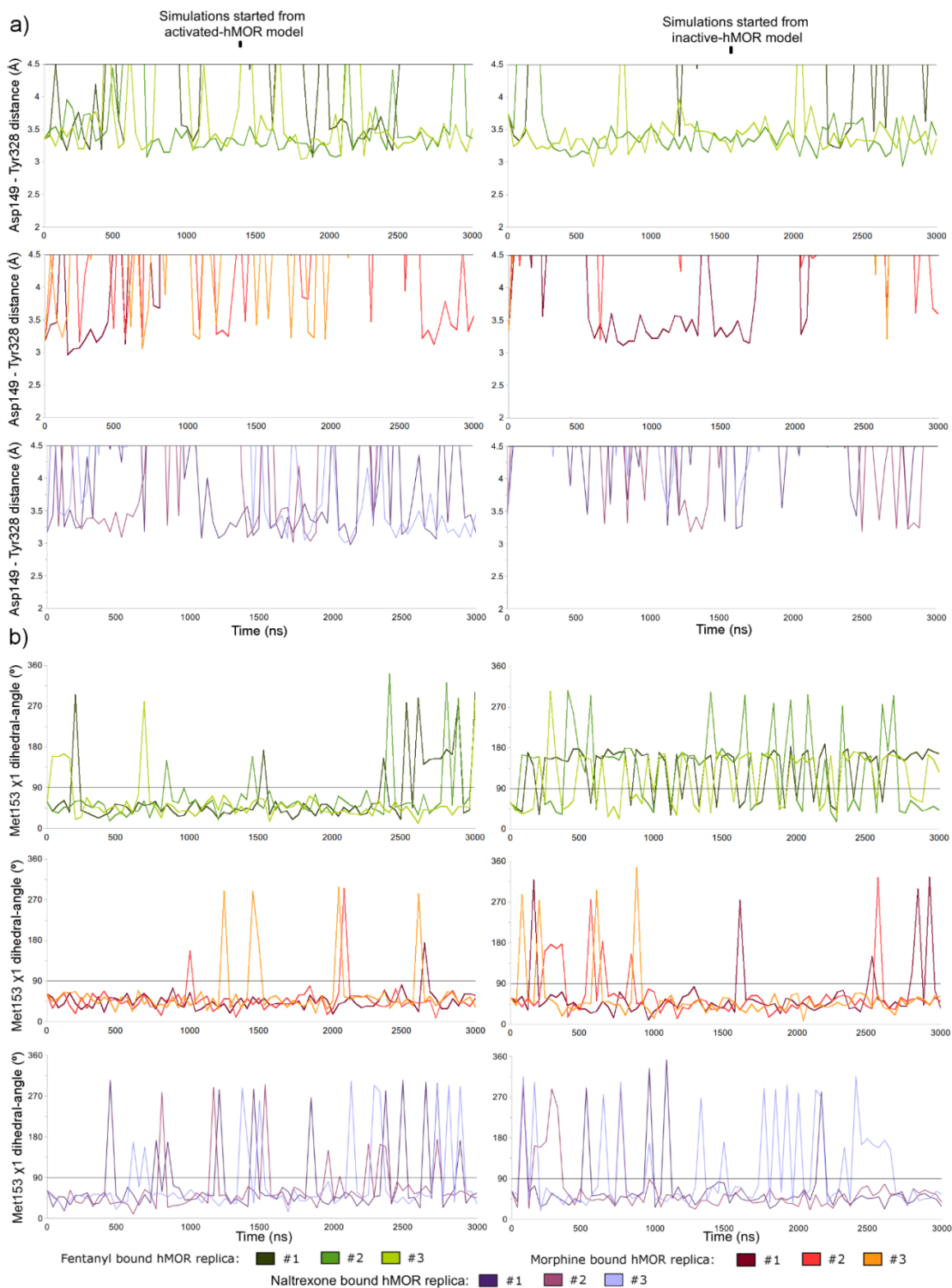
Supplementary Figure 15. Met153[3.36] conformational change in MD simulations. As a function of time, **a)** Asp149[3.32]-Tyr328[7.43] distance fluctuation within interaction formation distance (<4.5 Å), and **b)** Met153[3.36] χ1 dihedral angle, of replicas #1-3 with bound fentanyl, morphine or naltrexone (top, mid and bottom rows, green red or purple shades, respectively) starting from activated or inactive hMOR state (left or right columns, respectively). Straight lines represent thresholds of 4.5 Å or 90º for interaction formation distance or Met153[3.36] χ1 dihedral angle, respectively.

143
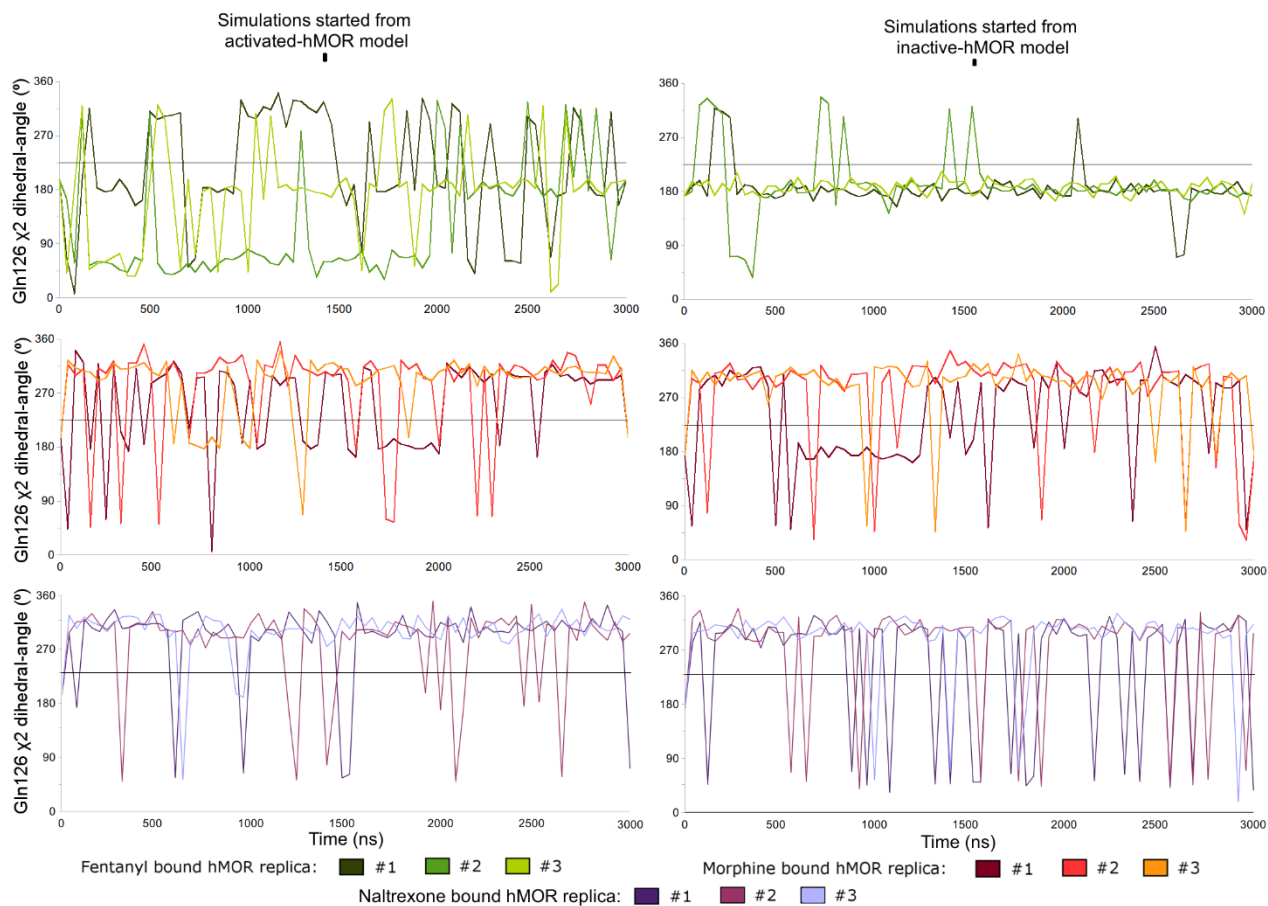
Supplementary Figure 16. Gln126[2.60] conformational change in MD simulations. Graphs showing as a function of time Gln126[2.60] χ2 dihedral angle conformational change of replicas #1-3 starting from activated or inactive state (left or right columns, respectively) with bound fentanyl, morphine or naltrexone (green, red or purple shades, respectively). Straight lines represent a threshold of 240º for Gln126[2.60] χ2 dihedral angle.
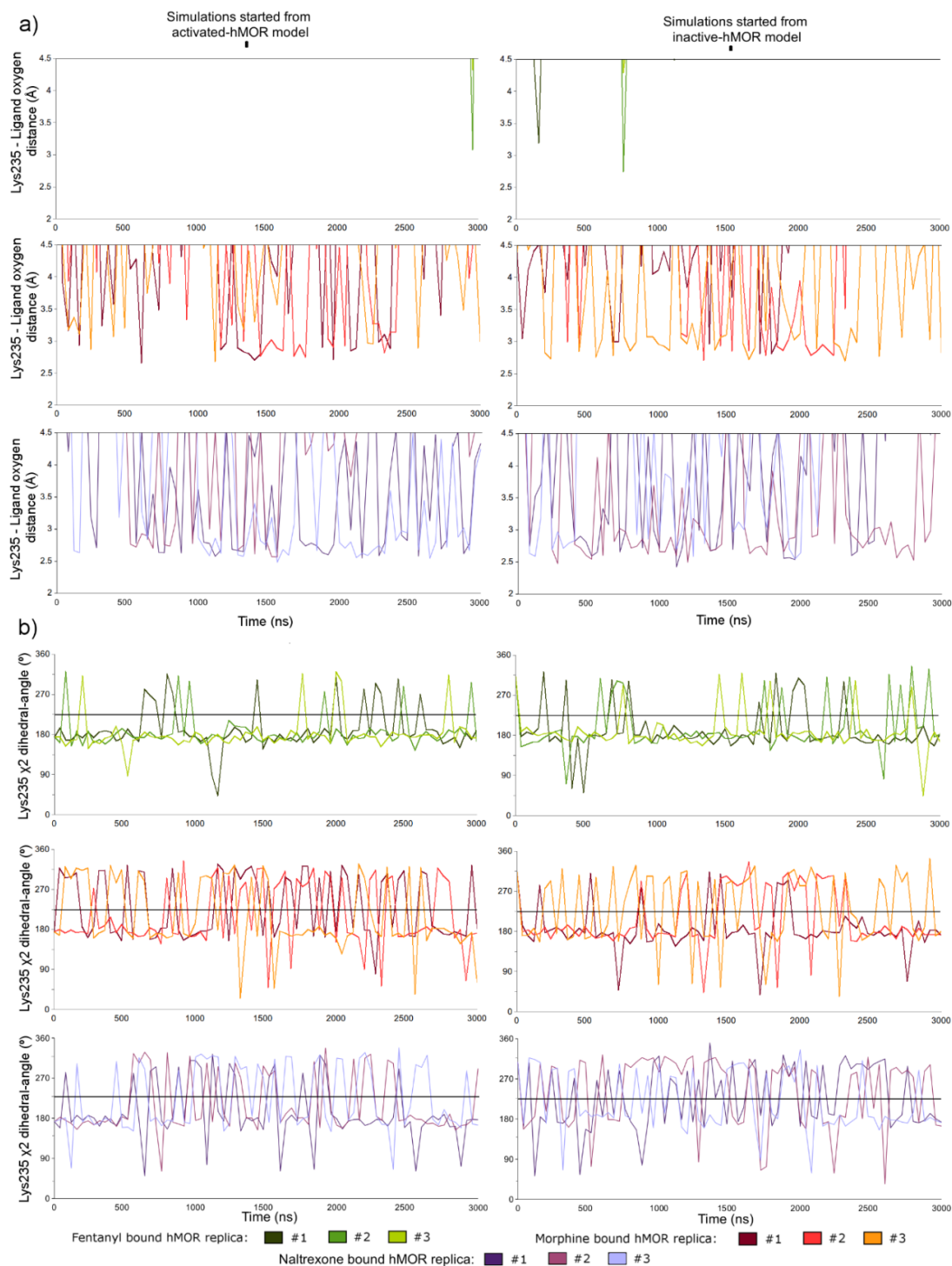
Supplementary Figure 17. Lys235$^{5.39}$ χ2 conformational change in MD simulations and interaction with ligand bound. Graphs showing as a function of time **a)** distance fluctuation between Lys235$^{5.39}$ amino group and respective ligand oxygen acceptors within interaction formation distance (<4.5 Å), and **b)** Lys235$^{5.39}$ χ2 dihedral angle conformational change, of replicas #1-3 starting from activated or inactive state (left or right columns, respectively) with bound fentanyl, morphine or naltrexone (green, red or purple shades, respectively). Straight lines represent thresholds of 4.5 Å or 240º for interaction formation distance or Lys235$^{5.39}$ χ2 dihedral angle, respectively.

145
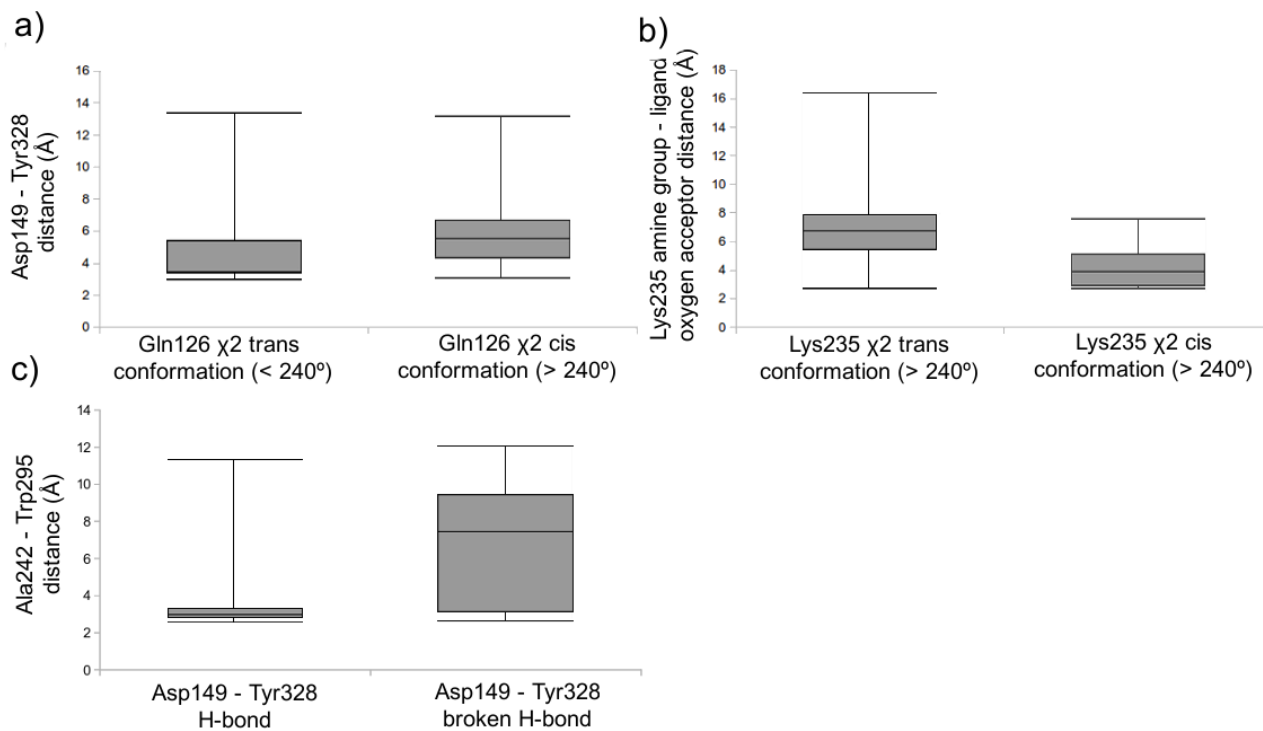
Supplementary Figure 18. Distribution of orthosteric pocket conformational changes (independent of agonist bound or starting receptor state) in MD simulations. Distribution of **a)** $Asp^{3.32}$-$Tyr328^{7.43}$ interaction distance with respect to $Gln126^{2.60}$ conformation, **b)** $Lys235^{5.39}$ amine group-ligand oxygen interaction distance and $Lys235^{5.39}$ conformation, or **c)** $Asp149^{3.32}$-$Tyr328^{7.43}$ H-bonding and $Ala242^{5.46}$-$Trp295^{6.48}$ interaction distance.
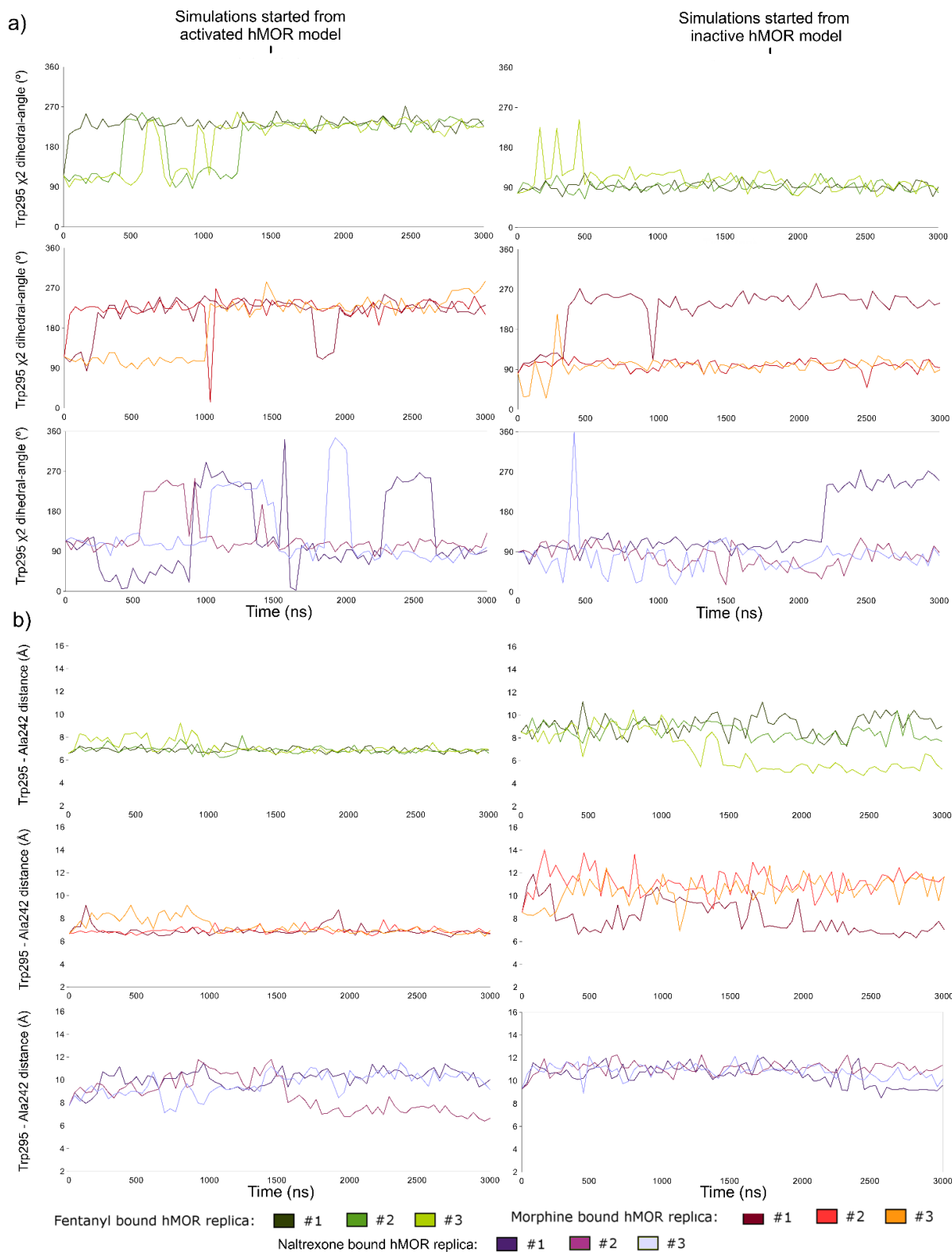
Supplementary Figure 19. Trp295[6.48] conformation and interaction with Ala242[5.46] in MD simulations. Graphs showing, as a function of time, **a)** Trp295[6.48] χ2 dihedral angle, and **b)** Trp295[6.48]-Ala242[5.46] distance, of replicas #1-3 with bound fentanyl, morphine or naltrexone (top, middle and bottom rows, coloured with green, red or purple shades, respectively) starting from activated or inactive hMOR states (left or right columns, respectively).

147

a)

	Active-like state of TM3	Inactive-like state of TM3
Asp149-Tyr328 H-bond presence	192 [164.1]	169 [196.9]
Asp149-Tyr328 H-bond absence	217 [244.9]	322 [294.1]

Chi2: 14.569
p-value: <0.001

	Active-like state of TM5	Inactive-like state of TM5
Asp149-Tyr328 H-bond presence	162 [146.8]	199 [214.2]
Asp149-Tyr328 H-bond absence	204 [219.2]	335 [319.8]

Chi2: 4.425
p-value: 0.035

	Active-like state of TM6	Inactive-like state of TM6
Asp149-Tyr328 H-bond presence	155 [135.5]	206 [225.5]
Asp149-Tyr328 H-bond absence	183 [202.5]	356 [336.5]

Chi2: 7.441
p-value: 0.006

	Active-like state of NPxxY	Inactive-like state of NPxxY
Asp149-Tyr328 H-bond presence	234 [218.6]	127 [142.4]
Asp149-Tyr328 H-bond absence	311 [326.4]	228 [212.6]

Chi2: 4.589
p-value: 0.032

	Active-like state of Arg-Thr	Inactive-like state of Arg-Thr
Asp149-Tyr328 H-bond presence	136 [121.5]	225 [239.5]
Asp149-Tyr328 H-bond absence	167 [181.5]	372 [357.5]

Chi2: 4.332
p-value: 0.037

b)

	Active-like state of TM3	Inactive-like state of TM3
Tyr150-ligand H-bond presence	275 [249.5]	274 [299.5]
Tyr150-ligand H-bond absence	134 [159.5]	217 [191.5]

Chi2: 12.259
p-value: <0.001

	Active-like state of TM5	Inactive-like state of TM5
Tyr150-ligand H-bond presence	267 [223.3]	282 [325.7]
Tyr150-ligand H-bond absence	99 [142.7]	252 [208.3]

Chi2: 37.032
p-value: <0.001

	Active-like state of TM6	Inactive-like state of TM6
Tyr150-ligand H-bond presence	220 [206.2]	329 [342.8]
Tyr150-ligand H-bond absence	118 [131.8]	233 [219.2]

Chi2: 3.803
p-value: 0.051

	Active-like state of NPxxY	Inactive-like state of NPxxY
Tyr150-ligand H-bond presence	298 [332.5]	251 [216.5]
Tyr150-ligand H-bond absence	247 [212.5]	104 [138.5]

Chi2: 23.206
p-value: <0.001

	Active-like state of Arg-Thr	Inactive-like state of Arg-Thr
Tyr150-ligand H-bond presence	206 [184.8]	343 [364.2]
Tyr150-ligand H-bond absence	97 [118.2]	254 [232.8]

Chi2: 9.372
p-value: 0.002

c)

	Active-like state of TM3	Inactive-like state of TM3
Lys235-ligand H-bond presence	157 [155.8]	186 [187.2]
Lys235-ligand H-bond absence	252 [253.2]	305 [303.8]

Chi2: 0.024
p-value: 0.876

	Active-like state of TM5	Inactive-like state of TM5
Lys235-ligand H-bond presence	137 [139.5]	206 [203.5]
Lys235-ligand H-bond absence	229 [226.5]	328 [330.5]

Chi2: 0.120
p-value: 0.728

	Active-like state of TM6	Inactive-like state of TM6
Lys235-ligand H-bond presence	98 [128.8]	245 [214.2]
Lys235-ligand H-bond absence	240 [209.2]	317 [347.8]

Chi2: 19.075
p-value: <0.001

	Active-like state of NPxxY	Inactive-like state of NPxxY
Lys235-ligand H-bond presence	146 [207.7]	197 [135.3]
Lys235-ligand H-bond absence	399 [337.3]	158 [219.7]

Chi2: 75.093
p-value: <0.001

	Active-like state of Arg-Thr	Inactive-like state of Arg-Thr
Lys235-ligand H-bond presence	95 [115.5]	248 [227.5]
Lys235-ligand H-bond absence	208 [187.5]	349 [369.5]

Chi2: 8.844
p-value: <0.001

Supplementary Figure 20. Statistical analyses to assess the association between orthosteric and intracellular metrics I. Chi2 statistical analysis of orthosteric metrics: **a)** Asp149[3.32]-Tyr328[7.43] H-bond, **b)** Tyr150[3.33]-ligand H-bond or **c)** Lys235[5.39]-ligand H-bond; comparing active- or inactive-like states of intracellular metrics, independently of the ligand bound or the starting state of the receptor: i) TM3 upward-, ii) TM5 inward-, iii) TM6 outward-, iv) NPxxY inward-movement, or v) Arg167[3.50]-Thr281[6.34] distance.

a)

	Active-like state of TM3	Inactive-like state of TM3
Trp295-Ala242 H-bond presence	210 [170.4]	165 [204.6]
Trp295-Ala242 H-bond absence	199 [238.6]	326 [286.4]

Chi2: 23.890
p-value: <0.001

	Active-like state of TM5	Inactive-like state of TM5
Trp295-Ala242 H-bond presence	286 [152.5]	89 [222.5]
Trp295-Ala242 H-bond absence	80 [213.5]	445 [311.5]

Chi2: 337.658
p-value: <0.001

	Active-like state of TM6	Inactive-like state of TM6
Trp295-Ala242 H-bond presence	296 [140.8]	79 [234.2]
Trp295-Ala242 H-bond absence	42 [197.2]	483 [327.8]

Chi2: 469.332
p-value: <0.001

	Active-like state of NPxxY	Inactive-like state of NPxxY
Trp295-Ala242 H-bond presence	342 [227.1]	33 [147.9]
Trp295-Ala242 H-bond absence	203 [317.9]	322 [207.1]

Chi2: 252.742
p-value: <0.001

	Active-like state of Arg-Thr	Inactive-like state of Arg-Thr
Trp295-Ala242 H-bond presence	295 [126.3]	80 [248.7]
Trp295-Ala242 H-bond absence	8 [176.7]	517 [348.3]

Chi2: 582.918
p-value: <0.001

b)

	Active-like state of TM3	Inactive-like state of TM3
Met153 *gauche*-conformation presence	373 [330.8]	355 [397.2]
Met153 *gauche*-conformation absence	36 [78.2]	136 [93.8]

Chi2: 51.541
p-value: <0.001

	Active-like state of TM5	Inactive-like state of TM5
Met153 *gauche*-conformation presence	339 [296.1]	389 [431.9]
Met153 *gauche*-conformation absence	27 [69.9]	145 [102.1]

Chi2: 54.941
p-value: <0.001

	Active-like state of TM6	Inactive-like state of TM6
Met153 *gauche*-conformation presence	296 [273.4]	432 [454.6]
Met153 *gauche*-conformation absence	42 [64.6]	130 [107.4]

Chi2: 15.648
p-value: <0.001

	Active-like state of NPxxY	Inactive-like state of NPxxY
Met153 *gauche*-conformation presence	413 [440.8]	315 [287.2]
Met153 *gauche*-conformation absence	132 [104.2]	40 [67.8]

Chi2: 23.330
p-value: <0.001

	Active-like state of Arg-Thr	Inactive-like state of Arg-Thr
Met153 *gauche*-conformation presence	275 [245.1]	453 [482.9]
Met153 *gauche*-conformation absence	28 [57.9]	144 [114.1]

Chi2: 28.786
p-value: <0.001

c)

Trp295-Ala242 distance		Descriptives		Levene		T-test		
		Mean	SD	F	Sig.	t	df	Sig.
TM3 state	Active-like	8.81	1.963	17.664	<0.001	2.617	898	0.009
	Inactive-like	8.47	1.864					
TM5 state	Active-like	7.71	1.651	13.624	<0.001	-12.850	898	<0.001
	Inactive-like	9.25	1.834					
TM6 state	Active-like	6.91	0.724	270.309	<0.001	-28.899	898	<0.001
	Inactive-like	9.66	1.653					
NPxxY state	Active-like	7.38	1.239	14.400	<0.001	-40.307	898	<0.001
	Inactive-like	10.53	0.979					
Arg-Thr state	Active-like	6.88	0.327	423.091	<0.001	-25.578	898	<0.001
	Inactive-like	9.51	1.774					

Supplementary Figure 21. Statistical analyses to assess the association between orthosteric and intracellular metrics II. Chi2 statistical analysis of orthosteric metrics of **a)** Trp295[6.48]-Ala242[5.46] H-bond or **b)** Met153[3.36] *gauche*- conformation selection; or **c)** T-test of Trp295[6.48]-Ala242[5.46] distance considering equal or unequal variances depending on the Levene test; comparing active- or inactive-like states of intracellular metrics, independently of the ligand bound or the starting state of the receptor: i) TM3 upward-, ii) TM5 inward-, iii) TM6 outward-, iv) NPxxY inward-movement, or v) Arg167[3.50]-Thr281[6.34] distance.
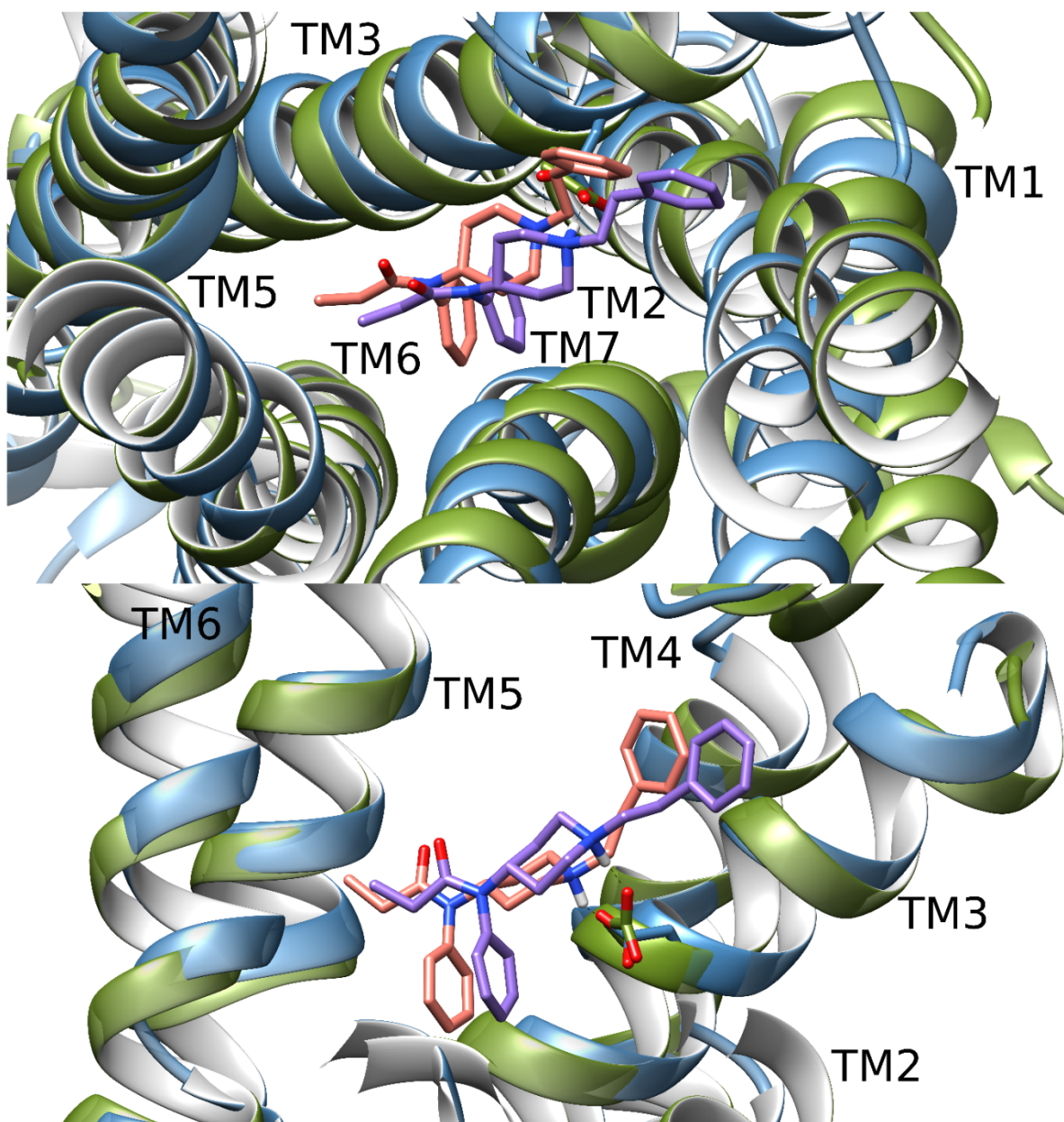
Supplementary Figure 22. Fentanyl docking in active MOR crystal structures. Upward and lateral view of docked fentanyl (purple) in activated hMOR model (green) compared with docked fentanyl (salmon) in fully active Gi-bound mMOR crystal structure (blue).